

Second harmonic generation in III-V integrated structures

by
Nicolas POULVELLARIE

Supervisors

Prof. Simon-Pierre GORZA
Université libre de Bruxelles
OPERA-Photonics

and

Prof. Bart KUYKEN
UGent
Department of Information Technology

Thesis presented in fulfilment of the requirements of the
PhD Degree in engineering sciences and technology (ULB) and in
Photonics Engineering (UGent)
Academic year 2020-2021

Nederlandse abstract

De laatste decennia is de niet-lineaire fotonica steeds meer in de belangstelling komen te staan. Dit is te danken aan de uitvinding van de laser en het eerste experimentele bewijs van een niet-lineair optisch proces in 1961 door Peter Franken en zijn team. Niet-lineaire fotonica heeft bewezen nuttig te zijn voor een groot aantal toepassingen. Het wordt vooral gebruikt voor frequentieomzetting en spectrale verbreding. Deze effecten worden nog steeds onderzocht met het oog op een beter begrip dat kan leiden tot nog efficiëntere processen en nieuwe technologische vooruitgang.

Bovendien heeft de opkomst van geïntegreerde fotonica een positieve invloed gehad op de niet-lineaire fotonica. Dankzij de hoge mate van opsluiting van het licht in structuren van een micrometer of zelfs een tiental nanometer, is de efficiëntie van de niet-lineaire fotonica blijven toenemen. Hierdoor is het mogelijk om centimeters grote platforms te verkrijgen waarvoor vroeger een hele laboratoriumtafel nodig was. In dit verband zijn ook andere vorderingen gemaakt. Golfgeleiders met laag verlies zijn ook ontwikkeld en verleggen momenteel nieuwe grenzen. De ontwerpen worden ingenieuzer en gesofisticeerder om geïntegreerde componenten te ontwikkelen zoals interferometers, mode-converters, resonatoren en nog veel meer.

Geïntegreerde fotonica en niet-lineaire fotonica is geschikte combinatie voor golflengteomzetting, spectroscopie, modulatie en nog veel meer. Voor onderzoekers was het dus niet meer dan een evidentie om deze twee aspecten samen te brengen. Eén onderwerp dat nog steeds aandacht behoeft, en dat sinds het begin de aandacht van de wetenschappelijke gemeenschap heeft gehouden, is het proces van tweede harmonische generatie.

Tweede harmonische generatie is experimenteel bewezen in 1961 door Peter Franken en zijn team. Niettemin heeft dit proces nog steeds voordelen voor de gemeenschap en kent het vele toepassingen zoals biologische beeldvorming of korte pulsmetingen.

Het is in deze context dat dit doctoraat plaatsvindt. Voor een beter begrip van dit specifieke niet-lineaire proces in geïntegreerde platforms, zullen we in dit proefschrift de eigenschappen van het tweede harmonische generatieproces bekijken in het geval van sterk begrensde elektromagnetische golven. Voor deze studie richten we ons op een bepaalde legering van elementen die III-V materialen zijn. Dit zijn materialen die, voor sommige ervan, een goede tweede orde niet-lineaire susceptibiliteit vertonen, alsook een CMOS compatibiliteit. De eigenschappen die van belang zijn voor deze doctoraalscriptie zullen in dit proefschrift worden uitgewerkt.

Voor een goed begrip van het onderwerp, begint deze dissertatie met een presentatie van concepten over niet-lineaire optica. De nadruk zal liggen op tweede harmonische generatie, maar voor een beter overzicht worden ook andere tweede orde niet-lineaire effecten gepresenteerd, evenals derde orde niet-lineaire effecten. Geïntegreerde fotonica wordt voorgesteld. De bijzonderheid van een sterk begrensd licht dat in een golfgeleider reist, zal in detail worden besproken. Niet-lineaire optica en geïntegreerde optica worden vervolgens met elkaar in verband gebracht en er wordt speciale aandacht besteed aan het proces van tweede harmonische generatie in geïntegreerde structuren. Hierna volgt een

presentatie van III-V materialen. De eigenschappen van deze materialen worden in dit deel besproken. Verbanden tussen deze materiaaleigenschappen en de eerste delen worden gelegd om nauwkeuriger op het onderwerp in te gaan. Verschillende fabricageprocessen die worden gebruikt om III-V-platforms te ontwerpen, worden ook in dit deel gepresenteerd. Dit is nodig om het fabricageproces te begrijpen dat is gebruikt voor de bestudeerde structuren.

Tenslotte worden de resultaten gepresenteerd die zijn verkregen in twee verschillende soorten structuren. Elk van deze twee structuren wordt eerst voorgesteld met een bepaald model om het proces van tweede harmonische generatie dat erin optreedt te begrijpen. Vervolgens worden numerieke simulaties uitgevoerd rond het ontwikkelde model en tenslotte worden de experimentele resultaten gepresenteerd en vergeleken met de resultaten van de simulaties. De twee structuren die in dit werk zijn gebruikt zijn de nanogolfgeleiders en de nanoringen.

De nanogolfgeleiders zijn eerst gebruikt om tweede harmonische generatie te bereiken in indium gallium fosfide via modale faseovereenstemming. Details over het gebruikte fabricageproces worden gegeven voor dit soort structuren met dit specifieke III-V-materiaal. Verschillende typen faseovereenstemming zijn hier gebruikt in nanodraden: het type I en het type II. De verschillen in het opwekkingsproces tussen deze twee worden toegelicht, evenals het verschil in efficiëntie en de afmetingen van de golfgeleider die nodig zijn om de efficiëntie te verhogen. De experimenten die in deze structuren zijn uitgevoerd, hebben het mogelijk gemaakt de omzettingsefficiëntie te meten van de pomp naar de tweede harmonische voor beide types van fase-afstemming. De verschillen tussen de theoretische simulaties en de experimentele resultaten in dit deel worden verklaard en helpen om de beperkingen te begrijpen die bij dergelijke experimenten kunnen optreden, zoals bijvoorbeeld het fabricageproces.

De nanoringen zijn vervolgens bestudeerd. Er wordt een uiteenzetting gegeven van de eigenschappen van dergelijke structuren die het belang ervan verklaren. Deze structuur maakt een hogere omzettingsefficiëntie mogelijk dan nanogolfgeleiders, doordat het licht verschillende keren rond loopt voordat het de ring verlaat en dus meerdere malen met het medium interageert. Voor dit type structuur is een ander III-V-materiaal gebruikt: galliumfosfide. Het specifieke fabricageproces voor dit materiaal en de nanoringen wordt gepresenteerd. Na de presentatie van het model wordt nagegaan aan welke voorwaarden moet worden voldaan om een tweede harmonische in een dergelijke structuur op te wekken door gebruik te maken van quasifase-matching. De eerste verkregen resultaten zijn veelbelovend, maar er is meer werk nodig, met name op dit gebied.

Zoals we kunnen zien, is dit proefschrift een compleet project voor de studie van het tweede harmonische generatie-effect. Het bevat delen over de ontwikkeling van numerieke modellen, simulaties rond deze modellen aangepast aan het materiaal in kwestie, fabricage van de structuren volgens het ontwerp gevonden tijdens de simulaties en die de beste resultaten bieden in overeenstemming met het gewenste resultaat. Tenslotte worden de structuren getest op een experimentele proefbank en vergeleken met de resultaten verkregen uit de modellen en simulaties.

Als conclusie, kan worden gesteld dat het in deze dissertatie gepresenteerde werk tot doel heeft een beter begrip te krijgen van het bijzondere tweede orde niet-lineaire effect dat tweede harmonische generatie is in sterk begrensde structuren van III-V materiaal. Het is ook mogelijk om de modellen die in dit proefschrift worden beschreven aan te passen aan andere soorten materialen, omdat dit afhangt van de symmetrie van het gebruikte kristal. Twee verschillende structuren worden gepresenteerd. De verkregen resultaten bieden een numerieke benadering van de tweede harmonische generatie in opgesloten structuren en geven inzicht in de beperkingen in deze specifieke structuur.

English abstract

For the last decades, nonlinear photonics has gained more and more interest over the years. This is thanks to the invention of the laser and the first experimental proof of nonlinear optical process in 1961 by Peter Franken and his team that nonlinear photonics has never stopped attracting the attention of researchers. Nonlinear photonics has proven to be useful for a lot of applications. It is mainly used when it comes to frequency conversion and spectral broadening. These effects are still under the research world scope for a better understanding that could lead to even more efficient processes and new technological advances.

In addition, the emerging of integrated photonics has had a positive impact on nonlinear photonics. Indeed, due to the high confinement of the light inside micrometer, and even nanometer, structures, the efficiency of the nonlinear photonics effects has never stopped increasing since. It allows obtaining in centimetres size platforms that required a whole laboratory bench before. Other advances have also been done in this context. Low-loss waveguides are also developed and break new limits currently. The designs become more ingenious and sophisticated to develop integrated components such as interferometers, mode converters, resonators, and much more.

Integrated photonics and nonlinear photonics are truly a great combination for wavelength conversion, spectroscopy, modulation, and much more. So, it was only obvious to researchers to join these two aspects. And one topic that still needs attention, and has kept the attention of the scientific community since its beginning, is the second harmonic generation process.

As we said, second harmonic generation has been experimentally proved in 1961 by Peter Franken and his team. Nevertheless, this process still benefits the community and has a lot of applications as biological imaging or short pulse measurement. And I think that this process still requires a better understanding and an in-depth study of integrated platforms.

This is in this context that this PhD takes place. For a better understanding of this particular nonlinear process in integrated platforms, we will see in this thesis the properties of the second harmonic generation process in the case of strongly confined electromagnetic waves. For this study, we focus on a particular alloy of elements that are III-V materials. These are materials that present, for some of them, a good second order nonlinear susceptibility as well as CMOS compatibility. There are different alloys possible, every one of them has its particularities. The characteristics of interest for this PhD matter will be developed in this thesis.

For a good comprehension of the topic, this thesis starts with a presentation of concepts about nonlinear optics. The focus will be on second harmonic generation, but other second-order nonlinear effects are presented for a better overview, as well as third-order nonlinear effects. Integrated photonics is presented. The particularity of a strongly confined light travelling inside a waveguide will be detailed. Nonlinear optics and integrated optics are then linked together and special attention to second harmonic generation pro-

cess in integrated structures is given. A presentation of III-V materials is following. The properties of these materials are discussed in this part. Links between these materials' properties and the first parts are made to be more accurate on the topic. Several fabrication processes used to conceive III-V platforms are also presented in this part. This is required to understand the fabrication process that has been used for the structures studied.

Finally, presentations of the results obtained in two different kinds of structures are made. Each of these two structures is first presented with a particular model to understand the second harmonic generation process that occurs in it. Numerical simulations are thus performed around the model developed and, finally, experimental results are presented and compared to the results from the simulations. The two structures that have been used in this work are the nanowires and the nanorings.

The nanowires have first been used to achieve second harmonic generation in indium gallium phosphide via modal phase matching. Details for the fabrication process used are given for those kinds of structures with this particular III-V material. Different types of phase matching have been used in nanowires here: type I and type II. The differences in the generation process between these two are explained, as well as their efficiency difference and the waveguide dimensions requirements to increase the efficiency. The experiments performed in these structures allowed to measure the conversion efficiency from the pump to the second harmonic for both types of phase matching. The differences observed between the theoretical simulations and the experimental results in this part are explained and help to understand the limitations that can be encountered in such experiments such as the fabrication process for instance.

The nanorings have then been studied. It is a widely used structure in neural networks or lasers, for instance. A presentation of the properties of such structures explaining their interest is made. Briefly, this structure allows higher conversion efficiency, compared to nanowires, since the light makes several roundtrips before exiting the ring and so interact several times with the medium. For this type of structure, another III-V material has been used: gallium phosphide. The particular fabrication process involved for this material and the nanorings is presented. After presenting the model, we see which conditions to fulfil to generate second harmonic in such a structure by using quasi-phase matching. The first results obtained are really promising, but more work is required on this topic in particular.

As we can see, this thesis is a complete project for the study of the second harmonic generation effect. It contains parts on numerical model development, simulations around these models adapted to the material of concern, fabrication of the structures according to the design found during the simulations, and which offer the best results in agreement with the result wanted. Finally, the structures are being tested on an experimental bench and compared to the results obtained from the models and simulations.

To conclude, the work presented in this thesis aims to a better understanding of the particular second-order nonlinear effect that is second harmonic generation in strongly confined structures made of III-V material. It is also possible to adapt models exposed in this thesis to different kinds of material, as it depends on the symmetry of the crystal used. Two different structures are presented. The results obtained offer a numerical approach to the second harmonic generation in confined structures and bring an understanding of the limitations in this particular structure.

Acknowledgements

I never knew that I will end up in a PhD study. Even up to the master degree level. I think I just met some peoples on my way that offer me opportunities to pursue my studies. This last step, the thesis, has been one of the biggest of all.

For this, I want to thank François Leo for the opportunity to work on this project. I also want to express my gratitude to my supervisors, Simon-Pierre Gorza for his patience and the time spend to answer my questions, and Bart Kuyken for the answers and interesting thoughts brought. All three of us offer me their time and knowledge, and I'm grateful for this. I also thank Marc Haelterman for his interest in the topic and the progress.

I want to thank all people from both research groups, past and present: OPERA and PRG. Thank you for the sympathetic company, the funny times, and also the critical thoughts on my subject. I am grateful to Fabrice Raineri, a member of the C2N group in Paris, for the reception when I went to visit them for the fabrication of the chips. I also thank them for the incredible technical knowledge that they have and shared with me.

I am particularly grateful to Maximilien Billet for always offering his help and granting it when it was needed. I also thank Carlos Mas Arabi for the enlightenment he brought me about theoretical aspects.

I thank Ibtissame Malouli, Alexandra Peereboom, and David Houssart for their administrative support.

I want to particularly thank Michael Fita Codina for all the tools he made for me and the time spent on it to offer the best quality possible. I also thank him for everything else that makes him a colleague, but also an excellent friend.

I also want to thank all my friends for their nice company and encouragement.

Finally, I want to thank my family for their moral support. And, most importantly, I want to thank my girlfriend and my daughter. My girlfriend for her incredible support and help and especially during the period of thesis writing. My daughter, although, for a one-year-old child, not very understanding of the importance of the writing part of the thesis, offers me the prettiest and most recomforting smiles.

Contents

Nederlandse abstract	i
English abstract	iii
Acknowledgements	v
List of figures	viii
List of tables	xi
1 Introduction	1
1.1 Nonlinear photonics	1
1.1.1 Basics principles	2
1.1.2 Second-order nonlinear effects	3
1.1.3 Third-order nonlinear effects	7
1.2 Integrated photonics	9
1.2.1 Interest and impact	9
1.2.2 Light propagation in integrated structures	11
1.2.2.1 Slab waveguide study	11
1.2.2.2 Buried waveguide study	13
1.2.3 Nonlinear photonics in integrated platforms	17
1.2.4 SHG in integrated platforms	20
2 III-V integrated photonics	28
2.1 III-V materials	29
2.1.1 State of the art on III-V materials	29
2.1.2 Optical properties of III-V materials	31
2.2 Integration of III-V materials	36
2.2.1 Material deposition on a substrate	36
2.2.1.1 Epitaxy process	36
2.2.1.2 Chemical vapour deposition	37
2.2.1.3 Physical deposition	39
2.2.2 Patterning of the III-V	41
2.2.2.1 Ultraviolet lithography	41
2.2.2.2 Electron-beam lithography	42
2.2.3 Etching	43
3 Second harmonic generation in III-V nanowires	55
3.1 State of the art	55
3.2 InGaP as a platform	56
3.2.1 Linear properties	56

3.2.2	Nonlinear properties	58
3.3	SHG in InGaP nanowires	58
3.3.1	Analytical model	59
3.3.1.1	Type I second harmonic generation model	59
3.3.1.2	Type I second harmonic generation nonlinear coefficient calculation	60
3.3.1.3	Type II second harmonic generation case	61
3.3.2	Numerical simulations	62
3.3.2.1	Type I second harmonic generation	62
3.3.2.2	Type II second harmonic generation	67
3.3.3	Experimental results	68
3.3.3.1	Type I second harmonic generation	74
3.3.3.2	Type II second harmonic generation	78
3.3.3.3	Summary of the results	81
3.4	AlGaAs as a nonlinear platform	84
3.4.1	Properties	84
3.4.2	Fabrication process particularities	84
3.4.3	Simulations	87
4	Second harmonic generation in III-V nanorings	94
4.1	Nanorings theory	94
4.1.1	Nanorings fundamentals	94
4.1.2	SHG in III-V nanorings	96
4.2	GaP as a platform	99
4.2.1	Properties of GaP	99
4.2.2	Simulations	100
4.2.3	Experimental results	102
4.2.3.1	Impact of the chip temperature and the angle of the optical fibre for the injection	104
4.2.3.2	Multimodal transmission and thermal effects	106
4.2.3.3	Research of the two quasi-phase matching points	108
5	Conclusion and perspectives	116

List of Figures

1.1	Representation of the sum-frequency generation effect	3
1.2	Second harmonic power as a function of the detuning and second harmonic amplitude during the propagation in a medium for different wavelength detunings	5
1.3	Representation of type I and type II phase-matching case	6
1.4	Schematic of the quasi-phase-matching process	7
1.5	Self-phase modulation impact on a gaussian shaped beam	8
1.6	Photonics integrated circuits applications	10
1.7	Rectangular waveguides profile geometry	11
1.8	Asymmetric slab waveguide representation with the refractive index profile	12
1.9	Schematic of the propagation of two different modes in a waveguide	13
1.10	All electric fields components of a mode in a rectangular waveguide	14
1.11	Modes components of different modes to see the symmetry link between the different components	16
1.12	Some modes profiles possible in a rectangular waveguide	17
1.13	Modal refractive indices for different modes in a rectangular waveguide . .	18
1.14	Optical frequency comb representation	19
1.15	Optical event horizon in a nonlinear waveguide	19
1.16	Optical frequency comb referencing via the second harmonic generation . .	20
2.1	Periodic table of the elements	28
2.2	Industrial applications of III-V materials	29
2.3	Mobility of charges inside different materials at room temperature	30
2.4	Evolution of solar panels conversion efficiency over the years	31
2.5	Bandgap energy of different materials as a function of their lattice constant	32
2.6	Refractive index of some III-V materials	33
2.7	Representation of frames in a rectangular waveguide for theoretical analysis	34
2.8	Chemical vapour deposition machines	38
2.9	Explanation of the bonding steps for material deposition on a substrate . .	39
2.10	Pictures of successful bondings	40
2.11	Transfer printing steps development	41
2.12	Ultraviolet lithography steps representation	42
2.13	Pictures of waveguide patterning via ebeam lithography with and without the fixed beam moving stage option	43
2.14	Isotropic, anisotropic and perfectly anisotropic explanation representation .	44
2.15	Plasma etching machines schematic	45
2.16	Pictures from scanning electron microscopes of integrated structures	46
3.1	Refractive index of the indium gallium phosphide material	57
3.2	Difference between the ordered and disordered state for indium gallium phosphide	57

3.3	Conversion efficiency for a type I second harmonic generation process with a transverse electric pump for different waveguide profiles	63
3.4	Conversion efficiency for a type I second harmonic generation process with a transverse magnetic pump for different waveguide profiles	64
3.5	Profiles of the transverse electric and transverse magnetic fundamental mode	64
3.6	Representation of the overlapping integral for different phase matched cases	66
3.7	Conversion efficiency for a type II second harmonic generation process with a transverse electric and a transverse magnetic pump for different waveguide profiles	67
3.8	Schematic of the wafers involved for bonding	69
3.9	Overview of a particular chip design used for nonlinear study	70
3.10	Representation of mode conversion via the refractive indices of different modes for different waveguide width	71
3.11	Extraction of the linear losses in a waveguide from a picture of the waveguide illumination	72
3.12	Overview of a chip used for nonlinear studies characteristics	73
3.13	Schematic of an experimental setup used for second harmonic generation studies	74
3.14	Type I phase-matching found for two different waveguides profiles	75
3.15	Second harmonic power measures for the type I process	76
3.16	Theoretical and experimental modes profiles pictures	78
3.17	Type II phase-matching parameters with the Poynting vector and the refractive indices for the modes involved	79
3.18	Second harmonic power measure for the type II phase-matching case	80
3.19	Mode conversion in a taper explanation with the refractive indices for different waveguide width	80
3.20	Theoretical and experimental profiles measured for the type II phase-matching case	81
3.21	Refractive index of the aluminium gallium arsenide material	84
3.22	Pictures of the chip on which to deposit the aluminium gallium arsenide .	85
3.23	Fabrication process presentation for the aluminium gallium arsenid project	86
3.24	Microscope picture of an aluminium gallium arsenide sample after processing and scanning electron microscope picture of a cross section	86
3.25	Schematic of the different configurations for the simulations about aluminium gallium arsenide	87
4.1	Ring resonators parameters representation	95
4.2	Presentation of the electric fields for second harmonic in a ring resonator .	97
4.3	Ring resonator framework	97
4.4	Quasi-phase-matching in a III-V ring resonator	98
4.5	Refractive index of gallium phosphide material	99
4.6	Modes profiles modification due to the curve in a ring resonator	100
4.7	Azimuthal number mismatch and Poynting vectors of the modes involved for a particular design	102
4.8	Microscope pictures of the rings and experimental setup used for their study	103
4.9	Transmission of gratings couplers for different injection fibre angles	104
4.10	Resonance measurement in a ring resonator	105
4.11	Resonance measurement and second harmonic power measured for different temperatures	105

4.12	Transmission of a multimodal ring resonator and second harmonic power measures	107
4.13	Second harmonic power measured for a backward and forward wavelength sweep	108
4.14	Measurement of the transmission and second harmonic for a large wave- length range	108
4.15	Numerical fit of two resonances to extract ring parameters	109
4.16	Large wavelength range measure of resonances and second harmonic power in a ring	110

List of Tables

2.1	Second-order nonlinear susceptibility of different materials	33
2.2	Pertinent optical properties for different materials	35
3.1	Conversion efficiency in nanowires comparison	82
3.2	phase-matching results for aluminium gallium arsenide in different scenarios	88
4.1	Quasi-phase-matching wavelength and efficiency for different widths from simulations	101
4.2	Quasi-phase-matching wavelength for different widths and heights for two different second harmonic modes	110

AlGaAs	aluminium gallium arsenide
BCB	benzocyclobutene
CMOS	complementary metal oxide semiconductor
DTU	Technical University of Denmark (Danmarks Tekniske Universitet)
FBMS	fixed beam moving stage
FDE	finite difference eigenmode
FSR	free spectral range
FWHM	full width at half maximum
FWM	four-wave mixing
GaP	gallium phosphide
GaAs	gallium arsenide
HDPCVD	high-density plasma chemical vapour deposition
HF	hydrofluoric acid
HSQ	hydrogen silsesquioxane
ICP	inductively coupled plasma
InGaP	indium gallium phosphide
InGaAs	indium gallium arsenide
InP	Indium Phosphide
LiNbO₃	lithium niobate
LPCVD	low-pressure chemical vapour deposition
MPM	modal phase-matching
OFC	optical frequency comb
PECVD	plasma-enhanced chemical vapor deposition
PPLN	periodically poled lithium niobate
PM	phase matching
QPM	quasi-phase matching
RF	radio frequency
RIE	reactive ion etching
Si	silicon
SiN	silicon nitride

SiO₂	silicon oxide
SH	second harmonic
SHG	second harmonic generation
SPM	self-phase modulation
TE	transverse electric
TM	transverse magnetic
TPA	two-photon absorption
UV	ultraviolet
XPM	cross-phase modulation

Chapter 1

Introduction

For the last decades, photonics is booming. The Optical Society of America lists 31 Nobel Prizes in physics related to optics. The expansion is even more important since the invention of the laser by Theodore Maiman. This invention has opened a new field that is nonlinear optics. That is because, typically, only lasers have the intensity required to trigger the nonlinear effects.

On another hand, the invention of the laser leads to a whole new world of telecommunications. The network is thus developing around optical communications rather than electrical ones. And so the technology necessary for such transmission such as lasers, modulators, multiplexer... continues to develop. The usage of optical components for these technologies is attractive. That's a reason why integrated photonics is a growing field too. Instead of meters-long systems for detection and demultiplexing, it can be done in a centimetre-scale chip made of equivalent devices.

The objective of this thesis is to study the combination of both nonlinear optics and integrated photonics. It focuses on a second-order nonlinear effect in particular, which is second harmonic generation. In this thesis, theoretical models have been studied and developed to explain the second harmonic generation process in integrated structures. These structures have then been fabricated and experimentally tested to compare with the previous models. In the case of this thesis, we want the device to be compatible with a telecommunication system, so we work with wavelengths around 1550 nm. We also want to generate an efficient second harmonic. III-V materials have thus been used. They indeed present a high potential for second-order nonlinear effects, as we will see later.

This chapter has for purpose to have a complete apprehension of the theory about second harmonic generation in integrated structures. For this, the nonlinear and integrated aspects of photonics will be presented. First, nonlinear photonics will be introduced and some important effects for our concern will be developed. Then, the importance and particularities of integrated photonics will be presented. Finally, both fields will be linked, as we will see that it is a great combination for frequency conversion.

1.1 Nonlinear photonics

Nonlinear optics is the study of the modification of the optical properties of a medium via its interaction with light. The first experimental nonlinear effect was observed 50 years from now by Peter Franken and his team [1]. This breakthrough in the photonic world was possible thanks to the invention of the laser one year before by Theodore Maiman. It is remarkable how the advent of this new technology leads to a whole new world of possibilities. Nonlinear effects offer better results with a high-power coherent light. So

the coming together of these two discoveries is not a surprise. The range of applications nowadays for nonlinear effects is huge, as it goes from active components as laser for the frequency conversion to passive ones with optical switching. In this chapter, second-order nonlinear effects will be presented. A short presentation about third-order nonlinearities will also be made here.

1.1.1 Basics principles

The basics of nonlinear photonics are to study the interaction of light with a medium. When an electromagnetic wave, such as light, interacts with an atom, this results in different outcomes according to the material and the parameters of the incoming electromagnetic wave. During the interaction, the electromagnetic wave creates a disturbance in the electronic cloud of the atoms. The electrons will then oscillate at the same frequency as the incoming wave. This negative charge oscillating linearly, in simple harmonic motion, about a stationary positive charge, generates an electromagnetic field oscillating at the same frequency as the incoming wave. This dipole acquires a polarization that characterizes the polarization density of the medium under the influence of the electric field. Naturally, we expect this polarization to be proportional to the electric field strength:

$$P(t) = \epsilon_0 \chi^{(1)} E(t), \quad (1.1)$$

where ϵ_0 is the vacuum permittivity and $\chi^{(1)}$ is the linear susceptibility. However, when a stronger electromagnetic wave hits the atom, the oscillation from this last one becomes more complex. We can however predict the behaviour of the polarization $P(t)$ by generalizing the relation 1.1 as a power series of the components of the electric field $E(t)$ of the incoming wave, as long as we are far from the medium resonances [2]:

$$P(t) = \epsilon_0 [\chi^{(1)} E(t) + \chi^{(2)} E(t)^2 + \chi^{(3)} E(t)^3 + \dots], \quad (1.2)$$

where $\chi^{(2)}$ and $\chi^{(3)}$ stand for the second and third-order nonlinear susceptibilities, respectively. In the equation 1.2, the fields $P(t)$ and $E(t)$ have been taken as scalar quantities. We first start with this approximation for simplicity. In the following parts, we will introduce the vector nature of these components and thus the tensorial nature of the susceptibility. In such a case, $\chi^{(1)}$ becomes a second-rank tensor, $\chi^{(2)}$ a third-rank one, and so on.

Let's now express the propagation of the light inside a nonlinear medium. To do so, we are going to start with Maxwell's equations. These equations are a set of partial differential equations used to describe how the electric flux density (\mathbf{D}), the electric field intensity (\mathbf{E}), the magnetic flux density (\mathbf{B}), and the magnetic field intensity (\mathbf{H}) are generated by the electric charge density (ρ) and the electric current density (\mathbf{J}), and how they vary with the changes of the magnetic and electric flux density through time:

$$\begin{aligned} \nabla \cdot \mathbf{D} &= \rho, \\ \nabla \cdot \mathbf{B} &= 0, \\ \nabla \times \mathbf{E} &= -\frac{\partial \mathbf{B}}{\partial t}, \\ \nabla \times \mathbf{H} &= \frac{\partial \mathbf{D}}{\partial t} + \mathbf{J} \end{aligned} \quad (1.3)$$

We are here considering a propagating dielectric medium in which there are no free charges ($\rho = 0$), and that contains no free current ($\mathbf{J} = 0$). Moreover, if we consider the material as

non-magnetic, we can relate the magnetic field as $\mathbf{B} = \mu_0 \mathbf{H}$. The material is considered as nonlinear, which leads us to relate the electric fields as $\mathbf{D} = \epsilon_0 \mathbf{E} + \mathbf{P}$ with \mathbf{P} the polarization vector. We can thus express the electric fields as:

$$\begin{aligned} \nabla \times \nabla \times \mathbf{E} &= -\frac{\partial \nabla \times \mathbf{B}}{\partial t} \\ &= -\mu_0 \left[\epsilon_0 \frac{\partial^2 \mathbf{E}}{\partial t^2} + \frac{\partial^2 \mathbf{P}}{\partial t^2} \right]. \end{aligned} \quad (1.4)$$

For a wave expressed as $\mathbf{E}(\mathbf{r}) = \mathbf{A}(\mathbf{r}) \exp(i\mathbf{k} \cdot \mathbf{r})$ where A is the field amplitude and k the wavenumber, we can approximate the term on the left by $(-\nabla^2 \mathbf{E})$. To do so, the slowly varying approximation must be valid which means that we need :

$$\left| \frac{d^2 A}{dz^2} \right| \ll \left| k \frac{dA}{dz} \right|. \quad (1.5)$$

We here, and for the rest of the study, consider a wave propagating along the z-axis. Under the slowly varying approximation 1.5, the expression 1.4 becomes:

$$\nabla^2 \mathbf{E} - \frac{n^2}{c^2} \frac{\partial^2 \mathbf{E}}{\partial t^2} = \frac{1}{\epsilon_0 c^2} \frac{\partial^2 \mathbf{P}^{NL}}{\partial t^2}, \quad (1.6)$$

with n the refractive index of the medium and c the light velocity in vacuum and $P^{NL} = \epsilon_0 [\chi^{(2)} E(t)^2 + \chi^{(3)} E(t)^3 + \dots]$. We understand from this last equation that the nonlinear polarization P^{NL} drives the electric field.

1.1.2 Second-order nonlinear effects

From this, we're going to have a closer look at a second-order nonlinear effect in particular: the sum-frequency generation. It is important to mention that not all materials are suitable for second-order nonlinear effects. These effects require a noncentrosymmetric crystal, which means crystals that do not exhibit inversion symmetry [2]. Moreover, this effect has been chosen as a first approach of the second-order nonlinear effects because it is a general case study. The second harmonic generation (SHG) effect is, indeed, a particular case of this effect.

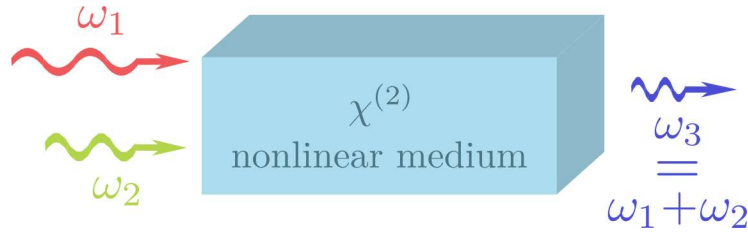


Figure 1.1: Representation of the sum-frequency generation effect where two pumps at a certain frequency interact in a $\chi^{(2)}$ nonlinear medium to generate a new wave at a frequency equal to the sum of both pump frequencies.

This effect, as represented in fig. 1.1, is when two incoming waves are generating a new wave by passing through a medium presenting second-order nonlinearities. The outgoing wave will oscillate at a frequency equal to the sum of both incoming ones. We can express each of the fields propagating in the z-direction as:

$$E_m(x, y, z, t) = A_m(x, y, z) \exp[i(k_m z - \omega_m t)] + c.c., \quad (1.7)$$

where E_m represents the electric field of the wave m oscillating at the frequency ω_m with an amplitude A_m and $k_m = \frac{n_m \omega_m}{c}$ is its associated wavenumber. In such a case, we can express the amplitude of the nonlinear polarization as $P_3 = 2\epsilon_0 \chi^{(2)} E_1 E_2$. We can thus express the wave equation 1.6 for the E_3 electric field as:

$$\left[\frac{d^2 A_3}{dz^2} + 2ik_3 \frac{dA_3}{dz} - k_3^2 A_3 + \frac{n_3^2}{c^2} \omega_3^2 A_3 \right] \exp[i(k_3 z - \omega_3 t)] = -\frac{2\chi^{(2)}}{c^2} \omega_3^2 A_1 A_2 \exp[i((k_1 + k_2)z - \omega_3 t)]. \quad (1.8)$$

We can notice here that $k_3 = n_3 \omega_3 / c$, resulting in the cancellation of the third and fourth terms on the left-hand side of equation 1.8. Also, we are still working under the slowly varying amplitude approximation, this means that the inequality 1.5 applies. The first term can then also be neglected here. The expression then becomes:

$$2ik_3 \frac{dA_3}{dz} \exp[i(k_3 z - \omega_3 t)] = -\frac{2\chi^{(2)}}{c^2} \omega_3^2 A_1 A_2 \exp[i((k_1 + k_2)z - \omega_3 t)]. \quad (1.9)$$

We can thus simplify the fast oscillation $\exp(-i\omega_3 t)$. The final expression then reads:

$$\frac{dA_3}{dz} = i \frac{\chi^{(2)} \omega_3^2}{k_3 c^2} A_1 A_2 \exp[i((k_1 + k_2 - k_3)z)] \quad (1.10)$$

By repeating the same derivation for the two pumps electric fields, we end up with:

$$\begin{aligned} \frac{dA_1}{dz} &= i \frac{\chi^{(2)} \omega_1^2}{k_1 c^2} A_2 A_3^* \exp[-i((k_1 + k_2 - k_3)z)], \\ \frac{dA_2}{dz} &= i \frac{\chi^{(2)} \omega_2^2}{k_2 c^2} A_3 A_1^* \exp[-i((k_1 + k_2 - k_3)z)]. \end{aligned} \quad (1.11)$$

We here introduce the phase-mismatch between the wavenumbers $\Delta k = k_1 + k_2 - k_3$. This parameter can be modified by tuning the dispersion of the propagation medium.

To analyze the influence of this parameter specifically, we here suppose that both amplitudes A_1 and A_2 are constant. It is a valid assumption as long as the conversion from the pumps to the generated field is not too important. This is better known as the undepleted pump approximation. With this assumption, we can solve the equation 1.10 and determine its amplitude at the end of the nonlinear medium of length L :

$$A_3(L) = i \frac{\chi^{(2)} \omega_3^2}{k_3 c^2} A_1 A_2 \int_0^L \exp[i(\Delta k z)] dz = i \frac{\chi^{(2)} \omega_3^2}{k_3 c^2} A_1 A_2 \frac{\exp[i(\Delta k L)] - 1}{i \Delta k}. \quad (1.12)$$

The intensity, which is defined as $P_m = |E_m|^2$, of the sum-frequency wave can thus be expressed as:

$$P_3(L) = \left(\frac{\chi^{(2)} \omega_3}{n_3 c} \right)^2 P_1 P_2 L^2 \sin^2 \left(\frac{\Delta k L}{2} \right). \quad (1.13)$$

In this last expression, we can see that the power of the wave at the sum frequency is maximum when the phase-mismatch is equal to zero. The expression of the second harmonic (SH) power P_{SH} found in the case of SHG when there is only one pump represented by a power P_p , is similar and reads:

$$P_{sh}(L) = \left(\frac{\chi^{(2)}\omega_{sh}}{n_{sh}c} \right)^2 P_p^2 L^2 \text{sinc}^2 \left(\frac{\Delta k L}{2} \right), \quad (1.14)$$

where Δk , in this case, is equal to $2k_p - k_{SH}$. The representation of the second harmonic power as a function of the phase-mismatch can also be seen in fig. 1.2(a). However, it is also interesting to see how the SH amplitude will vary along with the propagation for different phase-matching values.

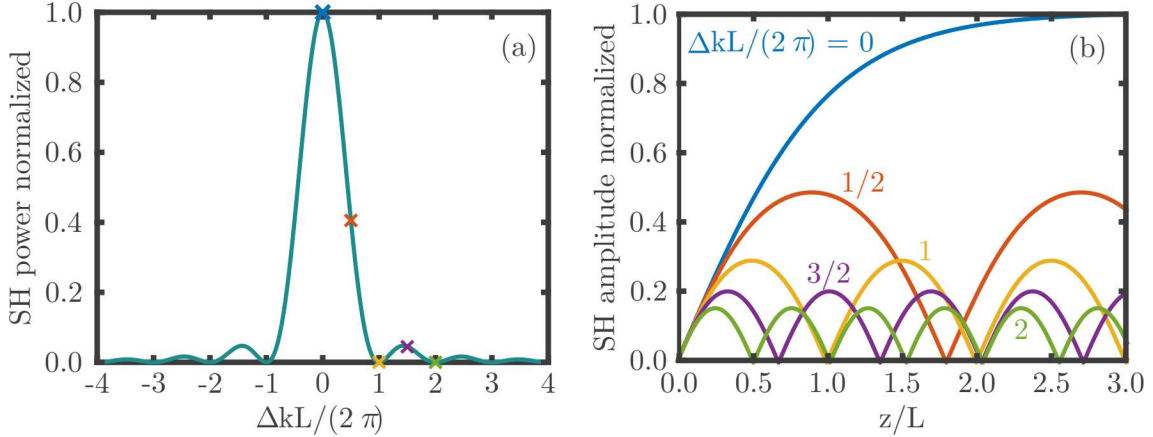


Figure 1.2: Evolution of the SH power as a function of the phase-mismatch (a) and SH amplitude during the propagation in a L long structure for different wavelength detunings (b). A cross has been placed on the left curve representing the position of each detuning represented on the right curve.

In the case of perfect phase-matching ($\Delta k = 0$), it has been shown in [3] that the SH amplitude follows a hyperbolic tangent function. When the phase-matching is different from 0, the amplitude is following a Jacobian elliptic function as represented in fig. 1.2(b). The maximum amplitude that can reach the generated wave for a given phase-mismatch value is defined, in the case where the SH power is zero at the beginning, by:

$$A_{shmax} = \frac{1}{\Delta k l / 4 + [1 + (\Delta k l / 4)^2]^{(1/2)}}, \quad (1.15)$$

where l is a characteristic interaction length for which around 75 % of the pumps will be converted to the SH wave and is expressed as $\sqrt{n_p n_{sh} c} / (\omega_p \chi^{(2)} |A_p(0)|)$ [3].

The most common way to achieve phase matching (PM) is to take advantage of the birefringence of the crystal, which is the property of a material for which the refractive index depends on the polarization direction of the electric field. In a birefringent medium, we define two different refractive indices: the ordinary refractive index (n_o) and the extraordinary refractive index (n_e). The first one is defined as the refractive index experienced by a wave polarized perpendicularly to the plane containing the propagation vector and the optical axis. The second one is when the polarization of the light is in the plane containing the propagation vector and the optic axis. In the case of III-V materials,

most of them have a zinc-blende structure. In this case, the birefringence is low [2]. It is thus not required to consider it, and thus we can do the assumption that $n_e(\omega) = n_o(\omega)$. For birefringent materials, the angle between the incoming waves' propagation vector and the material optic axis (the axis of the crystal for which the light suffers no birefringence) can be tuned to achieve PM.

The type I case happens when two photons, of two distinct waves, have the same polarization state and are used to generate a new photon at twice the frequency with a polarization state perpendicular to the pumps ones, as represented in fig. 1.3.

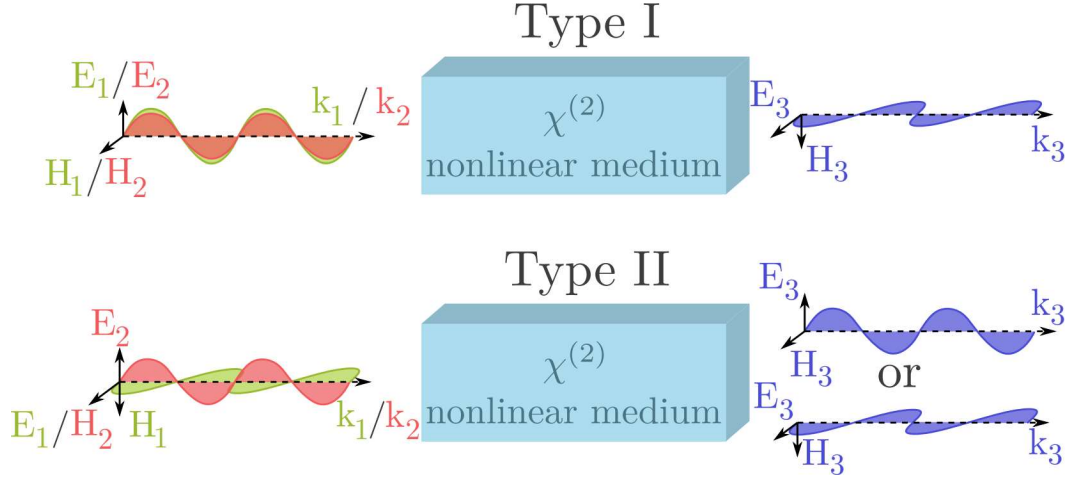


Figure 1.3: Representation of the type I and type II phase-matching interactions with two polarized pumps at the input. The type II case presents two solutions, as the second harmonic can be polarized along the same axis as any of the pumps.

The other case is the type II SHG process. In this case, the two pumps waves have a different, perpendicular polarization state and the wave generated has a polarization state along with one of those as seen in fig. 1.3.

The type II phase-matching interaction presented in fig. 1.3 is easy to picture for a sum-frequency generation process as two pumps are involved. Each of them is indeed polarized along a different axis. However, in the case of SHG, it seems more difficult to achieve. The trick is to put the pump in an intermediate polarization state so that we have a projection of the pump along both polarization axes.

Another commonly used method for SHG is the quasi-phase matching (QPM) [3, 4]. It is used to compensate for unsuitable properties of a material that will not allow standard PM otherwise. Indeed, we already said that the dispersion is responsible for the phase-mismatch [5, 6] and so no second-order nonlinear effect can be obtained from the material as it naturally is. To realize this, some materials can be periodically poled, as represented in fig. 1.4, to compensate the phase-mismatch due to the dispersion and thus enable a SHG process for instance [4].

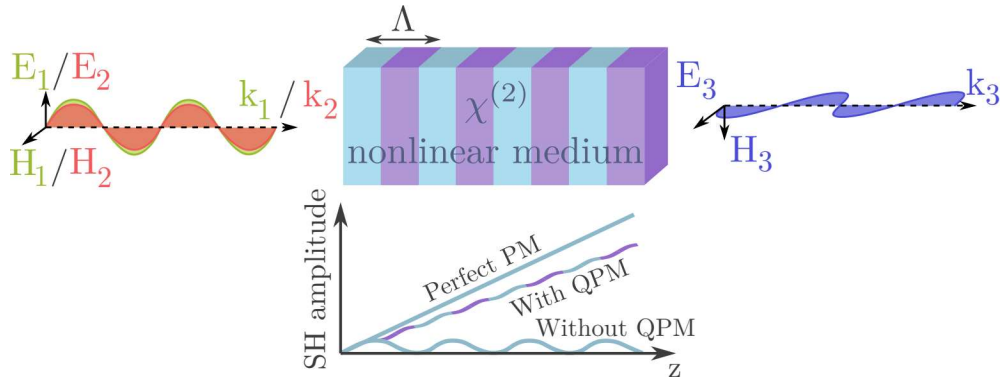


Figure 1.4: Representation of the QPM process that occurs in a periodically poled material.

The period defining the poling is written as $\Lambda = \frac{2\pi}{\Delta k}$. This value can thus be accurately chosen for a specific wavelength knowing the dispersion properties of the medium used. In the case of QPM, the amplitude grows with the propagation distance, but it doesn't reach the efficiency of a perfect phase-matching process. In the case of this thesis, we use QPM for SHG in III-V nanorings resonators. The particular symmetry of III-V materials makes QPM natural to achieve in this structure, as we will see later.

This ends the part on the second-order nonlinear effects. We are now going to take a brief look at some third-order nonlinear effects.

1.1.3 Third-order nonlinear effects

Unlike the second-order nonlinear effects presented before, third-order nonlinear effects can occur for both centrosymmetric and noncentrosymmetric media. One of the most famous effects when it comes to third-order nonlinearities is the Kerr effect. We first define a monochromatic light for which the electric field is written as $E(t) = E_0 \exp(i\omega t) + c.c.$ and such that the intensity I of the field is defined by $|E_0|^2$. Then the refractive index of the material can be written as [7]:

$$n = n_0 + n_2 I, \quad (1.16)$$

where $n_0 = (1 + \chi^{(1)})^{1/2}$ is the linear refractive index of the material, $n_2 = 3\chi^{(3)}/(4n_0)$ [8] is the nonlinear refractive index and I is the intensity of the electric field. When dealing with guided waves, it is also quite common to find the γ coefficient to express the efficiency of the third-order nonlinear process. This parameter is linked to the nonlinear refractive index by the relation [7]:

$$\gamma = \frac{\omega_0 n_2}{c A_{eff}}, \quad (1.17)$$

where A_{eff} is the effective area of the optical mode. This effect is the basis of two other effects that will be discussed below: the self-phase modulation (SPM) and the cross-phase modulation (XPM).

Concerning the SPM, it is a modification self-induced by an intense light on its phase. By defining the electric field as $E(x, y, t) = E_0(x, y) \exp(i\omega t + \phi)$ where $\phi = 2\pi/\lambda n z$, we can show that its instantaneous frequency $d\phi/dt$ changes over time. The refractive index is written as shown in eq. 1.16, the instantaneous frequency becomes $d\phi/dt =$

$(2\pi/\lambda)n_2(dI/dt)z$ and thus the frequency of the wave becomes $\omega' = \omega + d\phi/dt = \omega + (2\pi/\lambda)n_2(dI/dt)z$. We see that the phase will be different according to the intensity of the pulse, leading to a modification of the spectral content of the pulse.

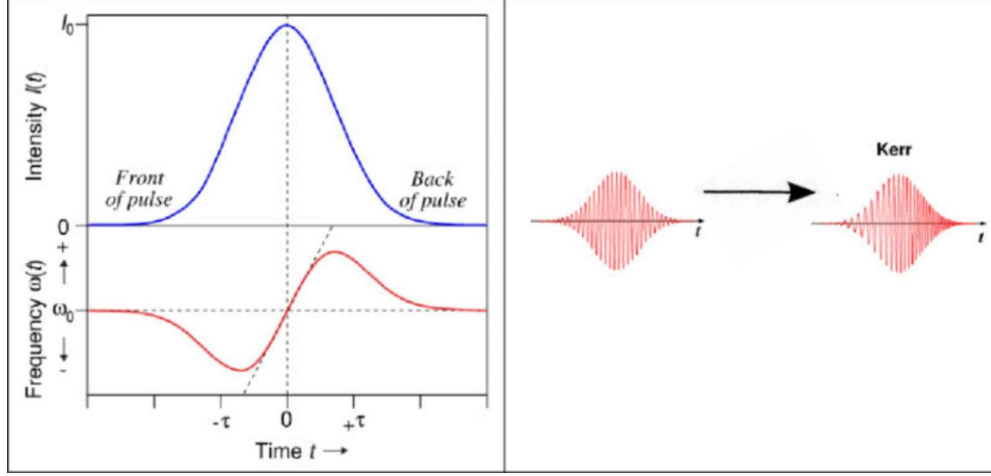


Figure 1.5: Representation of the SPM on a Gaussian pulse. Figure from [9]

The instantaneous frequency will thus change as shown in fig. 1.5, leading to the spectral content modification called chirp.

This effect is well-known in optical fibres and integrated waveguides as it modifies the spectral bandwidth [10]. It also allows the formation of solitons in the anomalous-dispersion regime [11, 12], self-cleaning of a pulse [13] or pulse compression [14].

In the case of the XPM, a pulse impact another one. The influence on the refractive index for the second pulse can be expressed as:

$$\Delta n_{(2)} = 2n_2 I_{(1)}. \quad (1.18)$$

It is coupled with SPM as the pump will also suffer some changes due to its high intensity. It is used for optical switching [15] or demultiplexing [16]. SPM is also used for passive mode-locking [17].

Another example of third-order nonlinear effects is the four-wave mixing (FWM). To understand this effect, we first define four interacting waves by:

$$\begin{aligned} \tilde{E}_j(\mathbf{r}, t) &= E_j(\mathbf{r}) \exp(-i(\omega_j t) + c.c.) \quad (j = 1, 2, 3, 4) \\ &= A_j(\mathbf{r}) \exp(\mathbf{k}_j \cdot \mathbf{r} - i(\omega_j t)) + c.c., \end{aligned} \quad (1.19)$$

with the nonlinear polarization in the medium being written as:

$$P_{NL,j} = \sum_{klm} \epsilon_0 \chi_{jklm}^{(3)} E_k E_l E_m. \quad (1.20)$$

We assume that each of the interacting waves follows the wave equation 1.6. And so, by injecting 1.20 in it, we can express the amplitudes as follows:

$$\begin{aligned}
\frac{dA_1}{dz} &= \frac{2n_2i\omega_1}{c} \left[(|A_1|^2 + 2|A_2|^2 + 2|A_3|^2 + 2|A_4|^2)A_1 + 2A_2^*A_3A_4 \exp(i\Delta kz) \right], \\
\frac{dA_2}{dz} &= \frac{2n_2i\omega_2}{c} \left[(|A_2|^2 + 2|A_3|^2 + 2|A_4|^2 + 2|A_1|^2)A_2 + 2A_1^*A_3A_4 \exp(i\Delta kz) \right], \\
\frac{dA_3}{dz} &= \frac{2n_2i\omega_3}{c} \left[(|A_3|^2 + 2|A_4|^2 + 2|A_1|^2 + 2|A_2|^2)A_3 + 2A_4^*A_1A_2 \exp(-i\Delta kz) \right], \\
\frac{dA_4}{dz} &= \frac{2n_2i\omega_4}{c} \left[(|A_4|^2 + 2|A_1|^2 + 2|A_2|^2 + 2|A_3|^2)A_4 + 2A_3^*A_1A_2 \exp(-i\Delta kz) \right],
\end{aligned} \tag{1.21}$$

with $\Delta k = k_3 + k_4 - k_1 - k_2$ the phase mismatch between the four waves. By taking a closer look at these equations, we can see that the first term $|A_i|^2 A_i$ represent the SPM presented earlier and the three following ones ($|A_j|^2 A_i$) are XPM terms. The last term is representative of the FWM process, and we see that there is also a phase-matching condition ruling the efficiency of the process.

In this part, we have seen different nonlinear effects. We mainly focused on second-order nonlinear effects as it is the main topic of this thesis. We still discussed third-order nonlinear effects for a better understanding of the topic. The following part is on integrated photonics, and we will make connections between what we have just seen about nonlinear optics and integrated photonic devices.

1.2 Integrated photonics

In this section, integrated photonics will be presented. The reason for the interest in such technology, as well as the impact that it has nowadays, will be developed. The waveguides considered in this thesis have subwavelength width and height, it is, of course of, interest to see the particularities of light propagation in such structures. As we will see, it is different from propagation in large areas waveguides. This part allows us to better understand the interactions with the material and how the nonlinear effects that we are aiming for are obtained. We will explore both the linear and nonlinear regimes. A highlight will be given to the SHG in these kinds of platforms to see the impact of this process and put this thesis in the state of the art.

1.2.1 Interest and impact

Integrated photonics is a field that has known an exploding interest for the last decades. The interest in optical communications instead of electric or radio waves has emerged in the early sixties with the development of lasers. Lasers are sources that provide a stable and coherent light. Lasers can be manipulated for information transmission via electro-optic modulators and then converted into an electrical signal via detectors. A complete communication system however required huge and expensive pieces of equipment. That's why integrated photonics made a breakthrough. The whole system is miniaturized and so cheaper and more convenient to use and implement. Moreover, complementary metal oxide semiconductor (CMOS) compatible platforms promise a low-cost fabrication process. We can see in fig. 1.6 some possible applications of integrated circuits.

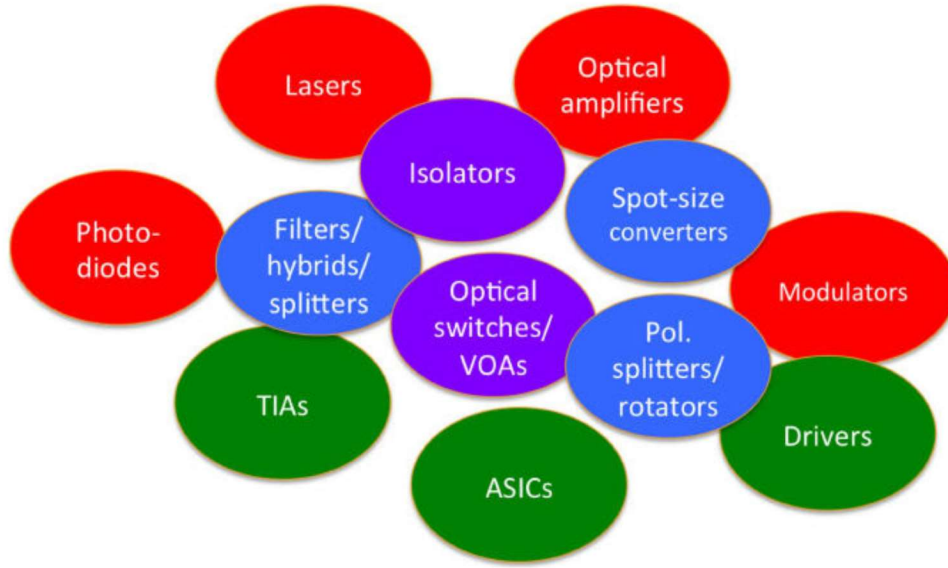


Figure 1.6: Possible photonics integrated circuits elements as it can be found in ref. [18]

Silicon is the heart of integrated photonics [19]. It is a material transparent for wavelength above 1100 nm which makes it suitable for telecommunications systems (between 1260 and 1625 nm commonly). It is also a material that can easily be integrated with electronic devices. Furthermore, the improvement of the fabrication processes for this material has led to very low linear losses [20]. It also offers a large index contrast with its cladding, which allows the light to be well confined inside the structure, important to avoid losses in a bent waveguide and to reduce space requirements. Structures based on silicon (Si) are widely used to make modulators [21–23], couplers [24, 25] and quantum photonics [26] for instance.

Another important material that found its place in integrated photonics is silicon nitride (SiN). SiN comes with advantages as well as some disadvantages compared to Si. For instance, it has a lower refractive index contrast at 1550 nm with silicon oxide (SiO₂) than Si (3.5 for Si and 2 for SiN compared to 1.5 for SiO₂). Which means lower confinement of the light. SiN, however, usually presents lower linear losses than Si. While the linear loss is usually around 1-2 dB/cm in silicon, it is usually an order of magnitude lower in silicon nitride [27, 28]. SiN also shows itself as an interesting material for nonlinear applications such as supercontinuum generation and frequency combs [29–31].

The development of integrated photonic technology and the maturity obtained over the last years also brought the possibility to build complex photonic circuits on a single chip [32]. The amount of possibilities that bring such technology is vast. We can thus see the emergence of nano processors that are used for deep learning and pattern recognition [33] as well as simulations of quantum transport [34]. This is also an attractive technology for quantum experiments as it requires stable and complex systems. We can thus use photonic integrated circuits for experiments such as single-photon sources [35] and entangled photons [36].

We can also couple the Si or SiN waveguide to other integrated devices for other purposes. For example, the Si (SiN) will be the travelling medium, as low linear losses are achieved in this material now, for the light emitted by an integrated laser [37, 38]. For this purpose, the development of fabrication processes to work with other materials (such as III-V or II-IV alloys) have emerged.

Other devices have also found their place in integrated photonics. For instance, photode-

tectors are now widely spread [39, 40]. And the fabrication processes now allow producing structures small enough to fabricate quantum wells and superlattices [41, 42], leading to smaller and smaller devices.

1.2.2 Light propagation in integrated structures

In this part, we are going to discuss the particularities of an electromagnetic wave propagating inside an integrated waveguide. As it is indeed different from bulk materials, it is important to take a closer look at this part. It shows the particularities to take into account for such propagation for the numerical simulations in the following parts.

The light is travelling through a core with a certain refractive index surrounded by a cladding with a lower refractive index. The first thing to take into account is the shape of the waveguide. Usually, integrated waveguides have a rectangular profile. However, this profile can take different forms, as shown in fig. 1.7.

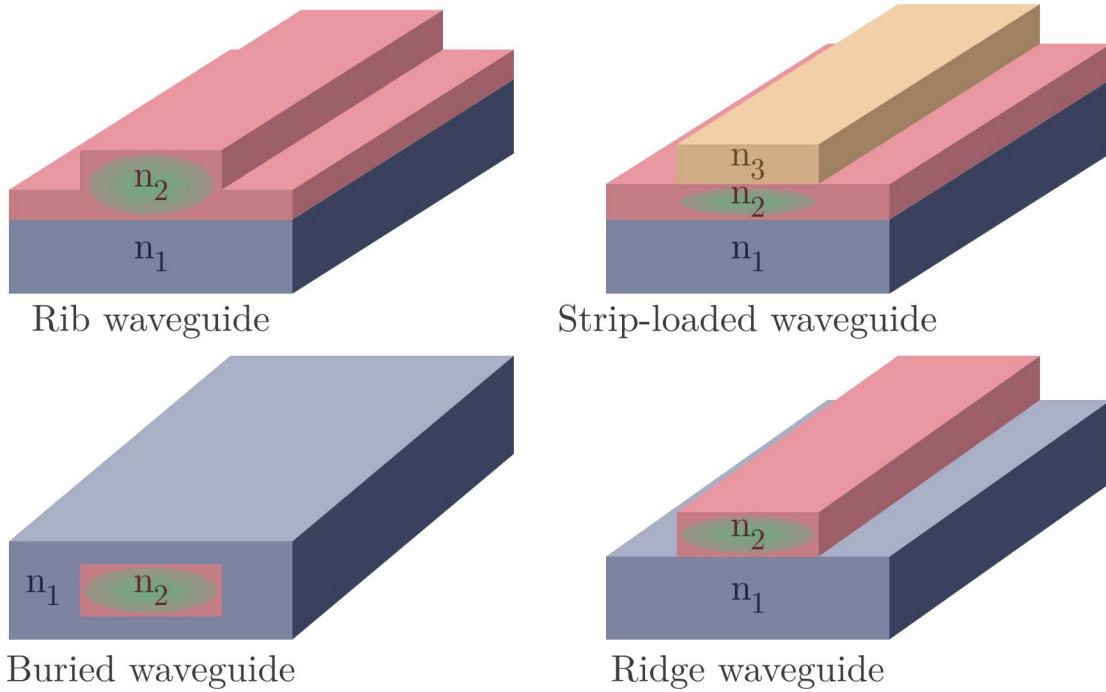


Figure 1.7: Representation of different waveguides with a rectangular profile. In all cases, the material with the refractive index $n_2 > n_1$ is the one where the light is propagating. In the case of strip-loaded waveguides, we also have $n_2 > n_3$. A representation of the area where the light is confined is represented with an oval shape for each structure.

We are going to study more in detail the particular optical electric field distribution of the light travelling inside these structures. To do so, we are first going to study the case of slab waveguides followed by rectangular buried waveguides.

1.2.2.1 Slab waveguide study

We are now going to focus on a planar slab waveguide, as represented in fig. 1.8. The planar slab waveguide is a useful case to understand the propagation in the structures presented in fig. 1.7.

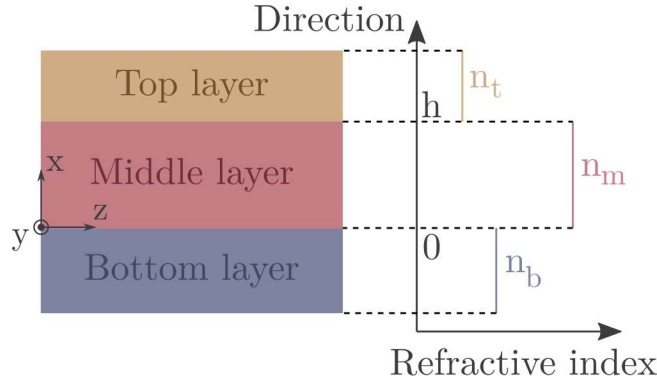


Figure 1.8: Sketch of an asymmetric slab waveguide (left) and the representation of refractive index profile of the waveguide (right).

For this study, we are considering a continuous, monochromatic wave propagating along the z -direction with the propagation constant β in an isotropic medium with a refractive index n at first. The electromagnetic field varies as:

$$\begin{aligned}\tilde{\mathbf{E}} &= \mathbf{E}(x, y) \exp [i(\omega t - \beta z)], \\ \tilde{\mathbf{H}} &= \mathbf{H}(x, y) \exp [i(\omega t - \beta z)].\end{aligned}\tag{1.22}$$

By substituting these two equations into Maxwell's equation 1.3, we obtain the following set of equations [43]:

$$\begin{cases} \frac{\partial E_z}{\partial y} + i\beta E_y &= -i\omega\mu_0 H_x, \\ -\frac{\partial E_z}{\partial x} - i\beta E_x &= -i\omega\mu_0 H_y, \\ \frac{\partial E_y}{\partial x} - \frac{\partial E_x}{\partial y} &= -i\omega\mu_0 H_z, \end{cases}\tag{1.23}$$

$$\begin{cases} \frac{\partial H_z}{\partial y} + i\beta H_y &= -i\omega\epsilon_0 n^2 E_x, \\ -\frac{\partial H_z}{\partial x} - i\beta H_x &= -i\omega\epsilon_0 n^2 E_y, \\ \frac{\partial H_y}{\partial x} - \frac{\partial H_x}{\partial y} &= -i\omega\epsilon_0 n^2 E_z. \end{cases}\tag{1.24}$$

In the slab waveguide, the electromagnetic fields E and H have no y -axis dependency as it is supposed infinite. Therefore, we set $\partial E/dy = 0$ and $\partial H/dy = 0$ [44].

Putting these relations into the sets of equations 1.23 and 1.24 leads to two independent electric solutions denoted respectively as transverse electric (TE) and transverse magnetic (TM). The TE solution satisfies the following wave equation:

$$\frac{\partial^2 E_y}{\partial x^2} = (\beta^2 - n^2 k^2) E_y,\tag{1.25}$$

where $k = \omega/c = \omega\sqrt{\epsilon_0\mu_0}$. We also have for this solution:

$$\begin{aligned}H_y &= E_x = E_z = 0, \\ H_x &= -\frac{\beta}{\omega\mu_0} E_y, \\ H_z &= j \frac{1}{\omega\mu_0} \frac{\partial E_y}{\partial x}.\end{aligned}\tag{1.26}$$

We are now taking the case where $n_m > n_b > n_t$ as represented in fig. 1.8 to express the electric field in each parts of the waveguide. Moreover, the boundary conditions require

that E_y and $\partial E_y / \partial x$ be continuous across the boundaries at $x = 0$ and $x = h$. For guided modes, we thus have the following set of equations for each material [45]:

$$\begin{cases} E_y = E_t \exp[-\gamma_t(x - h)] & \text{for } h < x \text{ (top layer),} \\ E_y = E_m \cos(\gamma_m x - \phi_m) & \text{for } 0 < x < h \text{ (middle layer),} \\ E_y = E_b \exp(\gamma_b x) & \text{for } x < 0 \text{ (bottom layer),} \end{cases} \quad (1.27)$$

where $\gamma_t^2 = \beta^2 - n_t^2 k^2$, $\gamma_m^2 = n_m^2 k^2 - \beta^2$ and $\gamma_b^2 = \beta^2 - n_b^2 k^2$. The boundary conditions also involve that, for $x = 0$:

$$\begin{cases} E_b & = E_m \cos(\phi_m), \\ \tan(\phi_m) & = \frac{\gamma_b}{\gamma_m}. \end{cases} \quad (1.28)$$

Similarly, for $x = h$:

$$\begin{cases} E_t & = E_m \cos(\gamma_m h - \phi_m), \\ \tan(\gamma_m h - \phi_m) & = \frac{\gamma_t}{\gamma_m}. \end{cases} \quad (1.29)$$

Finally, these relations result in an eigenvalue equation:

$$\gamma_m h = (m + 1)\pi - \arctan \frac{\gamma_m}{\gamma_b} - \arctan \frac{\gamma_m}{\gamma_t}, \quad (1.30)$$

where m is an integer denoting the mode number. This result shows that the modes that are guided inside waveguides are discrete solutions.

The modes shapes are distinct as shown in fig. 1.9 for $m = 0$ and $m = 1$.

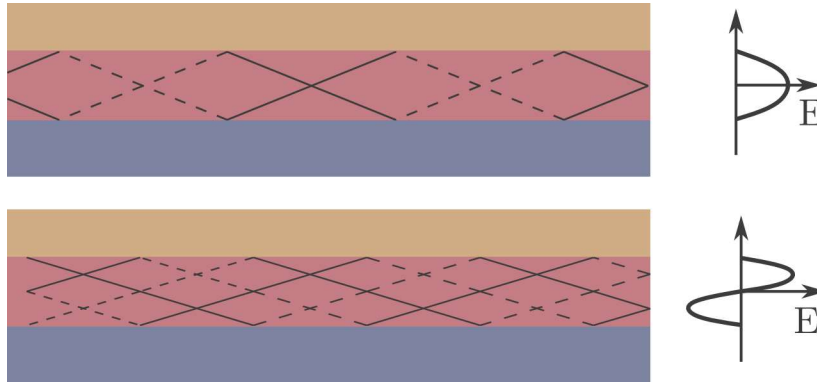


Figure 1.9: Formation of the fundamental mode (a) and a higher-order mode (b). The solid lines represent a positive phase front and the dashed lines a negative phase front.

Furthermore, it is important to know that each mode propagating inside the same medium has a different refractive index. This particularity will be more detailed later.

We have seen that light propagates in a rectangular slab waveguide with discrete solutions called modes that present different shapes as seen in fig. 1.12. We are now going to study the case of a buried waveguide and see more properties about the components of these modes.

1.2.2.2 Buried waveguide study

We are going to focus on a buried waveguide as represented in fig. 1.7 for the study of the modes. This is a symmetric structure in the x and y direction which is closer to the waveguides that will be used later.

The electric field of a wave propagating along the z-axis can be derived from Maxwell's equations from 1.1.1 and the conditions at the interfaces. It is thus expressed as:

$$\mathbf{E}(\mathbf{r}, z) = \mathbf{E}_0(\mathbf{r}) \exp[-i\beta z] \quad (1.31)$$

Where β is the propagation constant of the mode electric field and \mathbf{r} represents the position in the plane transverse to the propagation direction z.

This is a valid approximation in the case of a weakly guiding waveguide. Usually, optical waveguides that possess a core index n_{cor} close to the cladding index n_{cla} are called weakly guiding waveguides. The $\Delta = 1/2(1 - n_{cla}^2/n_{cor}^2)$ coefficient is thus used to estimate the guiding efficiency and if $\Delta \ll 1$, then we are in the case of a weakly guiding. For a weakly guiding mode, the longitudinal component E_z of the electric field can be expressed as a function of the transverse field components \mathbf{E}_t [46]:

$$E_z = \frac{i(2\Delta)^{1/2}}{V}(\rho \nabla_T \cdot \mathbf{E}_T), \quad (1.32)$$

where V is the waveguide parameter defined as $V = 2\pi\rho/\lambda(n_{cor}^2 - n_{cla}^2)^{1/2}$ and ρ is a linear dimension in the waveguide cross-section such as the thickness of the core is equal to 2ρ . This can be usually applied to the case of optical fibres.

However, this well-known approximation is no longer valid in such small structures, as we are no longer in the case of $\Delta \ll 1$. Indeed, in such confined conditions, the longitudinal component becomes quite important and cannot be neglected anymore [47]. In this context, the transverse component can be written as:

$$E_z = \frac{\lambda_0}{2i\pi n_{eff}} \nabla_T \cdot \mathbf{E}_T, \quad (1.33)$$

where \mathbf{E}_T represents the transverse electric field amplitude (E_x, E_y), ∇_T is the transverse gradient and n_{eff} is the effective index of the mode inside the medium. The longitudinal component, which can seem insignificant at first sight, will take all its meaning in our work, as we will see later. As a first example, we represent in fig. 1.10 the mode components of a fundamental mode propagating inside a 300 nm high and 800 nm wide Si waveguide calculated from a numerical solver.

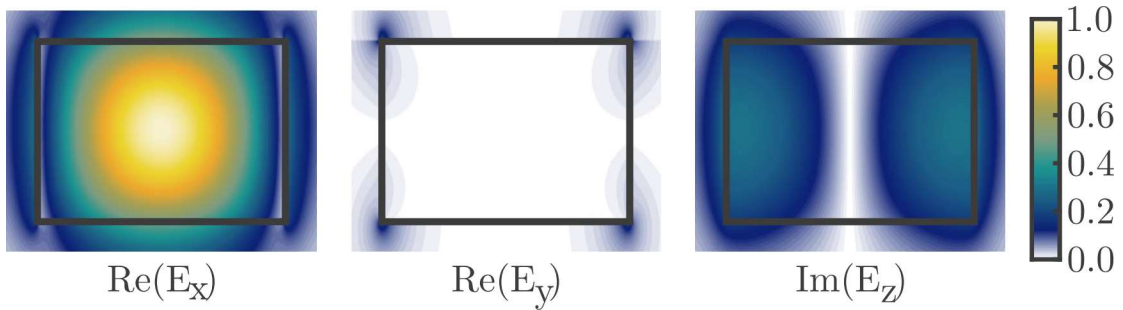


Figure 1.10: All the three electric field components of the fundamental mode in an 800 nm wide and 300 nm high Si waveguide.

We can also note from eq. 1.33 that the longitudinal component is purely imaginary, and this component will suffer a $\pi/2$ shift compared to its transverse counterparts. We can also note different particular cases. For instance, there is the case of a quasi-TE mode. In this case, we have $E_y \approx 0$. And so, the eq. 1.33 can be expressed as:

$$E_z = \frac{\lambda_0}{2j\pi n_{eff}} \frac{\partial E_x}{\partial x}, \quad (1.34)$$

And so, we can see that the symmetry along the x-axis of the longitudinal component E_z is the opposite of the longitudinal component. It means that an electric field with a symmetric (anti-symmetric) E_x component along the x-axis will have an anti-symmetric (symmetric) component E_z along x.

If we now take a quasi-TM mode for which $E_x \approx 0$, the eq. 1.33 become:

$$E_z = \frac{\lambda_0}{2j\pi n_{eff}} \frac{\partial E_y}{\partial y}, \quad (1.35)$$

In this case, a symmetric (anti-symmetric) E_y component along the y-axis will have an anti-symmetric (symmetric) component E_z along y.

If we now study the general case of a quasi-TE and quasi-TM mode, we can define the transverse component as:

$$E_z = \frac{\lambda_0}{2j\pi n_{eff}} \left(\frac{\partial E_x}{\partial x} + \frac{\partial E_y}{\partial y} \right), \quad (1.36)$$

An important point to raise in the case of a buried waveguide is that the E_y component of the electric field will have a symmetry opposite to the E_x component of the electric field in the x and y direction [46]. So E_y is symmetric (antisymmetric) along x (y) if E_x is antisymmetric (symmetric) along x (y). And so, this symmetry property leads to different symmetry cases for the longitudinal component E_z according to the symmetry of the two other components.

If E_x is symmetric (antisymmetric) along x and antisymmetric along y, then E_y is antisymmetric (symmetric) along x and symmetric along y. So E_z is antisymmetric (symmetric) along x and antisymmetric along y, as it can be seen in fig. 1.11 with the mode TE_{01} (TM_{40}). If E_x is symmetric (antisymmetric) along x and symmetric along y, then E_y is antisymmetric (symmetric) along x too and antisymmetric along y. So E_z is anti-symmetric (symmetric) along x and symmetric along y, as it can be seen in fig. 1.11 for the mode TE_{40} (TM_{21}).

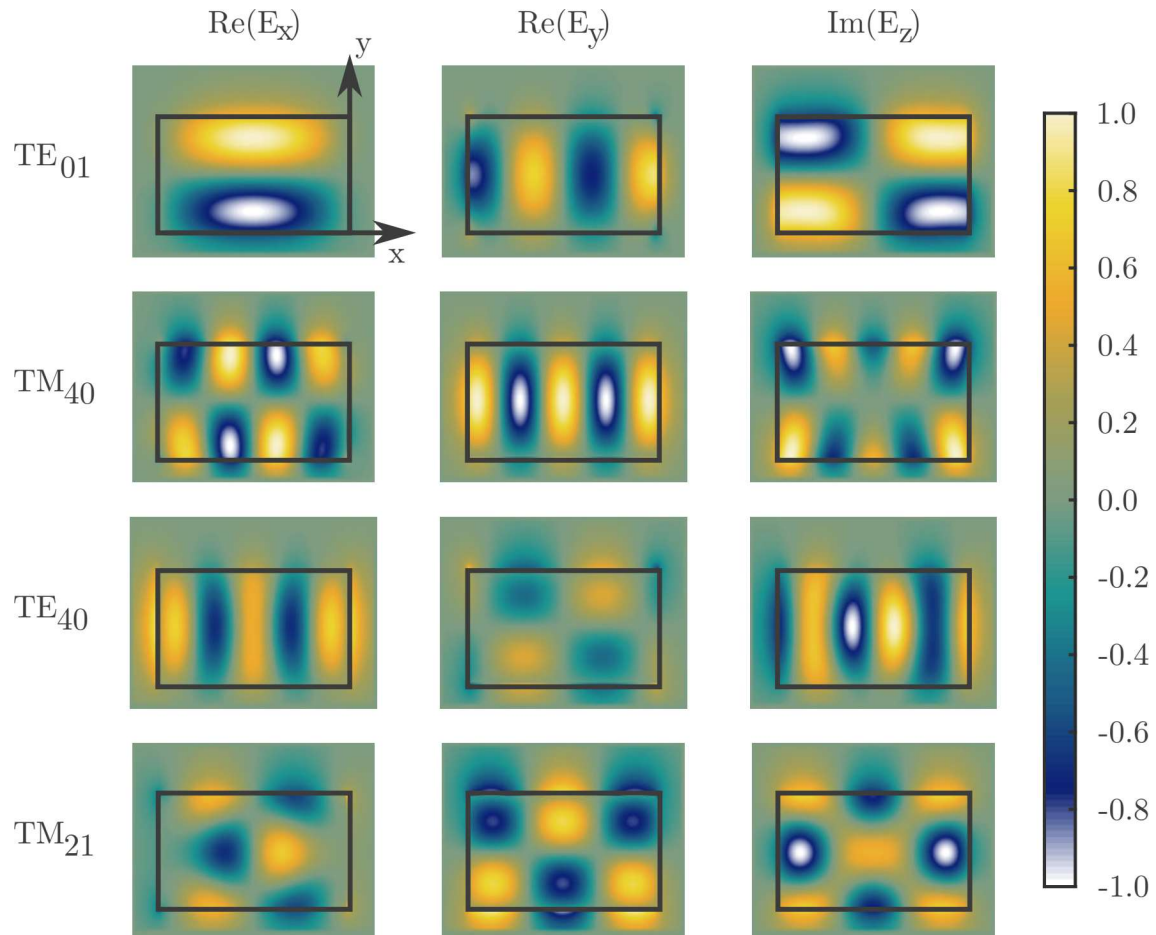


Figure 1.11: Modes components for an 800 nm wide and 320 nm high gallium phosphide buried waveguide at a 775 nm wavelength. Each component of the modes has been normalized to its max value for better visibility of the symmetry of the components of the modes.

As it can also be noticed in fig. 1.11, names were given to the modes represented. By convention, to distinguish the modes, the modes noted TE_{mn} will refer to its orientation with reference from the substrate. A mode that has a dominant electric field perpendicular to the substrate will be denoted as TM while a mode with a dominant electric field parallel to the interface between the substrate and the medium will be denoted as TE. At the same time, the m and n coefficients will be determined by the number of zeros from the main electric field component. For instance, a mode for which the dominant electric field is parallel to the interface between the substrate and the propagation medium which moreover presents two zeros in the vertical direction and only one in the horizontal direction will be named TE_{12} . In fig. 1.12 are represented some modes that can be obtained in a rectangular waveguide with their names from the convention described to better identify them.

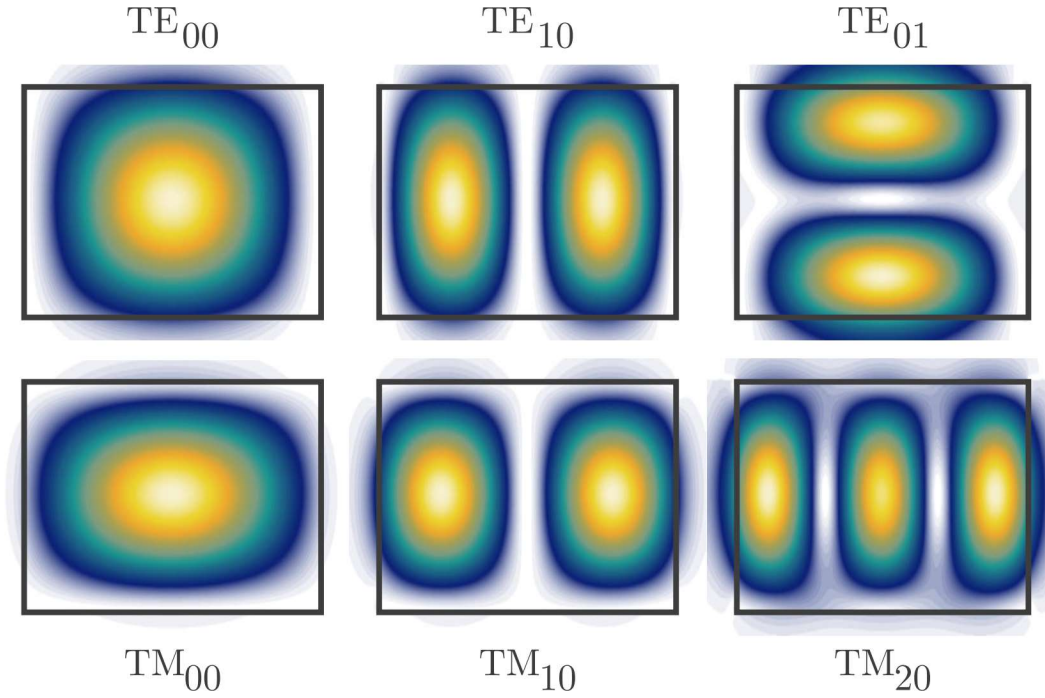


Figure 1.12: Representation of the Poynting vector of a few modes that propagate inside a 1000 nm wide and 500 nm high silicon waveguide. Their names are also given for each of them.

We here had an overview of how the propagation occurs and what is happening in rectangular waveguides. This is necessary as this profile is the most common one in integrated photonics. We saw the links between the symmetry of the components of the modes in the case of a buried waveguide. In the following parts, we work with ridge waveguides. It is a bit different from the example presented above as there is no more symmetry of the refractive index along the y -axis (see fig. 1.7). The modes are so not symmetric along the y -axis as they tend to be slightly shifted towards the substrate (silicon oxide in our case) which has a higher refractive index than the surrounding medium (air). Despite this difference from fully symmetric waveguides, the number of nodes and the general shape of the mode components look similar, which helps to experimentally identify the modes involved in the SHG process (we however stress that the waveguides are symmetric in x and thus the symmetry properties from eq. 1.34 are accurate).

The next part will present some nonlinear effects in integrated platforms to have a complete overview of the topic of this thesis.

1.2.3 Nonlinear photonics in integrated platforms

In this section, the focus is on the interest of nonlinear photonics in integrated structures and some applications of it. For this purpose, we are going to use what has been seen earlier about nonlinear effects and see how it applies in integrated structures.

As mentioned earlier, the strong confinement of the light ensures better interaction of the light with the material, which allows nonlinear effects to be achieved at lower power. It is one of the reasons why integrated nonlinear optics is so attractive. One of the first reasons to use integrated structures is for wavelength conversion. As we have seen earlier, for SHG for instance, the birefringence of the medium can be used to obtain a PM between the pump and the SH. We have also seen in fig. 1.12 that a rectangular waveguide can be

multimodal. We can take advantage of this and the fact that each mode that propagates with a different propagation constant $\beta = 2n_{eff}\pi/\lambda$ where n_{eff} is the effective index of the mode and λ the wavelength. We can thus use the effective refractive index to study the modes. All modes have, indeed, a different refractive index for a given waveguide as can be seen in fig. 1.13.

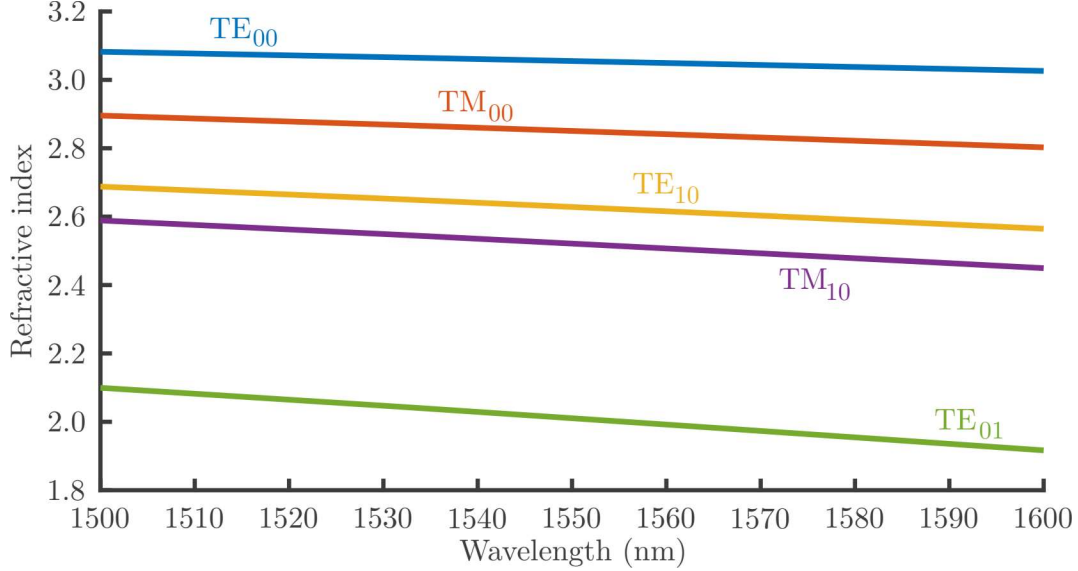


Figure 1.13: Refractive indices as a function of the wavelength of five modes for an 850 nm wide and 400 nm high Si waveguide.

The variation of the refractive index with the wavelength is also different for each mode. It is thus possible to satisfy the PM as long as the two modes have the same refractive index for a certain wavelength. This particular case of PM is called modal phase-matching (MPM). It is not limited to SHG [48, 49] as it can be applied to other effects. For instance, this PM is used to make an optical parametric oscillator or to achieve PM in the case of FWM [50–52]. Furthermore, it is possible to tailor the dispersive properties of a waveguide by changing its dimensions [53, 54]. This way, it is possible to obtain a certain PM at the desired wavelength.

MPM is not always needed in integrated structures. As proof, we can think of other nonlinear effects that are widely discussed in integrated photonics: supercontinuum. It consists in sending high-intensity pulses inside a nonlinear material and taking advantage of the third-order nonlinear effects (but not necessarily [55]) to broaden the pulse spectrum [56, 57]. Such sources are used in the domain of spectroscopy and fluorescence microscopy for instance [58].

Besides this, optical frequency comb (OFC) is a hot topic nowadays. The creation principle around OFC is close to the one of a supercontinuum. It consists of a succession of spectral lines equally spaced as shown in fig. 1.14. A way to generate OFC is the use of a continuous-wave laser that propagates inside a microring resonator with an important third-order nonlinearity [59].

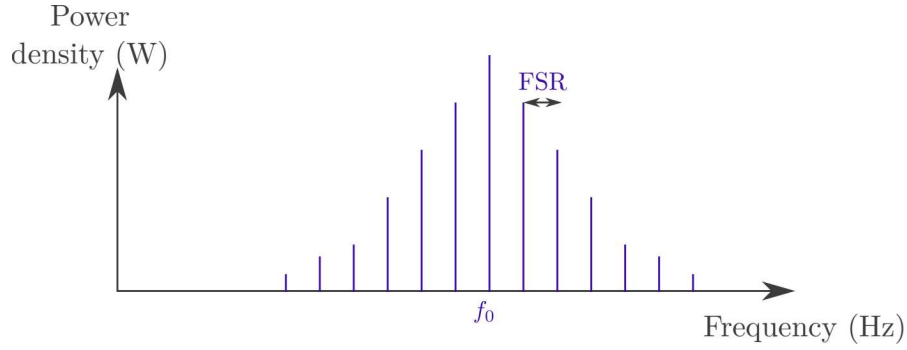


Figure 1.14: Schematic of an optical frequency comb. The central frequency f_0 of the laser is subject to cascaded FWM to generate the other frequencies.

It is really useful in spectroscopy as it allows us to determine an unknown frequency by measuring the beating between this one and the OFC [60, 61]. OFC are really under the scope as it has been awarded a Nobel Prize in 2005.

Another example of a nonlinear optical phenomenon in integrated structures is the observation of optical event horizons. Event horizons are, in astrophysics, a limit in a black hole beyond which nothing can escape the black hole. It is thus possible to measure an optical equivalent, which would be useful to understand black holes from the study of an optical experiment [62]. An example of an optical event horizon is shown in fig. 1.15.

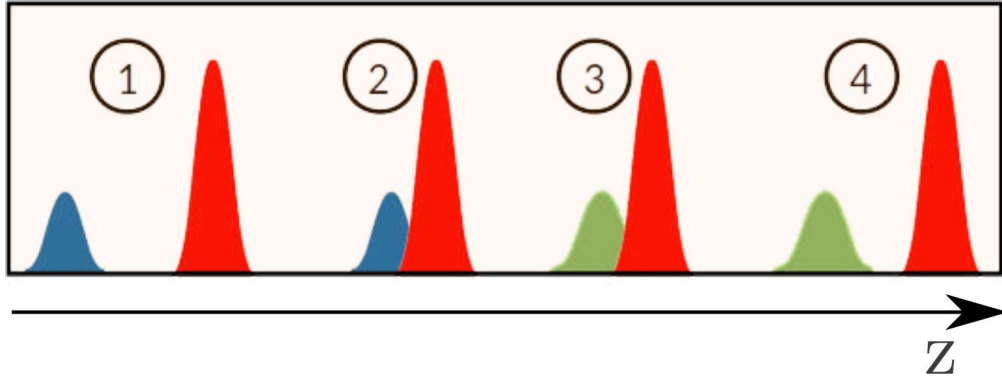


Figure 1.15: Example of the XPM effect where an intense pulse, the pump, is propagating along z inside a nonlinear medium. It propagates with another weaker pulse, the probe (step 1). Due to a different velocity in the dispersive medium, the probe will catch up with the pump (step 2). The Kerr effect will induce XPM and thus a shift of the probe wavelength (step 3). In this example, the resulting group velocity of the final probe is lower than the pump (step 4).

In this example, the pump creates the equivalent of an event horizon for the probe as it cannot go through it.

We have seen that nonlinear effects are really interesting coupled with integrated photonics. This combination allows obtaining useful devices for other domains like spectroscopy and microscopy and can also reproduce an optical equivalent of other phenomena. Nonlinear effects can also be used for light sources, to generate wavelength that will not be easily available otherwise [63, 64]. For the following part, we will see more in detail the case of the SHG process in integrated structures.

1.2.4 SHG in integrated platforms

In this section, we are going to have a closer look at the interest that SHG can have in integrated structures. A point will also be raised concerning the particularities of such a process in integrated structures. This brings the last piece to understand the following parts of this thesis. The idea to generate a SH inside an integrated structure is really attractive. Indeed, it could be a further step in the context of OFC which has been attracting a lot of attention for the last years [65, 66]. The SH is already used to measure and stabilize the OFC [67, 68]. Fig. 1.16 shows how the SH currently helps to characterize the OFC. This measure however requires to extract the comb from the medium where it is generated to pass it through a second-order nonlinear crystal. Integration of the SHG could allow to auto-reference the OFC in a single integrated structure [69].

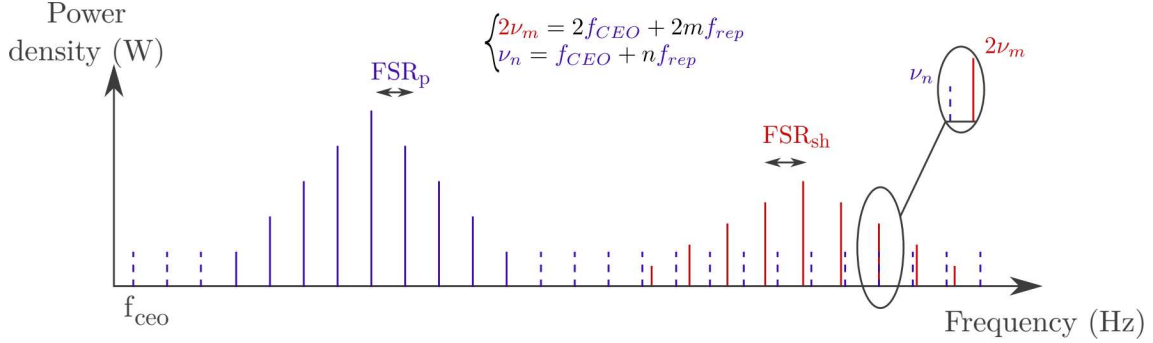


Figure 1.16: Schematic of the self-referencing for an optical frequency comb. A certain pump frequency line is doubled by SHG and the beat note that can be measured between this doubled frequency and another pump frequency line allows to know the carrier-envelope offset frequency (f_{CEO}) and the repetition frequency (f_{rep}) of the OFC. The equations, as an inset in the figure, show the relation between the two frequency lines considered.

Furthermore, OFC can also be generated from second-order nonlinearities[70–72]. However, such integrated solutions are not fully developed yet and still need an in-depth study.

The SHG process is also attractive as it allows reaching wavelengths that can be difficult to obtain otherwise. For instance, it is used to obtain blue or green lasers via an interaction with a nonlinear crystal [73, 74]. This leads to new sources for applications such as in the medical field, for laser skin resurfacing for instance. It is also used for microscopy purposes [75, 76], the autocorrelation of short pulses [77, 78]. We can thus easily understand the impact of SHG in the context of integrated optics, especially when looking at the impact area of OFC. We are now going to see more in detail an important aspect of SHG process.

Until now, we used a scalar description concerning SHG effect. The electric field needs, however, to be treated as a vector, with all its three components to correctly express the SHG in integrated structures. This requires the use of the general tensor expression of second-order nonlinear susceptibility [2]. We are here using the definition $d_{ijk} = \frac{1}{2}\chi_{ijk}^{(2)}$ and the notation contraction associated for simplicity. This contraction allows us to write only a 6x3 matrix instead of a 9x3 matrix. It is known as the intrinsic permutation symmetry and is always valid [2]. The contraction resulting is expressed:

jk	11	22	33	23/32	13/31	12/21
l	1	2	3	4	5	6

From these notations, we obtained the following tensor in a general case:

$$d_{il} = \begin{pmatrix} d_{11} & d_{12} & d_{13} & d_{14} & d_{15} & d_{16} \\ d_{21} & d_{22} & d_{23} & d_{24} & d_{25} & d_{26} \\ d_{31} & d_{32} & d_{33} & d_{34} & d_{35} & d_{36} \end{pmatrix}$$

Instead of the scalar expression 1.2, the space components of the SH polarization are linked to the pump electric fields components by:

$$\begin{pmatrix} P_x \\ P_y \\ P_z \end{pmatrix}_{SH} = \begin{pmatrix} d_{11} & d_{12} & d_{13} & d_{14} & d_{15} & d_{16} \\ d_{21} & d_{22} & d_{23} & d_{24} & d_{25} & d_{26} \\ d_{31} & d_{32} & d_{33} & d_{34} & d_{35} & d_{36} \end{pmatrix} \begin{pmatrix} E_x^2 \\ E_y^2 \\ E_z^2 \\ 2E_y E_z \\ 2E_x E_z \\ 2E_x E_y \end{pmatrix}_{Pump}$$

Besides, the knowledge of the crystallographic symmetry of the material used can lead to simplifications of the second-order nonlinear tensor [79].

If we take the example of lithium niobate (LiNbO3), a uniaxial crystal belonging to the 3m crystal class, the previous equality between the pump and SH can thus be written as:

$$\begin{pmatrix} P_x \\ P_y \\ P_z \end{pmatrix}_{SH} = \begin{pmatrix} 0 & 0 & 0 & 0 & d_{31} & d_{21} \\ d_{21} & -d_{21} & 0 & d_{31} & 0 & 0 \\ d_{31} & d_{31} & d_{33} & 0 & 0 & 0 \end{pmatrix} \begin{pmatrix} E_x^2 \\ E_y^2 \\ E_z^2 \\ 2E_y E_z \\ 2E_x E_z \\ 2E_x E_y \end{pmatrix}_{Pump}$$

We can see how the crystal symmetry knowledge simplifies the calculations of the SHG process. We can also see why it is important to use the vectorial definition in integrated waveguides because it is needed to take care of all three components of the electric fields.

In this chapter, we have seen the impact of nonlinear photonics in different fields and also exposed some important aspects to know for the understanding of this thesis. We have also seen the impact of integrated photonics and how both aspects of the photonic world can act together to obtain interesting, applicative and strong effects. The focus has been made on SHG as it is a wide applicative effect that can be further developed. In the following parts, we will be interested in a particular medium for the SHG effect: III-V materials.

Bibliography

1. Franken, P. A., Hill, A. E., Peters, C. W. & Weinreich, G. Generation of Optical Harmonics. en. *Physical Review Letters* **7**, 118–119. ISSN: 0031-9007. <https://link.aps.org/doi/10.1103/PhysRevLett.7.118> (2020) (Aug. 1961).
2. Boyd, R. W. *Nonlinear Optics 3rd Edition* 3rd ed. ISBN: 978-0-12-369470-6 (Elsevier, Mar. 2008).
3. Armstrong, J. A., Bloembergen, N., Ducuing, J. & Pershan, P. S. Interactions between Light Waves in a Nonlinear Dielectric. en. *Physical Review* **127**, 1918–1939. ISSN: 0031-899X. <https://link.aps.org/doi/10.1103/PhysRev.127.1918> (2021) (Sept. 1962).
4. Fejer, M., Magel, G., Jundt, D. & Byer, R. Quasi-phase-matched second harmonic generation: tuning and tolerances. en. *IEEE Journal of Quantum Electronics* **28**, 2631–2654. ISSN: 00189197. <http://ieeexplore.ieee.org/document/161322/> (2021) (Nov. 1992).
5. Wang, C. *et al.* Second harmonic generation in nano-structured thin-film lithium niobate waveguides. en. *Optics Express* **25**, 6963. ISSN: 1094-4087. <https://www.osapublishing.org/abstract.cfm?URI=oe-25-6-6963> (2020) (Mar. 2017).
6. Lu, J., Li, M., Zou, C.-L., Al Sayem, A. & Tang, H. X. Toward 1% single-photon anharmonicity with periodically poled lithium niobate microring resonators. en. *Optica* **7**, 1654. ISSN: 2334-2536. <https://www.osapublishing.org/abstract.cfm?URI=optica-7-12-1654> (2021) (Dec. 2020).
7. Agrawal, G. P. *Nonlinear fiber optics* Fifth edition. en. ISBN: 978-0-12-397023-7 (Elsevier/Academic Press, Amsterdam, 2013).
8. Del Coso, R. & Solis, J. Relation between nonlinear refractive index and third-order susceptibility in absorbing media. en. *Journal of the Optical Society of America B* **21**, 640. ISSN: 0740-3224, 1520-8540. <https://www.osapublishing.org/abstract.cfm?URI=josab-21-3-640> (2021) (Mar. 2004).
9. Kuriakose, V. C. & Porsezian, K. Elements of optical solitons: An overview. en. *Resonance* **15**, 643–666. ISSN: 0971-8044, 0973-712X. <http://link.springer.com/10.1007/s12045-010-0048-y> (2021) (July 2010).
10. Stolen, R. H. & Lin, C. Self-phase-modulation in silica optical fibers. en. *Physical Review A* **17**, 1448–1453. ISSN: 0556-2791. <https://link.aps.org/doi/10.1103/PhysRevA.17.1448> (2021) (Apr. 1978).
11. Liu, J. *et al.* Ultralow-power chip-based soliton microcombs for photonic integration. en. *Optica* **5**, 1347. ISSN: 2334-2536. <https://www.osapublishing.org/abstract.cfm?URI=optica-5-10-1347> (2020) (Oct. 2018).
12. Xiang, C. *et al.* Laser soliton microcombs on silicon. en. *arXiv:2103.02725 [physics]*. arXiv: 2103.02725. <http://arxiv.org/abs/2103.02725> (2021) (Mar. 2021).

13. Liu, Z., Wright, L. G., Christodoulides, D. N. & Wise, F. W. Kerr self-cleaning of femtosecond-pulsed beams in graded-index multimode fiber. en. *Optics Letters* **41**, 3675. ISSN: 0146-9592, 1539-4794. <https://www.osapublishing.org/abstract.cfm?URI=ol-41-16-3675> (2021) (Aug. 2016).
14. Ryan, A. T. & Agrawal, G. P. Pulse compression and spatial phase modulation in normally dispersive nonlinear Kerr media. en. *Optics Letters* **20**, 306. ISSN: 0146-9592, 1539-4794. <https://www.osapublishing.org/abstract.cfm?URI=ol-20-3-306> (2021) (Feb. 1995).
15. Sharping, J., Fiorentino, M., Kumar, P. & Windeler, R. All-optical switching based on cross-phase modulation in microstructure fiber. en. *IEEE Photonics Technology Letters* **14**, 77–79. ISSN: 1041-1135, 1941-0174. <http://ieeexplore.ieee.org/document/974167/> (2021) (Jan. 2002).
16. Olsson, B.-E. & Blumenthal, D. All-optical demultiplexing using fiber cross-phase modulation (XPM) and optical filtering. en. *IEEE Photonics Technology Letters* **13**, 875–877. ISSN: 1041-1135, 1941-0174. <http://ieeexplore.ieee.org/document/935833/> (2021) (Aug. 2001).
17. Hofer, M., Fermann, M. E., Haberl, F., Ober, M. H. & Schmidt, A. J. Mode locking with cross-phase and self-phase modulation. en. *Optics Letters* **16**, 502. ISSN: 0146-9592, 1539-4794. <https://www.osapublishing.org/abstract.cfm?URI=ol-16-7-502> (2021) (Apr. 1991).
18. Doerr, C. R. Silicon photonic integration in telecommunications. en. *Frontiers in Physics* **3**. ISSN: 2296-424X. <http://journal.frontiersin.org/Article/10.3389/fphy.2015.00037/abstract> (2021) (Aug. 2015).
19. Rahim, A. *et al.* Expanding the Silicon Photonics Portfolio With Silicon Nitride Photonic Integrated Circuits. en. *Journal of Lightwave Technology* **35**, 639–649. ISSN: 0733-8724, 1558-2213. <http://ieeexplore.ieee.org/document/7589975/> (2021) (Feb. 2017).
20. Turner-Foster, A. C. *et al.* Ultrashort free-carrier lifetime in low-loss silicon nanowaveguides. en. *Optics Express* **18**, 3582. ISSN: 1094-4087. <https://www.osapublishing.org/oe/abstract.cfm?uri=oe-18-4-3582> (2021) (Feb. 2010).
21. Liu, A. *et al.* High-speed optical modulation based on carrier depletion in a silicon waveguide. en. *Optics Express* **15**, 660. ISSN: 1094-4087. <https://www.osapublishing.org/oe/abstract.cfm?uri=oe-15-2-660> (2021) (Jan. 2007).
22. Reed, G. T., Mashanovich, G., Gardes, F. Y. & Thomson, D. J. Silicon optical modulators. en. *Nature Photonics* **4**, 518–526. ISSN: 1749-4885, 1749-4893. <http://www.nature.com/articles/nphoton.2010.179> (2021) (Aug. 2010).
23. Dong, P. *et al.* Wavelength-tunable silicon microring modulator. en. *Optics Express* **18**, 10941. ISSN: 1094-4087. <https://www.osapublishing.org/oe/abstract.cfm?uri=oe-18-11-10941> (2021) (May 2010).
24. Fukuda, H. *et al.* Silicon photonic circuit with polarization diversity. en. *Optics Express* **16**, 4872. ISSN: 1094-4087. <https://www.osapublishing.org/oe/abstract.cfm?uri=oe-16-7-4872> (2021) (Mar. 2008).
25. Taillaert, D. *et al.* Grating Couplers for Coupling between Optical Fibers and Nanophotonic Waveguides. en. *Japanese Journal of Applied Physics* **45**, 6071–6077. ISSN: 0021-4922, 1347-4065. <https://iopscience.iop.org/article/10.1143/JJAP.45.6071> (2021) (Aug. 2006).

26. O'Brien, J. L., Furusawa, A. & Vučković, J. Photonic quantum technologies. en. *Nature Photonics* **3**, 687–695. ISSN: 1749-4885, 1749-4893. <http://www.nature.com/articles/nphoton.2009.229> (2021) (Dec. 2009).
27. Shaw, M. J., Guo, J., Vawter, G. A., Habermehl, S. & Sullivan, C. T. Fabrication techniques for low-loss silicon nitride waveguides. en. *Journal of the Optical Society of America B* (eds Johnson, E. G., Nordin, G. P. & Suleski, T. J.) 109. <http://proceedings.spiedigitallibrary.org/proceeding.aspx?doi=10.1117/12.588828> (2021) (Jan. 2005).
28. Bauters, J. F. *et al.* Ultra-low-loss high-aspect-ratio Si₃N₄ waveguides. en. *Optics Express* **19**, 3163. ISSN: 1094-4087. <https://www.osapublishing.org/oe/abstract.cfm?uri=oe-19-4-3163> (2021) (Feb. 2011).
29. Okawachi, Y. *et al.* Octave-spanning frequency comb generation in a silicon nitride chip. en. *Optics Letters* **36**, 3398. ISSN: 0146-9592, 1539-4794. <https://www.osapublishing.org/abstract.cfm?URI=ol-36-17-3398> (2021) (Sept. 2011).
30. Spencer, D. T. *et al.* An Integrated-Photonics Optical-Frequency Synthesizer. en, 10.
31. Mayer, A. S. *et al.* Frequency comb offset detection using supercontinuum generation in silicon nitride waveguides. en. *Optics Express* **23**, 15440. ISSN: 1094-4087. <https://www.osapublishing.org/abstract.cfm?URI=oe-23-12-15440> (2021) (June 2015).
32. Bogaerts, W. *et al.* Programmable photonic circuits. en. *Nature* **586**, 207–216. ISSN: 0028-0836, 1476-4687. <http://www.nature.com/articles/s41586-020-2764-0> (2020) (Oct. 2020).
33. Shen, Y. *et al.* Deep learning with coherent nanophotonic circuits. en. *Nature Photonics* **11**, 441–446. ISSN: 1749-4885, 1749-4893. <http://www.nature.com/articles/nphoton.2017.93> (2021) (July 2017).
34. Harris, N. C. *et al.* Quantum transport simulations in a programmable nanophotonic processor. en. *Nature Photonics* **11**, 447–452. ISSN: 1749-4885, 1749-4893. <http://www.nature.com/articles/nphoton.2017.95> (2021) (July 2017).
35. Khasminskaya, S. *et al.* Fully integrated quantum photonic circuit with an electrically driven light source. en. *Nature Photonics* **10**, 727–732. ISSN: 1749-4885, 1749-4893. <http://www.nature.com/articles/nphoton.2016.178> (2021) (Nov. 2016).
36. Shadbolt, P. J. *et al.* Generating, manipulating and measuring entanglement and mixture with a reconfigurable photonic circuit. en. *Nature Photonics* **6**, 45–49. ISSN: 1749-4885, 1749-4893. <http://www.nature.com/articles/nphoton.2011.283> (2021) (Jan. 2012).
37. Latkowski, S. *et al.* Novel Widely Tunable Monolithically Integrated Laser Source. en. *IEEE Photonics Journal* **7**, 1–9. ISSN: 1943-0655, 1943-0647. <https://ieeexplore.ieee.org/document/7305755/> (2021) (Dec. 2015).
38. Komljenovic, T. *et al.* Photonic Integrated Circuits Using Heterogeneous Integration on Silicon. en. *Proceedings of the IEEE* **106**, 2246–2257. ISSN: 0018-9219, 1558-2256. <https://ieeexplore.ieee.org/document/8451879/> (2021) (Dec. 2018).
39. Ahn, D. *et al.* High performance, waveguide integrated Ge photodetectors. en. *Optics Express* **15**, 3916. ISSN: 1094-4087. <https://www.osapublishing.org/oe/abstract.cfm?uri=oe-15-7-3916> (2021) (2007).

40. Furchi, M. *et al.* Microcavity-Integrated Graphene Photodetector. en. *Nano Letters* **12**, 2773–2777. ISSN: 1530-6984, 1530-6992. <https://pubs.acs.org/doi/10.1021/nl204512x> (2021) (June 2012).
41. König, M. *et al.* Quantum Spin Hall Insulator State in HgTe Quantum Wells. en. *Science* **318**, 766–770. ISSN: 0036-8075, 1095-9203. <https://www.sciencemag.org/lookup/doi/10.1126/science.1148047> (2021) (Nov. 2007).
42. Fan, X. *et al.* SiGeC/Si superlattice microcoolers. en. *Applied Physics Letters* **78**, 1580–1582. ISSN: 0003-6951, 1077-3118. <http://aip.scitation.org/doi/10.1063/1.1356455> (2021) (Mar. 2001).
43. Okamoto, K. *Fundamentals of optical waveguides* 2nd ed. ISBN: 978-0-12-525096-2 (Elsevier, Amsterdam ; Boston, 2006).
44. Nishihara, H., Haruna, M., Suhara, T. & Nishihara, H. *Optical integrated circuits* eng. ISBN: 978-0-07-046092-8 (McGraw-Hill Book Comp, New York, 1989).
45. *Integrated optics* eng (eds Tamir, T. & Garmire, E.) *Topics in applied physics* **7**. ISBN: 978-0-387-07297-5 (Springer, Berlin Heidelberg, 1975).
46. Snyder, A. W. & Love, J. *Optical Waveguide Theory* en. ISBN: 978-1-4613-2813-1 (Chapman and Hall, Nov. 1983).
47. Driscoll, J. B. *et al.* Large longitudinal electric fields (E_z) in silicon nanowire waveguides. en. *Optics Express* **17**, 2797. ISSN: 1094-4087. <https://www.osapublishing.org/oe/abstract.cfm?uri=oe-17-4-2797> (2020) (Feb. 2009).
48. May, S., Kues, M., Clerici, M. & Sorel, M. Second-harmonic generation in AlGaAs-on-insulator waveguides. en. *Optics Letters* **44**, 1339. ISSN: 0146-9592, 1539-4794. <https://www.osapublishing.org/abstract.cfm?URI=ol-44-6-1339> (2020) (Mar. 2019).
49. Rutkowska, K. *et al.* Second Harmonic Generation in AlGaAs Nanowaveguides. en. *Acta Physica Polonica A* **120**, 725–731. ISSN: 0587-4246, 1898-794X. <http://przyrbwn.icm.edu.pl/APP/PDF/120/a120z4p35.pdf> (2020) (Oct. 2011).
50. De Luca, E., Sanatinia, R., Mensi, M., Anand, S. & Swillo, M. Modal phase matching in nanostructured zinc-blende semiconductors for second-order nonlinear optical interactions. en. *Physical Review B* **96**, 075303. ISSN: 2469-9950, 2469-9969. <http://link.aps.org/doi/10.1103/PhysRevB.96.075303> (2020) (Aug. 2017).
51. Luo, R. *et al.* Optical Parametric Generation in a Lithium Niobate Microring with Modal Phase Matching. en. *Physical Review Applied* **11**, 034026. ISSN: 2331-7019. <https://link.aps.org/doi/10.1103/PhysRevApplied.11.034026> (2021) (Mar. 2019).
52. Signorini, S. *et al.* Intermodal four-wave mixing in silicon waveguides. en. *Photonics Research* **6**, 805. ISSN: 2327-9125. <https://www.osapublishing.org/abstract.cfm?URI=prj-6-8-805> (2021) (Aug. 2018).
53. Turner, A. C. *et al.* Tailored anomalous group-velocity dispersion in silicon channel waveguides. en. *Optics Express* **14**, 4357. ISSN: 1094-4087. <https://www.osapublishing.org/oe/abstract.cfm?uri=oe-14-10-4357> (2021) (2006).
54. Mas, S., Caraquitena, J., Galán, J. V., Sanchis, P. & Martí, J. Tailoring the dispersion behavior of silicon nanophotonic slot waveguides. en. *Optics Express* **18**, 20839. ISSN: 1094-4087. <https://www.osapublishing.org/oe/abstract.cfm?uri=oe-18-20-20839> (2021) (Sept. 2010).

55. Jankowski, M., Langrock, C., Desiatov, B., Loncar, M. & Fejer, M. M. Supercontinuum Generation by Saturated $\chi^{(2)}$ Interactions. en. *arXiv:2102.12856 [physics]*. arXiv: 2102.12856. <http://arxiv.org/abs/2102.12856> (2021) (Feb. 2021).
56. Yu, M., Desiatov, B., Okawachi, Y., Gaeta, A. L. & Lončar, M. Coherent two-octave-spanning supercontinuum generation in lithium-niobate waveguides. en. *Optics Letters* **44**, 1222. ISSN: 0146-9592, 1539-4794. <https://www.osapublishing.org/abstract.cfm?URI=ol-44-5-1222> (2020) (Mar. 2019).
57. Kuyken, B., Billet, M., Leo, F., Yvind, K. & Pu, M. Octave-spanning coherent supercontinuum generation in an AlGaAs-on-insulator waveguide. en. *Optics Letters* **45**, 603. ISSN: 0146-9592, 1539-4794. <https://www.osapublishing.org/abstract.cfm?URI=ol-45-3-603> (2020) (Feb. 2020).
58. Dunsby, C. & French, P. M. W. en. in *Supercontinuum Generation in Optical Fibers* (eds Dudley, J. M. & Taylor, J. R.) 349–372 (Cambridge University Press, Cambridge, 2010). ISBN: 978-0-511-75046-5. https://www.cambridge.org/core/product/identifier/CB09780511750465A022/type/book_part (2021).
59. Kippenberg, T. J., Holzwarth, R. & Diddams, S. A. Microresonator-Based Optical Frequency Combs. en. *Science* **332**. Number: 6029 Reporter: Science, 555–559. ISSN: 0036-8075, 1095-9203. <http://www.sciencemag.org/cgi/doi/10.1126/science.1193968> (2019) (Apr. 2011).
60. Schuster, V. *et al.* Towards Dual Comb Spectroscopy in the Ultraviolet Spectral Region. en, 15.
61. Gasse, K. V. *et al.* An on-chip III-V-semiconductor-on-silicon laser frequency comb for gas-phase molecular spectroscopy in real-time. en, 17 (2020).
62. Pouvellarie, N. & Ciret, C. Optical event horizon in silicon-on-insulator waveguides. en, 4.
63. Darsow-Fromm, C., Schröder, M., Gurs, J., Schnabel, R. & Steinlechner, S. Highly-efficient generation of coherent light at 2128 nm via degenerate optical-parametric oscillation. en. *arXiv:2008.07193 [astro-ph, physics:physics, physics:quant-ph]*. arXiv: 2008.07193. <http://arxiv.org/abs/2008.07193> (2020) (Aug. 2020).
64. Placke, M. & Ramelow, S. Ultra strong parametric nonlinearities in AlGaAs-on-insulator waveguides. en. *arXiv:2008.11531 [physics, physics:quant-ph]*. arXiv: 2008.11531. <http://arxiv.org/abs/2008.11531> (2020) (Aug. 2020).
65. Diddams, S. A. The evolving optical frequency comb [Invited]. en. *Journal of the Optical Society of America B* **27**. Number: 11 Reporter: Journal of the Optical Society of America B, B51. ISSN: 0740-3224, 1520-8540. <https://www.osapublishing.org/abstract.cfm?URI=josab-27-11-B51> (2019) (Nov. 2010).
66. Udem, T., Holzwarth, R. & Hänsch, T. W. Optical frequency metrology. en. *Nature* **416**, 233–237. ISSN: 1476-4687, 0028-0836. <https://www.nature.com/articles/416233a> (2002).
67. Hall, J. L. Nobel Lecture: Defining and measuring optical frequencies. en. *Reviews of Modern Physics* **78**, 1279–1295. ISSN: 0034-6861, 1539-0756. <https://link.aps.org/doi/10.1103/RevModPhys.78.1279> (2021) (Nov. 2006).
68. Telle, H. *et al.* Carrier-envelope offset phase control: A novel concept for absolute optical frequency measurement and ultrashort pulse generation. en. *Applied Physics B* **69**, 327–332. ISSN: 0946-2171, 1432-0649. <http://link.springer.com/10.1007/s003400050813> (2021) (Oct. 1999).

69. Holzwarth, R. *et al.* Optical Frequency Synthesizer for Precision Spectroscopy. en. *Physical Review Letters* **85**, 2264–2267. ISSN: 0031-9007, 1079-7114. <https://link.aps.org/doi/10.1103/PhysRevLett.85.2264> (2021) (Sept. 2000).
70. Ricciardi, I. *et al.* Frequency comb generation in quadratic nonlinear media. en. *Physical Review A* **91**, 063839. ISSN: 1050-2947, 1094-1622. <https://link.aps.org/doi/10.1103/PhysRevA.91.063839> (2020) (June 2015).
71. Parisi, M. *et al.* AlGaAs waveguide microresonators for efficient generation of quadratic frequency combs. en. *Journal of the Optical Society of America B* **34**, 1842. ISSN: 0740-3224, 1520-8540. <https://www.osapublishing.org/abstract.cfm?URI=josab-34-9-1842> (2020) (Sept. 2017).
72. Leo, F. *et al.* Frequency-comb formation in doubly resonant second-harmonic generation. en. *Physical Review A* **93**, 043831. ISSN: 2469-9926, 2469-9934. <https://link.aps.org/doi/10.1103/PhysRevA.93.043831> (2020) (Apr. 2016).
73. Ono, M., Yasuda, K., Fukumoto, A. & Kaneko, M. A high density read-only optical disk system using superresolution and an SHG green laser. en. *Optical Data Storage* **2514**, 20–27. <https://www.spiedigitallibrary.org/conference-proceedings-of-spie/2514/1/High-density-read-only-optical-disk-system-using-superresolution-and/10.1117/12.218738.short> (1995).
74. Kitaoka, Y., Yokoyama, T., Mizuuchi, K. & Yamamoto, K. Miniaturized Blue Laser using Second Harmonic Generation. en. *Japanese Journal of Applied Physics* **39**, 3416–3418. ISSN: 0021-4922, 1347-4065. <https://iopscience.iop.org/article/10.1143/JJAP.39.3416> (2021) (June 2000).
75. Cicchi, R. *et al.* From molecular structure to tissue architecture: collagen organization probed by SHG microscopy. en. *Journal of Biophotonics* **6**, 129–142. ISSN: 1864063X. <http://doi.wiley.com/10.1002/jbio.201200092> (2021) (Feb. 2013).
76. Ajeti, V. *et al.* Structural changes in mixed Col I/Col V collagen gels probed by SHG microscopy: implications for probing stromal alterations in human breast cancer. en. *Biomedical Optics Express* **2**, 2307. ISSN: 2156-7085, 2156-7085. <https://www.osapublishing.org/boe/abstract.cfm?uri=boe-2-8-2307> (2021) (Aug. 2011).
77. Amat-Roldán, I., Cormack, I. G., Loza-Alvarez, P., Gualda, E. J. & Artigas, D. Ultrashort pulse characterisation with SHG collinear-FROG. en. *Optics Express* **12**, 1169. ISSN: 1094-4087. <https://www.osapublishing.org/oe/abstract.cfm?uri=oe-12-6-1169> (2021) (2004).
78. Taft, G. *et al.* Measurement of 10-fs laser pulses. en. *IEEE Journal of Selected Topics in Quantum Electronics* **2**, 575–585. ISSN: 1077260X. <http://ieeexplore.ieee.org/document/571757/> (2021) (Sept. 1996).
79. Zernike, F. & Midwinter, J. E. *Applied nonlinear optics* ISBN: 0-486-45360-X (Wiley, 1973).

Chapter 2

III-V integrated photonics

By definition, III-V materials are alloys constituted of at least one element from group III (boron, aluminium, gallium...) and at least one element from the group V (nitrogen, phosphorus, arsenic...) of the periodic table in fig. 2.1. These materials are well documented with various interesting properties [1]. They have been widely studied in the domain of electronics for their semi-conductive properties [2, 3]. They also attract a lot of attention in optoelectronic devices [4], especially in the domain of integrated lasers [5–7], detectors [8–11] and modulators [12–14].

--	--	--	--	--	--	--	--	--	--	--	--	--	--	--	--	--	--	--	--	--	--	--	--	--	--	--	--	--	--	--	--	--	--	--	--	--	--	--	--	--	--	--	--	--	--	--	--	--	--	--	--	--	--	--	--	--	--	--	--	--	--	--	--	--	--	--	--	--	--	--	--	--	--	--	--	--	--	--	--	--	--	--	--	--	--	--	--	--	--	--	--	--	--	--	--	--	--	--	--	--	--	--	--	--	--	--	--	--	--	--	--	--	--	--	--	--	--	--	--	--	--	--	--	--	--	--	--	--	--	--	--	--	--	--	--	--	--	--	--	--	--	--	--	--	--	--	--	--	--	--	--	--	--	--	--	--	--	--	--	--	--	--	--	--	--	--	--	--	--	--	--	--	--	--	--	--	--	--	--	--	--	--	--	--	--	--	--	--	--	--	--	--	--	--	--	--	--	--	--	--	--	--	--	--	--	--	--	--	--	--	--	--	--	--	--	--	--	--	--	--	--	--	--	--	--	--	--	--	--	--	--	--	--	--	--	--	--	--	--	--	--	--	--	--	--	--	--	--	--	--	--	--	--	--	--	--	--	--	--	--	--	--	--	--	--	--	--	--	--	--	--	--	--	--	--	--	--	--	--	--	--	--	--	--	--	--	--	--	--	--	--	--	--	--	--	--	--	--	--	--	--	--	--	--	--	--	--	--	--	--	--	--	--	--	--	--	--	--	--	--	--	--	--	--	--	--	--	--	--	--	--	--	--	--	--	--	--	--	--	--	--	--	--	--	--	--	--	--	--	--	--	--	--	--	--	--	--	--	--	--	--	--	--	--	--	--	--	--	--	--	--	--	--	--	--	--	--	--	--	--	--	--	--	--	--	--	--	--	--	--	--	--	--	--	--	--	--	--	--	--	--	--	--	--	--	--	--	--	--	--	--	--	--	--	--	--	--	--	--	--	--	--	--	--	--	--	--	--	--	--	--	--	--	--	--	--	--	--	--	--	--	--	--	--	--	--	--	--	--	--	--	--	--	--	--	--	--	--	--	--	--	--	--	--	--	--	--	--	--	--	--	--	--	--	--	--	--	--	--	--	--	--	--	--	--	--	--	--	--	--	--	--	--	--	--	--	--	--	--	--	--	--	--	--	--	--	--	--	--	--	--	--	--	--	--	--	--	--	--	--	--	--	--	--	--	--	--	--	--	--	--	--	--	--	--	--	--	--	--	--	--	--	--	--	--	--	--	--	--	--	--	--	--	--	--	--	--	--	--	--	--	--	--	--	--	--	--	--	--	--	--	--	--	--	--	--	--	--	--	--	--	--	--	--	--	--	--	--	--	--	--	--	--	--	--	--	--	--	--	--	--	--	--	--	--	--	--	--	--	--	--	--	--	--	--	--	--	--	--	--	--	--	--	--	--	--	--	--	--	--	--	--	--	--	--	--	--	--	--	--	--	--	--	--	--	--	--	--	--	--	--	--	--	--	--	--	--	--	--	--	--	--	--	--	--	--	--	--	--	--	--	--	--	--	--	--	--	--	--	--	--	--	--	--	--	--	--	--	--	--	--	--	--	--	--	--	--	--	--	--	--	--	--	--	--	--	--	--	--	--	--	--	--	--	--	--	--	--	--	--	--	--	--	--	--	--	--	--	--	--	--	--	--	--	--	--	--	--	--	--	--	--	--	--	--	--	--	--	--	--	--	--	--	--	--	--	--	--	--	--	--	--	--	--	--	--	--	--	--	--	--	--	--	--	--	--	--	--	--	--	--	--	--	--	--	--	--	--	--	--	--	--	--	--	--	--	--	--	--	--	--	--	--	--	--	--	--	--	--	--	--	--	--	--	--	--	--	--	--	--	--	--	--	--	--	--	--	--	--	--	--	--	--	--	--	--	--	--	--	--	--	--	--	--	--	--	--	--	--	--	--	--	--	--	--	--	--	--	--	--	--	--	--	--	--	--	--	--	--	--	--	--	--	--	--	--	--	--	--	--	--	--	--	--	--	--	--	--	--	--	--	--	--	--	--	--	--	--	--	--	--	--	--	--	--	--	--	--	--	--	--	--	--	--	--	--	--	--	--	--	--	--	--	--	--	--	--	--	--	--	--	--	--	--	--	--	--	--	--	--	--	--	--	--	--	--	--	--	--	--	--	--	--	--	--	--	--	--	--	--	--	--	--	--	--	--	--	--	--	--	--	--	--	--	--	--	--	--	--	--	--	--	--	--	--	--	--	--	--	--	--	--	--	--	--	--	--	--	--	--	--	--	--	--	--	--	--	--	--	--	--	--	--	--	--	--	--	--	--	--	--	--	--	--	--	--	--	--	--	--	--	--	--	--	--	--	--	--	--	--	--	--	--	--	--	--	--	--	--	--	--	--	--	--	--	--	--	--	--	--	--	--	--	--	--	--	--	--	--	--	--	--	--	--	--	--	--	--	--	--	--	--	--	--	--	--	--	--	--	--	--	--	--	--	--	--	--	--	--	--	--	--	--	--	--	--	--	--	--	--	--	--	--	--	--	--	--	--	--	--	--	--	--	--	--	--	--	--	--	--	--	--	--	--	--	--	--	--	--	--	--	--	--	--	--	--	--	--	--	--	--	--	--	--	--	--	--	--	--	--	--	--	--	--	--	--	--	--	--	--	--	--	--	--	--	--	--	--	--	--	--	--	--	--	--	--	--	--	--	--	--	--	--	--	--	--	--	--	--	--	--	--	--	--	--	--	--	--	--	--	--	--	--	--	--	--	--	--	--	--	--	--	--	--	--	--	--	--	--	--	--	--	--	--	--	--	--	--	--	--	--	--	--	--	--	--	--	--	--	--	--	--	--	--	--	--	--	--	--	--	--	--	--	--	--	--	--	--	--	--	--	--	--	--	--	--	--	--	--	--	--	--	--	--	--	--	--	--	--	--	--	--	--	--	--	--	--	--	--	--	--	--	--	--	--	--	--	--	--	--	--	--	--	--	--	--	--	--	--	--	--	--	--	--	--	--	--	--	--	--	--	--	--	--	--	--	--	--	--	--	--	--	--	--	--	--	--	--	--	--	--	--	--	--	--	--	--	--	--	--	--	--	--	--	--	--	--	--	--	--	--	--	--	--	--	--	--	--	--	--	--	--	--	--	--	--	--	--	--	--	--	--	--	--	--	--	--	--	--	--	--	--	--	--	--	--	--	--	--	--	--	--	--	--	--	--	--	--	--	--	--	--	--	--	--	--	--	--	--	--	--	--	--	--	--	--	--	--	--	--	--	--	--	--	--	--	--	--	--	--	--	--	--	--	--	--	--	--	--	--	--	--	--	--	--	--	--	--	--	--	--	--	--	--	--	--	--	--	--	--	--	--	--	--	--	--	--	--	--	--	--	--	--	--	--	--	--	--	--	--	--	--	--	--	--	--	--	--	--	--	--	--	--	--	--	--	--	--	--	--	--	--	--	--	--	--	--	--	--	--	--	--	--	--	--	--	--	--	--	--	--	--	--	--	--	--	--	--	--	--	--	--	--	--	--	--	--	--	--	--	--	--	--	--	--	--	--	--	--	--	--	--	--	--	--	--	--	--	--	--	--	--	--	--	--	--	--	--	--	--	--	--	--	--	--	--	--	--	--	--	--	--	--	--	--	--	--	--	--	--	--	--	--	--	--	--	--	--	--	--	--	--	--	--	--	--	--	--	--	--	--	--	--	--	--	--	--	--	--	--	--	--	--	--	--	--	--	--	--	--	--	--	--	--	--	--	--	--	--	--	--	--	--	--	--	--	--	--	--	--	--	--	--	--	--	--	--	--	--	--	--	--	--	--	--	--	--	--	--	--	--	--	--	--	--	--	--	--	--	--	--	--	--	--	--	--	--	--	--	--	--	--	--	--	--	--	--	--	--	--	--	--	--	--	--	--	--	--	--	--	--	--	--	--	--	--	--	--	--	--	--	--	--	--	--	--	--	--	--	--	--	--	--	--	--	--	--	--	--	--	--	--	--	--	--	--	--	--	--	--	--	--	--	--	--	--	--	--	--	--	--	--	--	--	--	--	--	--	--	--	--	--	--	--	--	--	--	--	--	--	--	--	--	--	--	--	--	--	--	--	--	--	--	--	--	--	--	--	--	--	--	--	--	--	--	--	--	--	--	--	--	--	--	--	--	--	--	--	--	--	--	--	--	--	--	--	--	--	--	--	--	--	--	--	--	--	--	--	--	--	--	--	--	--	--	--	--	--	--	--	--	--	--	--	--	--	--	--	--	--	--	--	--	--	--	--	--	--	--	--	--	--	--	--	--	--	--	--	--	--	--	--	--	--	--	--	--	--	--	--	--	--	--	--	--	--	--	--	--	--	--	--	--	--	--	--	--	--	--	--	--	--	--	--	--	--	--	--	--	--	--	--	--	--	--	--	--	--	--	--	--	--	--	--	--	--	--	--	--	--	--	--	--	--	--	--	--	--	--	--	--	--	--	--	--	--	--	--	--	--	--	--	--	--	--	--	--	--	--	--	--	--	--	--	--	--	--	--	--	--	--	--	--	--	--	--	--	--	--	--	--	--	--	--	--	--	--	--	--	--	--	--	--	--	--	--	--	--	--	--	--	--	--	--	--	--	--	--	--	--	--	--	--	--	--	--	--	--	--	--	--	--	--	--	--	--	--	--	--	--	--	--	--	--	--	--	--	--	--	--	--	--	--	--	--	--	--	--	--	--	--	--	--	--	--	--	--	--	--	--	--	--	--	--	--	--	--	--	--	--	--	--	--	--	--	--	--	--	--	--	--	--	--	--	--	--	--	--	--	--	--	--	--	--	--	--	--	--	--	--	--	--	--	--	--	--	--	--	--	--	--	--	--	--	--	--	--	--	--	--	--	--	--	--	--	--	--	--	--	--	--	--	--	--	--	--	--	--	--	--	--	--	--	--	--	--	--	--	--	--	--	--	--	--	--	--	--	--	--	--	--	--	--	--	--	--	--	--	--	--	--	--	--	--	--	--	--	--	--	--	--	--	--	--	--	--	--	--	--	--	--	--	--	--	--	--	--	--	--	--	--	--	--	--	--	--	--	--	--	--	--	--	--	--	--	--	--	--	--	--	--	--	--	--	--	--	--	--	--	--	--	--	--	--	--	--	--	--	--	--	--	--	--	--	--	--	--	--	--	--	--	--	--	--	--	--	--	--	--	--	--	--	--	--	--	--	--	--	--	--	--	--	--	--	--	--	--	--	--	--	--	--	--	--	--	--	--	--	--	--	--	--	--	--	--	--	--	--	--	--	--	--	--	--	--	--	--	--	--	--	--	--	--	--	--	--	--	--	--	--	--	--	--	--	--	--	--	--	--	--	--	--	--	--	--	--	--	--	--	--	--	--	--	--	--	--	--	--	--	--	--	--	--	--	--	--	--	--	--	--	--	--	--	--	--	--	--	--	--	--	--	--	--	--	--	--	--	--	--	--	--	--	--	--	--	--	--	--	--	--	--	--	--	--	--	--	--	--	--	--	--	--	--	--	--	--	--	--	--	--	--	--	--	--	--	--	--	--	--	--	--	--	--	--	--	--	--	--	--	--	--	--	--	--	--	--	--	--	--	--	--	--	--	--	--	--	--	--	--	--	--	--	--	--	--	--	--	--	--	--	--	--	--	--	--	--	--	--	--	--	--	--	--	--	--	--	--	--	--	--	--	--	--	--	--	--	--	--	--	--	--	--	--	--	--	--	--	--	--	--	--	--	--	--	--	--	--	--	--	--	--	--	--	--	--	--	--	--	--	--	--	--	--	--	--	--	--	--	--	--	--	--	--	--	--	--	--	--	--	--	--	--	--	--	--	--	--	--	--	--	--	--	--	--	--	--	--	--	--	--	--	--	--	--	--	--	--	--	--	--	--	--	--	--	--	--	--	--	--	--	--	--	--	--	--	--	--	--	--	--	--	--	--	--	--	--	--	--	--	--	--	--	--	--	--	--	--	--	--	--	--	--	--	--	--	--	--	--	--	--	--	--	--	--	--	--	--	--	--	--	--	--	--	--	--	--	--	--	--	--	--	--	--	--	--	--	--	--	--	--	--	--	--	--	--	--	--	--	--	--	--	--	--	--	--	--	--	--	--	--	--	--	--	--	--	--	--	--	--	--	--	--	--	--	--	--	--	--	--	--	--	--	--	--	--	--	--	--	--	--	--	--	--	--	--	--	--	--	--	--	--	--	--	--	--	--	--	--	--	--	--	--	--	--	--	--	--	--	--	--	--	--	--	--	--	--	--	--	--	--	--	--	--	--	--	--	--	--	--	--	--	--	--	--	--	--	--	--	--	--	--	--	--	--	--	--	--	--	--	--	--	--	--	--	--	--	--	--	--	--	--	--	--	--	--	--	--	--	--	--	--	--	--	--	--	--	--	--	--	--	--	--	--	--	--	--	--	--	--	--	--	--	--	--	--	--	--	--	--	--	--	--	--	--	--	--	--	--	--	--	--	--	--	--	--	--	--	--	--	--	--	--	--	--	--	--	--	--	--	--	--	--	--	--	--	--	--	--	--	--	--	--	--	--	--	--	--	--	--	--	--	--	--	--	--	--	--	--	--	--	--	--	--	--	--	--	--	--	--	--	--	--	--	--	--	--	--	--	--	--	--	--	--	--	--	--	--	--	--	--	--	--	--	--	--	--	--	--	--	--	--	--	--	--	--	--	--	--	--	--	--	--	--	--	--	--	--	--	--	--	--	--	--	--	--	--	--	--	--	--	--	--	--	--	--	--	--	--	--	--	--	--	--	--	--	--	--	--	--	--	--	--	--	--	--	--	--	--	--	--	--	--	--	--	--	--	--	--	--	--	--	--	--	--	--	--	--	--	--	--	--	--	--	--	--	--	--	--	--	--	--	--	--	--	--	--	--	--	--	--	--	--	--	--	--	--	--	--	--	--	--	--	--	--	--	--	--	--	--	--	--	--	--	--	--	--	--	--	--	--	--	--	--	--	--	--	--	--	--	--	--	--	--	--	--	--	--	--	--	--	--	--	--	--	--	--	--	--	--	--	--	--	--	--	--	--	--	--	--	--	--	--	--	--	--	--	--	--	--	--	--	--	--	--	--	--	--	--	--	--	--	--	--	--	--	--	--	--	--	--	--	--	--	--	--	--	--	--	--	--	--	--	--	--	--	--	--	--	--	--	--	--	--	--	--	--	--	--	--	--	--	--	--	--	--	--	--	--	--	--	--	--	--	--	--	--	--	--	--	--	--	--	--	--	--	--	--	--	--	--	--	--	--	--	--	--	--	--	--	--	--	--	--	--	--	--	--	--	--	--	--	--	--	--	--	--	--	--	--	--	--	--	--	--	--	--	--	--	--	--	--	--	--	--	--	--	--	--	--	--	--	--	--	--	--	--	--	--	--	--	--	--	--	--	--	--	--	--	--	--	--	--	--	--	--	--	--	--	--	--	--	--	--	--	--	--	--	--	--	--	--	--	--	--	--	--	--	--	--	--	--	--	--	--	--	--	--	--	--	--	--	--	--	--	--	--	--	--	--	--	--	--	--	--	--	--	--	--	--	--	--	--	--	--	--	--	--	--	--	--	--	--	--	--	--	--	--	--	--	--	--	--	--	--	--	--	--	--	--	--	--	--	--	--	--	--	--	--	--	--	--	--	--	--	--	--	--	--	--	--	--	--	--	--	--	--	--	--	--	--	--	--	--	--	--	--	--	--	--	--	--	--	--	--	--	--	--	--	--	--	--	--	--	--	--	--	--	--	--	--	--	--	--	--	--	--	--	--	--	--	--	--	--	--	--	--	--	--	--	--	--	--	--	--	--	--	--	--	--	--	--	--	--	--	--	--	--	--	--	--	--	--	--	--	--	--	--	--	--	--	--	--	--	--	--	--	--	--	--	--	--	--	--	--	--	--	--	--	--	--	--	--	--	--	--	--	--	--	--	--	--	--	--	--	--	--	--	--	--	--	--	--	--	--	--	--	--	--	--	--	--	--	--	--	--	--	--	--	--	--	--	--	--	--	--	--	--	--	--	--	--	--	--	--	--	--	--	--	--	--	--	--	--	--	--	--	--	--	--	--	--	--	--	--	--	--	--	--	--	--	--	--	--	--	--	--	--	--	--	--	--	--	--	--	--	--	--	--	--	--	--	--	--	--	--	--	--	--	--	--	--	--	--	--	--	--	--	--	--	--	--	--	--	--	--	--	--	--	--	--	--	--	--	--	--	--	--	--	--	--	--	--	--	--	--	--	--	--	--	--	--	--	--	--	--	--	--	--	--	--	--	--	--	--	--	--	--	--	--	--	--	--	--	--	--	--	--	--	--	--	--	--	--	--	--	--	--	--	--	--	--	--	--	--	--	--	--	--	--	--	--	--	--	--	--	--	--	--	--	--	--	--	--	--	--	--	--	--	--	--	--	--	--	--	--	--	--	--	--	--	--	--	--	--	--	--	--	--	--	--	--	--	--	--	--	--	--	--	--	--	--	--	--	--	--	--	--	--	--	--	--	--	--	--	--	--	--	--	--	--	--	--	--	--	--	--	--	--	--	--	--	--	--	--	--	--	--	--	--	--	--	--	--	--	--	--	--	--	--	--	--	--	--	--	--	--	--	--	--	--	--	--	--	--	--	--	--	--	--	--	--	--	--	--	--	--	--	--	--	--	--	--	--	--	--	--	--	--	--	--	--	--	--	--	--	--	--	--	--	--	--	--	--	--	--	--	--	--	--	--	--	--	--	--	--	--	--	--	--	--	--	--	--	--	--	--	--	--	--	--	--	--	--	--	--	--	--	--	--	--	--	--	--	--	--	--	--	--	--	--	--	--	--	--	--	--	--	--	--	--	--	--	--	--	--	--	--	--	--	--	--	--	--	--	--	--	--	--	--	--	--	--	--	--	--	--	--	--	--	--	--	--	--	--	--	--	--	--	--	--	--	--	--	--	--	--	--	--	--	--	--	--	--	--	--	--	--	--	--	--	--	--	--	--	--	--	--	--	--	--	--	--	--	--	--	--	--	--	--	--	--	--	--	--	--	--	--	--	--	--	--	--	--	--	--	--	--	--	--	--	--	--	--	--	--	--	--	--	--	--	--	--	--	--	--	--	--	--	--	--	--	--	--	--	--	--	--	--	--	--	--	--	--	--	--	--	--	--	--	--	--	--	--	--	--	--	--	--	--	--	--	--	--	--	--	--	--	--	--	--	--	--	--	--	--	--	--	--	--	--	--	--	--	--	--	--	--	--	--	--	--	--	--	--	--	--	--	--	--	--	--	--	--	--	--	--	--	--	--	--	--	--	--	--	--	--	--	--	--	--	--	--	--	--	--	--	--	--	--	--	--	--	--	--	--	--	--	--	--	--	--	--	--	--	--	--	--	--	--	--	--	--	--	--	--	--	--	--	--	--	--	--	--	--	--	--	--	--	--	--	--	--	--	--	--	--	--	--	--	--	--	--	--	--	--	--	--	--	--	--	--	--	--	--	--	--	--	--	--	--	--	--	--	--	--	--	--	--	--	--	--	--	--	--	--	--	--	--	--	--	--	--	--	--	--	--	--	--	--	--	--	--	--	--	--	--	--	--	--	--	--	--	--	--	--	--	--	--	--	--	--	--	--	--	--	--	--	--	--	--	--	--	--	--	--	--	--	--	--	--	--	--	--	--	--	--	--	--	--	--	--	--	--	--	--	--	--	--	--	--	--	--	--	--	--	--	--	--	--	--	--	--	--	--	--	--	--	--	--	--	--	--	--	--	--	--	--	--	--	--	--	--	--	--	--	--	--	--	--	--	--	--	--	--	--	--	--	--	--	--	--	--	--	--	--	--	--	--	--	--	--	--	--	--	--	--	--	--	--	--	--	--	--	--	--	--	--	--	--	--	--	--	--	--	--	--	--	--	--	--	--	--	--	--	--	--	--	--	--	--	--	--	--	--	--	--	--	--	--	--	--	--	--	--	--	--	--	--	--	--	--	--	--	--	--	--	--	--	--	--	--	--	--	--	--	--	--	--	--	--	--	--	--	--	--	--	--	--	--	--	--	--	--	--	--	--	--	--	--	--	--	--	--	--	--	--	--	--	--	--	--	--	--	--	--	--	--	--	--	--	--	--	--	--	--	--	--	--	--	--	--	--	--	--	--	--	--	--	--	--	--	--	--	--	--	--	--	--	--	--	--	--	--	--	--	--	--	--	--	--	--	--	--	--	--	--	--	--	--	--	--	--	--	--	--	--	--	--	--	--	--	--	--	--	--	--	--	--	--	--	--	--	--	--	--	--	--	--	--	--	--	--	--	--	--	--	--	--	--	--	--	--	--	--	--	--	--	--	--	--	--	--	--	--	--	--	--	--	--	--	--	--	--	--	--	--	--	--	--	--	--	--	--	--	--	--	--	--	--	--	--	--	--	--	--	--	--	--	--	--	--	--	--	--	--	--	--	--	--	--	--	--	--	--	--	--	--	--	--	--	--	--	--	--	--	--	--	--	--	--	--	--	--	--	--	--	--	--	--	--	--	--	--	--	--	--	--	--	--	--	--	--	--	--	--	--	--	--	--	--	--	--	--	--	--	--	--	--	--	--	--	--	--	--	--	--	--	--	--	--	--	--	--	--	--	--	--	--	--	--	--	--	--	--	--	--	--	--	--	--	--	--	--	--	--	--	--	--	--	--	--	--	--	--	--	--	--	--	--	--	--	--	--	--	--	--	--	--	--	--	--	--	--	--	--	--	--	--	--	--	--	--	--	--	--	--	--	--	--	--	--	--	--	--	--	--	--	--	--	--	--	--	--	--	--	--	--	--	--	--	--	--	--	--	--	--	--	--	--	--	--	--	--	--	--	--	--	--	--	--	--	--	--	--	--	--	--	--	--	--	--	--	--	--	--	--	--	--	--	--	--	--	--	--	--	--	--	--	--	--	--	--	--	--	--	--	--	--	--	--	--	--	--	--	--	--	--	--	--	--	--	--	--	--	--	--	--	--	--	--	--	--	--	--	--	--	--	--	--	--	--	--	--	--	--	--	--	--	--	--	--	--	--	--	--	--	--	--	--	--	--	--	--	--	--	--	--	--	--	--	--	--	--	--	--	--	--	--	--	--	--	--	--	--	--	--	--	--	--	--	--	--	--	--	--	--	--	--	--	--	--	--	--	--	--	--	--	--	--	--	--	--	--	--	--	--	--	--	--	--	--	--	--	--	--	--	--	--	--	--	--	--	--	--	--	--	--	--	--	--	--	--	--	--	--	--	--	--	--	--	--	--	--	--	--	--	--	--	--	--	--	--	--	--	--	--	--	--	--	--	--	--	--	--	--	--	--	--	--	--	--	--	--	--	--	--	--	--	--	--	--	--	--	--	--	--	--	--	--	--	--	--	--	--	--	--	--	--	--	--	--	--	--	--	--	--	--	--	--	--	--	--	--	--	--	--	--	--	--	--	--	--	--	--	--	--	--	--	--	--	--	--	--	--	--	--	--	--	--	--	--	--	--	--	--	--	--	--	--	--	--	--	--	--	--	--	--	--	--	--	--	--	--	--	--	--	--	--	--	--	--	--	--	--	--	--	--	--	--	--	--	--	--	--	--	--	--	--	--	--	--	--	--	--	--	--	--	--	--	--	--	--	--	--	--	--	--	--	--	--	--	--	--	--	--	--	--	--	--	--	--	--	--	--	--	--	--	--	--	--	--	--	--	--	--	--	--	--	--	--	--	--	--	--	--	--	--	--	--	--	--	--	--	--	--	--	--	--	--	--	--	--	--	--	--	--	--	--	--	--	--	--	--	--	--	--	--	--	--	--	--	--	--	--	--	--	--	--	--	--	--	--	--	--	--	--	--	--	--	--	--	--	--	--	--	--	--	--	--	--	--	--	--	--	--	--	--	--	--	--	--	--	--	--	--	--	--	--	--	--	--	--	--	--	--	--	--	--	--	--	--	--	--	--	--	--	--	--	--	--	--	--	--	--	--	--	--	--	--	--	--	--	--	--	--	--	--	--	--	--	--	--	--	--	--	--	--	--	--	--	--	--	--	--	--	--	--	--	--	--	--	--	--	--	--	--	--	--	--	--	--	--	--	--	--	--	--	--	--	--	--	--	--	--	--	--	--	--	--	--	--	--	--	--	--	--	--	--	--	--	--	--	--	--	--	--	--	--	--	--	--	--	--	--	--	--	--	--	--	--	--	--	--	--	--	--	--	--	--	--	--	--	--	--	--	--	--	--	--	--	--	--	--	--	--	--	--	--	--	--	--	--	--	--	--	--	--	--	--	--	--	--	--	--	--	--	--	--	--	--	--	--	--	--	--	--	--	--	--	--	--	--	--	--	--	--	--	--	--	--	--	--	--	--	--	--	--	--	--	--	--	--	--	--	--	--	--	--	--	--	--	--	--	--	--	--	--	--	--	--	--	--	--	--	--	--	--	--	--	--	--	--	--	--	--	--	--	--	--	--	--	--	--	--	--	--	--	--	--	--	--	--	--	--	--	--	--	--	--	--	--	--	--	--	--	--	--	--	--	--	--	--	--	--	--	--	--	--	--	--	--	--	--	--	--	--	--	--	--	--	--	--	--	--	--	--	--	--	--	--	--	--	--	--	--	--	--	--	--	--	--	--	--	--	--	--	--	--	--	--	--	--	--	--	--	--	--	--	--	--	--	--	--	--	--	--	--	--	--	--	--	--	--	--	--	--	--	--	--	--	--	--	--	--	--	--	--	--	--	--	--	--	--	--	--	--	--	--	--	--	--	--	--	--	--	--	--	--	--	--	--	--	--	--	--	--	--	--	--	--	--	--	--	--	--	--	--	--	--	--	--	--	--	--	--	--	--	--	--	--	--	--	--	--	--	--	--	--	--	--	--	--	--	--	--	--	--	--	--	--	--	--	--	--	--	--	--	--	--	--	--	--	--	--	--	--	--	--	--	--	--	--	--	--	--	--	--	--	--	--	--	--	--	--	--	--	--	--	--	--	--	--	--	--	--	--	--	--	--	--	--	--	--	--	--	--	--	--	--	--	--	--	--	--	--	--	--	--	--	--	--	--	--	--	--	--	--	--	--	--	--	--	--	--	--	--	--	--	--	--	--	--	--	--	--	--	--	--	--	--	--	--	--	--	--	--	--	--	--	--	--	--	--	--	--	--	--	--	--	--	--	--	--	--	--	--	--	--	--	--	--	--	--	--	--	--	--	--	--	--	--	--	--	--	--	--	--	--	--	--	--	--	--	--	--	--	--	--	--	--	--	--	--	--	--	--	--	--	--	--	--	--	--	--	--	--	--	--	--	--	--	--	--	--	--	--	--	--	--	--	--	--	--	--	--	--	--	--	--	--	--	--	--	--	--	--	--	--	--	--	--	--	--	--	--	--	--	--	--	--	--	--	--	--	--	--	--	--	--	--	--	--	--	--	--	--	--	--	--	--	--	--	--	--	--	--	--	--	--	--	--	--	--	--	--	--	--	--	--	--	--	--	--	--	--	--	--	--	--	--	--	--	--	--	--	--	--	--	--	--	--	--	--	--	--	--	--	--	--	--	--	--	--	--	--	--	--	--	--	--	--	--	--	--	--	--	--	--	--	--	--	--	--	--	--	--	--	--	--	--	--	--	--	--	--	--	--	--	--	--	--	--	--	--	--	--	--	--	--	--	--	--	--	--	--	--	--	--	--	--	--	--	--	--	--	--	--	--	--	--	--	--	--	--	--	--	--	--	--	--	--	--	--	--	--	--	--	--	--	--	--	--	--	--	--	--	--	--	--	--	--	--	--	--	--	--	--	--	--	--	--	--	--	--	--	--	--	--	--	--	--	--	--	--	--	--	--	--	--	--	--	--	--	--	--	--	--	--	--	--	--	--	--	--	--	--	--	--	--	--	--	--	--	--	--	--	--	--	--	--	--	--	--	--	--	--	--	--	--	--	--	--	--	--	--	--	--	--	--	--	--	--	--	--	--	--	--	--	--	--	--	--	--	--	--	--	--	--	--	--	--	--	--	--	--	--	--	--	--	--	--	--	--	--	--	--	--	--	--	--	--	--	--	--	--	--	--	--	--	--	--	--	--	--	--	--	--	--	--	--	--	--	--	--	--	--	--	--	--	--	--	--	--	--	--	--	--	--	--	--	--	--	--	--	--	--	--	--	--	--	--	--	--	--	--	--	--	--	--	--	--	--	--	--	--	--	--	--	--	--	--	--	--	--	--	--	--	--	--	--	--	--	--	--	--	--	--	--	--	--	--	--	--	--	--	--	--	--	--	--	--	--	--	--	--	--	--	--	--	--	--	--	--	--	--	--	--	--	--	--	--	--	--	--	--	--	--	--	--	--	--	--	--	--	--	--	--	--	--	--	--	--	--	--	--	--	--	--	--	--	--	--	--	--	--	--	--	--	--	--	--	--	--	--	--	--	--	--	--	--	--	--	--	--	--	--	--	--	--	--	--	--	--	--	--	--	--	--	--	--	--	--	--	--	--	--	--	--	--	--	--	--	--	--	--	--	--	--	--	--	--	--	--	--	--	--	--	--	--	--	--	--	--	--	--	--	--	--	--	--	--	--	--	--	--	--	--	--	--	--	--	--	--	--	--	--	--	--	--	--	--	--	--	--	--	--	--	--	--	--	--	--	--	--	--	--	--	--	--	--	--	--	--	--	--	--	--	--	--	--	--	--	--	--	--	--	--	--	--	--	--	--	--	--	--	--	--	--	--	--	--	--	--	--	--	--	--	--	--	--	--	--	--	--	--	--	--	--	--	--	--	--	--	--	--	--	--	--	--	--	--	--	--	--	--	--	--	--	--	--	--	--	--	--	--	--	--	--	--	--	--	--	--	--	--	--	--	--	--	--	--	--	--	--	--	--	--	--	--	--	--	--	--	--	--	--	--	--	--	--	--	--	--	--	--	--	--	--	--	--	--	--	--	--	--	--	--	--	--	--	--	--	--	--	--	--	--	--	--	--	--	--	--	--	--	--	--	--	--	--	--	--	--	--	--	--	--	--	--	--	--	--	--	--	--	--	--	--	--	--	--	--	--	--	--	--	--	--	--	--	--	--	--	--	--	--	--	--	--	--	--	--	--	--	--	--	--	--	--	--	--	--	--	--	--	--	--	--	--	--	--	--	--	--	--	--	--	--	--	--	--	--	--	--	--	--	--	--	--	--	--	--	--	--	--	--	--	--	--	--	--	--	--	--	--	--	--	--	--	--	--	--	--	--	--	--	--	--	--	--	--	--	--	--	--	--	--	--	--	--	--	--	--	--	--	--	--	--	--	--	--	--	--	--	--	--	--	--	--	--	--	--	--	--	--	--	--	--	--	--	--	--	--	--	--	--	--	--	--	--	--	--	--	--	--	--	--	--	--	--	--	--	--	--	--	--	--	--	--	--	--	--	--	--	--	--	--	--	--	--	--	--	--	--	--	--	--	--	--	--	--	--	--	--	--	--	--	--	--	--	--	--	--	--	--	--	--	--	--	--	--	--	--	--	--	--	--	--	--	--	--	--	--	--	--	--	--	--	--	--	--	--	--	--	--	--	--	--	--	--	--	--	--	--	--	--	--	--	--	--	--	--	--	--	--	--	--	--	--	--	--	--	--	--	--	--	--	--	--	--	--	--	--	--	--	--	--	--	--	--	--	--	--	--	--	--	--	--	--	--	--	--	--	--	--	--	--	--	--	--	--	--	--	--	--	--	--	--	--	--	--	--	--	--	--	--	--	--	--	--	--	--	--	--	--	--	--	--	--	--	--	--	--	--	--	--	--	--	--	--	--	--	--	--	--	--	--	--	--	--	--	--	--	--	--	--	--	--	--	--	--	--	--	--	--	--	--	--	--	--	--	--	--	--	--	--	--	--	--	--	--	--	--	--	--	--	--	--	--	--	--	--	--	--	--	--	--	--	--	--	--	--	--	--	--	--	--	--	--	--	--	--	--	--	--	--	--	--	--	--	--	--	--	--	--	--	--	--	--	--	--	--	--	--	--	--	--	--	--	--	--	--	--	--	--	--	--	--	--	--	--	--	--	--	--	--	--	--	--	--	--	--	--	--	--	--	--	--	--	--	--	--	--	--	--	--	--	--	--	--	--	--	--	--	--	--	--	--	--	--	--	--	--	--	--	--	--	--	--	--	--	--	--	--	--	--	--	--	--	--	--	--	--	--	--	--	--	--	--	--	--	--	--	--	--	--	--	--	--	--	--	--	--	--	--	--	--	--	--	--	--	--	--	--	--	--	--	--	--	--	--	--	--	--	--	--	--	--	--	--	--	--	--	--	--	--	--	--	--	--	--	--	--	--	--	--	--	--	--	--	--	--	--	--	--	--	--	--	--	--	--	--	--	--	--	--	--	--	--	--	--	--	--	--	--	--	--	--	--	--	--	--	--	--	--	--	--	--	--	--	--	--	--	--	--	--	--	--	--	--	--	--	--	--	--	--	--	--	--	--	--	--	--	--	--	--	--	--	--	--	--	--	--	--	--	--	--	--	--	--	--	--	--	--	--	--	--	--	--	--	--	--	--	--	--	--	--	--	--	--	--	--	--	--	--	--	--	--	--	--	--	--	--	--	--	--	--	--	--	--	--	--	--	--	--	--	--	--	--	--	--	--	--	--	--	--	--	--	--	--	--	--	--	--	--	--	--	--	--	--	--	--	--	--	--	--	--	--	--	--	--	--	--	--	--	--	--	--	--	--	--	--	--	--	--	--	--	--	--	--	--	--	--	--	--	--	--	--	--	--	--	--	--	--	--	--	--	--	--	--	--	--	--	--	--	--	--	--	--	--	--	--	--	--	--	--	--	--	--	--	--	--	--	--	--	--	--	--	--	--	--	--	--	--	--	--	--	--	--	--	--	--	--	--	--	--	--	--	--	--	--	--	--	--	--	--	--	--	--	--	--	--	--	--	--	--	--	--	--	--	--	--	--	--	--	--	--	--	--	--	--	--	--	--	--	--	--	--	--	--	--	--	--	--	--	--	--	--	--	--	--	--	--	--	--	--	--	--	--	--	--	--	--	--	--	--	--	--	--	--	--	--	--	--	--	--	--	--	--	--	--	--	--	--	--	--	--	--	--	--	--	--	--	--	--	--	--	--	--	--	--	--	--	--	--	--	--	--	--	--	--	--	--	--	--	--	--	--	--	--	--	--	--	--	--	--	--	--	--	--	--	--	--	--	--	--	--	--	--	--	--	--	--	--	--	--	--	--	--	--	--	--	--	--	--	--	--	--	--	--	--	--	--	--	--	--	--	--	--	--	--	--	--	--	--	--	--	--	--	--	--	--	--	--	--	--	--	--	--	--	--	--	--	--	--	--	--	--	--	--	--	--	--	--	--	--	--	--	--	--	--	--	--	--	--	--	--	--	--	--	--	--	--	--	--	--	--	--	--	--	--	--	--	--	--	--	--	--	--	--	--	--	--	--	--	--	--	--	--	--	--	--	--	--	--	--	--	--	--	--	--	--	--	--	--	--	--	--	--	--	--	--	--	--	--	--	--	--	--	--	--	--	--	--	--	--	--	--	--	--	--	--	--	--	--	--	--	--	--	--	--	--	--	--	--	--	--	--	--	--	--	--	--	--	--	--	--	--	--	--	--	--	--	--	--	--	--	--	--	--	--	--	--	--	--	--	--	--	--	--	--	--	--	--	--	--	--	--	--	--	--	--	--	--	--	--	--	--	--	--	--	--	--	--	--	--	--	--	--	--	--	--	--	--	--	--	--	--	--	--	--	--	--	--	--	--	--	--	--	--	--	--	--	--	--	--	--	--	--	--	--	--	--	--	--	--	--	--	--	--	--	--	--	--	--	--	--	--	--	--	--	--	--	--	--	--	--	--	--	--	--	--	--	--	--	--	--	--	--	--	--	--	--	--	--	--	--	--	--	--	--	--	--	--	--	--	--	--	--	--	--	--	--	--	--	--	--	--	--	--	--	--	--	--	--	--	--	--	--	--	--	--	--	--	--	--	--	--	--	--	--	--	--	--	--	--	--	--	--	--	--	--	--	--	--	--	--	--	--	--	--	--	--	--	--	--	--	--	--	--	--	--	--	--	--	--	--	--	--	--	--	--	--	--	--	--	--	--	--	--	--	--	--	--	--	--	--	--	--	--	--	--	--	--	--	--	--	--	--	--	--	--	--	--	--	--	--	--	--	--	--	--	--	--	--	--	--	--	--	--	--	--	--	--	--	--	--	--	--	--	--	--	--	--	--	--	--	--	--	--	--	--	--	--	--	--	--	--	--	--	--	--	--	--	--	--	--	--	--	--	--	--	--	--	--	--	--	--	--	--	--	--	--	--	--	--	--	--	--	--	--	--	--	--	--	--	--	--	--	--	--	--	--	--	--	--	--	--	--	--	--	--	--	--	--	--	--	--	--	--	--	--	--	--	--	--	--	--	--	--	--	--	--	--	--	--	--	--	--	--	--	--	--	--	--	--	--	--	--	--	--	--	--	--	--	--	--	--	--	--	--	--	--	--	--	--	--	--	--	--	--	--	--	--	--	--	--	--	--	--	--	--	--	--	--	--	--	--	--	--	--	--	--	--	--	--	--	--	--	--	--	--	--	--	--	--	--	--	--	--	--	--	--	--	--	--	--	--	--	--	--	--	--	--	--	--	--	--	--	--	--	--	--	--	--	--	--	--	--	--	--	--	--	--	--	--	--	--	--	--	--	--	--	--	--	--	--	--	--	--	--	--	--	--	--	--	--	--	--	--	--	--	--	--	--	--	--	--	--	--	--	--	--	--	--	--	--	--	--	--	--	--	--	--	--	--	--	--	--	--	--	--	--	--	--	--	--	--	--	--	--	--	--	--	--	--	--	--	--	--	--	--	--	--	--	--	--	--	--	--	--	--	--	--	--	--	--	--	--	--	--	--	--	--	--	--	--	--	--	--	--	--	--	--	--	--	--	--	--	--	--	--	--	--	--	--	--	--	--	--	--	--	--	--	--	--	--	--	--	--	--	--	--	--	--	--	--	--	--	--	--	--	--	--	--	--	--	--	--	--	--	--	--	--	--	--	--	--	--	--	--	--	--	--	--	--	--	--	--	--	--	--	--	--	--	--	--	--	--	--	--	--	--	--	--	--	--	--	--	--	--	--	--	--	--	--	--	--	--	--	--	--	--	--	--	--	--	--	--	--	--	--	--	--	--	--	--	--	--	--	--	--	--	--	--	--	--	--	--	--	--	--	--	--	--	--	--	--	--	--	--	--	--	--	--	--	--	--	--	--	--	--	--	--	--	--	--	--	--	--	--	--	--	--	--	--	--	--	--	--	--	--	--	--	--	--	--	--	--	--	--	--	--	--	--	--	--	--	--	--	--	--	--	--	--	--	--	--	--	--	--	--	--	--	--	--	--	--	--	--	--	--	--	--	--	--	--	--	--	--	--	--	--	--	--	--	--	--	--	--	--	--	--	--	--	--	--	--	--	--	--	--	--	--	--	--	--	--	--	--	--	--	--	--	--	--	--	--	--	--	--	--	--	--	--	--	--	--	--	--	--	--	--	--	--	--	--	--	--	--	--	--	--	--	--	--	--	--	--	--	--	--	--	--	--	--	--	--	--	--	--	--	--	--	--	--	--	--	--	--	--	--	--	--	--	--	--	--	--	--	--	--	--	--	--	--	--	--	--	--	--	--	--	--	--	--	--	--	--	--	--	--	--	--	--	--	--	--	--	--	--	--	--	--	--	--	--	--	--	--	--	--	--	--	--	--	--	--	--	--	--	--	--	--	--	--	--	--	--	--	--	--	--	--	--	--	--	--	--	--	--	--	--	--	--	--	--	--	--	--	--	--	--	--	--	--	--	--	--	--	--	--	--	--	--	--	--	--	--	--	--	--	--	--	--	--	--	--	--	--	--	--	--	--	--	--	--	--	--	--	--	--	--	--	--	--	--	--	--	--	--	--	--	--	--	--	--	--	--	--	--	--	--	--	--	--	--	--	--	--	--	--	--	--	--	--	--	--	--	--	--	--	--	--	--	--	--	--	--	--	--	--	--	--	--	--	--	--	--	--	--	--	--	--	--	--	--	--	--	--	--	--	--	--	--	--	--	--	--	--	--	--	--	--	--	--	--	--	--	--	--	--	--	--	--	--	--	--	--	--	--	--	--	--	--	--	--	--	--	--	--	--	--	--	--	--	--	--	--	--	--	--	--	--	--	--	--	--	--	--	--	--	--	--	--	--	--	--	--	--	--	--	--	--	--	--	--	--	--	--	--	--	--	--	--	--	--	--	--	--	--	--	--	--	--	--	--	--	--	--	--	--	--	--	--	--	--	--	--	--	--	--	--	--	--	--	--	--	--	--	--	--	--	--	--	--	--	--	--	--	--	--	--	--	--	--	--	--	--	--	--	--	--	--	--	--	--	--	--	--	--	--	--	--	--	--	--	--	--	--	--	--	--	--	--	--	--	--	--	--	--	--	--	--	--	--	--	--	--	--	--	--	--	--	--	--	--	--	--	--	--	--	--	--	--	--	--	--	--	--	--	--	--	--	--	--	--	--	--	--	--	--	--	--	--	--	--	--	--	--	--	--	--	--	--	--	--	--	--	--	--	--	--	--	--	--	--	--	--	--	--	--	--	--	--	--	--	--	--	--	--	--	--	--	--	--	--	--	--	--	--	--	--	--	--	--	--	--	--	--	--	--	--	--	--	--	--	--	--	--	--	--	--	--	--	--	--	--	--	--	--	--	--	--	--	--	--	--	--	--	--	--	--	--	--	--	--	--	--	--	--	--	--	--	--	--	--	--	--	--	--	--	--	--	--	--	--	--	--	--	--	--	--	--	--	--	--	--	--	--	--	--	--	--	--	--	--	--	--	--	--	--	--	--	--	--	--	--	--	--	--	--	--	--	--	--	--	--	--	--	--	--	--	--	--	--	--	--	--	--	--	--	--	--	--	--	--	--	--	--	--	--	--	--	--	--	--	--	--	--	--	--	--	--	--	--	--	--	--	--	--	--	--	--	--	--	--	--	--	--	--	--	--	--	--	--	--	--	--	--	--	--	--	--	--	--	--	--	--	--	--	--	--	--	--	--	--	--	--	--	--	--	--	--	--	--	--	--	--	--	--	--	--	--	--	--	--	--	--	--	--	--	--	--	--	--	--	--	--	--	--	--	--	--	--	--	--	--	--	--	--	--	--	--	--	--	--	--	--	--	--	--	--	--	--	--	--	--	--	--	--	--	--	--	--	--	--	--	--	--	--	--	--	--	--	--	--	--	--	--	--	--	--	--	--	--	--	--	--	--	--	--	--	--	--	--	--	--	--	--	--	--	--	--	--	--	--	--	--	--	--	--	--	--	--	--	--	--	--	--	--	--	--	--	--	--	--	--	--	--	--	--	--	--	--	--	--	--	--	--	--	--	--	--	--	--	--	--	--	--	--	--	--	--	--	--	--	--	--	--	--	--	--	--	--	--	--	--	--	--	--	--	--	--	--	--	--	--	--	--	--	--	--	--	--	--	--	--	--	--	--	--	--	--	--	--	--	--	--	--	--	--	--	--	--	--	--	--	--	--	--	--	--	--	--	--	--	--	--	--	--	--	--	--	--	--	--	--	--	--	--	--	--	--	--	--	--	--	--	--	--	--	--	--	--	--	--	--	--	--	--	--	--	--	--	--	--	--	--	--	--	--	--	--	--	--	--	--	--	--	--	--	--	--	--	--	--	--	--	--	--	--	--	--	--	--	--	--	--	--	--	--	--	--	--	--	--	--	--	--	--	--	--	--	--	--	--	--	--	--	--	--	--	--	--	--	--	--	--	--	--	--	--	--	--	--	--	--	--	--	--	--	--	--	--	--	--	--	--	--	--	--	--	--	--	--	--	--	--	--	--	--	--	--	--	--	--	--	--	--	--	--	--	--	--	--	--	--	--	--	--	--	--	--	--	--	--	--	--	--	--	--	--	--	--	--	--	--	--	--	--	--	--	--	--	--	--	--	--	--	--	--	--	--	--	--	--	--	--	--	--	--	--	--	--	--	--	--	--	--	--	--	--	--	--	--	--	--	--	--	--	--	--	--	--	--	--	--	--	--	--	--	--	--	--	--	--	--	--	--	--	--	--	--	--	--	--	--	--	--	--	--	--	--	--	--	--	--	--	--	--	--	--	--	--	--	--	--	--	--	--	--	--	--	--	--	--	--	--	--	--	--	--	--	--	--	--	--	--	--	--	--	--	--	--	--	--	--	--	--	--	--	--	--	--	--	--	--	--	--	--	--	--	--	--	--	--	--	--	--	--	--	--	--	--	--	--	--	--	--	--	--	--	--	--	--	--	--	--	--	--	--	--	--	--	--	--	--	--	--	--	--	--	--	--	--	--	--	--	--	--	--	--	--	--	--	--	--	--	--	--	--	--	--	--	--	--	--	--

Figure 2.1: Periodic table of the elements from sciencenotes website [15]. The group III elements can be seen in the thirteenth column, while the group V element can be seen in the fifteenth column.

In this section, some interesting properties will be presented and linked to applications to show the impact that III-V materials currently have. Then, the highlight will be on optical properties of these materials for the subject in which we are interested: the second-order nonlinear properties. This will also show the initial parameters linked to fabrication processes that will follow.

For the usage of these materials full potential, it is indeed important to develop a fabrication process stable and reliable. Even if the processing of these materials is well-developed

in the literature, it is not trivial to keep a reliable process that offers an adequate quality for photonics applications, especially because any nanometer range defect or variation can affect the whole property of the light propagation. In this section, we will show general concepts about III-V materials fabrication. We will also make a state of the art of III-V technological processing that I used during my PhD to fabricate III-V integrated waveguides for nonlinear applications. Some of them were already developed when I arrived, and others had to be developed or optimized.

2.1 III-V materials

2.1.1 State of the art on III-V materials

In this part, we are going to see the impact of the III-V alloys in the modern world technology devices through different examples of their applications and explanations of their success. III-V materials are widely used and developed in electro-optical devices in particular. From sources like light-emitting diodes and semiconductor lasers to detection systems such as photodiodes via electro-optic modulators. If we focus on integrated structures, we can find a few examples of their implementation. If we take the example of IBM research field, we can find the favourite III-V materials used for several applications in fig. 2.2.

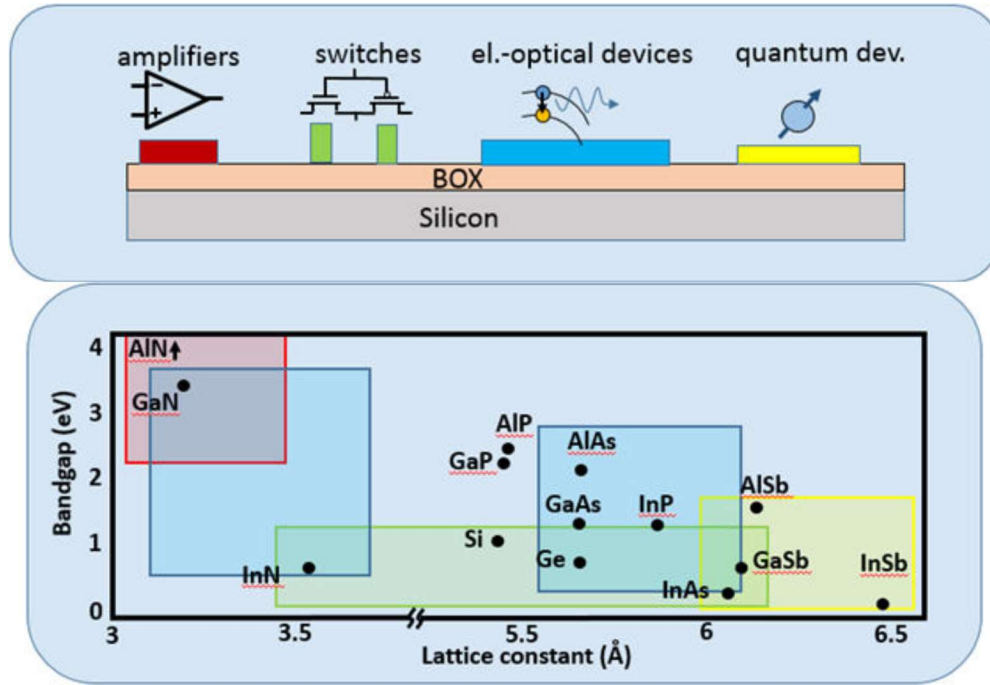


Figure 2.2: Four different devices that can be made from III-V materials (top) and the materials used to create them (bottom) as it can be found on IBM website. The colour of the device on top is reported on the bottom image to show which material is used to make it [16].

As we can see, III-V materials are well-known for being useful to make electronic devices [17].

One particular element that we can talk about are the integrated transistors. As the Moore law predicts an exponential increase of the number of transistors on a microprocessor chip

with time and as the silicon-based devices start to show some limitations, studies have been performed to find an alternative, and it seems that III-V transistors will be a great alternative to the actual ones [18, 19]. It seems that certain III-V materials show higher electron mobility, as can be seen in fig. 2.3, as well as fast frequency response, important elements to an efficient metal–oxide–semiconductor field-effect transistor (MOSFET).

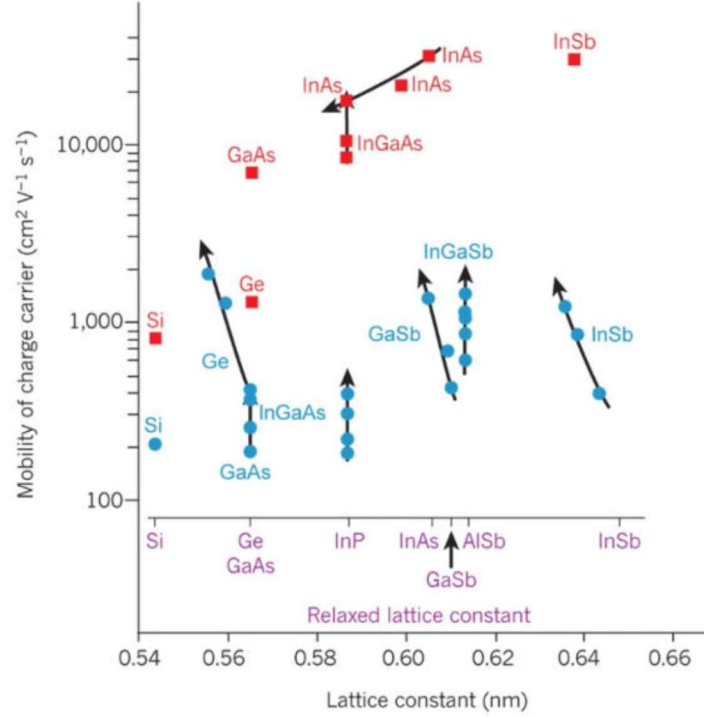


Figure 2.3: Highest mobility at room temperature of holes (blue dots) and electrons (red squares) in inversion layers and quantum wells as a function of the actual semiconductor lattice constant [20].

In photonics, they also have a huge success due to the fact some of them possess a direct bandgap, resulting in a better optical absorption or emission with electrical stimulation [21].

For instance, they are used for large structures such as solar panels. Even if silicon-based solar panels are the most common ones when it comes to public access [22], III-V materials are also used in the spatial field [23, 24]. They present a higher performance than their silicon equivalent and are a really promising material for this purpose. Standard silicon solar panels usually reached 20 % efficiency while III-V solar panels efficiency is more around 25 % as can be seen in fig. 2.4 and recent studies even reached 47.1 % of efficiency [25].

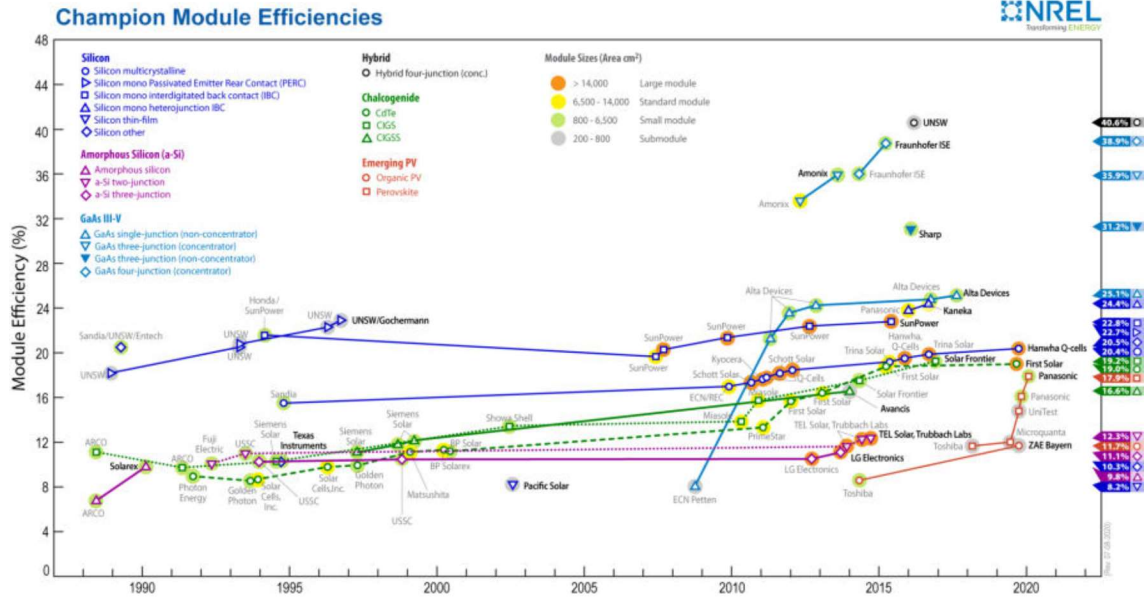


Figure 2.4: Curves of the evolution of conversion efficiency of solar panels over the years for different materials. This figure is taken from the National Renewable Energy Laboratory website [26]

On another side, their direct bandgap allows the creation of efficient integrated lasers, modulators [27, 28] and photodetectors as well [29, 30]. Individually, these components are already amazing for various applications. Together, they are key elements for telecommunication. A field that is also growing incredibly fast and in which III-V materials can perfectly fit. Examples of III-V devices for telecommunication applications can be found on OMMIC website for instance [31]. These alloys are also used in cameras with indium gallium arsenide sensors (as the ones from Hamamatsu [32] or Raptor Photonics [33]).

Even without taking into account their astonishing electrical properties, III-V materials are also interesting materials for optical frequency conversion. They usually have a high nonlinear coefficient, as we will develop later, which makes them interesting for nonlinear processes. Some of them possess, in fact, a second-order nonlinear susceptibility around 200 pm/V [34–36] while other material like LiNbO₃ (a reference in second-order nonlinear effects) exhibits a second-order nonlinear susceptibility 3 times lower [37]. Concerning third-order nonlinearities, they can present a nonlinear refractive index with an order of magnitude greater than Si [38–41]. Furthermore, the fabrication processes developed for III-V materials have been developed such that it allows the fabrication of micrometre-scale structures for nonlinear purposes [42].

As we’ve just seen here, III-V materials are widely used for their electrical and optical properties. Indeed, they possess advantageous properties in those fields and the versatility that they offer is also a great asset. The optical properties will now be explored further in detail.

2.1.2 Optical properties of III-V materials

We are here going to see some optical properties of III-V materials. The linear and second-order nonlinear properties of these materials especially, those being the most important properties for SHG processes.

First, by their very nature III-V materials can absorb a photon when this one possesses energy larger than the bandgap. While this can be useful for many applications (detectors and lasers for instance), it is a problem in our case. Even if it doesn't absorb photons at the pump wavelength, it could absorb photons generated at the SH wavelength. On another side, it could be also troublesome at the pump wavelength as two photons could be absorbed too, resulting in the two-photon absorption (TPA) effect. The absorption of the pump wavelength reduces its power and could reduce the efficiency of the targeted SHG process. A potential solution is to use an alloy composed of three different elements (like InGaAs for instance). This allows tuning the bandgap energy by engineering the proportion of elements in the material as can be seen in fig. 2.5.

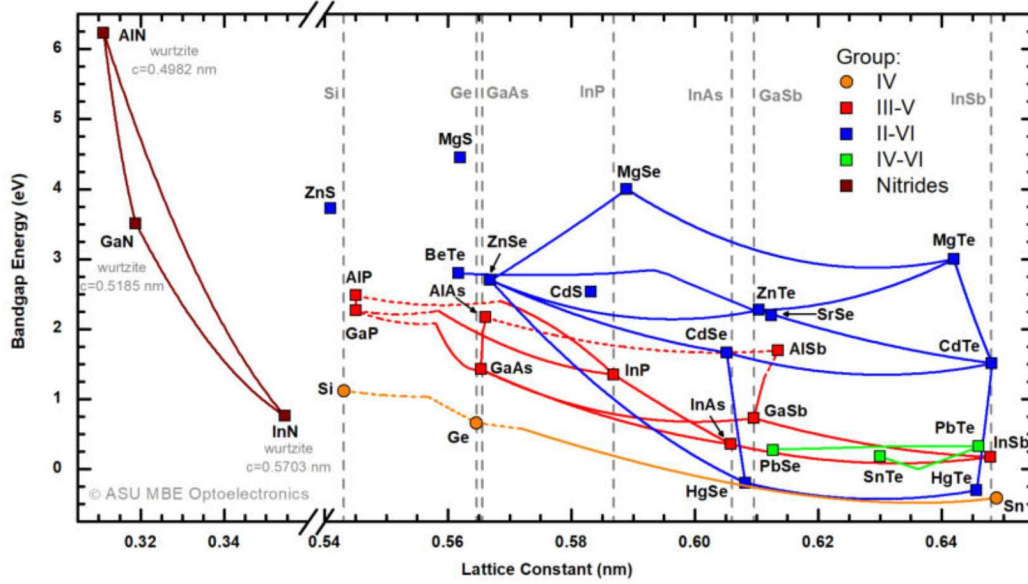


Figure 2.5: Bandgap energy of different materials as a function of the lattice constant of the material. The dashed lines represent indirect bandgap ternary alloys while the solid lines represent ternary alloys with a direct bandgap. The figure comes from the Arizona State University website [43]

The material must therefore be chosen carefully according to the intended use. For instance, gallium antimony (GaSb) possesses a bandgap around 1 eV, which means that it will not be interesting for studies at a wavelength below 1200 nm as it is absorbent below this wavelength.

On another hand, several studies have been performed to calculate or measure the complex refractive index of those materials and some are represented in fig. 2.6. The fit functions of the real and imaginary parts of the complex refractive index are represented here. We can define it as $\underline{n} = n + i\xi$ where n is the refractive index and ξ is the extinction coefficient, responsible for attenuation in the material.

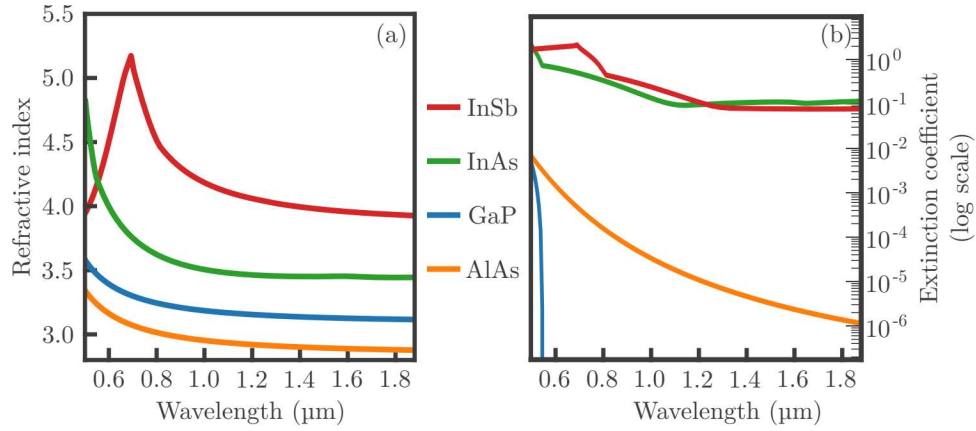


Figure 2.6: Real component of the complex refractive index (a) and imaginary component in logarithmic scale (b) for four different III-V materials. The materials considered are AlAs (orange line) [44], InAs (green line), InSb (red line) and GaP (blue line) [45].

Materials with very different bandgap (as can be seen in fig. 2.5) have been chosen. We can see that the refractive index of these materials is large compared to air or SiO₂ (typically 1.45 at 1.2 μm). This makes these materials interesting for integration as a high-index contrast means higher light confinement inside the structure. On the other side, the extinction coefficient is different from one material to another for a wavelength in the range of a SH generated from a telecom wavelength (around 775 nm) for instance. It can be significant as it can be null.

Concerning nonlinear effects, III-V materials are, for most of them, zinc-blende structure ($\bar{4}3m$ group). Some other III-V materials are wurtzite structures (gallium nitride and aluminium nitride for instance). These last ones will not be discussed in this thesis. Furthermore, III-V materials show a high second-order nonlinear susceptibility compared to LiNbO₃ as seen in table 2.1.

Material	Maximum second-order nonlinear susceptibility d_{il} (pm/V)	Source
GaAs	178.0	[46]
GaP	93.0	[46]
InP	134.5	[46]
AlAs	113.5	[46]
InGaP	110.0	[34]
AlGaAs	90.0	[36]
LiNbO ₃	31.5	[37]

Table 2.1: Second-order nonlinear susceptibility for different III-V materials and LiNbO₃ as a comparison.

The particular symmetry of the $\bar{4}$ group leads to simplifications in the second-order nonlinear susceptibility tensor that we have seen in part 1.1 [47]. In such cases, there are only three non-zero components and all of them are equal to each other as long as Kleinman's symmetry is valid [48]. The second-order nonlinear susceptibility tensor is thus written :

$$d_{il} = \begin{pmatrix} 0 & 0 & 0 & d_{14} & 0 & 0 \\ 0 & 0 & 0 & 0 & d_{14} & 0 \\ 0 & 0 & 0 & 0 & 0 & d_{14} \end{pmatrix}.$$

To understand how to use this particular tensor to find the conditions for SHG, we focus on a rectangular cross-section waveguide in a (xyz) framework where x is the horizontal component, y is the vertical one and the wave is propagating along the z-axis as represented in fig. 2.7. We here take the example where x, y, and z correspond to the [100], [010], and [001] axis of the crystal, respectively. The x,y, and z-axis could, of course, be any of these three crystallographic axes as long as it respects an orthonormal frame. Using this tensor, we can define the polarization of the SH wave as a function of the amplitude of the pump's electric field components:

$$\begin{pmatrix} P_x \\ P_y \\ P_z \end{pmatrix}_{SH} = \begin{pmatrix} 0 & 0 & 0 & d_{14} & 0 & 0 \\ 0 & 0 & 0 & 0 & d_{14} & 0 \\ 0 & 0 & 0 & 0 & 0 & d_{14} \end{pmatrix} \begin{pmatrix} E_x^2 \\ E_y^2 \\ E_z^2 \\ 2E_y E_z \\ 2E_x E_z \\ 2E_x E_y \end{pmatrix}_{Pump}$$

We can notice that the SHG process needs two distinct components of the pump electric field. For instance, to generate a SH that oscillates along the x-axis, we need an electric field component of the pump along the y and the z axes.

Another possibility is to rotate the waveguide to align the direction of propagation with a different axis of the III-V crystal than the [100] or [001] crystallographic axis (depending on the patterning of the waveguide). The second-order nonlinear tensor will thus change according to the angle, and so will the tensor components as it is expressed in a new frame. This new reference frame (x'y'z'), expressing the rotation, is represented as in fig. 2.7.

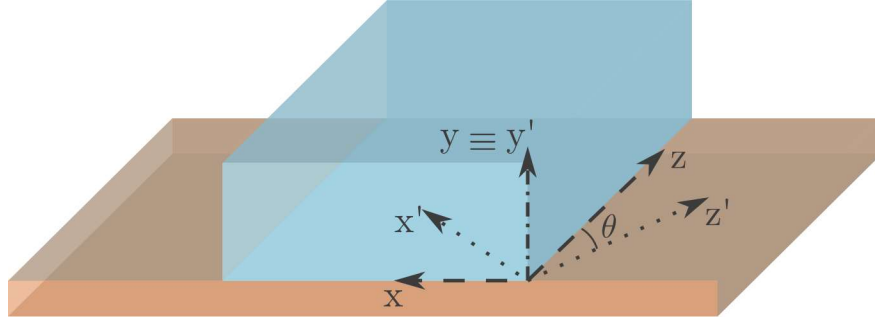


Figure 2.7: Representation of a III-V waveguide in a (xyz) frame where x, y and z correspond to the [100], [010] and [001] axis of the crystal respectively. There is also a (x'y'z') frame that is a rotation of the first frame of an angle θ around the y-axis.

To compute the second-order tensor in the new frame, we need to apply a rotation matrix to the framework. This matrix can be written as:

$$\begin{pmatrix} x \\ y \\ z \end{pmatrix} = \begin{pmatrix} \cos \theta & 0 & -\sin \theta \\ 0 & 1 & 0 \\ \sin \theta & 0 & \cos \theta \end{pmatrix} \begin{pmatrix} x' \\ y' \\ z' \end{pmatrix}$$

By applying this rotation matrix, we obtain a global expression of the III-V crystal second-order nonlinearity according to the angle of the waveguide.

$$D(\theta) = \begin{pmatrix} 0 & 0 & 0 & d_{14} \cos(2\theta) & 0 & 2d_{14} \cos \theta \sin \theta \\ 2d_{14} \cos \theta \sin \theta & 0 & -2d_{14} \cos \theta \sin \theta & 0 & d_{14} \cos(2\theta) & 0 \\ 0 & 0 & 0 & -2d_{14} \cos \theta \sin \theta & 0 & d_{14} \cos(2\theta) \end{pmatrix}$$

From this result, we can express the SH polarization according to the electric field components of the pump wave. As we got:

$$\begin{pmatrix} P_x \\ P_y \\ P_z \end{pmatrix} = D(\theta) \begin{pmatrix} E_x E_x \\ E_y E_y \\ E_z E_z \\ E_y E_z + E_z E_y \\ E_x E_z + E_z E_x \\ E_x E_y + E_y E_x \end{pmatrix}$$

One of the most common ways to use integrated III-V waveguides as a SHG platform is to pattern the waveguide such as the waves propagate along a different crystallographic axis from the [100] (or [001]) direction of the crystal [49, 50]. For instance, staying within the same frame as fig. 2.7, in the particular case of an angle θ equals to 45° between the [100] (or [001]) crystallographic axis and the propagation direction, it is possible to generate a SH polarized along the y-axis with only the x component of the pump polarization.

III-V materials can also be used for third-order nonlinear effects such as four-wave mixing or Kerr effect [51–53]. In this case, the expression of the tensor can also be simplified due to III-V particularities. As it involves a 4th rank tensor, it will not be written. However, we still present the simplifications in the case of zinc-blende structure in the work frame defined in fig. 2.7. Indeed, among the 81 elements composing the $\chi_{ijkl}^{(3)}$ tensor for which $i, j, k, l = x, y, z$, only 21 are non-zero and 4 of them are independent [54]. These are:

$$\begin{aligned} xxxx &= yyyy = zzzz \\ yyzz &= zzyy = xxyy = yyxx = xxzz = zzxx \\ yzyz &= zyyz = xzzx = zxzx = xyxy = yxyx \\ yzzy &= zyyz = xzzx = zxzx = xyxy = yxyx \end{aligned}$$

In experimental studies, only one component of the tensor is commonly used at a time and thus measured [55, 56]. Furthermore, to characterize the efficiency of such processes, the nonlinear refractive index (or Kerr coefficient) n_2 , expressed in m^2/W , is commonly used. A comparison between different materials is presented in table 2.2 to compare their respective third-order nonlinear properties. Two commonly used materials for third-order nonlinear effects have first been chosen, followed by III-V materials that will be used in this thesis.

Material	Refractive index	n_2 (m^2/W)	Reference
Si	3.478	4.5×10^{-18}	[38]
SiN	1.996	2.4×10^{-19}	[57]
indium gallium phosphide (InGaP)	3.105	1.3×10^{-17}	[39]
aluminium gallium arsenide (AlGaAs)	3.178	2.0×10^{-17}	[40]
gallium phosphide (GaP)	3.055	1.2×10^{-17}	[41]

Table 2.2: Comparison of refractive index and nonlinear refractive index for different bulk materials at 1550 nm

Table 2.2 shows that III-V materials are interesting for third-order nonlinear effects. Indeed, the high index contrast with the air allows strong confinement of the light and the strong nonlinear refractive index offers a strong conversion efficiency. In general, III-V materials shows a higher nonlinear refractive index than Si for a refractive index almost equivalent.

We particularly focused on an integrated platform where the properties of III-V materials are best used. We have indeed seen before that the interest around III-V materials and their integration via different applications. In each case, however, the common point is that a reliable fabrication process is needed. For micro-structures fabrication, several processes have been put in place and are needed for such a small structure. Even in the case of solar panels, as big as they might be, they are fabricated from few inches wafers and a deposition technique called metal-organic vapour-phase epitaxy (MOVPE) is commonly used for this deposition [58, 59]. In the next part, we are going to explore more in detail the whole production process of such devices.

2.2 Integration of III-V materials

When it comes to the fabrication of structures, different ways are possible. In this chapter, we are going to see a complete process flow of fabrication from the III-V material growing to the waveguide patterning. For each step, we will explore different approaches to the process flow for a better overview, and we will discuss the advantages and the limitations of each of them.

2.2.1 Material deposition on a substrate

The first step in the fabrication process flow is the deposition of the material. For this step, we distinguish here three different ways to do it: epitaxy, chemical vapour deposition (CVD) and manual deposition. Each one is present with its particularities and differences.

2.2.1.1 Epitaxy process

The first method is a direct growth of the desired material on top of a substrate [60, 61]. In the case of this thesis, it is a method that has been used to create wafers for the other processes that we will see here. It is a common technique, used in general for thin layers deposition.

There are different ways to grow a material on another. The most common way is epitaxial growth, where the crystal is grown along with a certain crystallographic orientation. We can distinguish two kinds of epitaxial processes: homoepitaxy and heteroepitaxy. We will not develop too much the first one as it consists of deposition of the same material as the substrate but with the difference that this new layer can be purer than the substrate or doped [62].

The second process implies two different materials. In this case, it is important to take care of the lattice mismatch of the two materials [63]. As it can be seen in fig. 2.5, each material has its lattice constant that can match with another material or not. If this constant does not match between the material to be deposited and the substrate, this can lead to defects in the resulting layer. As they do not have the same lattice constant, there will be deformation due to the intention of the grown material to match the substrate. It leads to a mismatch dislocation which induces threading dislocations [64–66]. According to the size of both mesh, the layer will be either strained (if the lattice constant of the layer deposited is higher than the substrate one) or relaxed (in the opposite case). It is also used to voluntarily strain a material because it can lead to some nonlinear effects that the material will not have naturally [67, 68]. As an example of a correct combination, we can cite the combination of InGaP and AlGaAs that we will see later which can, in the correct proportion, be a perfect match.

There are different epitaxial ways to grow materials. One of the most famous is the molecular beam epitaxy [69]. It consists of heating a material to produce an evaporated beam of particles. The material is then travelling in a very low-pressure environment (lower than 10^{-10} Torr) to the substrate. The material finally condensates on the substrate to create the wanted layer. It is a technique that is used to grow crystalline structures (like III-V materials or silicon) but that cannot be used for amorphous materials (such as amorphous silicon or SiN). It is widely used for semiconductors fabrication and has imposed itself as a strong tool in the nanotechnology fabrication field [70].

2.2.1.2 Chemical vapour deposition

Another widely used method for growing semiconductors crystals is chemical vapour deposition. Different processes have been developed around this basis. These techniques are commonly used for amorphous silicon and SiN deposition for instance, compared to the epitaxy technique exposed before, as those techniques allow the deposition of non-crystalline materials. These techniques are, however, not fully developed for a III-V material deposition yet but is a subject of study [71, 72]. The first case that we will treat here is the low-pressure chemical vapour deposition (LPCVD). It consists of a gas travelling inside a chamber at low pressure (commonly few mTorr) and a high temperature (between 350 and 950 °C usually). The gas is undergoing a thermal decomposition on the wafer, resulting in a new layer. For a Si deposition, usually, SiH_4 or SiH_2Cl_2 are used while NH_3 and N_2O are also added to deposit SiN and SiO_2 respectively. A scheme of a typical LPCVD machine is represented in fig. 2.8(a). It is a commonly used technique for deposition as its conformality is excellent, and it is the only one that allows doing the deposition on several wafers at the same time resulting in a faster process, even if the deposition rate is slower than the following two.

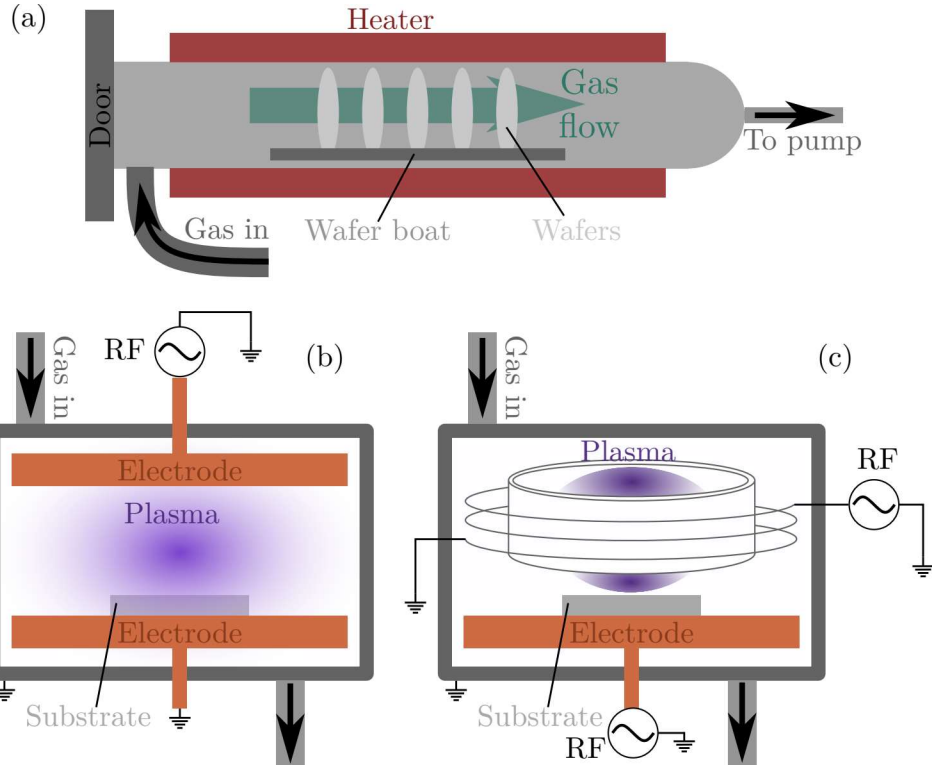


Figure 2.8: Representation of different processes using chemical vapour deposition. The LPCVD (a) with its gas travelling through the chamber, the plasma-enhanced chemical vapour deposition machine (b) with the two electrodes and the high-density plasma chemical vapour deposition machine (c) with an inductively coupled plasma.

The other two types of material deposition use plasma. A mix of gases is excited by a radio frequency (RF) wave at 13,56 MHz to create a plasma from these gases as represented in fig. 2.8(b) and (c). The plasma, sustaining inside the chamber, is then diffused through the sheath to adsorb on and interact with the substrate surface. This results in a material deposition over the substrate standing in the chamber. The products other than the deposited ones are then extracted from the chamber by a pump. The plasma-enhanced chemical vapor deposition (PECVD) and high-density plasma chemical vapour deposition (HDPCVD) differs mainly in the way the plasma is formed. The second case differs as it's involving an inductively coupled plasma resulting in a higher density plasma. On another hand, the HDPCVD requires two RF sources to work: one to create the plasma and the other to accelerate the ions to the wafer. Also, the operating pressure of a PECVD machine is between 500 and 5000 mTorr while the one for HDPCVD is commonly between 5 and 30 mTorr. For those three machines, other parameters should be taken into account of course (temperature, uniformity of the layer...) to determine which one is the best to use according to the needs.

In the case of this thesis, only LPCVD and PECVD are available. LPCVD is used to obtain the silicon oxide layer on silicon substrate wafers employed, as it is a fast process to obtain several wafers. PECVD was used for materials deposition such as silicon oxide or silicon nitride on our chip for its deposition rate higher than LPCVD for a single chip.

We focused on the epitaxial deposition for now. The next following techniques consist of direct deposition of an existing material layer on a substrate instead of an atom by atom deposition.

2.2.1.3 Physical deposition

The first technique of this kind explained here is the flip-chip technique. The name is revealing the nature of the technique as it consists in flipping the chip to deposit a structure, commonly a laser, on top of a waveguide [73, 74]. The waveguide is usually physically maintained with electrical contacts of pedestals [73, 75]. The size of the structure deposited with this technique depends on the structure deposited, of course. From what I've read, it usually has an area from hundreds of millimetres square to several tenths of millimetres square samples. It can also be quite challenging as the alignment is one of the most important parts of the resulting quality and this alignment can be difficult [76]. This process is also limited by the dimensions of the chip that has to be flipped and the quality of the surface. However, it is getting rid of the previous method due to the lattice mismatch that limits the performance.

Another technique that is quite popular nowadays is the bonding technique [77–79]. This involves taking a certain material and putting it on top of a substrate. Both materials are stuck together thanks to a polymer.

In our case, we usually cleave a part of a III-V wafer to bond on the substrate. The area of these cleaved dies for the fabrication of a single chip is usually around 1 cm². Furthermore, the polymer used is a dilution of benzocyclobutene (BCB) and mesitylene. The mix is spin-coated on top of the substrate and heated at 150°C for 10 minutes. Then the material is deposited on top to finally follow a curing process where the polymer is heated under a low-pressure environment, allowing to get rid of potential bubbles in the adhesive layer between the substrate and the material bond. The full curing process that has been used in the incoming bonded chips fabrication processes is presented in fig. 2.9.

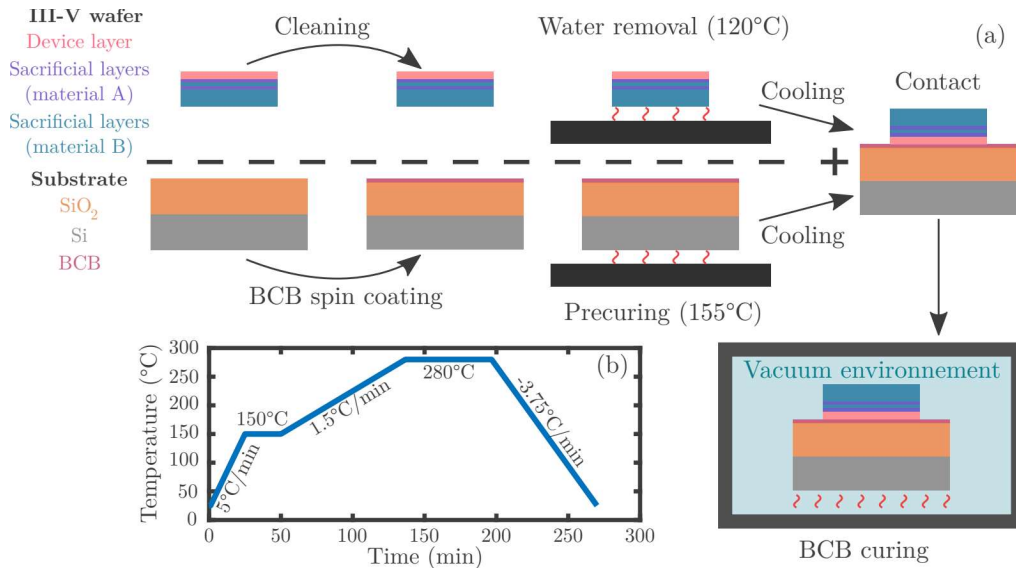


Figure 2.9: Different steps of the bonding technique (a) and representation of the temperature variations as a function of time that occurs inside the chamber under a vacuum environment (b).

The ratio between both chemicals and the spin coating speed defines the thickness of the polymer layer between the substrate and the material [80] [81]. Moreover, the optical properties of BCB are not an issue as our experiments will be in the transparency windows of BCB and the absorption will start to be troublesome if the wavelength involved is above 3 μm [82] which will never be the case here. It also possesses a low refractive index that is

comparable to the one of SiO_2 [83] which could allow good confinement of the light inside the waveguides for materials with a refractive index similar to Si.

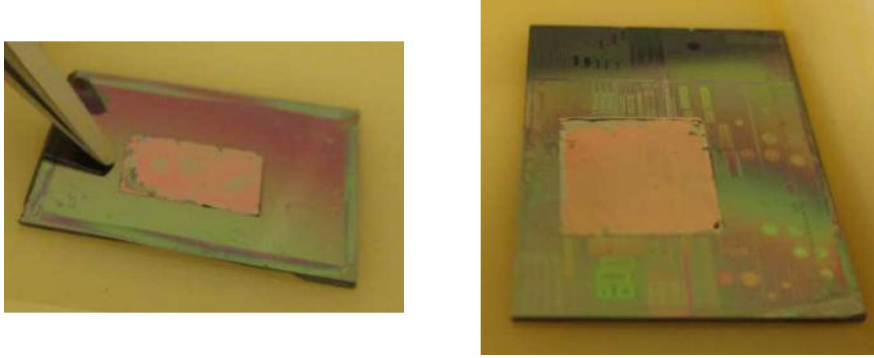


Figure 2.10: Two AlGaAs bondings a blank silicon wafer (left picture) and on a silicon wafer with SiN structures. The pictures here are taken after the bonding and after the over-layers removal process.

The last technique that we will talk about is transfer printing. It is quite a new technique but that has some advantages since it avoids the waste of material, unlike the bonding. Indeed, it consists of taking a small part of the material from the original wafer and depositing it thanks to a stamp on the substrate [84]. We thus understand that the material size deposited on the substrate highly depends on the stamp size involved. For instance, the stamp that has been used in our case is a 1 mm long and 60 μm polydimethylsiloxane stamp. We understand that it is not as interesting for large structures compared to the bonding technique. It is however possible to deposit several structures at once with some stamps [85]. This way, it is interesting for massive production. The material, once deposited, is holding on the substrate thanks to a polymer such as BCB that we already know from earlier. It is quite polyvalent as it also enables depositing lasers directly on top of a waveguide structure [86]. It requires however quite a big thickness as it needs to be taken by the stamp easily and to not get deformed during the transportation to the substrate. The steps for this process can be seen in fig. 2.11.

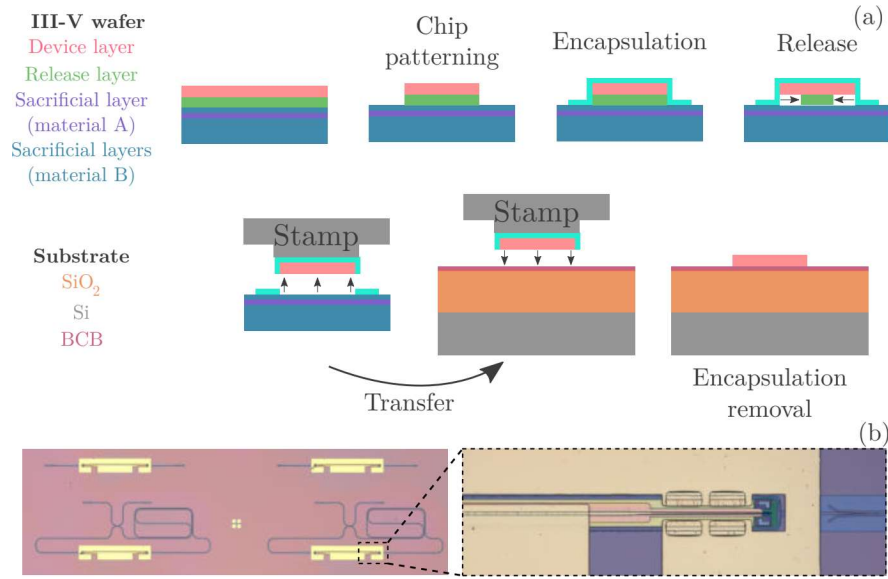


Figure 2.11: Basics steps of the transfer printing process are shown here to put the material from its original wafer to a different substrate (a). Successful transfer printing of semiconductors optical amplifiers on top of SiN waveguides are also shown here (b)

After the deposition of the material on the substrate, the BCB still needs to follow the same curing process as for the bonding technique.

We have seen here how it is possible to deposit thin layers of a III-V material on a substrate. For all the solutions that have been exposed there, patterning is required. Even if it is possible to take structure already patterned with the transfer printing technique [85, 87], this step is always required at some point.

2.2.2 Patterning of the III-V

Once the material is deposited, we would like to give it the shape of the structure wanted. To do so, we pattern another layer at first, deposited on top of the material.

We can cite two main techniques for the patterning of the materials that are the photolithography and electron-beam (ebeam) lithography.

2.2.2.1 Ultraviolet lithography

The first process involves ultraviolet (UV) light to pattern the medium. It is a well-known and widely used process called UV lithography. It requires depositing a resin on top of the material to etch by spin coating, to obtain a uniform layer of resin on the material, that is sensitive to UV light. The resin deposited will be partially exposed to UV light. Some parts will be protected by a physical mask designed beforehand and linked to the nature of the resin used (see fig. 2.12). It is also of interest to mention that some resin (like the TI35E employed, which is a positive resin) can be fully re-illuminated after the mask exposure, without a mask this time, to inverse the property of the resin. And so, a positive resin for instance will use the same mask as a negative one thanks to this extra step.

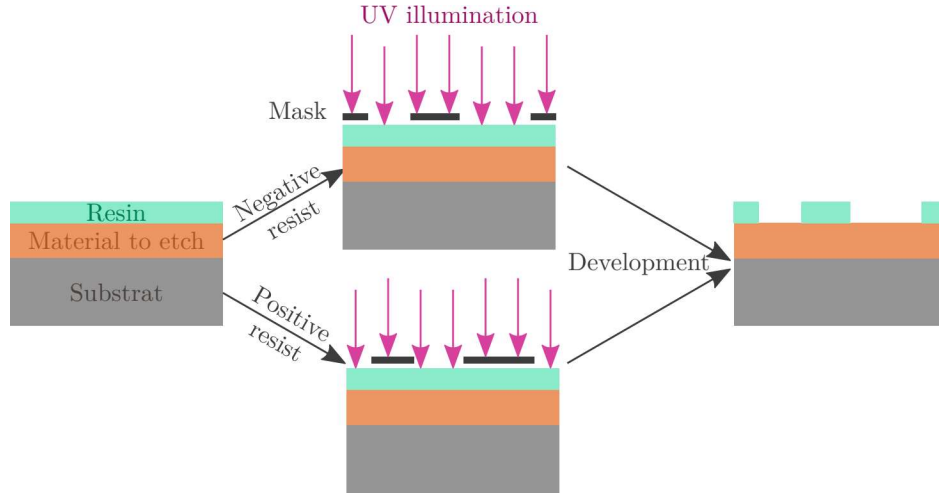


Figure 2.12: UV lithography steps representation for both a positive and a negative resist.

After the illumination step, the chip will be placed in a chemical bath for development. Thanks to this step, the unwanted part of the resin will be removed, and the final pattern will be engraved on the resin. This will act as a protective mask for the final etching process of the material. This kind of lithography is however limited by the optical system in place. Indeed, the critical dimension (CD) of a structure with this kind of process is defined as: $CD = k_1 \frac{\lambda}{NA}$. Where k_1 is a process-related coefficient that is between 0,3 and 0,9 according to the lithography system, λ is the wavelength used and NA is the numerical aperture as seen from the wafer. The dimension limitation is thus directly linked to the wavelength, which is a limiting factor. That's the reason why processes such as extreme ultraviolet lithography appeared as their wavelength is much smaller and so the critical dimension is proportionally reduced [1, 88, 89].

2.2.2.2 Electron-beam lithography

Another kind of patterning process which is extremely popular is electron-beam lithography. It can theoretically allow reaching structure dimensions below 10 nm where UV lithography is usually limited to 16 nm. The process is quite similar to the one explained earlier and presented in fig. 2.12 concerning the mask and the resist. The main difference, in this case, is that the mask is a computer-aided designed mask, whereas the UV lithography required a physical mask. The first one is thus much easier to modify quickly compared to the physical mask. The resin used in this process is also different as it has to react with electrons and not with UV light.

Finally, the nature of the source employed for the resin patterning is different. In this process, an electron beam is employed to pattern the resist.

The electron-beam lithography is defined by a writing field, as can be seen in fig. 2.13 which is the area where the device can pattern the resin. If we want to pattern a structure higher than the writing field, the electron beam will need to "jump" to another writing area. During this step, a misalignment between the two writing fields, better known as stitching, can occur. To correct this kind of misalignment, a solution is to use a fixed beam moving stage (FBMS) method. In this case, the beam is not moving while the stage is travelling to pattern the resin. We can see in fig. 2.13(b) and (c) the result for such a technique compared to a big structure without FBMS for the same structure.

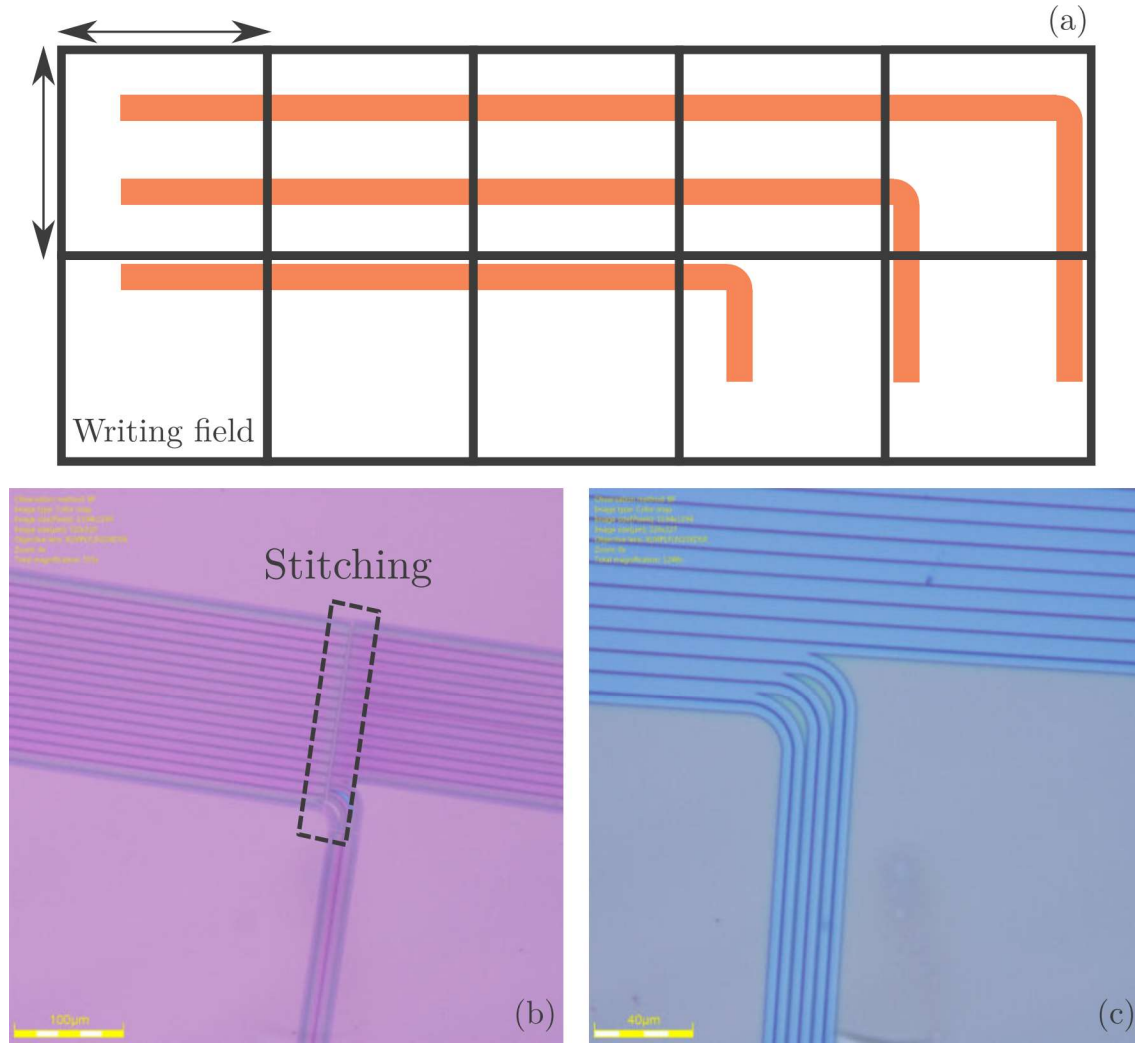


Figure 2.13: Representation of a writing field for a given structure (a). The result of the patterning without the use of FBMS results in the presence of stitching (b) compared to the same structure while using the FBMS process (c).

In the case without using the FBMS technique, we can see that there is no continuity in the waveguides which correspond to the edge of the writing field. On the other side, while using the FBMS, the waveguide doesn't present any stitching.

We've seen how we can pattern the resist that is over the material in which we want to create our structures. After this, we now need to etch the material that is now protected by a resin mask. However, it is sometimes required to deposit another material as a hard mask between the material to be patterned and the resin according to the resin properties. For instance, it is required to deposit a hard mask when using the ARP-6200 resin (which is a positive resist) but there is no need for such a thing when it comes to the hydrogen silsesquioxane (HSQ) resin (a negative resin) [90].

2.2.3 Etching

The last step of a waveguide fabrication process is to pattern it. It is now time to give a shape to our waveguide that will correspond to the needs. Once more, there are different ways of etching materials.

The first one is called wet etching. As its name suggests, it involves chemicals to react with the material and remove the unwanted part. This is done by protecting the part of the material that we want to preserve. It is commonly the role of the resin from the patterning process.

When different materials are involved, the element to take into account is the selectivity of the chemical for a couple of materials. The selectivity is defined as the ratio between both etch rates of the two materials studied for a given solution. Indeed, each material reacts differently with a certain chemical. This allows etching a material without hurting too much the other one. We can consider, for instance, the case of citric acid ($C_6H_8O_7$) which, combined with hydrogen peroxide (H_2O_2) is a great combination for indium gallium arsenide (InGaAs) ($In_{0.53}Ga_{0.47}As$ to be more accurate) and Indium Phosphide (InP) wafers as a $C_6H_8O_7:H_2O_2$ solution in the 7:1 proportion presents an etch rate around 142,1 nm/min and 0,3 nm/min respectively resulting in a selectivity of 473,67 [91]. We can notice that hydrogen peroxide is an important element in this solution. This is because it acts like an oxidizer agent that allows the reaction with the acid agent. That's why it usually appears in this kind of process [92, 93].

Although it is a widely used method as it is highly selective and cheap, it can also have a disadvantage. During wet etching, the process is usually anisotropic as it depends on the orientation of the crystal [94, 95]. The result is a trapezoidal cross-section as seen in fig. 2.14. For some materials, the etching can be isotropic [96] but this also leads to a particular and unwanted cross-section as represented in fig. 2.14. The perfect case would be a perfectly anisotropic etching as can be seen in fig. 2.14. Other methods have thus been developed to overcome the wet etching issue, like the dry etching that we are going to present.

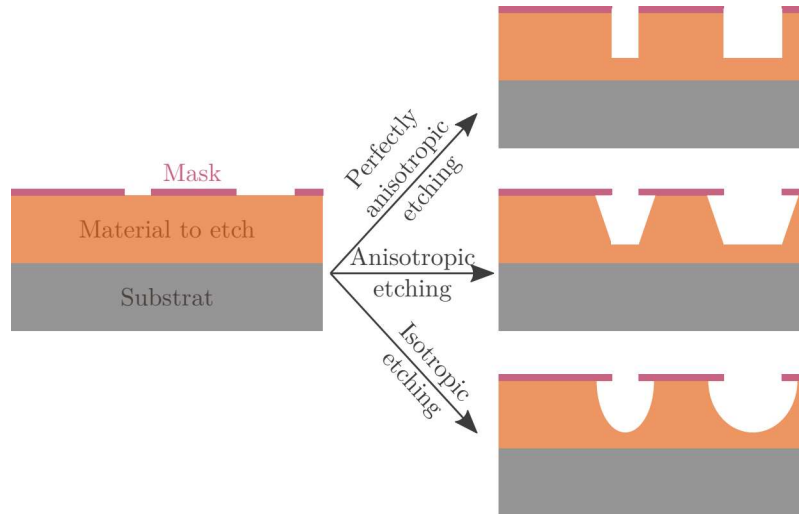


Figure 2.14: Representation of difference between perfectly anisotropic, anisotropic and isotropic etching for the same sample. In these cases, the material is protected by a patterned mask beforehand.

The dry etching consists of the use of gases in a low-pressure environment and electrical stimulation to generate plasma in the chamber. In this case, we can define two main methods. The first one is the reactive ion etching (RIE) technique and the second is the inductively coupled plasma (ICP) technique. They are quite similar except for an extra RF power source used for the ICP machine as can be seen in fig. 2.15. In both cases, the process consists in placing the chip to etch on a plate that is connected to a RF source.

Usually, this source is oscillating at a 13,56 MHz frequency with a power of 100 W. This has the effect to cause the break-down of the molecules in the gas inside the chamber and so ionizing it. A direct current electric field is then applied to the plate, which leads to the attraction of the plasma toward it and so the chip. The collision between the plasma and the surface of the chip will induce an etching of the chip. The fact that a RF source is added to the ICP process is to decouple the ion current and the ion energy, allowing a wider range of processes.

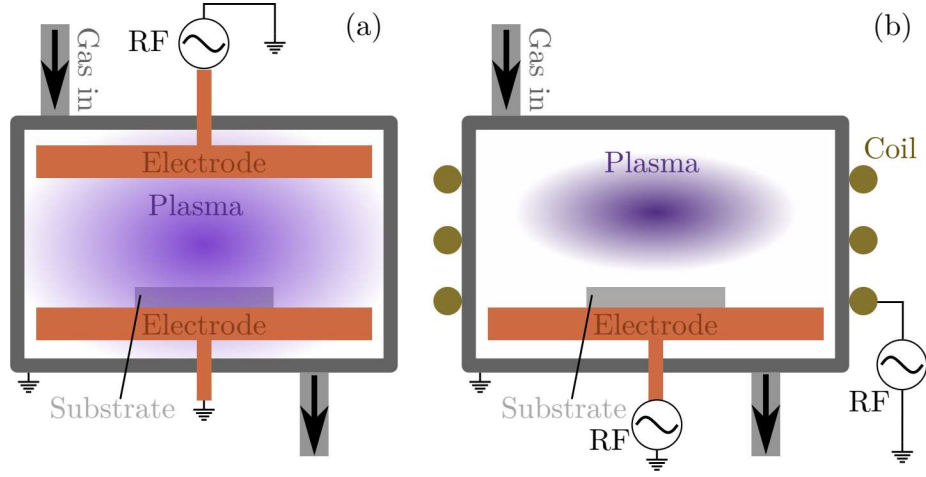


Figure 2.15: Difference between the operation of a RIE machine (a) and an ICP machine.

This method is thus widely used as the last step of fabrication, to etch the final structures, as it allows better control.

To conclude the chapter on the integration of III-V nonlinear materials, we show in fig. 2.16 some final structures were obtained with III-V material from other research groups while the structures fabricated in the context of this thesis will be presented later.

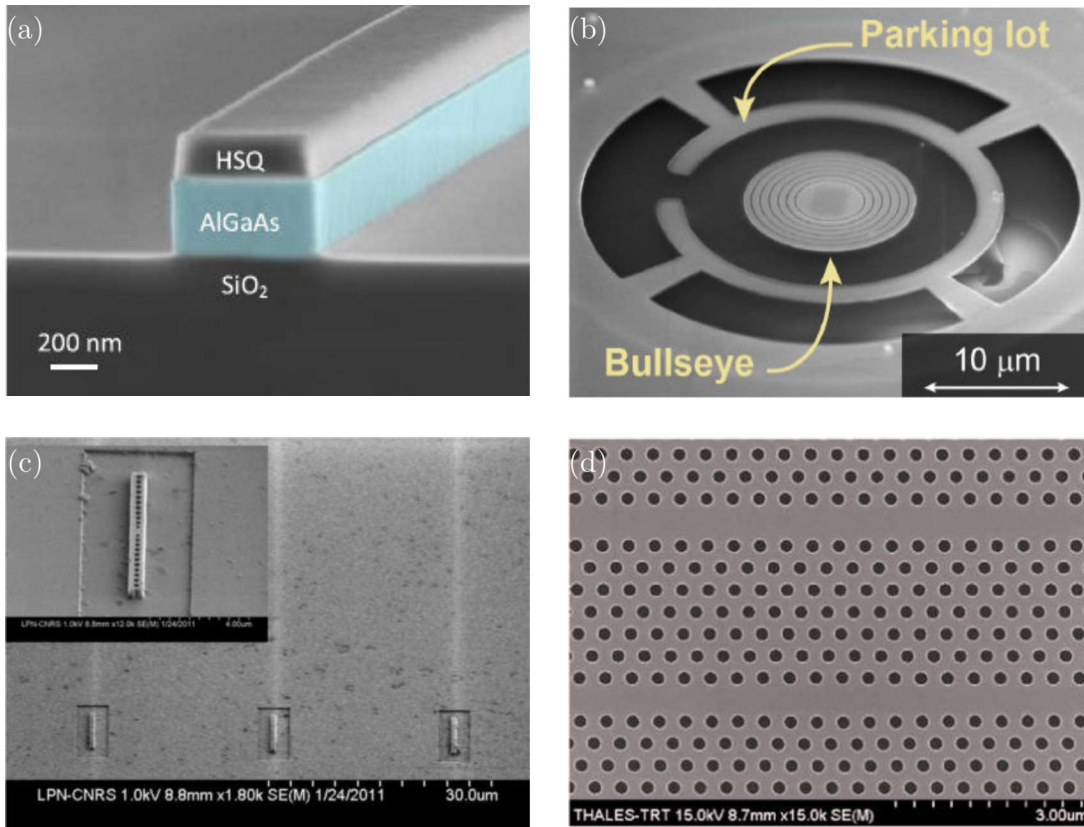


Figure 2.16: We can here see several examples of what is possible with III-V materials with a waveguide structure (a) from [97], a bullseye resonator[98], a nanolaser made of photonic crystals [99] and a photonic crystals nanocavity [100]

We have seen here why it is interesting to integrate these alloys in our context due to their optical properties. We've also seen how we can fabricate structures made of these materials and some results that have already been obtained, which let believe in the feasibility. In the following parts, we're going to study the second-order nonlinear effects in III-V alloys that have been fabricated using methods explained there. The fabrication processes were adapted to the materials chosen according to our objectives.

Bibliography

1. Adachi, S. *Properties of semiconductor alloys: group-IV, III-V and II-VI semiconductors* en. OCLC: 636379620. ISBN: 978-0-470-74369-0 (Wiley, Chichester, 2009).
2. Convertino, C., Zota, C. B., Schmid, H., Ionescu, A. M. & Moselund, K. E. III–V heterostructure tunnel field-effect transistor. en. *Journal of Physics: Condensed Matter* **30**, 264005. ISSN: 0953-8984, 1361-648X. <https://iopscience.iop.org/article/10.1088/1361-648X/aac5b4> (2021) (July 2018).
3. Mimura, T., Hiyamizu, S., Fujii, T. & Nanbu, K. A New Field-Effect Transistor with Selectively Doped GaAs/n-Al_xGa_{1-x}As Heterojunctions. en. *Japanese Journal of Applied Physics* **19**, L225–L227. ISSN: 0021-4922, 1347-4065. <https://iopscience.iop.org/article/10.1143/JJAP.19.L225> (2021) (May 1980).
4. Mokkapati, S. & Jagadish, C. III-V compound SC for optoelectronic devices. en. *Materials Today* **12**, 22–32. ISSN: 13697021. <https://linkinghub.elsevier.com/retrieve/pii/S1369702109701105> (2021) (Apr. 2009).
5. Mauthe, S. *et al.* Hybrid III-V Silicon Photonic Crystal Cavity Emitting at Telecom Wavelengths. en, 10.
6. Chen, S. *et al.* Electrically pumped continuous-wave III–V quantum dot lasers on silicon. en. *Nature Photonics* **10**, 307–311. ISSN: 1749-4885, 1749-4893. <http://www.nature.com/articles/nphoton.2016.21> (2021) (May 2016).
7. Bimberg, D. *et al.* InGaAs–GaAs Quantum-Dot Lasers. en. *IEEE JOURNAL OF SELECTED TOPICS IN QUANTUM ELECTRONICS* **3**, 10 (1997).
8. Sun, J., Han, M., Gu, Y., Yang, Z.-x. & Zeng, H. Recent Advances in Group III-V Nanowire Infrared Detectors. en. *Advanced Optical Materials* **6**, 1800256. ISSN: 21951071. <http://doi.wiley.com/10.1002/adom.201800256> (2021) (Sept. 2018).
9. Dai, X. *et al.* GaAs/AlGaAs Nanowire Photodetector. en. *Nano Letters* **14**, 2688–2693. ISSN: 1530-6984, 1530-6992. <https://pubs.acs.org/doi/10.1021/nl5006004> (2021) (May 2014).
10. Grein, C. H., Young, P. M., Flatté, M. E. & Ehrenreich, H. Long wavelength InAs/InGaSb infrared detectors: Optimization of carrier lifetimes. en. *Journal of Applied Physics* **78**, 7143–7152. ISSN: 0021-8979, 1089-7550. <http://aip.scitation.org/doi/10.1063/1.360422> (2021) (Dec. 1995).
11. Besikci, C. 111-v infrared detectors on Si substrates. en, 9.
12. Tsuzuki, K. *et al.* 40 Gbit/s n–i–n InP Mach–Zehnder modulator with a p voltage of 2.2 V. en, 3.
13. Baig, S. A. *et al.* An Ultrafast Switchable Terahertz Polarization Modulator Based on III–V Semiconductor Nanowires. en. *Nano Letters* **17**, 2603–2610. ISSN: 1530-6984, 1530-6992. <https://pubs.acs.org/doi/10.1021/acs.nanolett.7b00401> (2021) (Apr. 2017).

14. Doerr, C. R. *et al.* Compact High-Speed InP DQPSK Modulator. en. *IEEE Photonics Technology Letters* **19**, 1184–1186. ISSN: 1041-1135. <http://ieeexplore.ieee.org/document/4268353/> (2021) (Aug. 2007).
15. <https://sciencenotes.org/printable-periodic-table/>
16. <https://www.zurich.ibm.com/st/nanodevices/monolithicgrowth.html>
17. Barrigón, E., Heurlin, M., Bi, Z., Monemar, B. & Samuelson, L. Synthesis and Applications of III–V Nanowires. en. *Chemical Reviews* **119**, 9170–9220. ISSN: 0009-2665, 1520-6890. <https://pubs.acs.org/doi/10.1021/acs.chemrev.9b00075> (2021) (Aug. 2019).
18. Del Alamo, J. A. *et al.* Nanometer-Scale III-V MOSFETs. en. *IEEE Journal of the Electron Devices Society* **4**, 205–214. ISSN: 2168-6734. <http://ieeexplore.ieee.org/document/7506284/> (2021) (Sept. 2016).
19. Takagi, S. *et al.* III–V/Ge channel MOS device technologies in nano CMOS era. en. *Japanese Journal of Applied Physics* **54**, 06FA01. ISSN: 0021-4922, 1347-4065. <https://iopscience.iop.org/article/10.7567/JJAP.54.06FA01> (2021) (June 2015).
20. Del Alamo, J. A. Nanometre-scale electronics with III–V compound semiconductors. en. *Nature* **479**, 317–323. ISSN: 0028-0836, 1476-4687. <http://www.nature.com/articles/nature10677> (2021) (Nov. 2011).
21. Kalt, H. *Optical Properties of III–V Semiconductors* en (eds Cardona, M., Fulde, P., von Klitzing, K., Queisser, H.-J. & Lotsch, H. K. V.) ISBN: 978-3-642-63527-4. <http://link.springer.com/10.1007/978-3-642-58284-4> (2021) (Springer Berlin Heidelberg, Berlin, Heidelberg, 1996).
22. Ranjan, S., Balaji, S., Panella, R. A. & Ydstie, B. E. Silicon solar cell production. en. *Computers & Chemical Engineering* **35**, 1439–1453. ISSN: 00981354. <https://linkinghub.elsevier.com/retrieve/pii/S009813541100161X> (2021) (Aug. 2011).
23. Li, J. *et al.* A Brief Review of High Efficiency III-V Solar Cells for Space Application. en. *Frontiers in Physics* **8**, 631925. ISSN: 2296-424X. <https://www.frontiersin.org/articles/10.3389/fphy.2020.631925/full> (2021) (Feb. 2021).
24. Bett, A. W. *et al.* Overview about Technology Perspectives for High Efficiency Solar Cells for Space and Terrestrial Applications. en, 7.
25. Geisz, J. F. *et al.* Six-junction III–V solar cells with 47.1% conversion efficiency under 143 Suns concentration. en. *Nature Energy* **5**, 326–335. ISSN: 2058-7546. <http://www.nature.com/articles/s41560-020-0598-5> (2021) (Apr. 2020).
26. <https://www.nrel.gov/pv/module-efficiency.html>
27. Han, Y. *et al.* Bufferless 15 μm III-V lasers grown on Si-photonics 220 nm silicon-on-insulator platforms. en. *Optica* **7**, 148. ISSN: 2334-2536. <https://www.osapublishing.org/abstract.cfm?URI=optica-7-2-148> (2021) (Feb. 2020).
28. Seifried, M. *et al.* Monolithically Integrated CMOS-Compatible III–V on Silicon Lasers. en. *IEEE Journal of Selected Topics in Quantum Electronics* **24**, 1–9. ISSN: 1077-260X, 1558-4542. <https://ieeexplore.ieee.org/document/8353716/> (2021) (Nov. 2018).
29. Law, H., Nakano, K. & Tomasetta, L. III-V alloy heterostructure high speed avalanche photodiodes. en. *IEEE Journal of Quantum Electronics* **15**, 549–558. ISSN: 0018-9197. <http://ieeexplore.ieee.org/document/1070061/> (2021) (July 1979).

30. Yuan, Y. *et al.* III-V on silicon avalanche photodiodes by heteroepitaxy. en. *Optics Letters* **44**, 3538. ISSN: 0146-9592, 1539-4794. <https://www.osapublishing.org/abstract.cfm?URI=ol-44-14-3538> (2021) (July 2019).
31. <https://www.ommic.com/all-our-products/>
32. <https://www.hamamatsu.com/eu/en/product/cameras/ingaas-cameras/index.html>
33. <https://www.raptorphotonics.com/product-type/swir>
34. Ueno, Y., Ricci, V. & Stegeman, G. I. Second-order susceptibility of Ga_{0.5}In_{0.5}P crystals at 1.5 μ m and their feasibility for waveguide quasi-phase matching. en. *Journal of the Optical Society of America B*, 9 (1997).
35. Shoji, I., Kondo, T., Kitamoto, A., Shirane, M. & Ito, R. Absolute scale of second-order nonlinear-optical coefficients. en. *Journal of the Optical Society of America B* **14**, 2268. ISSN: 0740-3224, 1520-8540. <https://www.osapublishing.org/abstract.cfm?URI=josab-14-9-2268> (2021) (Sept. 1997).
36. Scaccabarozzi, L. *et al.* Enhanced second-harmonic generation in AlGaAs/Al_xO_y tightly confining waveguides and resonant cavities. en. *Optics Letters* **31**, 3626. ISSN: 0146-9592, 1539-4794. <https://www.osapublishing.org/abstract.cfm?URI=ol-31-24-3626> (2021) (Dec. 2006).
37. Miller, R. C. & Savage, A. Temperature dependence of the optical properties of ferroelectric LiNbO₃ and LiTaO₃. en. *Applied Physics Letters* **9**, 169–171. ISSN: 0003-6951, 1077-3118. <http://aip.scitation.org/doi/10.1063/1.1754695> (2021) (Aug. 1966).
38. Dinu, M., Quochi, F. & Garcia, H. Third-order nonlinearities in silicon at telecom wavelengths. en. *Applied Physics Letters* **82**, 2954–2956. ISSN: 0003-6951, 1077-3118. <http://aip.scitation.org/doi/10.1063/1.1571665> (2021) (May 2003).
39. Dave, U. D. *et al.* Nonlinear properties of dispersion engineered InGaP photonic wire waveguides in the telecommunication wavelength range. en. *Optics Express* **23**, 4650. ISSN: 1094-4087. <https://www.osapublishing.org/abstract.cfm?URI=oe-23-4-4650> (2021) (Feb. 2015).
40. Lacava, C., Pusino, V., Minzioni, P., Sorel, M. & Cristiani, I. Nonlinear properties of AlGaAs waveguides in continuous wave operation regime. en. *Optics Express* **22**, 5291. ISSN: 1094-4087. <https://www.osapublishing.org/oe/abstract.cfm?uri=oe-22-5-5291> (2021) (Mar. 2014).
41. Wilson, D. J. *et al.* Integrated gallium phosphide nonlinear photonics. en. *Nature Photonics* **14**. arXiv: 1808.03554, 57–62. ISSN: 1749-4885, 1749-4893. <http://arxiv.org/abs/1808.03554> (2020) (Jan. 2020).
42. Kolodny, S., Kozin, V. & Iorsh, I. Enhancement of second-harmonic generation in micropillar resonator due to the engineered destructive interference. en. *arXiv:2103.02258 [physics]*. arXiv: 2103.02258. <http://arxiv.org/abs/2103.02258> (2021) (Mar. 2021).
43. <https://mbe.engineering.asu.edu/research/downloads/>
44. Rakić, A. D. & Majewski, M. L. Modeling the optical dielectric function of GaAs and AlAs: Extension of Adachi's model. en. *Journal of Applied Physics* **80**, 5909–5914. ISSN: 0021-8979, 1089-7550. <http://aip.scitation.org/doi/10.1063/1.363586> (2021) (Nov. 1996).

45. Adachi, S. Optical dispersion relations for GaP, GaAs, GaSb, InP, InAs, InSb, Al_xGa_{1-x}As, and In_{1-x}Ga_xAs. en. *Journal of Applied Physics* **66**, 6030–6040. ISSN: 0021-8979, 1089-7550. <http://aip.scitation.org/doi/10.1063/1.343580> (2021) (Dec. 1989).
46. Phillips, J. C. & Van Vechten, J. A. Nonlinear Optical Susceptibilities of Covalent Crystals. en. *Physical Review* **183**, 709–711. ISSN: 0031-899X. <https://link.aps.org/doi/10.1103/PhysRev.183.709> (2021) (July 1969).
47. Zernike, F. & Midwinter, J. E. *Applied nonlinear optics* ISBN: 0-486-45360-X (Wiley, 1973).
48. Kleinman, D. A. Nonlinear Dielectric Polarization in Optical Media. en. *Physical Review* **126**, 1977–1979. ISSN: 0031-899X. <https://link.aps.org/doi/10.1103/PhysRev.126.1977> (2021) (June 1962).
49. Duchesne, D. *et al.* Second harmonic generation in AlGaAs photonic wires using low power continuous wave light. en. *Optics Express* **19**, 12408. ISSN: 1094-4087. <https://www.osapublishing.org/oe/abstract.cfm?uri=oe-19-13-12408> (2020) (June 2011).
50. Anthur, A. P. *et al.* Second harmonic generation in gallium phosphide nano-waveguides. en. *Optics Express* **29**, 10307. ISSN: 1094-4087. <https://www.osapublishing.org/abstract.cfm?URI=oe-29-7-10307> (2021) (Mar. 2021).
51. Eckhouse, V. *et al.* Highly efficient four wave mixing in GaInP photonic crystal waveguides. en. *Optics Letters* **35**, 1440. ISSN: 0146-9592, 1539-4794. <https://www.osapublishing.org/abstract.cfm?URI=ol-35-9-1440> (2021) (May 2010).
52. Leo, K. *et al.* Subpicosecond four-wave mixing in GaAs/Al_xGa_{1-x}As quantum wells. en. *Physical Review B* **44**, 5726–5737. ISSN: 0163-1829, 1095-3795. <https://link.aps.org/doi/10.1103/PhysRevB.44.5726> (2021) (Sept. 1991).
53. Hamilton, C. J. *et al.* Localized Kerr-type nonlinearities in GaAs/AlGaAs multiple quantum well structures at 1.55 μm . en. *Applied Physics Letters* **68**, 3078–3080. ISSN: 0003-6951, 1077-3118. <http://aip.scitation.org/doi/10.1063/1.116428> (2021) (May 1996).
54. Boyd, R. W. *Nonlinear Optics 3rd Edition* 3rd ed. ISBN: 978-0-12-369470-6 (Elsevier, Mar. 2008).
55. Sun, C.-K. *et al.* Scanning second-harmonic/third-harmonic generation microscopy of gallium nitride. en, 4.
56. Miragliotta, J. & Wickenden, D. K. Nonlinear electroreflectance from gallium nitride using optical second-harmonic generation. en. *Physical Review B* **53**, 1388–1397. ISSN: 0163-1829, 1095-3795. <https://link.aps.org/doi/10.1103/PhysRevB.53.1388> (2021) (Jan. 1996).
57. Ikeda, K., Saperstein, R. E., Alic, N. & Fainman, Y. Thermal and Kerr nonlinear properties of plasma-deposited silicon nitride/ silicon dioxide waveguides. en. *Optics Express* **16**, 12987. ISSN: 1094-4087. <https://www.osapublishing.org/oe/abstract.cfm?uri=oe-16-17-12987> (2021) (Aug. 2008).
58. Dimroth, F., Bett, A., Giesen, C. & Heuken, M. Optimized 9×2-inch MOVPE reactor for the growth of Al-containing antimonides. en. *Journal of Crystal Growth* **272**, 706–710. ISSN: 00220248. <https://linkinghub.elsevier.com/retrieve/pii/S0022024804010176> (2021) (Dec. 2004).

59. Law, D. C. *et al.* *Lightweight, Flexible, High-Efficiency III-V Multijunction Cells* en. in *2006 IEEE 4th World Conference on Photovoltaic Energy Conference* (IEEE, Waikoloa, HI, May 2006), 1879–1882. ISBN: 978-1-4244-0016-4. <http://ieeexplore.ieee.org/document/4060028/> (2021).
60. Daudin, B. *et al.* Stranski-Krastanov growth mode during the molecular beam epitaxy of highly strained GaN. en. *Physical Review B* **56**, R7069–R7072. ISSN: 0163-1829, 1095-3795. <https://link.aps.org/doi/10.1103/PhysRevB.56.R7069> (2021) (Sept. 1997).
61. Eason, R. *et al.* en. in *Laser Growth and Processing of Photonic Devices* 55–84 (Elsevier, 2012). ISBN: 978-1-84569-936-9. <https://linkinghub.elsevier.com/retrieve/pii/B978184569936950002X> (2021).
62. Matsunami, H. & Kimoto, T. Step-controlled epitaxial growth of SiC: High quality homoepitaxy. en. *Materials Science and Engineering: R: Reports* **20**, 125–166. ISSN: 0927796X. <https://linkinghub.elsevier.com/retrieve/pii/S0927796X97000053> (2021) (Aug. 1997).
63. Zur, A. & McGill, T. C. Lattice match: An application to heteroepitaxy. en. *J. Appl. Phys.* **55**, 10 (2014).
64. Wang, Y., Liang, W., Petrov, P. K. & Alford, N. M. Dissociation of misfit and threading dislocations in Ba_{0.75}Sr_{0.25}TiO₃ epitaxial film. en. *Materials Characterization* **62**, 294–297. ISSN: 10445803. <https://linkinghub.elsevier.com/retrieve/pii/S1044580311000131> (2021) (Mar. 2011).
65. Rockett, A. & Kiely, C. J. Energetics of misfit- and threading-dislocation arrays in heteroepitaxial films. en. *Physical Review B* **44**, 1154–1162. ISSN: 0163-1829, 1095-3795. <https://link.aps.org/doi/10.1103/PhysRevB.44.1154> (2021) (July 1991).
66. Pichaud, B., Putero, M. & Burle, N. Elemental Dislocation Mechanisms Involved in the Relaxation of Heteroepitaxial Semiconducting Systems. en, 17.
67. Khurgin, J. B., Stievater, T. H., Pruessner, M. W. & Rabinovich, W. S. On the origin of the second-order nonlinearity in strained Si-SiN structures. en. *Journal of the Optical Society of America B* **32**, 2494. ISSN: 0740-3224, 1520-8540. <https://www.osapublishing.org/abstract.cfm?URI=josab-32-12-2494> (2021) (Dec. 2015).
68. Cazzanelli, M. *et al.* Second-harmonic generation in silicon waveguides strained by silicon nitride. en. *Nature Materials* **11**, 148–154. ISSN: 1476-1122, 1476-4660. <http://www.nature.com/articles/nmat3200> (2021) (Feb. 2012).
69. Moustakas, T. D. Molecular Beam Epitaxy: Thin Film Growth and Surface Studies. en. *MRS Bulletin* **13**, 29–36. ISSN: 0883-7694, 1938-1425. <http://link.springer.com/10.1557/S0883769400063892> (2021) (Nov. 1988).
70. McCray, W. P. MBE deserves a place in the history books. en. *Nature Nanotechnology* **2**, 259–261. ISSN: 1748-3387, 1748-3395. <http://www.nature.com/articles/nnano.2007.121> (2021) (May 2007).
71. Bouchkour, Z. *et al.* Aluminum nitride nano-dots prepared by plasma enhanced chemical vapor deposition on Si(111). en. *Surface and Coatings Technology* **205**, S586–S591. ISSN: 02578972. <https://linkinghub.elsevier.com/retrieve/pii/S0257897211000235> (2021) (July 2011).

72. Cheng, F. *et al.* Chemical Vapor Deposition of GaP and GaAs Thin Films From $[\text{}^n\text{Bu}_2\text{Ga}(\mu\text{-E}^t\text{Bu}_2)_2\text{Ga}^n\text{Bu}_2]$ ($\text{E} = \text{P or As}$) and $\text{Ga}(\text{P}^t\text{Bu}_2)_3$. en. *Chemistry of Materials* **23**, 5217–5222. ISSN: 0897-4756, 1520-5002. <https://pubs.acs.org/doi/10.1021/cm202158a> (2021) (Dec. 2011).
73. Lu, H. *et al.* Flip-chip integration of tilted VCSELs onto a silicon photonic integrated circuit. en. *Optics Express* **24**, 16258. ISSN: 1094-4087. <https://www.osapublishing.org/abstract.cfm?URI=oe-24-15-16258> (2021) (July 2016).
74. Mitze, T. *et al.* Hybrid integration of III/V lasers on a silicon-on-insulator (SOI) optical board in *IEEE International Conference on Group IV Photonics, 2005*. 2nd ISSN: 1949-209X (Sept. 2005), 210–212.
75. Moscoso-Martir, A. *et al.* Hybrid silicon photonics flip-chip laser integration with vertical self-alignment en. in *2017 Conference on Lasers and Electro-Optics Pacific Rim (CLEO-PR)* (IEEE, Singapore, Singapore, July 2017), 1–4. ISBN: 978-1-5090-6290-4. <http://ieeexplore.ieee.org/document/8118971/> (2021).
76. Theurer, M. *et al.* Flip-Chip Integration of InP to SiN Photonic Integrated Circuits. en. *Journal of Lightwave Technology* **38**, 2630–2636. ISSN: 0733-8724, 1558-2213. <https://ieeexplore.ieee.org/document/8985330/> (2021) (May 2020).
77. Bauters, J. F. *et al.* Planar waveguides with less than 01 dB/m propagation loss fabricated with wafer bonding. en. *Optics Express* **19**, 24090. ISSN: 1094-4087. <https://www.osapublishing.org/oe/abstract.cfm?uri=oe-19-24-24090> (2020) (Nov. 2011).
78. Roelkens, G. *et al.* III-V/Si photonics by die-to-wafer bonding. en. *Materials Today* **10**, 36–43. ISSN: 13697021. <https://linkinghub.elsevier.com/retrieve/pii/S1369702107701785> (2020) (July 2007).
79. Ottaviano, L., Pu, M., Semenova, E. & Yvind, K. Low-loss high-confinement waveguides and microring resonators in AlGaAs-on-insulator. en. *Optics Letters* **41**, 3996. ISSN: 0146-9592, 1539-4794. <https://www.osapublishing.org/abstract.cfm?URI=ol-41-17-3996> (2020) (Sept. 2016).
80. Manwar, R., Simpson, T., Bakhtazad, A. & Chowdhury, S. Fabrication and characterization of a high frequency and high coupling coefficient CMUT array. en. *Microsystem Technologies* **23**, 4965–4977. ISSN: 0946-7076, 1432-1858. <http://link.springer.com/10.1007/s00542-016-3225-4> (2021) (Oct. 2017).
81. Aras, F. G., Orhan, E. O. & Karaçali, I. Benzocyclobutene (BCB 4022-35) Polymer Thin Films by Spin Coating Method. en. *Lecture Notes on Photonics and Optoelectronics* **1**, 9–13. ISSN: 23013753. <http://www.lnpo.net/index.php?m=content&c=index&a=show&catid=27&id=15> (2021) (2013).
82. Roelkens, G. *et al.* Silicon-Based Photonic Integration Beyond the Telecommunication Wavelength Range. en. *IEEE Journal of Selected Topics in Quantum Electronics* **20**, 394–404. ISSN: 1077-260X, 1558-4542. <http://ieeexplore.ieee.org/document/6718100/> (2021) (July 2014).
83. Guo, S., Gustafsson, G., Hagel, O. J. & Arwin, H. Determination of refractive index and thickness of thick transparent films by variable-angle spectroscopic ellipsometry: application to benzocyclobutene films. en. *Applied Optics* **35**, 1693. ISSN: 0003-6935, 1539-4522. <https://www.osapublishing.org/abstract.cfm?URI=ao-35-10-1693> (2020) (Apr. 1996).

84. De Groote, A. *et al.* Transfer-printing-based integration of single-mode waveguide-coupled III-V-on-silicon broadband light emitters. en. *Optics Express* **24**, 13754. ISSN: 1094-4087. <https://www.osapublishing.org/abstract.cfm?URI=oe-24-13-13754> (2021) (June 2016).
85. Carlson, A., Bowen, A. M., Huang, Y., Nuzzo, R. G. & Rogers, J. A. Transfer Printing Techniques for Materials Assembly and Micro/Nanodevice Fabrication. en. *Advanced Materials* **24**, 5284–5318. ISSN: 09359648. <http://doi.wiley.com/10.1002/adma.201201386> (2021) (Oct. 2012).
86. Zhang, J. *et al.* Transfer-printing-based integration of a III-V-on-silicon distributed feedback laser. en. *Optics Express* **26**, 8821. ISSN: 1094-4087. <https://www.osapublishing.org/abstract.cfm?URI=oe-26-7-8821> (2021) (Apr. 2018).
87. Trindade, A. J. *et al.* Heterogeneous integration of gallium nitride light-emitting diodes on diamond and silica by transfer printing. en. *Optics Express* **23**, 9329. ISSN: 1094-4087. <https://www.osapublishing.org/abstract.cfm?URI=oe-23-7-9329> (2021) (Apr. 2015).
88. Bjorkholm, J. E. EUV Lithography—The Successor to Optical Lithography? en. *EUV Lithography*, 8.
89. Pirati, A. *et al.* EUV lithography performance for manufacturing: status and outlook en. in (eds Panning, E. M. & Goldberg, K. A.) (San Jose, California, United States, Mar. 2016), 97760A. <http://proceedings.spiedigitallibrary.org/proceeding.aspx?doi=10.1117/12.2220423> (2021).
90. Loboda, M. J. & Toskey, G. A. Understanding hydrogen silsesquioxane-based dielectric film processing. *Solid State Technology* **41**, 99. <https://www.felcomllc.com/uploads/SolidStateTecharticleDC19982.pdf> (2020) (1998).
91. DeSalvo, G. C., Tseng, W. F. & Comas, J. Etch Rates and Selectivities of Citric Acid/Hydrogen Peroxide on GaAs, Alo.3Gao.7As, Ino.2Gao.8As, Ino.3Gao.7As, Ino.s2Alo.48As, and InP. en, 5.
92. Flemish, J. R. & Jones, K. A. Selective Wet Etching of GalnP, GaAs, and InP in Solutions of HCl, CH₃COOH, and H₂O₂. en. *J. Electrochem. Soc.* **140**. Number: 3 Reporter: J. Electrochem. Soc., 4 (1993).
93. Fourre, H. Selective wet etching of lattice-matched InGaAs/InAlAs on InP and metamorphic InGaAs/InAlAs on GaAs using succinic acid/hydrogen peroxide solution. en. *Journal of Vacuum Science & Technology B: Microelectronics and Nanometer Structures* **14**, 3400. ISSN: 0734211X. <http://scitation.aip.org/content/avs/journal/jvstb/14/5/10.1116/1.588543> (2021) (Sept. 1996).
94. Mu, X. *et al.* Laminar flow used as “liquid etch mask” in wet chemical etching to generate glass microstructures with an improved aspect ratio. en. *Lab on a Chip* **9**, 1994. ISSN: 1473-0197, 1473-0189. <http://xlink.rsc.org/?DOI=b904769g> (2021) (2009).
95. Kovacs, G., Maluf, N. & Petersen, K. Bulk micromachining of silicon. en. *Proceedings of the IEEE* **86**, 1536–1551. ISSN: 00189219. <http://ieeexplore.ieee.org/document/704259/> (2021) (Aug. 1998).
96. Van Toan, N., Toda, M. & Ono, T. An Investigation of Processes for Glass Micromachining. en. *Micromachines* **7**, 51. ISSN: 2072-666X. <http://www.mdpi.com/2072-666X/7/3/51> (2021) (Mar. 2016).

97. Pu, M., Ottaviano, L., Semenova, E. & Yvind, K. Efficient frequency comb generation in AlGaAs-on-insulator. en. *Optica*, 4 (Aug. 2016).
98. Carvalho, N. C. *et al.* High-Frequency GaAs Optomechanical Bullseye Resonator. en. *arXiv:2008.03429 [physics]*. arXiv: 2008.03429. <http://arxiv.org/abs/2008.03429> (2020) (Aug. 2020).
99. Halioua, Y. *et al.* Hybrid III-V semiconductor/silicon nanolaser. en. *Optics Express* **19**, 9221. ISSN: 1094-4087. <https://www.osapublishing.org/oe/abstract.cfm?uri=oe-19-10-9221> (2021) (May 2011).
100. Combrié, S., Rossi, A. D., Tran, Q. V. & Benisty, H. GaAs photonic crystal cavity with ultrahigh Q: microwatt nonlinearity at 1.55 μm . en, 3.

Chapter 3

Second harmonic generation in III-V nanowires

We have seen in part 1.2.4 how the SHG process works in integrated platforms. We especially saw how the second-order nonlinear susceptibility is used with all the electric fields components of both the pump and SH and we also noted some particular aspects of the electric field propagation in strongly confined structures in the part 1.2.2. Combining these two aspects, we can adapt the previous theoretical models 1.10, 1.11 and the second-order nonlinear susceptibility tensor from 1.2.4 to the particular case of III-V material.

In this chapter, we will first focus on the ternary alloy that is indium gallium phosphide (InGaP). In our case, it is composed of an equal proportion of indium and gallium which means that it can be written as $\text{In}_{0.5}\text{Ga}_{0.5}\text{P}$. For simplicity, we will just call it InGaP for the rest of this thesis. At first, we will focus on the properties of the material itself, whether it is in the linear or the nonlinear regime. Both are essential to characterize and achieve the SHG process. Next, a simulation study will be presented using the theory developed about SHG in integrated platforms and adapted to III-V materials specificities. Experimental results will then be presented and the link between them and the previous simulations performed will of course be done.

Finally, we will discuss another project involving another III-V material that I worked with. The material is the aluminium gallium arsenide with an equal proportion of aluminium and gallium ($\text{Al}_{0.5}\text{Ga}_{0.5}\text{As}$) that we will simply call AlGaAs for the rest of the thesis. In this case, the material of the 13th group is either aluminium or gallium atoms while the material from the 15th group is an arsenic atom. We will see its properties, but also present the particular fabrication process that it involves. Some simulation results about the possibility of SHG process have also been obtained and will be presented and commented on.

3.1 State of the art

We have seen in section 2.1.2 some properties of III-V materials. III-V materials are attractive for second-order nonlinearities due to their high second-order nonlinear susceptibility, as can be seen in 2.1, and a high refractive index, similar to silicon, as seen in fig. 2.6 allowing high confinement of the light. A problem that restrained their usage is their crystallographic symmetry. Due to their zinc-blende structure, they indeed lack birefringence which makes phase-matching impossible in bulk material [1]. To compensate for this lack of birefringence, solutions have thus been developed. For instance, it

is possible to induce an artificial birefringence by creating a multilayer waveguide with a III-V and another material [1, 2]. Another solution has been to periodically poled the crystallographic orientation along which the waves are propagating [3]. This way, a QPM is induced to generate a SH inside the III-V material.

To simplify the fabrication processes of these structures, another solution has emerged: modal phase-matching (MPM). At a given wavelength, every mode propagates with a different refractive index. It is thus possible to find a waveguide geometry for which modes at the pump and the SH wavelength achieve phase-matching [4–6]. It allows to work with uniform waveguides and just requires finding the correct waveguide profiles to achieve the phase-matching condition. This solution is the most used nowadays in III-V nanowires [7–10] and leads to normalized conversion efficiency as high as $47000 \text{ \%} \cdot \text{W}^{-1} \cdot \text{cm}^{-2}$ ($4000 \text{ \%} \cdot \text{W}^{-1}$) [8]. These results are way higher than those obtained via MPM in LiNbO₃ waveguides, a reference for second-order nonlinearities. The maximum normalized conversion efficiency obtained via MPM in LiNbO₃ is $650 \text{ \%} \cdot \text{W}^{-1} \cdot \text{cm}^{-2}$ ($36 \text{ \%} \cdot \text{W}^{-1}$) [11]. The results obtained in III-V materials are even higher than the ones obtained in periodically poled lithium niobate (PPLN) waveguides. In PPLN, the SH is generated via QPM, a common method for LiNbO₃. At the time of the writing of this thesis, the maximum normalized conversion efficiency reached in this material is $2600 \text{ \%} \cdot \text{W}^{-1} \cdot \text{cm}^{-2}$ ($416 \text{ \%} \cdot \text{W}^{-1}$) [12].

In the following sections, we are going to study the case of MPM, as it presents really interesting results for SHG, in InGaP material. As seen in table 2.1, InGaP is a III-V material that shows a high potential for second-order nonlinearities. A comparison with the current state of the art will also be made to better place this work in the current context.

3.2 InGaP as a platform

In this part, we will take a closer look at the InGaP material. It is a III-V material that is used in solar cells [13, 14] and diodes [15] as examples. As far as we are concerned, the nonlinear properties of this material are the most important characteristics. It is indeed a fascinating and promising material concerning its nonlinear properties, as we will develop later. For the needs of our subject, we will mainly focus on the second-order nonlinearities, but we will also take a quick look at the third-order nonlinearities in this material for a better overview of its nonlinear properties. At first, let's develop the linear properties of this material.

3.2.1 Linear properties

One of the most important things to have a look at in our context is the refractive index of the material, especially its evolution according to the wavelength. The effective refractive index, required to achieve the PM condition that we already discussed in section 1.2.4, depends on the geometry of the waveguide and the refractive index of the bulk material. For this purpose, we can thus refer to previous studies and find in the literature the refractive index of the bulk material [16]. It has been measured, by an ellipsometry method, for a very large wavelength range that InGaP refractive index is following the curve represented in fig. 3.1.

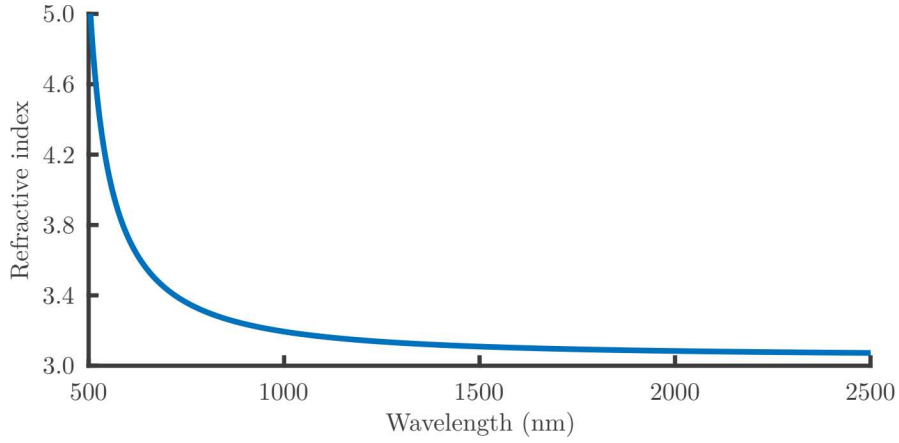


Figure 3.1: InGaP refractive index taken from R. Ferrini and al. study [16] as a function of the wavelength. The wavelength range is limited between 500 nm and 2500 nm for better visibility and because it is the range of interest for our experiments.

We can see from fig. 3.1 that the refractive index of InGaP offers a high index contrast with air. This means that InGaP patterned structures allow strong confinement of the light, which is interesting as it significantly increases the interaction between the light and the material. We can also note that, in the range of interest delimited in the figure, the refractive index is comparable to the one of Si that we can also find in literature [17]. On another hand, it is interesting to note that InGaP can exist under two states: an ordered one and a disordered one [18]. In the ordered case, the indium and gallium atoms are all aligned in alternating planes with the $[\bar{1}11]$ axis as a symmetry axis. In the disordered state, the indium and gallium atoms are randomly distributed in the III-atoms locations as is shown in fig. 3.2. In this last case, we also lose the symmetry of the ordered state.

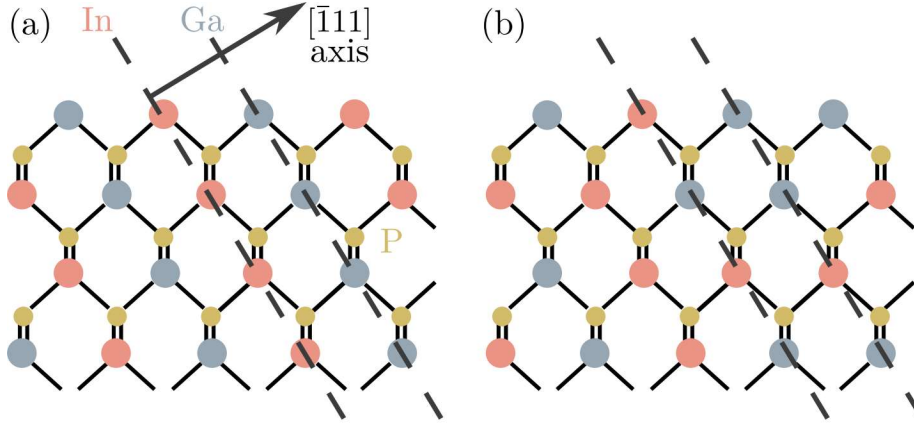


Figure 3.2: Ordered InGaP crystal (a) and example of a disordered InGaP crystal (b)

Indeed, the amount of disordering alters the crystal symmetry as the ordered state is associated with a $3m$ symmetry class while the disordered state is associated with a $\bar{4}3m$ one. This amount of disordering will also have an impact on the bandgap. InGaP is a material that possesses a large bandgap as can be seen in fig. 2.5. It can however vary according to its amount of disordering. Indeed, the disordered state possesses a larger bandgap than the ordered one [19, 20]. In this report, we are studying a disordered state InGaP material. The value of the material bandgap used is $E_g(\text{InGaP}) = 1.9$ eV, which is

equivalent to the energy of a photon at a 652.55 nm wavelength. This means that there is no TPA while we work with a pump wavelength between 1500 and 1600 nm, making it a very good material for telecom purposes in general as the range used in such applications is usually between 1530 and 1625 nm (C and L bands). Also, in the case of the SHG process, this means that there is no absorption at the SH wavelength.

Now that we learned more about some linear properties of InGaP which are essential in the case of SHG processes, we will be able to find the PM condition of our structure, as we'll see later. But first, we are going to take a closer look at the nonlinear properties of the material to be able to characterize the nonlinear effects that we are aiming for.

3.2.2 Nonlinear properties

The disordered InGaP material, like most of the III-V materials, possesses a $\bar{4}3m$ symmetry as we also just remembered before. This symmetry induces some particular properties that we have already seen in part 2.1.2. As a reminder from this part, the second-order nonlinear susceptibility tensor d_{il} of InGaP can be simplified like this:

$$d_{il} = \begin{pmatrix} 0 & 0 & 0 & d_{14} & 0 & 0 \\ 0 & 0 & 0 & 0 & d_{14} & 0 \\ 0 & 0 & 0 & 0 & 0 & d_{14} \end{pmatrix}$$

In the case of InGaP, the second-order nonlinear susceptibility $d_{14} = \chi_{123/132}^{(2)}/2$ has been measured to be as high as 110 pm/V [18]. It makes it higher than other materials such as LiNbO₃, a reference when it comes to SHG processes [11, 12, 21] which has a maximum value of 31.5 pm/V [22]. It is however in the same order of magnitudes as other III-V materials such as gallium arsenide (GaAs) (119 pm/V [23]) or AlGaAs for instance (90 pm/V [2]). This makes InGaP, and other III-V in general, very good materials for second-order nonlinear effects.

To complete the overview of this material, it is also interesting to mention that it can be an attractive material for its third-order nonlinear effects, such as four-wave mixing, as well. We can refer to table 2.2 and what has been said around it to understand why InGaP is interesting for third-order nonlinearities. A high index contrast with air, meaning high confinement of the light, as well as a higher nonlinear refractive index compared to Si and SiN makes InGaP an interesting material for third-order nonlinear effects. Just looking at these, this could signify that InGaP is more interesting, but the current fabrication processes reveal that Si and SiN are still leading in this field as the linear losses obtained are still lower in these materials [24, 25].

To conclude about the InGaP material properties, we saw that it has a high second-order nonlinear susceptibility as well as a high nonlinear refractive index. These coupled with a high refractive index makes it a great platform for nonlinear photonic experiments. The bandgap of this material as well as the CMOS compatibility also supports the interest in this material

3.3 SHG in InGaP nanowires

We have first seen the aspects around SHG and how it is occurring inside integrated platforms in part 1.2.4. We have also seen different properties and interests of III-V materials in 2.1. At last, we focused on the specific case of InGaP material to see its intrinsic properties. Here, we will mix all these elements to see how we can theoretically

express the SHG process and support our models with experiments. We will here study two kinds of phase-matching, the type I and the type II that we already exposed in 1.1.1. To keep the presentation clear and complete in each part, we will focus on the type I SHG process at first and then the type II case.

3.3.1 Analytical model

In this part, a development of the model for the study of SHG as well as simulations around it is shown. We have seen in previous parts 1.1.1 and 1.2.4 some aspects of the SHG process. We saw that parameters like the refractive index and the second-order susceptibility of the material are crucial elements. We will start to see how we can find these parameters and others like the linear loss are used to develop the model of the SHG process in a III-V nanowaveguide.

3.3.1.1 Type I second harmonic generation model

To study the SHG process, we need to determine the evolution of both the pump and the SH. To do so, we will first start to develop the expressions 1.11 and 1.10 from 1.1.1 in the context of type I SHG in III-V material. We first consider that the waveguide, along which the waves are propagating, is aligned with the z-axis of a Cartesian frame (xyz). In this frame, we express the electric field as a superposition of two modes:

$$\mathbf{E} = a_1(z)\mathbf{e}_{a_1}(\mathbf{r}_\perp, \omega_0)e^{i(\beta_a z - \omega_0 t)} + b(z)\mathbf{e}_b(\mathbf{r}_\perp, 2\omega_0)e^{i(\beta_b z - 2\omega_0 t)} + c.c., \quad (3.1)$$

where a represents the pump amplitude and b the SH one normalized such that $|a|^2$ and $|b|^2$ are carrying the power of the pump and the SH respectively. The propagation constants are represented by β_a for the pump at the carrier frequency ω_0 and β_b for the SH at the carrier frequency $2\omega_0$. The orthonormal vectorial electric profiles of the modes represented here by $\mathbf{e}_a(x, y, \omega_0)$ and $\mathbf{e}_b(x, y, 2\omega_0)$ satisfy the usual orthonormality condition $\int [\mathbf{e}_n(\mathbf{r}_\perp) \times \mathbf{h}_m^*(\mathbf{r}_\perp)] \cdot \mathbf{z} dA = \delta_{nm}$ [26]. We thus adapt the equations 1.11 and 1.10 for this case. The result can be read as:

$$\frac{da}{dz} = i\kappa^* a(z)^* b(z) \exp(-i\Delta\beta z) - \alpha_a a(z), \quad (3.2)$$

$$\frac{db}{dz} = a(z)^2 \kappa \exp(i\Delta\beta z) - \alpha_b b(z). \quad (3.3)$$

The phase mismatch between the pump and the SH is represented by $\Delta\beta$ and is expressed as $\Delta\beta = 2\beta_a - \beta_b$, the coefficient $\alpha_{a,b}$ are respectively the linear loss of the pump and the SH and κ is the nonlinear coefficient defined previously 1.1.1. In our study, we make the hypothesis that there is no depletion of the pump which allows us to neglect the parametric down-conversion terms in equation 3.2. This means that equation 3.2 will no longer be dependant on the SH power (which is cancelling the first term of the equality for the pump) so the pump variations will only be due to the linear loss in the waveguide. This simplification is possible as the pump power will be much higher than the SH power. So the fluctuations that could be induced by the SH on the pump are negligible. This approximation leads to analytically solve the equation 3.3 to express the SH power $P_{sh} = |b|^2$ like:

$$P_{sh} = 4|\kappa|^2 P_p^2 \left| \frac{\sinh(\Phi L/2)}{\Phi} \right|^2 \exp[-(\alpha_a + \alpha_b/2)L], \quad (3.4)$$

where $\Phi = \alpha_a - \alpha_b/2 + i\Delta\beta$, L represents the total length of the waveguide and P_p is the pump power. In the particular case of a lossless waveguide, 3.4 then becomes the well-known expression $P_{sh} = |\kappa L P_p \text{sinc}(\Delta\beta L)|^2$ about SHG processes from part 1.2.4. From the expression 3.4 and the classical theoretical expression 1.14, we can define an effective length L_{eff} such as $P_{sh} = |\kappa|^2 P_p^2 L_{eff}^2$ when the PM condition is fulfilled. This leads to:

$$L_{eff} = 2 \frac{\exp(-\alpha_a L) - \exp(-\alpha_b L/2)}{\alpha_b - 2\alpha_a}. \quad (3.5)$$

This effective length, which takes the linear loss into account, represents the length of the waveguide if this one was lossless. It can also be proved that, by using the Taylor series for the exponential, when the linear loss tends to zero, the effective length becomes equal to the length of the material. It may be of interest to look at this, especially when the linear losses of the structure are non-negligible like in our case, but that will come later.

3.3.1.2 Type I second harmonic generation nonlinear coefficient calculation

The SH power thus depends on different parameters: the length of the waveguide, linear losses, the pump power, the phase mismatch and the nonlinear coefficient. The length is already known as we have defined it during the fabrication process. Even if it can change in the end due to the cleave, it is a physical value that can hardly be accurately changed afterwards, and it can easily be measured with precision. Linear losses are also intrinsic characteristics of the waveguide that depend on the fabrication process and material quality. These losses, therefore, requires an experimental study to be determined. In the case of the pump power, it can easily be tuned during the experiments. Furthermore, to obtain the highest conversion efficiency possible in a waveguide, we need to consider the case of a perfectly phase-matched process by tuning the pump wavelength. This will put the $\Delta\beta$ value equal to zero. The only unknown parameter to know the SH power is thus the nonlinear coefficient, which can numerically be evaluated. We know that this coefficient depends on the overlap between the modes components and the intrinsic properties of the nonlinear medium. It also depends, as seen in part 2.1.2, on the angle between the propagation direction of the optical wave and the [100], [010] or [001] axis of the crystal (depending on the growth direction of the crystal and the patterning of the waveguide). That's why we introduce a new frame (x'y'z') here, like in fig. 2.7 from 2.1.2, which is the frame of the crystal. It will allow us to define the rotation matrix seen in 2.1.2 to apply to the second-order nonlinear tensor to find its properties along the direction wanted. As a reminder from 2.1.2, in this new frame, the waveguide will always be defined as belonging to the x'z' (010) plane. Indeed, we define the x' axis as equivalent to the [100] crystallographic direction while the z' axis is along the [001] axis of the crystal. Finally, y' axis is equivalent to the [010] crystallographic axis and is always collinear to the y-axis of the waveguide frame. We understand from this definition that, when the waves are propagating along the [001] axis of the crystal, the x and x' axis are superimposed. We will furthermore define the angle θ as the angle between the x and x' (or z and z') axes. We can define the nonlinear coefficient according to this rotation angle between the

propagation axis and the [001] axis of the crystal such as it has been done in [27]:

$$\begin{aligned} \kappa(\theta) = \frac{\epsilon_0 \omega_0}{2N_a \sqrt{N_b}} \iint_A \chi_{xyz}^{(2)} [& (e_b^{x*} \cos \theta - e_b^{z*} \sin \theta) (e_a^y) (e_a^x \sin \theta + e_a^z \cos \theta) \\ & + (e_b^{y*}) (e_a^x \cos \theta - e_a^z \sin \theta) (e_a^x \sin \theta + e_a^z \cos \theta) \\ & + (e_b^{x*} \sin \theta + e_b^{z*} \cos \theta) (e_a^y) (e_a^x \cos \theta - e_a^z \sin \theta)] dx dy, \end{aligned} \quad (3.6)$$

where N_a and N_b are the normalization constants of the pump and the SH respectively expressed as:

$$N_j = \frac{1}{2} \iint_A \mathbf{e}_j \times \mathbf{h}_j^* dx dy.$$

We can see with this expression how all the electric field components impact the efficiency of the SHG process. We can particularly notice the importance of the longitudinal component in this expression. Indeed, several studies only consider the transverse modes and neglect the longitudinal one [4, 28], which is crucial when it comes to strongly confined modes as seen in part 1.2.

This process is now fully expressed thanks to eq. 3.6 coupled with the eq. 3.4, we will thus now focus on the equivalent development in the type II SHG case.

3.3.1.3 Type II second harmonic generation case

We already know that the type II SHG case is a bit different as there are two pumps fields to take into account. In this case, we then express the electric field as a superposition of three different modes:

$$\begin{aligned} \mathbf{E} = & a_1(z) \mathbf{e}_{a_1}(\mathbf{r}_\perp, \omega_0) e^{i(\beta_{a_1} z - \omega_0 t)} \\ & + a_2(z) \mathbf{e}_{a_2}(\mathbf{r}_\perp, \omega_0) e^{i(\beta_{a_2} z - \omega_0 t)} \\ & + b(z) \mathbf{e}_b(\mathbf{r}_\perp, 2\omega_0) e^{i(\beta_b z - 2\omega_0 t)} + c.c.. \end{aligned} \quad (3.7)$$

In such process, the previous propagation equations in the waveguide frame ($x'y'z'$) can be written as [29]:

$$\frac{da_1}{dz} = -\frac{\alpha_{a_1}}{2} a_1 + i\kappa_{12}^* b a_2^* \exp(-i\Delta\beta z) \quad (3.8)$$

$$\frac{da_2}{dz} = -\frac{\alpha_{a_2}}{2} a_2 + i\kappa_{12}^* b a_1^* \exp(-i\Delta\beta z) \quad (3.9)$$

$$\frac{db}{dz} = -\frac{\alpha_b}{2} b + 2i\kappa_{12} a_1 a_2 \exp(i\Delta\beta z), \quad (3.10)$$

where α_{a_1} , α_{a_2} and α_b are the linear loss coefficients of the respective modes, $\Delta\beta = \beta_{a_1} + \beta_{a_2} - \beta_b$ is the wavenumber mismatch and κ_{12} is the nonlinear coefficient in the type II case. We still work under the condition of undepleted pumps, which leads us to analytically express the SH power as:

$$P_{sh} = 16 |\kappa_{12}|^2 \frac{P_1 P_2}{|\Phi|^2} \left| \sinh \left(\frac{\Phi}{2} z \right) \right|^2 \exp \left[- \left(\frac{\alpha_b}{2} + \alpha_a \right) z \right], \quad (3.11)$$

where $\alpha_{a_1} = \alpha_{a_2} = \alpha_a$ and $\Phi = \alpha_b/2 - \alpha_a + i\Delta\beta$. $P_{1,2} = |a_{1,2}|^2$ are the input powers at the pump wavelength. To maximize the conversion, we set $P_1 = P_2 = P_0/2$ with P_0 the

total input power of the pump. In this case, we can also define an effective length L_{eff} expression. By applying the same methodology as before, we find that it has the same expression as 3.5.

Now that there are three different modes involved, the expression of the nonlinear coefficient is thus different and reads:

$$\begin{aligned} \kappa_{12}(\theta) = & \frac{\epsilon_0 \omega_0}{\sqrt{N_{a1} N_{a2} N_b}} \iint_A \chi_{xyz}^{(2)} [e_b^{x*} ((e_{a1}^y e_{a2}^z + e_{a2}^y e_{a1}^z) \cos(2\theta) + (e_{a1}^y e_{a2}^x + e_{a1}^x e_{a2}^y) \sin(2\theta)) \\ & + e_b^{y*} ((e_{a1}^x e_{a2}^z + e_{a1}^z e_{a2}^x) \cos(2\theta) + (e_{a1}^x e_{a2}^x - e_{a1}^z e_{a2}^z) \sin(2\theta)) \\ & + e_b^{z*} ((e_{a1}^y e_{a2}^x + e_{a1}^x e_{a2}^y) \cos(2\theta) - (e_{a1}^y e_{a2}^z + e_{a2}^y e_{a1}^z) \sin(2\theta))] dx dy. \end{aligned} \quad (3.12)$$

This concludes the development of the models in both type I and type II PM cases. The next step is to calculate the nonlinear coefficient from equations 3.6 and 3.12. To do so, we need to get the components of the modes that are involved in the SHG process. For this purpose, we use a finite difference eigenmode solver (Lumerical) to simulate our structure and extract the components of the modes for both the pump (or pumps in the type II case) and the SH.

3.3.2 Numerical simulations

Numerical simulations are required for the design of the waveguides. Indeed, the implementation of the models developed earlier allows finding the dimensions of the waveguide that could offer the best efficiency possible. That's why the simulations are done for different widths and heights. It also helps to have a better understanding of the process and the importance of the vectorial model used to express the optical modes. Indeed, the results obtained linked to the theoretical models just developed will help us to understand the impact of each term of 3.6 and 3.12.

The numerical study is performed here for InGaP based waveguides. The profile of the structures for the numerical simulations is adapted for each type of PM to best match the actual structure that will result from the manufacturing process. For this reason, we first analyse an air-clad InGaP nanowire in the case of type I.

3.3.2.1 Type I second harmonic generation

In this case, the simulations are performed for the fundamental TE pump as well as for the fundamental TM mode at a fixed wavelength of 1550 nm. The simulations have been performed by looking for MPM between the pump considered and SH higher-order modes.

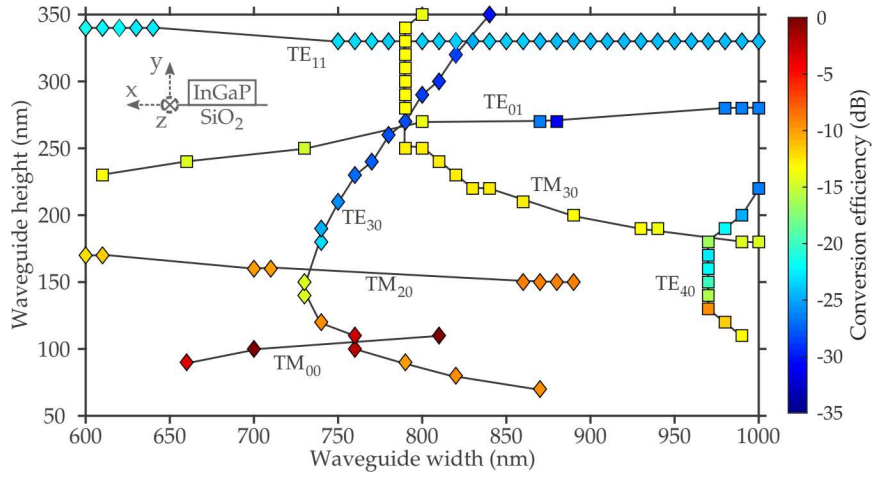


Figure 3.3: Type I SH conversion efficiency for a TE fundamental pump mode at a 1550 nm wavelength as a function of the width and the height of an InGaP air-clad waveguide. The colourmap shows the nonlinear coefficient of the process normalized by the max value found ($\kappa_{max} = 2816\sqrt{W}/m$) as a reference and is obtained for an 810 nm wide and 110 nm high waveguide. The squares represent a waveguide aligned along the [001] crystallographic axis while the diamonds represent the waveguide at a 45° angle from this crystallographic axis. [27]

From figure 3.3, we can notice that it is for thin waveguides that the conversion efficiency is the most important. Stronger confinement of the light inside the waveguide is indeed important to obtain a better conversion efficiency as more power is contained inside the nonlinear medium leading to a stronger interaction between the two waves. Concerning the width, the nonlinear coefficient value depends on the nature of the SH higher-order mode. We can notice that the nonlinear coefficient value increase with the width for the TM_{00} and the TM_{20} . It is due to the confinement of the SH inside the structure. Indeed, for smaller widths, as the height is not important either, the TM modes tend to propagate around the waveguide and not the nonlinear material. It thus leads to reducing the nonlinear coefficient. For the TE_{10} however, the nonlinear coefficient decrease with the width. It is because the area of the waveguide increase and thus reduce the nonlinear interaction between the pump and SH modes.

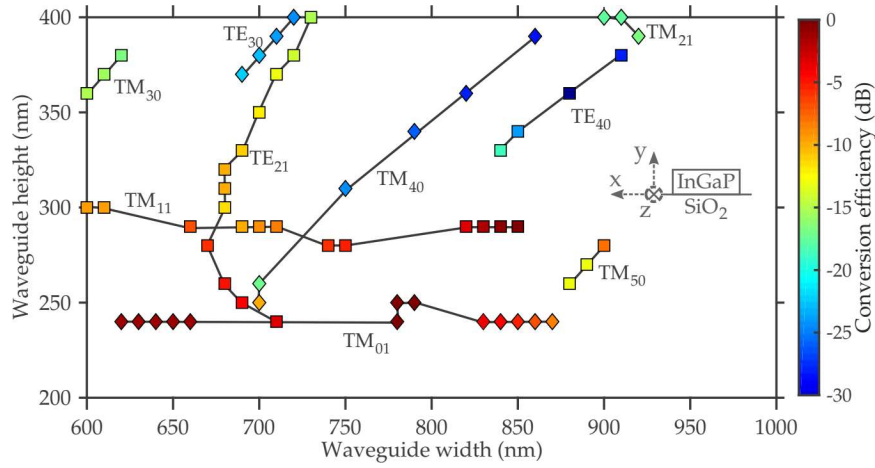


Figure 3.4: Type I SH conversion efficiency for a TM fundamental pump mode as a function of the width and the height of an InGaP air-clad waveguide. The colourmap shows the efficiency of the process normalized by the max value found ($\kappa_{max} = 2021 \sqrt{W}/m$) as a reference for an 850 nm wide and 290 nm high waveguide. The squares represent a waveguide along the [001] crystallographic axis while the diamonds represent the waveguide at a 45° angle from the [001] crystallographic axis.

In the other case of a TM pump, the first thing to note is that the conversion efficiency is lower compared to a TE pump case. We can also see in figure 3.4 that we need thicker waveguides to obtain a high conversion efficiency. This can be explained by the fact that the TM fundamental mode of the pump is more difficult to confine inside a thin structure as can be seen in fig. 3.5.

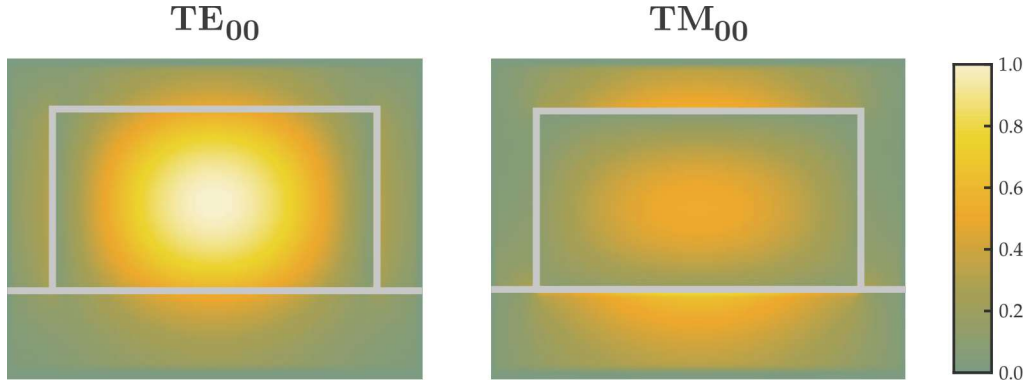


Figure 3.5: Main component of the TE_{00} (E_x) mode (left) at 1550 nm and main component of the TM_{00} (E_y) mode (right) at the same wavelength. Both modes are from an 800 nm wide and 300 nm high waveguide.

For the modes shown in fig. 3.5, the effective area calculated for both these modes is $0.26 \mu m^2$ in the case of the TE_{00} mode and $0.42 \mu m^2$ for the TM_{00} . The waveguide area is $0.24 \mu m^2$, meaning that, as it is possible to see in the figure, an important part of the TM_{00} mode is propagating around the waveguide and not inside the non-linear medium. The mode effective area is calculated via the common formula $A_{eff} = (\int |E|^2 dA)^2 / \int |E|^4 dA$ [30]) with A_{eff} the effective area, A the area of the waveguide and E the total electric field of the mode.

On another point, it is possible to explain why a given PM is possible with a 0° angle and not for a 45° and vice versa. It is actually due to the symmetry of the modes involved

in the process. Indeed, for a given mode with a symmetric x component with respect to the y -axis, both the y and z components will be antisymmetric [26]. On the contrary, when the x component is antisymmetric, both the y and z components are symmetric. And so, if we take a look at the expression for an angle θ between the propagation axis and [001] axis of the crystal equal to 0° , the expression (3.6) can thus be written as:

$$\kappa(0^\circ) = \frac{\epsilon_0 \omega_0}{2N_a \sqrt{N_b}} \iint_A \chi_{xyz}^{(2)} (e_b^{x*} e_a^y e_a^z + e_b^{y*} e_a^x e_a^z + e_b^{z*} e_a^y e_a^x) dx dy. \quad (3.13)$$

We see that, for a TE fundamental mode, the dominating term will be: $e_b^{y*} e_a^x e_a^z$. For a non-zero integral, the y component of the SH electric field has to be antisymmetric along the x -axis. This is also the case with all the modes found for this particular pump polarization state: TE₀₁ (x component is symmetric), TM₃₀ (y component is antisymmetric) and TE₄₀ (x component is symmetric). In the case of a TM fundamental pump, the dominating term will be: $e_b^{x*} e_a^y e_a^z$. It thus requires this time that the x component of the SH mode is symmetric for the integral to be non-zero which means that the y component has to be antisymmetric in this case. Which is the case for the modes found there: TM₃₀ (y component is antisymmetric), TM₁₁ (y component is antisymmetric), TE₂₁ (x component is symmetric), TM₅₀ (y component is antisymmetric) and TE₄₀ (x component is symmetric).

If we now look at the case of waves propagating along a 45° angle from the [001] crystallographic axis, we can see that it becomes quite different. The efficiency, in this case, can be expressed like this:

$$\kappa(45^\circ) = \frac{\epsilon_0 \omega_0}{2N_a \sqrt{N_b}} \iint_A \chi_{xyz}^{(2)} \left[e_a^y (e_a^x e_b^{x*} - e_b^{z*} e_a^z) + \frac{e_b^{y*}}{2} (e_a^x e_a^x - e_a^z e_a^z) \right] dx dy. \quad (3.14)$$

We see that, for a TE fundamental mode, the dominating term is: $\frac{e_b^{y*}}{2} (e_a^x e_a^x - e_a^z e_a^z)$. The x component being symmetric, the z component of the pump will be antisymmetric and so the whole part $(e_a^x e_a^x - e_a^z e_a^z)$ is symmetric. Leading to the fact that the y component of the SH needs to be symmetric in this case. This condition is fulfilled by the modes found for this case: TE₁₁, TE₃₀, TM₂₀ and TM₀₀. For a TM fundamental mode, the dominating term is: $e_a^y (e_a^x e_b^{x*} - e_b^{z*} e_a^z)$. The y component is symmetric along the x -axis and thus the x component of the SH has to be antisymmetric for the process to generate anything. For the modes found in the simulations, this is actually what is happening: TE₃₀, TM₀₁, TM₄₀ and TM₂₁.

For a better understanding, examples of the overlap results for a TE fundamental (TE₀₀) pump for both an angle of 0° and an angle of 45° from the [001] axis of the crystal can be seen in fig. 3.6. The SH mode chosen for the PM in the case of a waveguide with a 0° angle from the [001] axis of the crystal is the TE₀₁ while the TM₂₀ is chosen for the PM at a 45° angle. The equations 3.14 and 3.13 are applied to both PM to see the difference and to better understand why the overlap is equal to zero in one case and not the other.

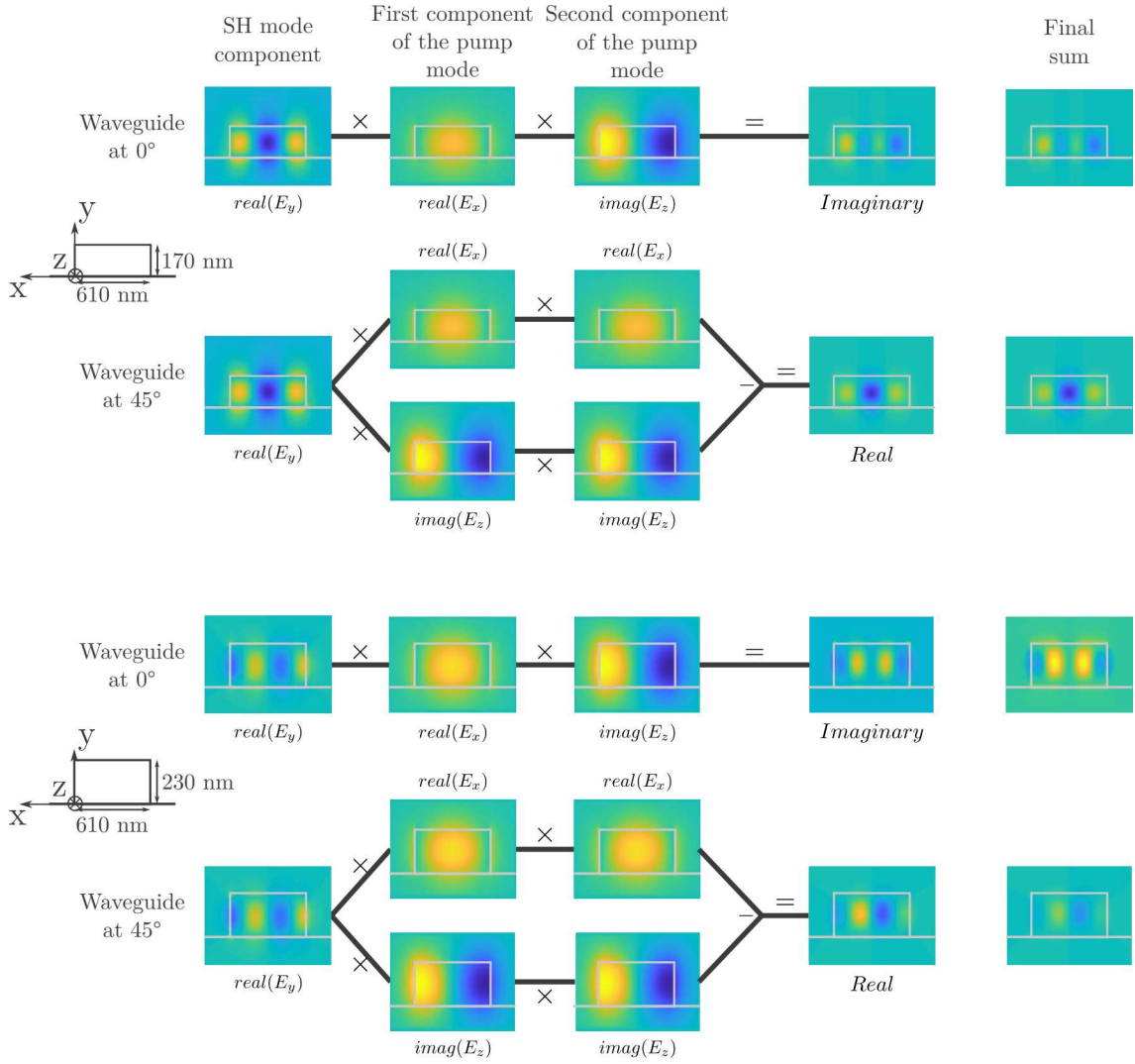


Figure 3.6: Example of the overlap result for the PM between the TE_{00} pump mode at 1550 nm and two different SH modes. The first PM occurs in a 170 nm high and 610 nm wide waveguide between the TE_{00} and the TM_{20} while the second PM is in a 230 nm high waveguide and 610 nm wide waveguide between the TE_{00} and the TE_{01} . Only the elements resulting in a non-zero product are presented here for better readability. We show the relevant components, the result of the product (and difference) and the final sum which is the sum of all the terms in the integrals 3.14 or 3.13.

In the example shown in fig. 3.6, we can notice that in a 170 nm high and 610 nm wide waveguide at a 0° angle from the $[001]$ axis of the crystal, the mode product result is symmetric along the x-axis and antisymmetric in the y-axis. The result of the integration of such results along both directions is thus equal to zero. On the other hand, for the same PM with a waveguide at 45° , the result is symmetric in both directions. This leads to an integral result different from zero. The same reasoning can be applied in the 230 nm high and 610 nm wide waveguide case to understand why the conversion efficiency is different from zero for a waveguide along the $[001]$ axis of the crystal only.

3.3.2.2 Type II second harmonic generation

For the case of type II PM, we study an InGaP nanowire with a 200 nm top layer of HSQ. That's because the fabrication process for the chip involved there is different and involved HSQ as an overlayer (see 2.2.3 for more fabrication details). In this case, the pump modes are both the TE and TM fundamental modes at a 1550 nm wavelength.

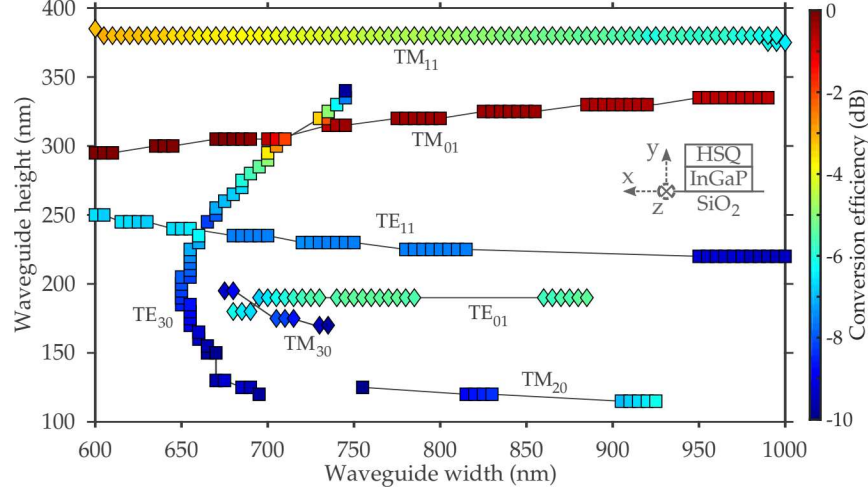


Figure 3.7: Type II SH conversion efficiency in the case of type II PM as a function of the width and the height of an InGaP waveguide with an HSQ top layer for a TE_{00} and TM_{00} pump modes. The colourmap shows the efficiency of the process by using the max value found ($\kappa_{max} = 3500i\sqrt{W}/m$) as a reference and is found for a 605 nm wide and 295 nm high waveguide. The squares represent the waves propagating along the $[001]$ crystallographic axis while the diamonds represent the waves propagating at a 45° angle. [31]

We are here noticing that it's not with the thinner structures that the most efficient generation occurs but for thicker waveguides. This difference is because we need both a TE and a TM pump at the same time and the TM component of the pump is less confined inside the structure as said earlier. A thicker waveguide leads to a higher overlap between the three modes involved which improves the conversion efficiency. Concerning the symmetry of the modes required for the SHG process, the same analysis as before can be performed. In the case of waves propagating along the $[001]$ axis of the crystal, the expression 3.12 will become:

$$\begin{aligned} \kappa_{12}(0^\circ) = \frac{\epsilon_0\omega_0}{\sqrt{N_{a1}N_{a2}N_b}} \iint_A \chi_{xyz}^{(2)} [e_b^{*x}(e_{a1}^y e_{a2}^z + e_{a1}^z e_{a2}^y) \\ + e_b^{*y}(e_{a1}^z e_{a2}^x + e_{a1}^x e_{a2}^z) \\ + e_b^{*z}(e_{a1}^x e_{a2}^y + e_{a1}^y e_{a2}^x)] dx dy, \end{aligned} \quad (3.15)$$

which, in the case of a TE fundamental mode as the first pump and a TM fundamental mode as the second one, it can be simplified as:

$$\kappa_{12}(0^\circ) \approx \frac{\epsilon_0\omega_0}{\sqrt{N_{a1}N_{a2}N_b}} \iint_A \chi_{xyz}^{(2)} [e_{a1}^x (e_b^{*y} e_{a2}^z + e_b^{*z} e_{a2}^y) + e_b^{*x} e_{a1}^z e_{a2}^y] dx dy. \quad (3.16)$$

In this case, we see that the most important part of the integral would be $e_b^{*z} e_{a1}^x e_{a2}^y$ as it involves the two main electric field components for the pump modes chosen. If we only consider, at first, that term, the result of the integral is non-zero when the z component of

the SH mode is symmetric. As seen in section 1.2.2.1, it implies that the y component of the SH mode is symmetric. And its x component is antisymmetric. With these symmetries conditions, finally, all the integrated terms are different from zero. These terms could thus increase or decrease the nonlinear coefficient. A condition that is fulfilled by the following modes: TM₀₁, TE₁₁, TE₃₀ and TM₂₀.

Along the 45° angle, the simplified expression of the nonlinear coefficient with the same pump modes become:

$$\kappa_{12}(45^\circ) \approx \frac{\epsilon_0 \omega_0}{\sqrt{N_{a1} N_{a2} N_b}} \iint_A \chi_{xyz}^{(2)} \left(e_b^{*x} e_{a1}^x e_{a2}^y - e_b^{*y} e_{a1}^z e_{a2}^z - e_b^{*z} e_{a1}^z e_{a2}^y \right) dx dy. \quad (3.17)$$

The term $e_b^{*x} e_{a1}^x e_{a2}^y$ seems to be the most important part of the integral as it contains the x component of our TE pump and y component of our TM one. To obtain a non-zero value of the integral from this term, it is required for the x component of the SH to be symmetric as the x component of the first pump and the y component of the second one are symmetric. It is indeed observed for the modes found in the simulations: TE₀₁, TM₃₀, and TM₁₁. Furthermore, if we use the symmetry properties seen in section 1.2.2.1, the symmetry of the x component of the SH involves that the z component is antisymmetric as well as the y component. Finally, with these symmetry conditions, the other elements of the integral are also different from zero. They can thus not be neglected and may increase or decrease the nonlinear coefficient.

To conclude this section, both PM types were studied there and the conversion efficiency in each case. We show that thin waveguides can lead to more efficient type I processes. Thinner waveguides are however more difficult to fabricate due to the high tolerance of the geometry required. Also, fabrication defects (like the roughness) can be even more troublesome as it leads to higher linear loss. On the other side, we have seen that the type II case is more efficient for thicker waveguides, making it less sensitive to these small variations and thus easier to fabricate. Also, we can notice that the most efficient process is encountered when the waves are propagating with a 45° angle from the [001] crystallographic axis in the type I case while, for the type II, it is the most efficient when the waves propagate along the [001] crystallographic axis.

3.3.3 Experimental results

In this part, we are first going to take a closer look at the waveguides structures involved in these experiments. Two different chips have been used for the case of type I SHG with different structure types. Both of them have been fabricated with a different process, and we will first see the shapes before going into details into the results. Then, we will see the setup used for the measurements. Finally, the results obtained will be presented and discussed starting, as before, with the type I SHG process followed by the type II one.

At first, we are going to take a closer look at the original wafer shown in fig. 3.8 used for the fabrication of the chips. It is a wafer of 320 nm high of InGaP with two sacrificial layers of 200 nm each (of GaAs and InGaP) and one substrate layer of 350 μm of GaAs. It was bonded on a Si substrate with a 3 μm top layer of SiO₂ according to the process already explained in part 2.2.1. A thin layer of SiO₂ of approximately 20 nm has been deposited on the InGaP to increase the adhesion with the SiO₂ from the substrate. The bonding and substrate removal steps were the same for both chips, but the patterning and etching processes were quite different afterwards.

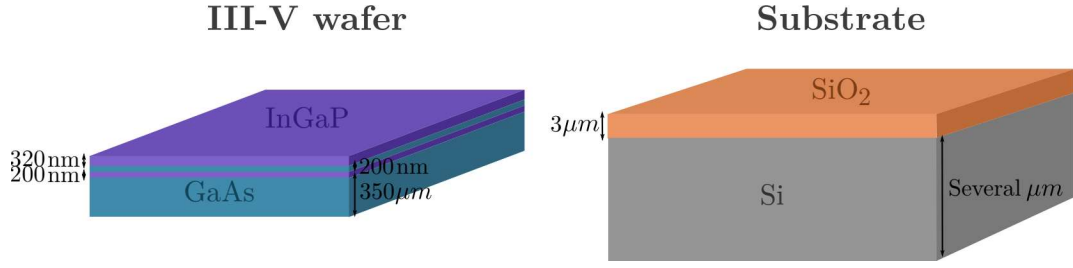


Figure 3.8: Representation of the two wafers used for the fabrication of the chips. On the left, the III-V wafer with all the sacrificial layers and substrate. On the right, the substrate wafer where the III-V material is bonded.

The first chip that we consider here presents a Z-like shape as seen in fig. 3.9(a). It was patterned this way to put the cleave direction of both the InGaP (the [101] axis) and the Si substrate (the [101] axis) along the same axis and to obtain the best conversion efficiency. Indeed, each crystal has a cleavage plane according to its properties. When cleaved, the crystal will follow this preferential direction. If the material bonded and the substrate don't have the same cleave direction, the main cleave will be along the cleave direction of the substrate (as it is the thickest layer) but the facets of the bonded material could be damaged in the process as it will mainly follow its cleaving direction. That's why it is useful to cleave the substrate and the bonded material along their cleave axis, for a better quality of the facets as can be seen in fig. 3.9(b). On another hand, for both the type I and the type II SHG cases, the best conversion efficiency has been found along the [001] axis of the crystal with the material thickness that we have (320 nm). It is thus of interest to propagate along this crystallographic axis. To summarize, it is to improve the quality of the facets that the waveguide got two parts perpendicular to the [101] axis of the crystal, while the middle part is to improve the SH conversion efficiency. It also allows having different propagation lengths along this axis, interesting for the study of the process as the SH power depends on the propagation length.

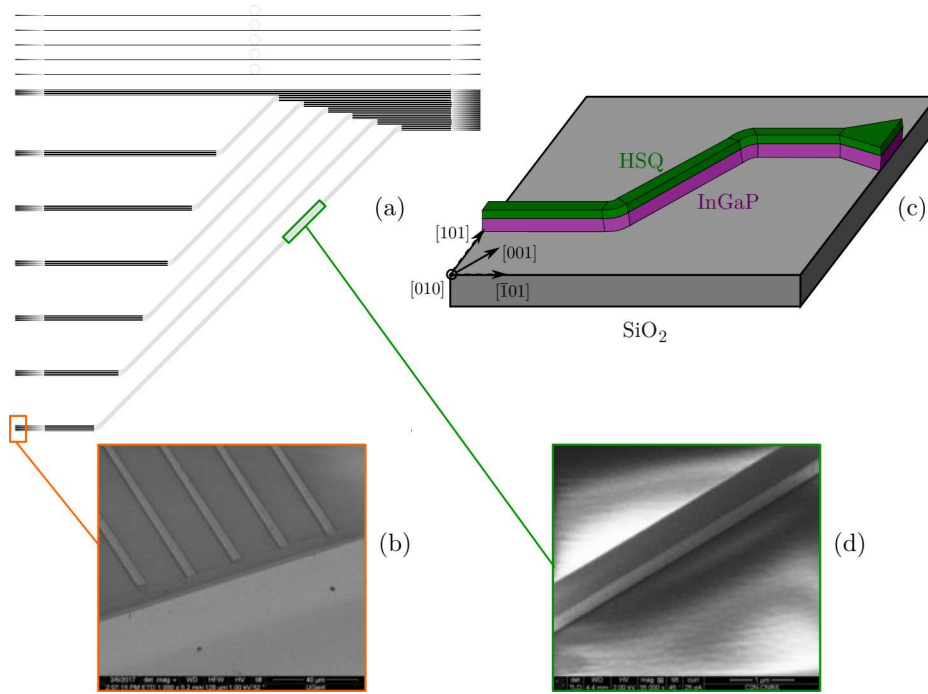


Figure 3.9: Layout used to pattern the first chip (a). An enlarged view of the facets of the waveguides is shown in (b). A sketch of the actual waveguide is represented in (c) where we can also see the different layers of interest. Finally, we can observe the smoothness of the waveguide edge on (d).

Some rings have also been added to the mask for further experiments in another chapter. The design should be formed of waveguides with the same straight section length on both sides of the part at 45° , but the last cleaving step was tricky to perform and so it was not possible to have the same length on both sides. Furthermore, both sides should have a taper but it was only possible to keep one of them as represented on the sketch of fig. 3.9(c). At the beginning of the waveguides, we got a $5\text{ }\mu\text{m}$ wide and $200\text{ }\mu\text{m}$ long taper. The absence of taper on a side is a good thing in our experiments. Indeed, the taper may introduce problems in some cases as it can act like a mode converter [32]. It is a well-known issue and can be used for this purpose specifically [33]. As can be seen in fig.3.10, it can be tricky to inject a quasi-TM fundamental pump. We can observe several crossing points between the TM_{00} mode and TE higher-order modes. This means that a mode conversion is possible from the TM_{00} mode to a TE mode. This will reduce the amount of power of the TM mode propagating in the following waveguide. This problem is however absent when it comes to the TE_{00} mode.

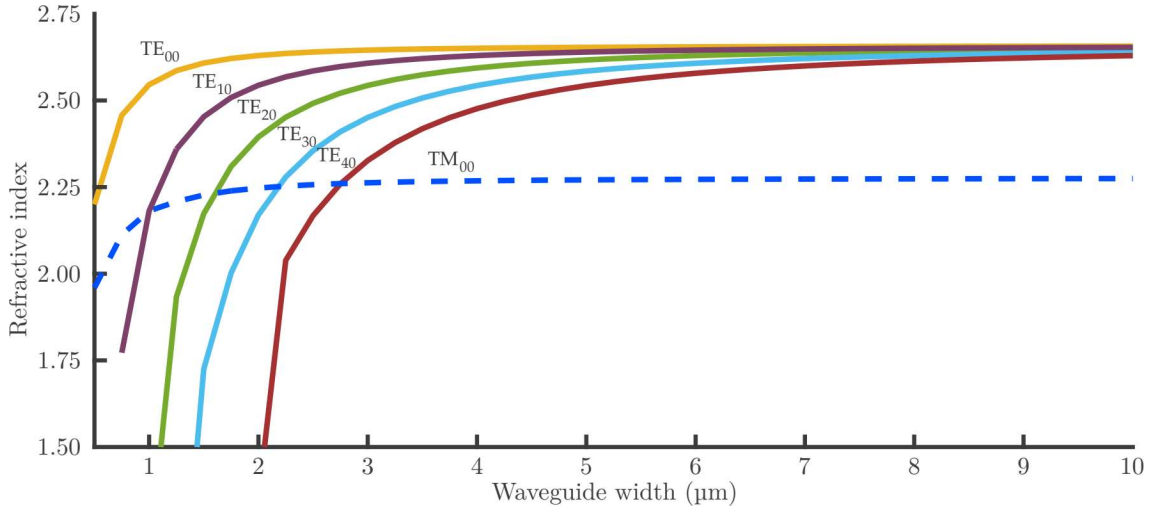


Figure 3.10: Modes indices for different modes as a function of the InGaP waveguide width for a 320 nm high material at a 1550 nm wavelength. Only six modes have been represented here. The TE modes are represented in solid lines while the TM mode is represented by dashed lines. The crossings between the TM_{00} mode and the others represent a possible conversion of energy from this one to other TE higher-order modes

It still is a great asset on the injection side and the mode conversion that we just addressed could happen for the SH mode, preventing the mode observation. This chip has furthermore been patterned with HSQ negative resist, a well-known resist for ultra-high-resolution electron beam [34], resulting in a 200 nm top layer similar to SiO_2 and smooth edges as can be seen in fig. 3.9(d).

From this chip, we first need to extract the linear losses of both the pump and the SH. Indeed, as seen in the coupled equations systems 3.2-3.3 and 3.10, the linear losses play an important role in these experiments as they limit the conversion efficiency. In our case, we use two different wavelengths for our experiments: the pump around 1550 nm and its SH. We thus need to know these losses for each wavelength as seen in the models. A common way to extract these losses is to measure the power at the output of the waveguide with a lensed fibre while knowing the power at the input injected with another lensed fibre. This way, we can determine the total losses of the system (the linear losses added to the loss from the coupling between the lensed fibres and the waveguide). In the case of this chip, due to an unfortunate lack of symmetry induced by the taper, we cannot assume the coupling loss at the entrance/exit of the waveguide to be equal. This prevents extracting the propagation loss from the method described above and another technique has to be used. A way for measuring the linear losses is to measure the diffusion pattern with a camera placed on top of the waveguides for each wavelength as can be seen in fig. 3.11(a) and (b). By extracting the intensity measured by the camera, as the length of the waveguide is exactly known, it is possible to extract the linear losses of the structure. Indeed, the optical power P_{out} in W measured at the output of a medium of a length L with an attenuation a in m^{-1} from an input power P_{in} is written $P_{out} = P_{in} \exp(-aL)$. By expressing the optical powers in decibels (dB), the expression becomes $P_{out}(dB) = P_{in}(dB) - \alpha L$ with $\alpha = 10 \log[\exp(1)]$. It is thus possible to use a linear fit from the power extracted and converted in decibels to find the linear loss of the medium.

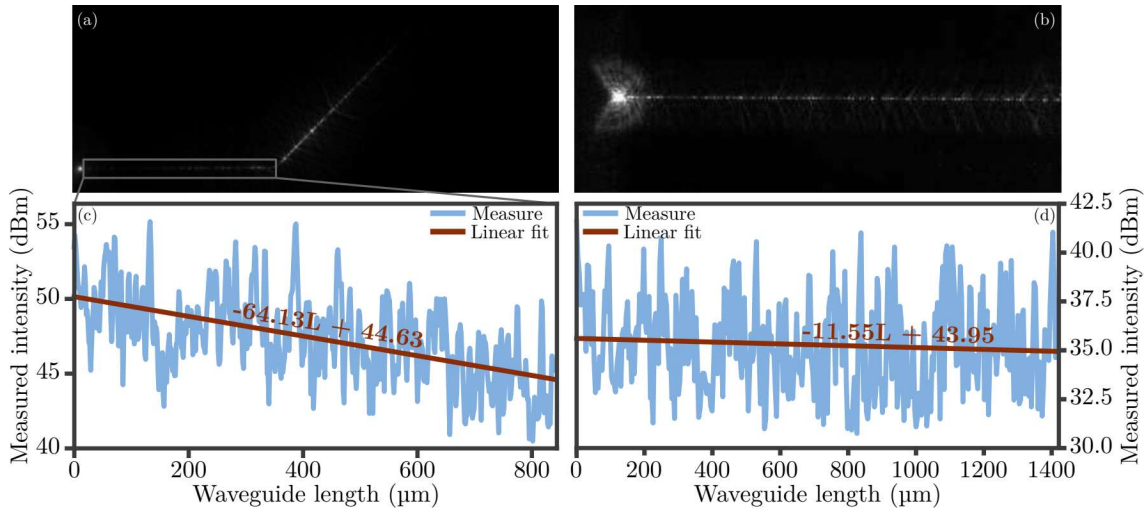


Figure 3.11: Observation of SH from above the waveguide during the SHG process for a pump coming from the left side (a) and observation of the pump at low power (b). We can see the SH being generated in the middle part of the waveguide and then being attenuated due to the linear losses in the final part of the waveguide (a). The SH (c) and pump (d) intensities measured are fitted with a linear function to extract the linear losses of the mode. The equations found from the fit are added to the curve and written with the length L in centimeters.

The linear losses for the pump have been measured to be around 12 dB/cm at the pump wavelength and 64 dB/cm at the SH wavelength as we can see in fig. 3.11(d) and (c) respectively.

The second chip is different in shape as it presents a L-like pattern as seen in fig. 3.12(a). This has been chosen to have different propagation lengths too. We inject the pump from the shorter length to neglect the nonlinear process along this part and only focus on the process along the longest part. It has undergone a different fabrication process in the end. This time, a positive resist has been involved as well as the FBMS technique (see 2.2.2 for more details). A 200 nm SiN hard mask was deposited for the final etching process step as the positive resist doesn't provide a protective mask as the HSQ does. After the etching process, another etching run has been performed to remove the SiN hard mask. It results in a 20 nm remaining SiN top layer on the InGaP waveguide as represented on the sketch of fig. 3.12(b). Furthermore, due to a too-small distance between two successive waveguides, an unequal width of the waveguide has been observed. Indeed, during the ebeam process and because the waveguides are close, there was a transmission of the electrons when one waveguide was patterned to the neighbouring waveguides. This leads to a variation of the width and a higher roughness on the sides. This can be seen in fig. 3.12(c) where the width of the waveguides according to the distance is plotted. Indeed, around the bending areas, two waveguides (a short and a long one) become close to each other. That's where the long waveguide starts being thinner. Also, because the chip has been bonded at a 45° degree angle according to the [001] axis of both InGaP and Si, the facets are sometimes crooked as can be seen in fig. 3.12(d).

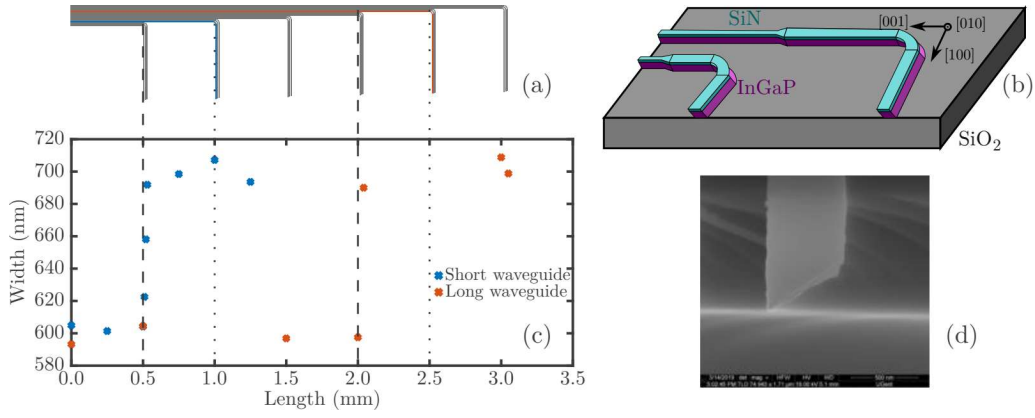


Figure 3.12: The theoretical GDS file represent in (a) as it should have been patterned. A representation of the chip is shown on (b) to see how it varies with the propagation. The real width of the waveguide according to the length is shown on (c). The concerned waveguides have been coloured on (a) to compare it with the curve. It is also shown with dashed lines where the width variation is. A scanning electron microscope (SEM) picture of a cleaved facet is also shown here (d)

To extract the linear losses from this chip, we applied the technique explained before with a lensed fibre at the input and one at the output. As we got different waveguide lengths available, it is possible to extract the coupling losses and propagation losses. However, it is more difficult to evaluate it accurately as the waveguide width is changing during the propagation and the roughness is quite random for each waveguide. The linear loss is thus higher in the thinner part of the waveguide, due to a higher roughness, and the linear loss is different from one waveguide to another due to the randomness of the issue during the patterning process here. It is not possible to use the same technique as before where a picture from the top of the waveguide is involved, as the SHG process occurs all along the waveguide. So, there is no part of the waveguide where there are only linear losses involved. To evaluate the losses in these waveguides, the usual technique of a lensed fibre at the input and another one at the output has been used. This way, we can evaluate the linear losses by assuming that the coupling and collecting sides have the same coupling loss. A source at the pump wavelength and another one at the SH wavelength have been used. We finally estimated the linear loss for the pump wavelength around 22 dB/cm while this value raised to 90 dB/cm at the SH wavelength and the insertion loss due to the lensed fibre is evaluated at 12 dB. The linear loss measured at the SH wavelength is probably underestimated as it has been measured for a fundamental mode at the SH wavelength while a higher-order mode is involved in the SHG process. It is still a good approximation to evaluate the effective nonlinearity of the process.

Now that the differences of each chip involved in the experiments have been exposed, let's take a closer look at the experimental setup used to study the SHG in these structures. It was the same for both chips and it is presented in fig. 3.13. It has however been adapted as the first chip has the output of the waveguide at the opposite side of the input one and the second chip has the output at 90° compared to the input of the waveguide.

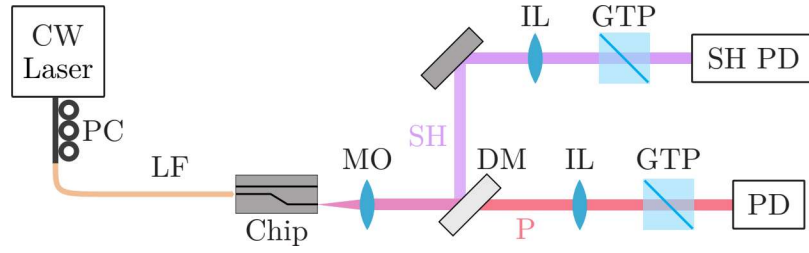


Figure 3.13: Experimental setup for the SHG process study. A continuous-wave (CW) laser goes through a polarization controller (PC) before being injected into the chip thanks to a lensed fibre (LF). The light is collected with a microscope objective (MO) before being split by a dichroic mirror (DM). Each wave goes through an imaging lens (L) and a Glan-Taylor polarizer (GTP). The power is finally measured by a dedicated photodiode (PD). [35]

With this setup, we can control the polarization of the incoming wave with a polarization controller. It allows exciting the desired fundamental pump mode in the structure that will induce the SHG process. The light is then injected inside the waveguide thanks to a lensed fibre and collected at the output by a high numerical aperture ($NA = 0.9$) microscope objective. The high numerical aperture allows us to collect a maximum of the light at the output of the waveguide. It has been chosen to efficiently collect the SH principally. This microscope objective is part of the imaging system put in place here. The microscope is a MPLFLN100xBDP from Olympus. It has been chosen for its high numerical aperture and a working distance of 1 mm. This working distance makes it comfortable to work with because of the space requirements of the mechanical parts. Its 1.8 mm focal length coupled to the 750 mm focal length imaging lens offers a total magnification of $G = f_{IL}/f_{MO} \approx 417$. The imaging lenses have been chosen as explained earlier to obtain an important magnification that will allow the mode profiles to be observed. The pump and SH waves are split after the microscope objective thanks to a dichroic mirror with a cutoff wavelength at 1000 nm. Both waves will then be measured on a dedicated photodiode after going through the imaging lens. The photodiode is an indium gallium arsenide photodiode for the pump as it is sensible to light with a wavelength between 800 and 1700 nm. To measure the SH, a silicon photodiode has been chosen as it can detect wavelengths in a range from 450 to 1020 nm. This last one has also been chosen as it can also detect power until -90 dBm, an important point as the SH power detected is low as we will see later in this thesis. Those photodiodes will be replaced by cameras to observe the profiles of the modes. The camera used to observe the SH is made of a silicon sensor for the same reasons as the chosen photodiode. For the pump, however, the camera is made of an indium gallium phosphide sensor, efficient in the short-wave infrared part of the light spectrum (from 700 to 2500 nm). Glan-Taylor polarizers, with an adapted coating according to the wavelength analyzed, have also been placed on the path of the waves to analyze the polarization of the outcoming waves as it is a clue on the nature of the mode measured.

3.3.3.1 Type I second harmonic generation

Concerning the first chip, the best result was observed in the 810 nm wide and 320 nm high waveguide. For this design, the PM wavelength was theoretically found at 1563.3 nm as can be seen in fig. 3.14(a) and occurs between the TE_{00} pump mode and the TM_{30} SH higher-order mode. The x component of the pump is symmetric along the x-axis, while the y and z components are antisymmetric along the x-axis. To get an overlap integral

between the pump and the SH modes different from zero along the $[001]$ axis of the crystal, the symmetry properties of the SH mode are restricted, as seen in section 3.3.2.1. The x component of the SH mode is symmetric while the y and z components are antisymmetric. Considering the numerically computed field components and a propagation along the $[001]$ axis, a nonlinear coefficient κ of $260i (\sqrt{W} \cdot m)^{-1}$ is expected.

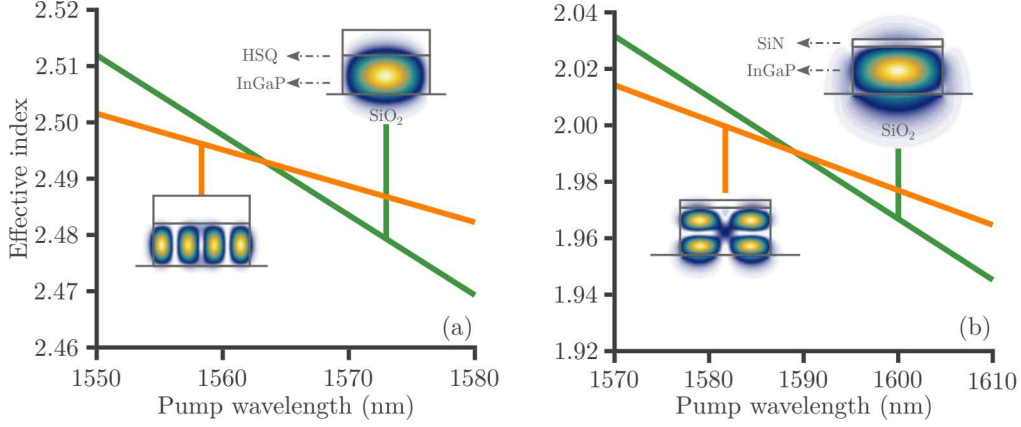


Figure 3.14: phase-matching in the type I PM case. The effective refractive index is shown for both the pump and the SH. The associated Poynting vector is also shown here. The figure on the left corresponds to the first chip while the second chip is associated with the one on the right.

At first, a wavelength sweep has been performed with the pump laser to find the PM wavelength. It has been found at 1550 nm as shown in the fig. 3.15(a). It was only observed, thanks to the camera put on top of the chip, along the $[001]$ axis of the crystal as it can be seen in fig. 3.15(b). We can also see some fast oscillations on the experimental results due to a Fabry-Perot effect. Indeed, the two facets of the waveguides act as mirrors in this case. The free spectral range (FSR) of those oscillations has been measured to be 75 pm which is equivalent to a 4.6 mm long waveguide. This result is compatible with the actual length of the waveguide measured to be 4.4 mm. We also observed, while performing a wavelength sweep, that the SH pattern was changing and took a shape close to the theory seen in part 1.1.1. It revealed some points of the SH power as a function of the wavelength measured as can be seen in fig. 3.15(b).

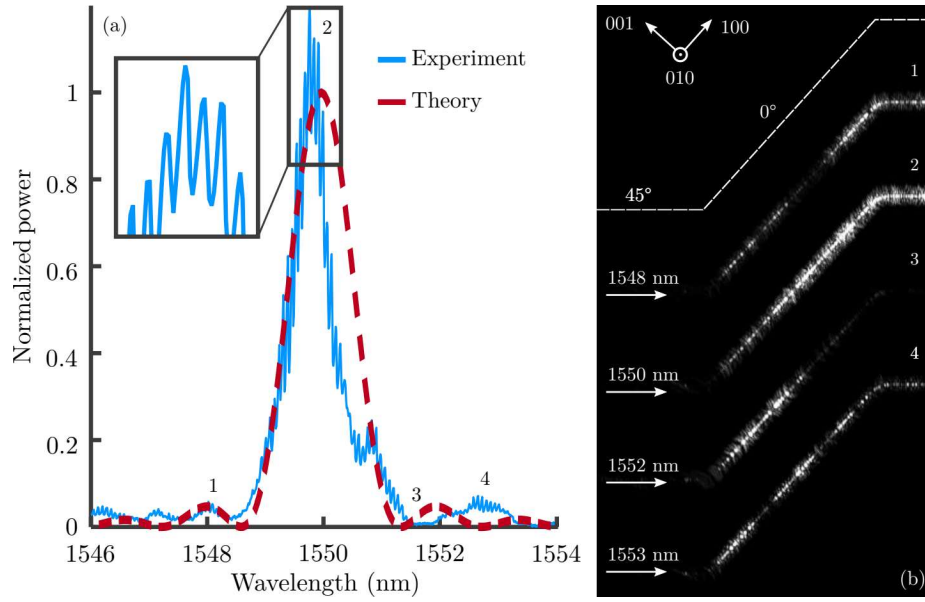


Figure 3.15: Normalized SH power as a function of the wavelength (a). The experimental results are represented here and superimposed to the theoretical results from equations 3.4 and top pictures of the illumination of the waveguides during the SHG process (b) for different input wavelengths as numbered in figure (a). Enlargement has been performed on a part of the sinc shape curve and can be seen in the inset to show the oscillations. [35]

Thanks to the eq. 3.4, we can determine the absolute square value of the nonlinear coefficient from the pump and SH power, the length and linear losses of the waveguide and the phase mismatch between the pump and the SH. The fact that we can only extract the absolute square value is the reason why we got the absolute value of the nonlinear coefficient. The measurements of the nonlinear coefficient are performed in the case of $\Delta\beta = 0$ as it is more convenient. The pump power used for this measurement is 2.5 mW while the SH power measured is in a range of 0.5 nW to 2 nW depending on the waveguide. The injection loss is estimated to be 12 dB while the collection loss has been neglected as a high numerical aperture (0.9) microscope objective is used. For the waveguide considered, the absolute value of the nonlinear coefficient measured in this waveguide is around $7.75 (\sqrt{\text{W}}.\text{m})^{-1}$, way lower than the theoretical absolute value of $260 (\sqrt{\text{W}}.\text{m})^{-1}$. On another hand, the fig. 3.15 shows that the width of the function linked to the wavelength sweep measured experimentally is in good agreement with the theory. On the other hand, the SH collection wasn't efficient enough to calculate a convincing conversion efficiency because of the angled facet (see fig. 3.12(d)). This last point added makes it a very difficult structure to efficiently study both the conversion efficiency and the SH mode profile.

The second chip has a different width from the first one. From this chip, we were able to extract results from two different waveguides. The first one is the shorter waveguide (0.4 mm long) of the two while the other one is 1.9 mm long. The waveguide profile used is a 600 nm wide waveguide now for the same height, 320 nm. With this width, a PM wavelength is theoretically found around 1590.0 nm between the mode TM_{00} at the pump wavelength and the TM_{11} mode at the SH wavelength as can be seen in fig. 3.14(b). The x component of the pump is antisymmetric along the x-axis, while the y and z components are symmetric along the x-axis. Concerning the TM_{11} SH mode, the x component is symmetric along the x-axis while the y and z components are antisymmetric along this same axis. This allows the overlap integral to be different from zero along the [001] crystallographic axis. A nonlinear coefficient of $57i (\sqrt{\text{W}}.\text{m})^{-1}$ is expected for a waveguide

along the [001] axis of the crystal for this couple of modes. As it was mentioned before, the width of these waveguides isn't constant during the propagation. The exact width and length has been measured and can be seen in fig. 3.12(c). As expected, the SHG process only occurs when the width of the waveguide is narrower. If we wanted to see the SHG process in the wider part of the same waveguide, we should have significantly increased the wavelength, which was not possible with the source used. On another side, the polarization of the SH has been measured and it reveals the predominance of the TM components. In the shorter waveguide, we measured the absolute value of the nonlinear coefficient to be $27 (\sqrt{W}.m)^{-1}$ which is lower than the theoretical value of $57i (\sqrt{W}.m)^{-1}$ but still of the same order of magnitude.

We then replaced the SH photodiode with a CCD camera to take benefits of the imaging system and try to measure the mode profile of the SH mode. The result is a bit deformed compared to the theoretical modes. Indeed, as can be seen in fig. 3.16, the aspect ratio seems different as it looks larger in height. Also, the separation between all the lobes is not clear. The aspect ratio deformation is the reason why we also performed a measurement of a fundamental mode at the SH wavelength with a suitable laser. We can see in fig. 3.16 that the aspect ratio for a fundamental mode is also different from the theoretical expectations. The waveguide being only 320 nm high, at the SH wavelength, it is not possible to have a satisfying resolution due to the circular aperture of our system. To be more explicit, we are working here with a microscope objective that has a numerical aperture of 0.9 as we already said before and a 1.8 mm focal length. This means that the effective aperture diameter of the microscope is 3.24 mm. With this equipment and for this process, the Airy disk will have a radius around 525 nm at the SH wavelength. We, therefore, understand that it is not that troublesome in the horizontal orientation as the waveguide is 600 nm wide, but it becomes a problem in the vertical orientation as it is only 320 nm high. Simulations of the imaging result that can be expected from our system with the modes considered in our measurements in fig. 3.16.

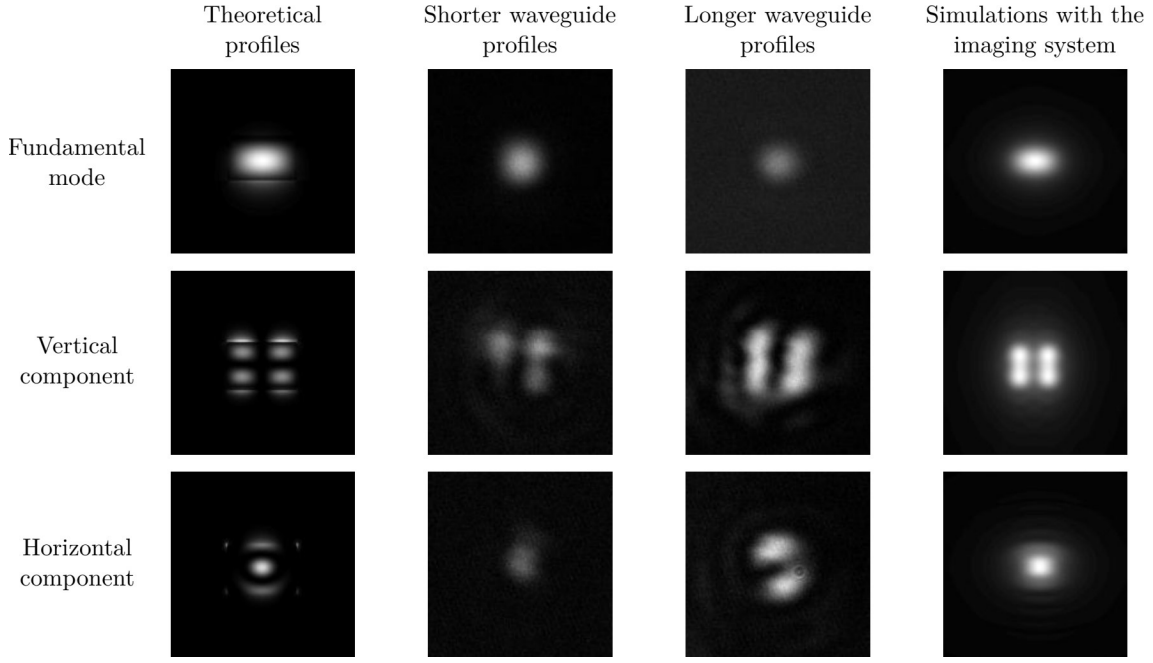


Figure 3.16: Pictures of the modes theoretically obtained from a mode solver (first column) for a fundamental mode, the E_y and E_x electric field components of the mode SH mode involved in the process in the second chip. The fundamental mode has been obtained thanks to a laser at the SH wavelength.

As we can see, the result obtained during the experiments is predictable when we take into consideration the resolution limit of the imaging system.

In the case of the longer waveguide, the absolute value of the nonlinear coefficient has been measured to be as high as $68 (\sqrt{W}.m)^{-1}$ for the same process. This value is, this time, a bit higher than the theoretical one but we are still in the same order of magnitude. It could be imputed to an overestimation of the linear losses for this waveguide as we already said that it was difficult to accurately define with those waveguides. The mode profile was also measured as can be seen in fig. 3.16, and the result for the vertical component is significantly close to the theoretical one knowing that we can't resolve perfectly the SH mode. All these results put together are really convincing proof of the necessity of the vectorial model around type I SHG in integrated structures. We have also shown some theoretical results around SHG especially around the PM with the different shapes of the light inside the waveguide (see fig. 3.15).

3.3.3.2 Type II second harmonic generation

We will now focus our study on the type II SHG process. The experiments for this specific case were only performed in the first chip presented. An 850 wide and 320 nm high waveguide is used so the PM aimed is among the most efficient conversion efficiency possible if we refer to fig. 3.7. It occurs between the TE_{00} and TM_{00} pump modes and the TM_{01} SH mode. The TE_{00} mode presents a symmetry of its x component along the x-axis while the y and z components are antisymmetric. The opposite goes for the TM_{00} mode as its x component is antisymmetric along the x-axis and the y and z components are symmetric. Therefore, to have an overlap integral different from zero, the SH mode needs to have a x component antisymmetric along the x-axis and both other components

symmetric. Which is a condition fulfilled by the TM_{01} mode as presented in section 3.3.2.2. In this case, the theoretical nonlinear coefficient is $\kappa_{12} = i3200 (\sqrt{W}.m)^{-1}$. As the height of our waveguide is a bit different from the point in the figure for the same width (325 nm), the PM wavelength expected for our structure is around 1536 nm as seen in fig. 3.17 instead of 1550 nm for the theoretical figure.

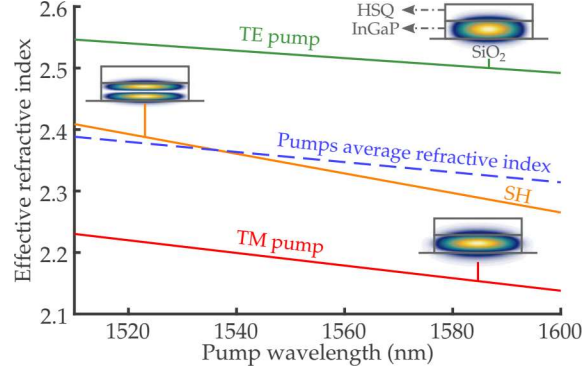


Figure 3.17: phase-matching in the type II PM case. The effective refractive index is shown for both pumps, the SH and the average of the pumps to better notice the PM point. The Poynting vector is also added to the associated wave. [31]

It has been measured that the maximum SH power is measured when the polarization of the pump is constituted of a TE and a TM component. The polarization axis of the Glan-Taylor polarizer is at 45° , a sign of a type II SHG process. To confirm that, a comparison of the SH power at the output of the waveguide for three polarization states of the pump is performed and the result can be seen in fig. 3.18. The pump power is equal to 25 mW for this experiment (which correspond to a pump power of 3.8 mW before the part of the waveguide along the [001] crystallographic axis). Concerning the SH power, it has been calculated to be equal to 2 μ W, in the optimal case, after the part of the waveguide along the [001]. We can see that, as expected, there is almost no SH power for a quasi-TE or quasi-TM pump and that it becomes way more efficient when the pump is in both states at the same time. A power sweep has also been performed as is shown by the inset of fig. 3.18. A slope of 2 with a logarithmic scale is measured, which is expected for this kind of process. The nonlinear coefficient, measured in the case of a phase mismatch between the pump and the SH equals 0, from this experiment is around $\kappa_{12} = 500 (\sqrt{W}.m)^{-1}$ which is lower than the theoretical value of $3200 (\sqrt{W}.m)^{-1}$ expected. This can be explained by higher linear losses than expected, as explained earlier. Indeed, the linear losses have a huge impact on the result as it has been shown with eq. 3.5. It could also be the result of an overestimated efficiency of the collection part of the setup than it is.

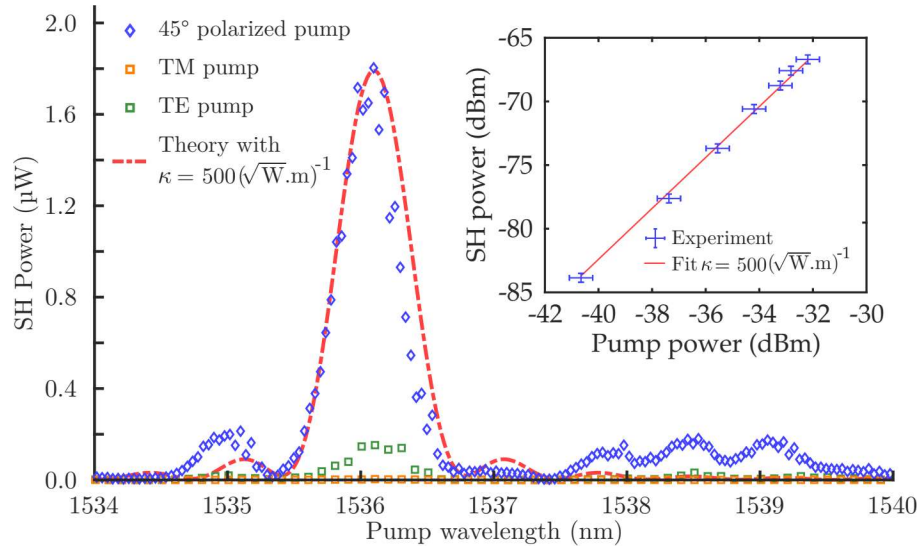


Figure 3.18: Representation of the SH power as a function of the wavelength for three different polarization states of the pump: quasi-TE, quasi-TM and an equal mix of both. The theoretical curve obtained from the expression 3.10 with a nonlinear coefficient of $500 (\sqrt{W.m})^{-1}$ has been added to the curve. The SH power as a function of the pump power in the case of a perfect PM is also shown in the inset and fit with eq. 3.11 for the same nonlinear coefficient. [31]

For this experiment, a measurement of the profile of the SH has also been tried. As discussed earlier, due to the limitations of the optical system, it seems impossible in the current configuration to see the SH mode present in fig.3.17. As there is only a visible zero along the y-axis of the waveguide, the lobes of the mode are not in the resolution domain. An attempt of an imagery measurement from both sides of the waveguide is made to see if it is nevertheless possible to extract any information from it. If we want to take a look at the mode profile from the taper, as discussed before, a mode conversion can occur. The overlapping point of the refractive indices can be seen in fig. 3.19.

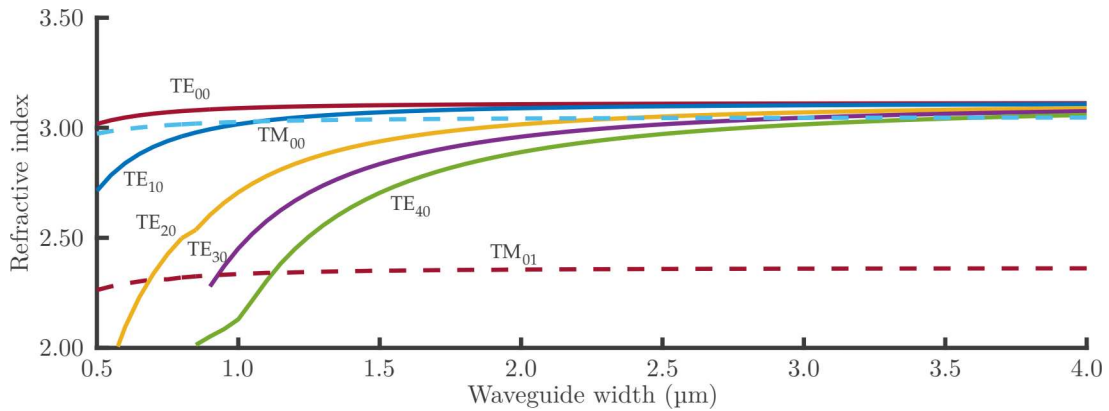


Figure 3.19: Refractive index for different modes as a function of the waveguide width at a 775 nm wavelength. Only seven modes have been represented here. The TM modes are represented in dashed lines while the TE modes are solid lines. The crossings between the TM_{01} mode and the others represent a possible transmission of energy from this one to other TE higher-order modes

This phenomenon is indeed observed during a measurement with the Si camera and cap-

tured as it is shown in fig. 3.20. The mode expected is completely different from the expected one and, from what we just saw, it seems clear that it has been converted from the expected mode to another one. While trying to observe the mode from the side without taper, it has been confirmed that the imaging was impossible as can be seen in fig. 3.20. The result observed can't confirm the SH mode from its profile.

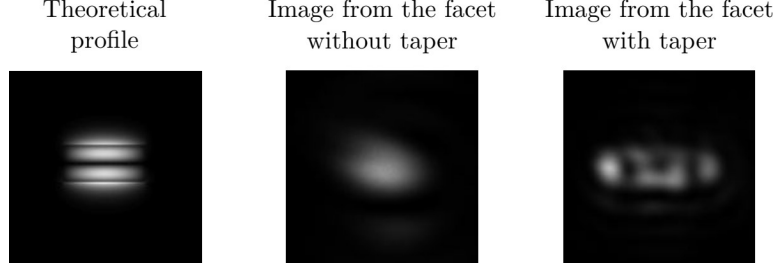


Figure 3.20: On the left, we can see the theoretical mode profile that is involved in the SHG process and found previously from the simulations. In the middle is a picture from a camera taken at the output of the waveguide without the taper. On the right is the same measure but from the tapered facet of the waveguide. The scale for this last picture has been divided by two for better visibility.

Even if this last measurement is not possible in the current configuration, the other results coupled tend to prove the theoretical expectations, except for the efficiency. As we said, the losses limit the conversion efficiency in our experiments. One way to check this is by applying equation 3.5 for the linear loss of chip 1 with the dimensions of our waveguide, we find an effective length equal to $700 \mu\text{m}$ for a 1.43 mm long waveguide. If we come back to the first experiment with the type I PM, the effective length for the shorter waveguide of 0.4 mm results in 0.29 mm while the longer one of 1.9 mm long results in an effective length of 0.46 mm . We thus cannot take advantage of the full potential of the waveguides used. It is quite clear that the linear losses are a big deal in these experiments. A better fabrication process could lead to fewer losses and will be better for this kind of experiment. The difference between the simulations and the theory could also be imputed to the uncertainty of the collection power at the output. As it is really sensitive to the facet at the output, a bad cleave, in this case, can lead to different results.

3.3.3.3 Summary of the results

To summarize the previous results obtained, we can compare them to the state of the art from 2.1.1. For easier comparison, the following table grouped the results. Two different efficiencies, usually found in the literature, have been reported here: the normalized conversion efficiency expressed in $\% / (\text{W} \cdot \text{cm}^2)$ and the conversion efficiency expressed in $\% / \text{W}$. They both have different physical meanings. The normalized conversion efficiency (equals to $|\kappa|^2$) represents the process efficiency (material potential and modes overlap), while the conversion efficiency (equals to P_{sh}/P_p^2) considers the waveguide properties (length and linear losses). This last one thus depends on the fabrication process quality.

Material	Phase-matching type	Pump wavelength (nm)	Normalized conversion efficiency (%/(W.cm ²))	Conversion efficiency (%/W)	Reference
AlGaAs	MPM (type I)	1560	1202	86.9	[10]
		1536	30	0.7	[5]
	MPM (type II)	1583	13.8	21.9	[4]
GaAs	MPM (type I)	2010	13000	250	[7]
		1968-1979	47000	4000	[8]
GaP	MPM (type I)	1270-1360	0.4	0.009	[9]
InGaP	MPM (type I)	1550	0.601	0.0015	This work
		1572	7.29	0.0063	
		1566	46.24	0.0968	
	MPM (type II)	1536	2500	12.28	
LiNbO3	MPM (type I)	1546	650	36	[11]
		1520-1580	41	0.37	[28]
PPLN	QPM	1510-1620	2600	416	[12]
		1530-1580	1900	17.73	[36]
		1540	4600	4.14	[37]

Table 3.1: Comparison of the conversion efficiency in nanowires for different materials.

In table 3.1, we can see that the efficiencies I obtained in this work are below what is already done concerning the type I phase-matching case. When it comes to the type II phase-matching case, the normalized conversion efficiency is larger than what is done in GaP, AlGaAs and LiNbO3. The result is also in the same order of magnitude as what is obtained in PPLN, a widely used material for SHG. The results are, however, an order of magnitude under current records obtained in GaAs, which is another III-V material. The bandgap of GaAs is, however, equal to 1.424 eV as we have seen in fig. 2.5. It is such that the SH wavelength has to be over 871 nm not to be absorbed by the material. That's why a pump wavelength of around 2 μm is used for GaAs [7, 8]. It means that GaAs is not suitable for telecom wavelength applications compared to the other materials in table 3.1.

As we have seen in our previous experiments, linear losses are a limiting factor. If we could get rid of these, it would significantly increase the conversion efficiency. Considering the type II case, which is the most efficient experiment performed in this chapter, the conversion efficiency would indeed rise to 51.12 %/W. Furthermore, we said that, in theory, we would expect a nonlinear coefficient equal to $3200 (\sqrt{\text{W.m}})^{-1}$. This value leads to a normalized conversion efficiency of $102400 \text{ \%}/(\text{W.cm}^2)$. In the case of our lossy, 1.43 mm long waveguide, it would lead to a conversion efficiency equal to 501.76 %/W. Moreover, in the perfect case of a lossless waveguide, the conversion efficiency becomes equal to $2093.98 (\sqrt{\text{W.m}})^{-1}$. In this perfect case, we are in the same order of magnitude than the actual record in GaAs [8]. As we said, the normalized conversion efficiency takes care of the material potential, and the modes overlap. InGaP material presents a high potential as it has a high second-order nonlinear susceptibility (110 pm/V for the record). In the end, the most important issue seems to come from the experimental overlap between the pump and the SH. Inhomogeneity of the dimensions could explain this issue. It is proof that a good fabrication process is required to increase conversion efficiency. We could also wonder what would be the conversion efficiency in the case of a better mode overlap than the ones we experimentally got. By this, I mean if the nonlinear

interaction occurs between fundamental (TE or TM) modes for both the pump and the SH. To do so, we need to ignore the PM condition for a while and just focus on the modes overlap. For this, we consider the dimensions of the waveguides used in the previous experiments. Concerning the first experiment in an 810 nm wide and 320 nm high waveguide, we calculated a theoretical normalized conversion efficiency along the [001] crystallographic axis equal to $676 \text{ \%}/(\text{W.cm}^2)$ at a 1563.3 nm wavelength. If we now consider an interaction between the TM_{00} pump mode and the TE_{00} SH mode, which is the most efficient interaction found, considering only fundamentals modes, at the same wavelength and along the same crystallographic axis, the normalized conversion efficiency drops to $56.73 \text{ \%}/(\text{W.cm}^2)$. If we propagate along the [101] crystallographic axis, however, we calculate a normalized conversion efficiency equal to $264072.65 \text{ \%}/(\text{W.cm}^2)$ between the TE_{00} pump mode and the TM_{00} SH mode. By applying the same methodology to the other waveguides dimensions, we find for the 600 nm wide and 320 nm high waveguide a conversion efficiency equal to $1274.49 \text{ \%}/(\text{W.cm}^2)$ for a TM_{00} pump mode and the TE_{00} SH mode along the [001] crystallographic axis at a 1590 nm wavelength. As a reminder, the theoretical normalized conversion efficiency for the previous experiment is $32.49 \text{ \%}/(\text{W.cm}^2)$. Along the [101] crystallographic axis, the normalized conversion efficiency is as high as $349043.46 \text{ \%}/(\text{W.cm}^2)$ between the TE_{00} pump mode and the TM_{00} SH mode. Concerning the type II PM case, the waveguide is 850 nm wide and 320 high. A PM was found at a 1536 nm wavelength between the TE_{00} and TM_{00} pump mode and the TM_{01} SH mode. The theoretical conversion efficiency for this interaction is equal to $102400 \text{ \%}/(\text{W.cm}^2)$ along the [001] crystallographic axis. Considering only fundamentals modes, the best conversion efficiency at this wavelength has been found between the TE_{00} and TM_{00} pump modes and the TM_{00} SH mode. In this case, the normalized conversion efficiency is equal to $23.41 \text{ \%}/(\text{W.cm}^2)$. Along the [101] crystallographic axis, however, the maximum normalized conversion efficiency has been calculated to be equal at $155946.01 \text{ \%}/(\text{W.cm}^2)$ between the TE_{00} and TM_{00} pump modes and the TE_{00} SH mode, which is the same order of magnitude as the theoretical normalized conversion efficiency considered in the previous experiment. We can thus note that, along the [001] crystallographic axis, the best-normalized conversion efficiency isn't necessarily for fundamental modes. This proves the impact of the longitudinal component as a better mode overlap doesn't lead to better normalized conversion efficiency. However, propagation along the [101] crystallographic offers a better normalized conversion efficiency with the fundamental modes. It could be explained by the components of the modes involved in the nonlinear overlap 3.14. By taking a closer look at the type II PM case, the modes used in our experiments result in a normalized conversion efficiency similar to the case with fundamental modes. It was indeed the most efficient interaction as shown in fig. 3.7.

We saw in this part the development of an analytical model to express SHG process in nanowires. We have been able to compare the two different PM cases with their operating method and efficiency. Type II has presented itself as the most efficient case here and also allows working with thicker structure which may be less restrictive regarding the fabrication process. We have tested these models through experiments. For instance, we measured the polarization of the modes, the SH power as a function of the wavelength as well as a function of the pump power and the mode profile in the type I case. The results obtained are really convincing and promising. It has also been explained that the most limiting aspect is the linear loss of the medium. With lower linear losses, we could be able to achieve more significant conversion efficiency.

We will now see another usage of another III-V material via a different project. It comes from a collaboration in which I participated as a manufacturer of the chips and also provides some simulations about SHG.

3.4 AlGaAs as a nonlinear platform

During my PhD, I worked on another project for the Technical University of Denmark (Danmarks Tekniske Universitet) (DTU). For this project, the light is first coupled, thanks to a grating coupler, inside a silicon nitride (SiN) waveguide. The light is then coupled to a III-V material (AlGaAs in this case) to benefit the nonlinear effects. We also first benefit from the low linear losses of the SiN at the beginning and better manufacturing processes of this material.

3.4.1 Properties

We already know from table 2.1 that AlGaAs as a nonlinear susceptibility $\chi^{(2)}$ equals 180 pm/V [2] which is close to the InGaP one (220 pm/V). Besides, we can see the refractive index as a function of the wavelength for this material in fig. 3.21 [38]. It also possesses a bandgap around 2 eV which makes it also insensitive to TPA at telecom wavelength. Furthermore, studies show that it is a very interesting material for third-order nonlinear experiments [39].

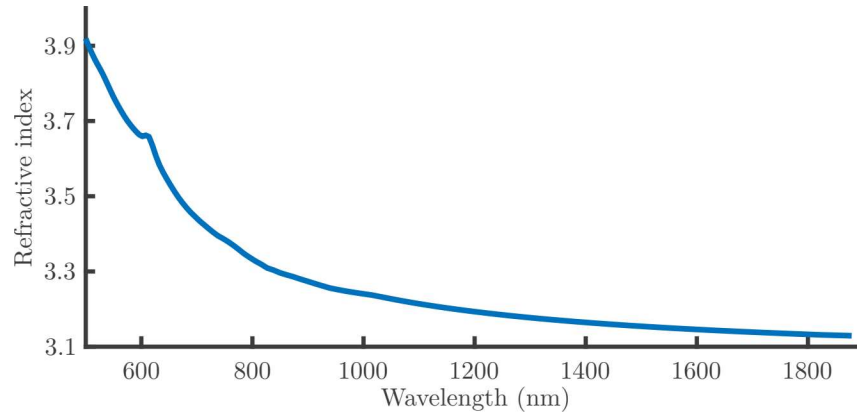


Figure 3.21: AlGaAs refractive index from the literature [38] as a function of the wavelength. The wavelength has been limited between 500 nm and 1900 nm for better visibility and because it is the range of interest for our experiments.

It is a material quite similar to the material that we've studied in the previous section, but the projects involved there are completely different in the first place. As a part of a collaboration with DTU, we have studied the feasibility and the efficiency of SHG process in their structure.

3.4.2 Fabrication process particularities

The fabrication process around AlGaAs is different from the last one because it involves more steps due to the particularity of the project that we discussed a bit earlier. In this case, we don't bond the III-V material on a blank substrate, but we have to bond it on an existing chip with already existing patterns. The first step therefore includes some processes on this chip to make it ready to host the AlGaAs. The part of the chip that we are interested in (in the orange rectangle in fig. 3.22) is composed of SiN straight waveguides (and spots) in which the light is injected thanks to grating couplers. The idea here is to first take advantage of the very low linear loss and nonlinear potential of the SiN [40–42] to inject the light and propagates and then use inverted tapers to couple the

light from the SiN waveguide to the III-V material bonded on top of the SiN waveguide and patterned as wanted [43]. This way, we take advantage of the nonlinearity of the III-V material and are less restricted by the linear loss of it. For this to be efficient, the distance between both waveguides needs to be small. As we can see in figure 3.23, the SiO₂ layer on top of the SiN is quite thick. So, the first thing to do is to reduce the SiO₂ layer for a good energy transfer. To do so, a RIE machine is used with an O₂ and SF₆ recipe to reduce this layer up to approximately 500 nm. The recipe being well known in Ghent university cleanroom, the etch rate to know how long the sample can be left inside the machine is 300 nm/min.

Then, we need to open the markers on the chip (shown by green rectangles in fig. 3.22). This means that we locally remove the SiO₂ on top of these markers. This needs to be done early for the last patterning step. At the very end of the process, the III-V material that we deposit will have to be patterned at specific places and these markers are references for the ebeam machine. For the machine to be able to perceive them, we have to open them as the layer on top of them can be too thick and thus shift the alignment of the III-V patterning.

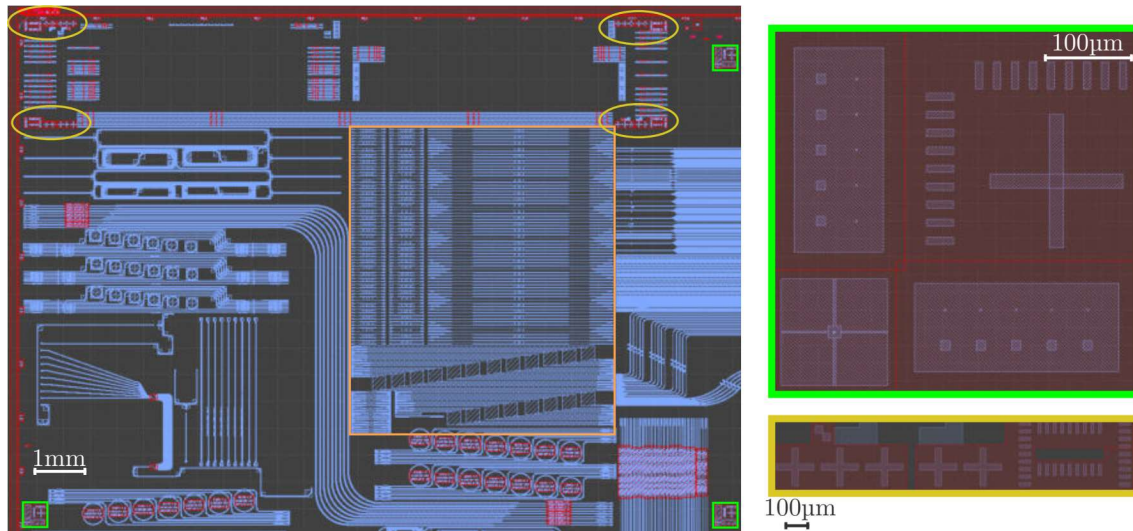


Figure 3.22: GDS file of the SiN chip used for the project. It shows the region of interest for the bonding of the III-V in orange, the UV markers in green and the ebeam markers in yellow.

As it is the same material that hides the markers as the first removed one and which is still present in lower proportion, we need to protect the rest of the chip to only process on the markers. To do so, we use the UV lithography process, as seen in 2.2.2, with a custom mask specific to the SiN chip. Once it has been performed, a hydrofluoric acid (HF) solution is used to remove the SiO₂. The etching process will be followed at different times thanks to a profilometer to be sure to etch the correct amount of SiO₂. The markers finally opened, we then need to bond the III-V material on top of this chip. We will apply the bonding process already developed in the 2.2.1 part but skip the deposition of SiO₂ on the III-V material as several tests performed at DTU have shown that it is not required. The adhesive solution is composed of BCB and mesitylene in the proportion 1:8 to have a 50 nm final layer of BCB between the chip and the III-V material. Once the bonding is performed, we have to perform the substrate removal step. This part of the process is the most critical here. The AlGaAs layer is attacked on the side

Once the bonding is done and promising, the chips are sent to DTU for the patterning and etching part of the chip. The structure finished, we took a look at possible SHG PM with the structures designed by the DTU team.

3.4.3 Simulations

In this section, we will see the simulations performed for the structure in AlGaAs. There are three particularities to take into account in this case. The first one is that, due to the grating coupler used for the injection, it is only possible to couple the fundamental TE pump inside the structure. We thus limit our simulations to this mode. The second point to take into account is the possibility to bury the AlGaAs structure. Both cases are thus taken into account: when there is no cladding around the AlGaAs layer and when there is a SiO_2 cladding as it can be seen in fig. 3.25(a)-(b). Finally, the third thing to keep in mind is that to take advantage of all the places available, sometimes the structure is not on top of SiN but, on top of SiO_2 as represented in fig. 3.25(c)-(d). The coupling region of the III-V is still on top of SiN but the main structure is not necessarily. It doesn't change anything for the fabrication process, it's just more structure in another place than the first targeted one to increase the number of structures available in the end.

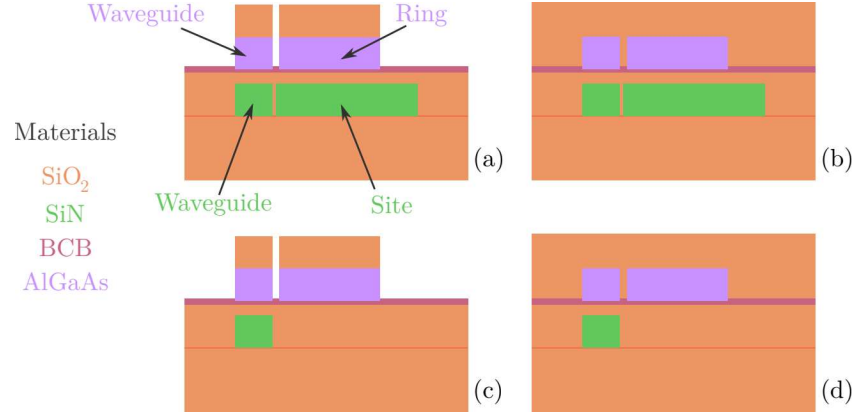


Figure 3.25: Representation of the four configurations possible for the simulations with AlGaAs. There is the case with SiN under the AlGaAs ring, where no SiO_2 has been deposited after the dry etching process (a), the top layer of SiO_2 is due to the use of HSQ for the ebeam lithography process. There is the case where some SiO_2 has been deposited and the structure is now buried (b). There are also the cases where SiO_2 is under the AlGaAs ring, where the structure is not buried (c) and where it is buried (d).

The simulations have been performed for a wavelength from 1500 nm to 1600 nm, following the possibilities of the grating coupler which also act as a filter. All the results of the simulations as explained there are reported inside table 3.2.

Configuration	Width (nm)	phase-matching wavelength (nm)	κ $(\sqrt{W}.\text{m})^{-1}$
SiN under and SiO ₂ cladding	400	/	/
	450	1543.38	-0.6 139.9
	500	1566.74 1588.46	-91.99 51.81
	550	1552.00 1583.11	42.13 67.75
	600	1530.00 1594.50	36.94 -53.69
SiN under and SiO ₂ on top only	400	/	/
	450	1545.85	-1.26i
	500	1583.29	-98.84
	550	1572.30 1597.54	63.07 63.57
	600	1501.99 1540.69	-16.63 50.84
SiO ₂ under and SiO ₂ cladding	400	1500.00 1514.42	-3+2.5i 114.88
	450	1545.76	-0.21 65.75
	500	1568.98 1591.37	42.68 -13.46
	550	1553.40 1585.21	12.66 31.13
	600	1530.00 1596.49	26.30 24.52
SiO ₂ under and SiO ₂ on top only	400	1526.52 1536.07	-0.88i -268.59
	450	1549.24 1565.67	146.5 -0.51
	500	1586.52	-99.33
	550	1574.36	-28.52
	600	1502.60 1541.78	-16.76 26.69

Table 3.2: Phase-matching wavelength and efficiency for different widths and in the four configurations possible for the project analysed

We can see there that there is some interesting PM possible to achieve in these structures. For instance, the 400 nm wide waveguide with SiO₂ on top and under is fascinating as it appears to be efficient and at a wavelength that is easily reachable by common lasers. The results have been communicated, and the study is still under process at DTU.

In this chapter, we studied in detail the SHG effects in nanowires waveguides and confirmed the theoretical models developed by experiments. The results obtained are showing a good agreement with the theory and are very encouraging in the understanding and the development of efficient SHG in III-V structures. We showed, in particular, the need to use a vectorial definition of the electric fields for such a process in strongly confined waveguides. The observation of the modes profiles and their comparison with

the theoretical ones, the SH power measured for a pump wavelength and power are all evidence supporting the models here. We also noticed the burden that is linear losses in our experiments and, with further engineering and fabrication development, a stronger conversion efficiency could be obtained. On this point, another way to increase significantly the conversion is to use another kind of integrated structure: the ring resonator. It is with this objective in mind and a better understanding of the physic behind the process that the following studies have been done.

Bibliography

1. Fiore, A., Berger, V., Rosencher, E., Bravetti, P. & Nagle, J. Phase matching using an isotropic nonlinear optical material. en. *Nature* **391**, 463–466. ISSN: 0028-0836, 1476-4687. <http://www.nature.com/articles/35091> (2021) (Jan. 1998).
2. Scaccabarozzi, L. *et al.* Enhanced second-harmonic generation in AlGaAs/Al_xO_y tightly confining waveguides and resonant cavities. en. *Optics Letters* **31**, 3626. ISSN: 0146-9592, 1539-4794. <https://www.osapublishing.org/abstract.cfm?URI=ol-31-24-3626> (2021) (Dec. 2006).
3. Yu, X., Scaccabarozzi, L., Harris Jr., J. S., Kuo, P. S. & Fejer, M. M. Efficient continuous wave second harmonic generation pumped at 1.55 μm in quasi-phase-matched AlGaAs waveguides. en. *Optics Express* **13**, 10742. ISSN: 1094-4087. <https://www.osapublishing.org/oe/abstract.cfm?uri=oe-13-26-10742> (2021) (2005).
4. Duchesne, D. *et al.* Second harmonic generation in AlGaAs photonic wires using low power continuous wave light. en. *Optics Express* **19**, 12408. ISSN: 1094-4087. <https://www.osapublishing.org/oe/abstract.cfm?uri=oe-19-13-12408> (2020) (June 2011).
5. Ducci, S. *et al.* Continuous-wave second-harmonic generation in modal phase matched semiconductor waveguides. en. *Applied Physics Letters* **84**, 2974–2976. ISSN: 0003-6951, 1077-3118. <http://aip.scitation.org/doi/10.1063/1.1703847> (2021) (Apr. 2004).
6. Rao, S. V., Moutzouris, K. & Ebrahimzadeh, M. Nonlinear frequency conversion in semiconductor optical waveguides using birefringent, modal and quasi-phase-matching techniques. en. *Journal of Optics A: Pure and Applied Optics* **6**, 569–584. ISSN: 1464-4258, 1741-3567. <https://iopscience.iop.org/article/10.1088/1464-4258/6/6/013> (2021) (June 2004).
7. Chang, L. *et al.* Heterogeneously Integrated GaAs Waveguides on Insulator for Efficient Frequency Conversion. en. *Laser & Photonics Reviews* **12**, 1800149. ISSN: 18638880. <http://doi.wiley.com/10.1002/lpor.201800149> (2020) (Oct. 2018).
8. Stanton, E. J. *et al.* Efficient second harmonic generation in nanophotonic GaAs-on-insulator waveguides. en. *Optics Express* **28**, 9521. ISSN: 1094-4087. <https://www.osapublishing.org/abstract.cfm?URI=oe-28-7-9521> (2020) (Mar. 2020).
9. Anthur, A. P. *et al.* Second harmonic generation in gallium phosphide nano-waveguides. en. *Optics Express* **29**, 10307. ISSN: 1094-4087. <https://www.osapublishing.org/abstract.cfm?URI=oe-29-7-10307> (2021) (Mar. 2021).
10. May, S., Kues, M., Clerici, M. & Sorel, M. Second-harmonic generation in AlGaAs-on-insulator waveguides. en. *Optics Letters* **44**, 1339. ISSN: 0146-9592, 1539-4794. <https://www.osapublishing.org/abstract.cfm?URI=ol-44-6-1339> (2020) (Mar. 2019).

11. Luo, R., He, Y., Liang, H., Li, M. & Lin, Q. Semi-Nonlinear Nanophotonic Waveguides for Highly Efficient Second-Harmonic Generation. en. *Laser & Photonics Reviews* **13**, 1800288. ISSN: 18638880. <http://doi.wiley.com/10.1002/lpor.201800288> (2021) (Mar. 2019).
12. Wang, C. *et al.* Ultrahigh-efficiency wavelength conversion in nanophotonic periodically poled lithium niobate waveguides. en. *Optica*, 4 (Nov. 2018).
13. Takamoto, T., Ikeda, E., Kurita, H. & Ohmori, M. Over 30% efficient InGaP/GaAs tandem solar cells. en. *Applied Physics Letters* **70**, 381–383. ISSN: 0003-6951, 1077-3118. <http://aip.scitation.org/doi/10.1063/1.118419> (2021) (Jan. 1997).
14. Meijer, A., Huijbregts, M. A. J., Schermer, J. J. & Reijnders, L. Life-cycle assessment of photovoltaic modules: Comparison of mc-Si, InGaP and InGaP/mc-Si solar modules. en. *Progress in Photovoltaics: Research and Applications* **11**, 275–287. ISSN: 1062-7995, 1099-159X. <http://doi.wiley.com/10.1002/pip.489> (2021) (June 2003).
15. Svensson, C. P. T. *et al.* Monolithic GaAs/InGaP nanowire light emitting diodes on silicon. en. *Nanotechnology* **19**, 305201. ISSN: 0957-4484, 1361-6528. <https://iopscience.iop.org/article/10.1088/0957-4484/19/30/305201> (2021) (July 2008).
16. Ferrini, R. *et al.* Optical functions of InGaP/GaAs epitaxial layers from 0.01 to 5.5 eV. en. *The European Physical Journal B - Condensed Matter* **27**. Number: 4 Reporter: The European Physical Journal B - Condensed Matter, 449–458. ISSN: 1434-6028, 1434-6036. <http://www.springerlink.com/openurl.asp?genre=article&id=doi:10.1140/epjb/e2002-00177-x> (2019) (June 2002).
17. Schinke, C. *et al.* Uncertainty analysis for the coefficient of band-to-band absorption of crystalline silicon. en. *AIP Advances* **5**, 067168. ISSN: 2158-3226. <http://aip.scitation.org/doi/10.1063/1.4923379> (2021) (June 2015).
18. Ueno, Y., Ricci, V. & Stegeman, G. I. Second-order susceptibility of Ga_{0.5}In_{0.5}P crystals at 1.5 μ m and their feasibility for waveguide quasi-phase matching. en. *Journal of the Optical Society of America B*, 9 (1997).
19. Moriarty, G. *et al.* Optical and structural properties of InGaP heterostructures. en. *Thin Solid Films* **364**, 244–248. ISSN: 00406090. <https://linkinghub.elsevier.com/retrieve/pii/S0040609099008949> (2021) (Mar. 2000).
20. Ernst, P. *et al.* Band-gap reduction and valence-band splitting of ordered GaInP₂. en. *Applied Physics Letters* **67**, 2347–2349. ISSN: 0003-6951, 1077-3118. <http://aip.scitation.org/doi/10.1063/1.114340> (2021) (Oct. 1995).
21. Boes, A. *et al.* Improved second harmonic performance in periodically poled LNOI waveguides through engineering of lateral leakage. en. *Optics Express* **27**, 23919. ISSN: 1094-4087. <https://www.osapublishing.org/abstract.cfm?URI=oe-27-17-23919> (2020) (Aug. 2019).
22. Miller, R. C. & Savage, A. Temperature dependence of the optical properties of ferroelectric LiNbO₃ and LiTaO₃. en. *Applied Physics Letters* **9**, 169–171. ISSN: 0003-6951, 1077-3118. <http://aip.scitation.org/doi/10.1063/1.1754695> (2021) (Aug. 1966).
23. Shoji, I., Kondo, T., Kitamoto, A., Shirane, M. & Ito, R. Absolute scale of second-order nonlinear-optical coefficients. en. *Journal of the Optical Society of America B* **14**, 2268. ISSN: 0740-3224, 1520-8540. <https://www.osapublishing.org/abstract.cfm?URI=josab-14-9-2268> (2021) (Sept. 1997).

24. Wilson, D. J. *et al.* Integrated gallium phosphide nonlinear photonics. en. *Nature Photonics* **14**, arXiv: 1808.03554, 57–62. ISSN: 1749-4885, 1749-4893. <http://arxiv.org/abs/1808.03554> (2020) (Jan. 2020).
25. Tran, M. *et al.* Ultra-Low-Loss Silicon Waveguides for Heterogeneously Integrated Silicon/III-V Photonics. en. *Applied Sciences* **8**, 1139. ISSN: 2076-3417. <http://www.mdpi.com/2076-3417/8/7/1139> (2021) (July 2018).
26. Snyder, A. W. & Love, J. *Optical Waveguide Theory* en. ISBN: 978-1-4613-2813-1 (Chapman and Hall, Nov. 1983).
27. Ciret, C. *et al.* Influence of longitudinal mode components on second harmonic generation in III-V-on-insulator nanowires. en. *Optics Express* **28**, 31584. ISSN: 1094-4087. <https://www.osapublishing.org/abstract.cfm?URI=oe-28-21-31584> (2020) (Oct. 2020).
28. Wang, C. *et al.* Second harmonic generation in nano-structured thin-film lithium niobate waveguides. en. *Optics Express* **25**, 6963. ISSN: 1094-4087. <https://www.osapublishing.org/abstract.cfm?URI=oe-25-6-6963> (2020) (Mar. 2017).
29. Afshar V., S. & Monro, T. M. A full vectorial model for pulse propagation in emerging waveguides with subwavelength structures part I: Kerr nonlinearity. en. *Optics Express* **17**, 2298. ISSN: 1094-4087. <https://www.osapublishing.org/oe/abstract.cfm?uri=oe-17-4-2298> (2020) (Feb. 2009).
30. Agrawal, G. P. *Nonlinear fiber optics* Fifth edition. en. ISBN: 978-0-12-397023-7 (Elsevier/Academic Press, Amsterdam, 2013).
31. Poulvellarie, N. *et al.* Efficient type II second harmonic generation in an indium gallium phosphide on insulator wire waveguide aligned with a crystallographic axis. en. *Optics Letters* **46**, 1490. ISSN: 0146-9592, 1539-4794. <https://www.osapublishing.org/abstract.cfm?URI=ol-46-6-1490> (2021) (Mar. 2021).
32. Gallacher, K. *et al.* Ultra-broadband mid-infrared Ge-on-Si waveguide polarization rotator. en. *APL Photonics*, 9 (2020).
33. Vermeulen, D. *et al.* *Efficient Tapering to the Fundamental Quasi-TM Mode in Asymmetrical Waveguides* en. in (2010), 2.
34. Grigorescu, A., van der Krogt, M., Hagen, C. & Kruit, P. 10nm lines and spaces written in HSQ, using electron beam lithography. en. *Microelectronic Engineering* **84**, 822–824. ISSN: 01679317. <https://linkinghub.elsevier.com/retrieve/pii/S0167931707000408> (2021) (May 2007).
35. Poulvellarie, N. *et al.* Second-harmonic generation enabled by longitudinal electric-field components in photonic wire waveguides. en. *Physical Review A* **102**, 023521. ISSN: 2469-9926, 2469-9934. <https://link.aps.org/doi/10.1103/PhysRevA.102.023521> (2020) (Aug. 2020).
36. Chen, J.-Y. *et al.* Efficient and highly tunable second-harmonic generation in Z-cut periodically poled lithium niobate nanowaveguides. en. *Optics Letters* **45**, 3789. ISSN: 0146-9592, 1539-4794. <https://www.osapublishing.org/abstract.cfm?URI=ol-45-13-3789> (2021) (July 2020).
37. Rao, A. *et al.* Actively-monitored periodic-poling in thin-film lithium niobate photonic waveguides with ultrahigh nonlinear conversion efficiency of $4600\% \text{W}^{-1} \text{cm}^{-2}$. en. *Optics Express* **27**, 25920. ISSN: 1094-4087. <https://www.osapublishing.org/abstract.cfm?URI=oe-27-18-25920> (2021) (Sept. 2019).

38. Papatryfonos, K. *et al.* Refractive indices of MBE-grown $\text{Al}_x\text{Ga}_{(1-x)}\text{As}$ ternary alloys in the transparent wavelength region. en. *AIP Advances* **11**, 025327. ISSN: 2158-3226. <https://aip.scitation.org/doi/10.1063/5.0039631> (2021) (Feb. 2021).
39. Pu, M., Ottaviano, L., Semenova, E. & Yvind, K. Efficient frequency comb generation in AlGaAs-on-insulator. en. *Optica*, 4 (Aug. 2016).
40. Baets, R. *et al.* *Silicon Photonics: silicon nitride versus silicon-on-insulator* en. in *Optical Fiber Communication Conference* (OSA, Anaheim, California, 2016), Th3J.1. ISBN: 978-1-943580-07-1. <https://www.osapublishing.org/abstract.cfm?URI=OFC-2016-Th3J.1> (2021).
41. Shaw, M. J., Guo, J., Vawter, G. A., Habermehl, S. & Sullivan, C. T. Fabrication techniques for low-loss silicon nitride waveguides. en. *Journal of the Optical Society of America B* (eds Johnson, E. G., Nordin, G. P. & Suleski, T. J.) 109. <http://proceedings.spiedigitallibrary.org/proceeding.aspx?doi=10.1117/12.588828> (2021) (Jan. 2005).
42. Okawachi, Y. *et al.* Octave-spanning frequency comb generation in a silicon nitride chip. en. *Optics Letters* **36**, 3398. ISSN: 0146-9592, 1539-4794. <https://www.osapublishing.org/abstract.cfm?URI=ol-36-17-3398> (2021) (Sept. 2011).
43. Pu, M., Liu, L., Ou, H., Yvind, K. & Hvam, J. M. Ultra-low-loss inverted taper coupler for silicon-on-insulator ridge waveguide. en. *Optics Communications* **283**, 3678–3682. ISSN: 00304018. <https://linkinghub.elsevier.com/retrieve/pii/S0030401810005018> (2021) (Oct. 2010).

Chapter 4

Second harmonic generation in III-V nanorings

The principle behind a resonator is that a light wave travelling inside will be resonant if its optical path length is equal to a whole number of its wavelength. If this condition is respected, it will result in a wave propagating in the resonator. Resonators can exist in different forms. One of the most common forms is the bulk-optical resonator. It is indeed the basics of lasers [1–4].

The emergence of integrated photonics has also brought resonators to its panel of elements. Microring resonators are elements that can be used to act like a wavelength filter [5, 6] and are a great asset in the integrated photonics world [7]. They are useful in different applications such as modulators [8], lasers [9] or chemical sensors [10] to name just a few. In this chapter, we are going to see why and how we can use ring resonators for SHG with III-V materials.

To do so, a brief explanation of the fundamentals of ring resonators and how we can use them in the context of SHG will be presented. We will then put this topic in the particular case of III-V materials.

Then, we will focus on a III-V material that has not been presented yet: GaP. We will use its relevant properties in numerical simulations thanks to the theory defined.

Finally, experimental results obtained from a GaP platform results will be presented.

4.1 Nanorings theory

In this part, we will start to see the general theory about nanorings to better understand them and the experimental results presented later. Then, the focus will be on the second-order nonlinear effects in such a structure and, finally, we will apply this theory to III-V material to see how it reacts in such particular geometry.

4.1.1 Nanorings fundamentals

A ring resonator is an element that is known for its filtering abilities. It is first defined by a FSR which is the spectral spacing between two successive resonances and that is linked to its physical parameters and properties of the medium. Indeed, the FSR of a ring resonator is expressed as:

$$FSR_\nu = \frac{c}{n_g L}, \quad (4.1)$$

where c is the light velocity in the void, n_g is the group index of the mode propagating inside the ring and L is the circumference of the ring equal to $2\pi R$ with R the ring radius of the ring. It can be expressed via the wavelength instead, as $FSR_\lambda = \frac{\lambda^2}{n_g L}$ with λ the central wavelength.

To inject the light inside the ring, different systems exist (prism and tapered fibre for instance). Here, we focus on an injection via what is called a bus waveguide. The bus waveguide is put at a certain distance, called a gap, from the ring and the light is coupled inside the ring by following the coupled modes' theory [11]. From this model, different parameters are defined as can be seen in fig. 4.1(a). In the classical case of such a structure, we define three parameters which are the transmitted electric field from the bus waveguide (ring) [12] to the ring (bus) by the coefficient k . The part of the electric field that isn't transmitted inside the ring (bus) and that will continue in the same waveguide is symbolized by r . By definition, we have $r^2 + k^2 = 1$. These parameters are in a direct link to the coupling length between the bus waveguide and the ring and the gap between those two. Finally, we need to take into account the losses of the medium via a parameter which is expressed as $a^2 = \exp(-\alpha L)$ where α is the power linear attenuation expressed in m^{-1} and L is the length of the medium considered.

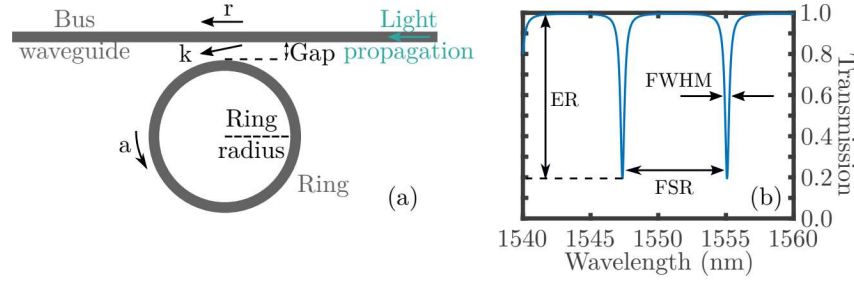


Figure 4.1: Sketch of a ring resonator with the different parameters represent (a) as well as an example of the transmission as a function of the wavelength (b). The parameters for this example are $a = 0.96$; $r = 0.9$ and $n_g = 3.3$ for a $15 \mu\text{m}$ ring radius.

We can thus define the transmission function of the system with these parameters as:

$$T = \frac{a^2 - 2ra \cos \phi + r^2}{1 - 2ar \cos \phi + (ar)^2}, \quad (4.2)$$

where $\phi = \beta L$ with β the propagation constant equal to $\frac{2n_g\pi}{\lambda}$ and λ the wavelength. We can so plot the transmission function of the ring as can be seen in fig 4.1(b). Apart from the FSR parameter already defined, we can note in this figure the extinction ratio (ER) of the function and also the full width at half maximum (FWHM) value. This last one is a good indication of the properties of the ring experimentally speaking. Indeed, during our experiments, we will be able to obtain the transmission function and so find the ring parameters. To do so, we will use the expression of the FWHM in this case, which is:

$$FWHM = \frac{(1 - ra)\lambda_{\text{resonance}}}{\pi n_g L \sqrt{ra}},$$

where $\lambda_{\text{resonance}}$ is the wavelength for which a resonance is measurable in the fig. 4.1(b). As we can extract the group index of the material from the FSR, the only unknown parameters in this last equation are r and a . These parameters can be extracted experimentally by fitting a resonance with a Lorentzian function [12].

In the case of ring resonators, we also use the finesse and the quality factor to define a ring. The finesse is defined as the ratio of the FSR with the FWHM while the quality factor Q is equal to the resonant wavelength divided by the FWHM. The physical meanings of these parameters are to represent the number of round-trips that the electric field will perform before being lost by the attenuation of the medium or coupled to the bus waveguide.

We tried here to give a summary of the main properties of a ring resonator. It is an important element in optical telecommunications [13, 14] and much more [11]. They are also widely used in the context of nonlinear photonics [15–17].

The filtering particularity of ring resonators has also been coupled to nonlinear properties and their ability to create new frequencies. As an example, third-order nonlinear effects for instance are widely used for supercontinuum generation [18, 19]. As a ring resonator is known for its filtering abilities, we understand that coupling nonlinear effects and ring resonators together could lead to what we call an OFC [20–22]. OFC is a hot topic nowadays due to its high impact in a lot of fields [23]. We will now go deeper in the context of second-order nonlinear properties to see how the SHG process is occurring in such structures.

4.1.2 SHG in III-V nanorings

In this part, we will see the theoretical development of the SHG process in nanorings. We will see it from a global perspective of the process in nanorings and then see how it applies to the case of III-V materials that we are interested in. To keep the same approach as the SHG in wire waveguides, we will first express the variations of the SH electric field as a function of the pump and other useful parameters.

We first denote the temporal part of the electric fields as $A_{k,n}(t) = a_k(t) \exp(i\omega_n t)$ where n is either the pump (p) or the SH (sh), a_k is the complex amplitude of the mode normalized such that $|a_k|^2$ is carrying the energy of the mode that pulsates at ω_n . In such a case, we can define the coupled temporal equations that link the pump and the SH amplitudes like this [24]:

$$\begin{aligned} \frac{da_p}{dt} &= \left(i\omega_p - \frac{1}{\tau_p} \right) a_p + i\omega_1 \beta_1 a_p^* a_{sh} + \sqrt{\frac{2}{\tau_{e,p}}} s_p^+, \\ \frac{da_{sh}}{dt} &= \left(i\omega_{sh} - \frac{1}{\tau_{sh}} \right) a_{sh} + i\omega_2 \beta_2 a_p^2, \end{aligned} \quad (4.3)$$

in which ω_p (ω_{sh}) is the pump (SH) pulsation, $1/\tau_p$ ($1/\tau_{sh}$) represents the sum of the pump (SH) decay rate to the bus waveguide $1/\tau_{e,p}$ ($1/\tau_{e,sh}$) with the intrinsic decay $1/\tau_{i,p}$ ($1/\tau_{i,sh}$) (linked to the absorption). Finally, s_p^+ represents the time-dependent amplitude of the pump from the bus waveguide to the ring normalized, such as $|s^+|^2$ is carrying the mode power. We can also define s_k^- , which is the amplitude coupled from the waveguide to the bus waveguide and is equal to a_k/τ_k . A representation is shown in fig. 4.2.

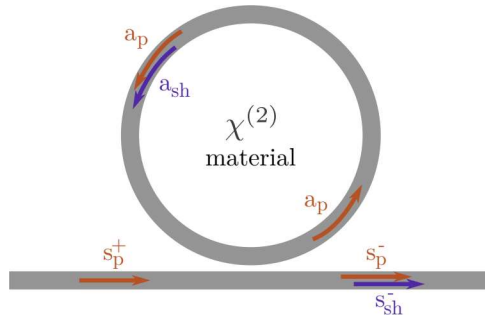


Figure 4.2: Representation of the electric fields in the structure for the SHG model developed

The key parameters of this model are the nonlinear coefficients β_1 and β_2 between the pump and SH modes. The coefficient for the SH is defined as [25]:

$$\beta_2 = \frac{1}{4} \frac{\int \sum_{ijk} \epsilon_0 \chi_{ijk}^{(2)} [E_{pi}(E_{shj}^* E_{pk} + E_{pj} E_{shk}^*)] dx dy}{(\int \epsilon_p |E_p|^2 d\mathbf{r}) (\int \epsilon_{sh} |E_{sh}|^2 dx dy)^{1/2}}, \quad (4.4)$$

where ϵ_p and ϵ_{sh} are respectively the permittivity of the material at the pump and the SH wavelength. We only define β_2 here as it is related to β_1 via the conservation of energy $\omega_p \beta_1 = \omega_{sh} \beta_2^*$.

Moreover, since our structure in which the SHG occurs as a cylindrical symmetry, it is interesting to write the equation 4.4 in a cylindrical frame as represented in fig. 4.3.

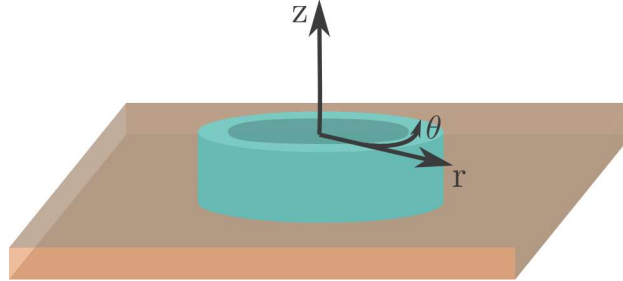


Figure 4.3: Representation of a ring resonator in a cylindrical coordinate system

As a reminder, the modes components expression to switch from the Cartesian frame to a cylindrical one is as follows:

$$\begin{aligned} E_x &= E_r \cos \theta - E_\theta \sin \theta, \\ E_y &= E_r \sin \theta + E_\theta \cos \theta, \\ E_z &= E_z. \end{aligned}$$

We thus find the following expression for the nonlinear coefficient [26]:

$$\begin{aligned}
\beta_2 &= \int_0^{2\pi} \beta^+ \exp[i(2m_p - m_{sh} + 2)\theta] + \beta^- \exp[i(2m_p - m_{sh} - 2)\theta] d\theta, \\
\beta^\pm &= \frac{1}{4} \left(\frac{\int \epsilon_0 \chi_{ijk}^{(2)} (2[E_{pr} E_{p\theta} E_{shz}^* + E_{pz} (E_{p\theta} E_{shr}^* + E_{pr} E_{sh\theta}^*)]) r dr dz}{(\int \epsilon_p |E_p|^2 r dr dz) (\int \epsilon_{sh} |E_{sh}|^2 r dr dz)^{1/2}} \right. \\
&\quad \left. \pm i \frac{\int \epsilon_0 \chi_{ijk}^{(2)} [(E_{pr}^2 - E_{p\theta}^2) E_{shz}^* + 2(E_{pr} E_{shr}^* - E_{p\theta} E_{sh\theta}^*) E_{pz}] r dr dz}{(\int \epsilon_p |E_p|^2 r dr dz) (\int \epsilon_{sh} |E_{sh}|^2 r dr dz)^{1/2}} \right). \tag{4.5}
\end{aligned}$$

From the equations above, we can see that the conversion is maximized when the QPM condition $\Delta m = 2m_p - m_{sh} = \pm 2$ with $m_p = 2n_p\pi/(\lambda_p R)$ (where n_p is the refractive index of the pump and R the ring radius) the azimuthal number of the pump and m_{sh} the azimuthal number of the SH. This differs from the wire waveguides case, for which only one PM wavelength can be found for a couple of pump and SH modes. Let's note that each QPM point is associated with an individual efficiency, and thus for the same couple of modes.

Moreover, we can see that, if we want to generate a SH in a ring resonator, we should not achieve phase matching in this case. Indeed, the condition required being $\Delta m = \pm 2$, it is a different kind of process called quasi-phase matching that has to be achieved here [27].

We have already seen some theory around QPM in 1.1.1. It is a common method that has a lot of success. For instance, experiments have been performed in $LiNbO_3$, by polling of the material to achieve the QPM conditions [28, 29]. When it comes to, III-V materials it's however quite easier. In fact, due to the symmetry of these materials that we already discussed before, we can remember that a 90° rotation of the crystal leads to a total inversion of the crystal. This means that the effective nonlinear susceptibility becomes the opposite when the crystal is 90° rotated as represented in fig. 4.4.

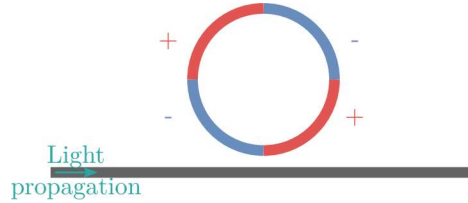


Figure 4.4: Representation of the inversion of the crystal symmetry that occurs in the case of a III-V microring resonator

We can therefore understand that this naturally leads to the fulfilment of the QPM condition. So, the SHG effect should be present at the condition that the azimuthal numbers equality $\Delta m = \pm 2$ is fulfilled.

Finally, it is possible to express the SH harmonic power at the output with the non-linear overlap from 4.5 and the characteristics of the ring [30]:

$$P_{sh} = \frac{1}{\omega_p \epsilon_0^3} |\beta_2|^2 P_p^2 \frac{Q_p^4 Q_{sh}^2}{Q_{c,p}^2 Q_{c,sh}}, \tag{4.6}$$

for which Q_k is the loaded quality factor, as seen in 4.1.1, of the mode $k = p, sh$ and $Q_{c,k}$ is the external coupling quality factor. We can define the loaded quality factor as dependent on the external coupling quality factor and the intrinsic quality factor $1/Q_k = 1/Q_{i,k} + 1/Q_{c,k}$. The different quality factors are linked to the previous decay rates as

$Q_{i,k} = \omega_k \tau_{i,k}/2$ and $Q_{c,k} = \omega_k \tau_{c,k}/2$. Furthermore, we can see that we can express a conversion efficiency coefficient in W^{-1} that depends on the coupled of modes interacting and that is defined as $|\beta_2|^2/\omega_p \epsilon_0^3$.

We have seen how we can express the SH and pump electric field in a microresonator and the coupling factor that linked them. This allows us to determine the efficiency of the SH and to have an analytical expression of the SH power expected for a given couple of modes. We have also seen how the parameters of the ring are important for such a process and so is the fabrication process. To experimentally test these models, the choice has been on GaP as we will see in what follows.

4.2 GaP as a platform

Gallium phosphide, a recently emerged material in this field, has already offered some nice results in nonlinear photonics [31–34] and deserves some attention. It is a material similar to InGaP concerning the crystal symmetry but still different in other aspects. We will see there how this material can also be a good platform for nonlinear integrated photonics.

4.2.1 Properties of GaP

In this section, we will develop the properties of GaP and put it into perspective with the previous material already studied. We will mainly focus on the relevant comparison points considering our context. First, let's take a look at the refractive index of this material shown in fig. 4.5.

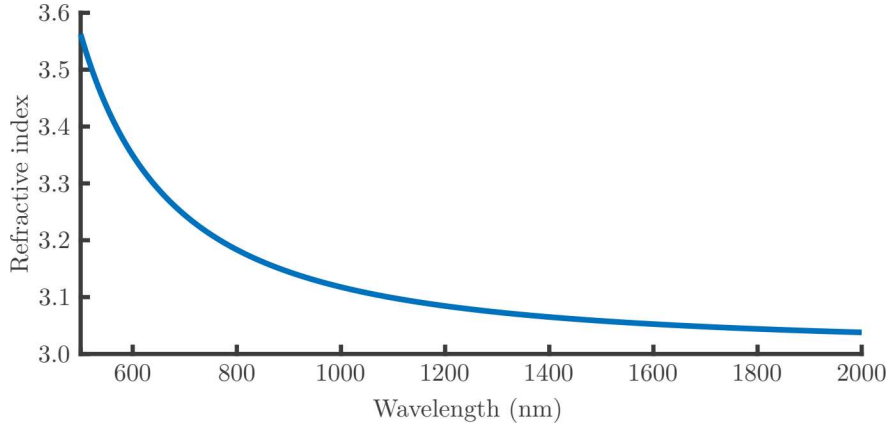


Figure 4.5: Refractive index of the GaP material. It has been limited to the 500 nm to 2000 nm range for better visibility and because it is our range of interest.

At first sight, it is in the same range of refractive index as the two previous III-V materials that are InGaP and AlGaAs in the 600 nm to 2000 nm range. Meaning that it presents the same advantages concerning the strong confinement due to the high refractive index contrast. GaP material as a bandgap which is equal to 2.24 eV [35] which still means that there is no TPA at telecom wavelength as it corresponds to a 553.5 nm wavelength.

We have just seen that the linear properties of GaP are similar to the ones of InGaP. We are now going to take a look at the nonlinear properties of this material, see if it's a good alternative for the experiments that we are trying to achieve. The second-order nonlinear susceptibility $\chi^{(2)}$ has been measured to be as high as 200 pm/V [36]. Which is in close range of the one measured for InGaP (220 pm/V as a reminder). Concerning the

third-order nonlinearities, as we have already noticed in table 2.2, the potential of GaP is also similar to its InGaP cousin.

All of these elements put together mean that GaP is a good alternative to InGaP for the kind of process that we are interested in. Furthermore, we can manage to develop the whole fabrication process (from the transfer printing to the final dry etching) in Ghent cleanroom. Concerning InGaP, the last step of dry etching had to be performed in the laboratoire de photonique et de nanostructures (LPN) group in Paris. The independence of the manufacturing process was an asset at some point. Also, some recent works have shown that GaP can exhibit very low linear losses [37]. Something that we didn't manage to obtain with InGaP for the moment. So this makes it even more interesting for experiments.

4.2.2 Simulations

In this part, we're going to use the refractive index from the previous part to perform structures simulations. To do so, we designed on Lumerical software a rectangular profile with varying width and 300 nm high structure. This height corresponds to an available GaP wafer that can be used for fabrication processes. The structures used will also be fabricated using the transfer printing technique, as presented in 2.2.1. For this reason, a ring radius of 15 μm has been taken into account as it corresponds to the maximum ring radius that we can reach via the stamp from the transfer printing machine. The ring radius has to be taken into account as it will change the profile of the mode propagating as can be seen in fig. 4.6. This curving could lead to a non-zero overlap as it will break the symmetry of the mode inside the nonlinear structure.

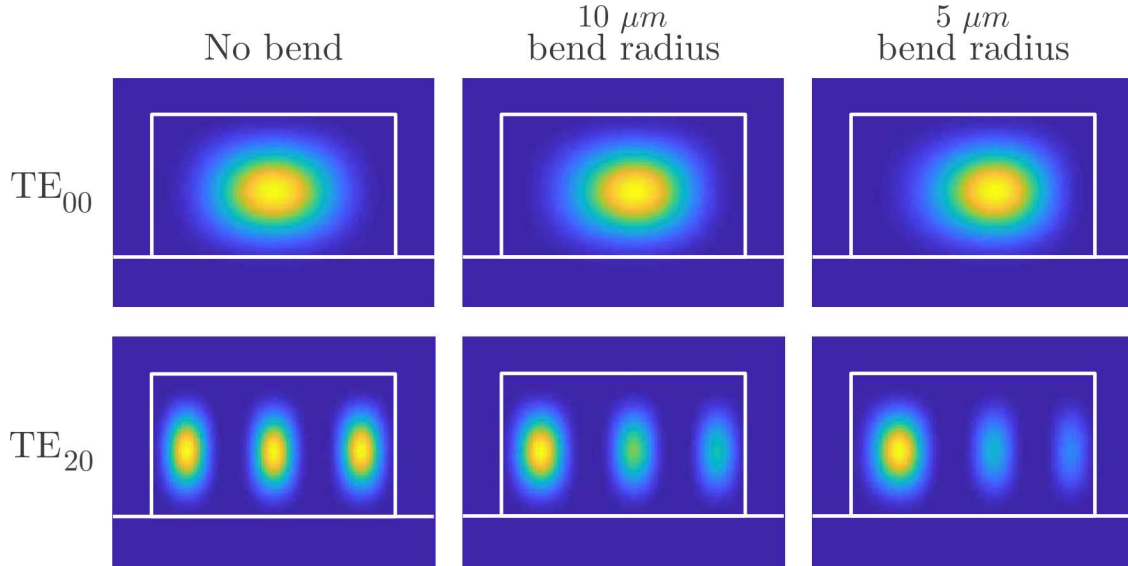


Figure 4.6: Pictures of the mode asymmetry engendered by the curve of the ring for three different ring radius (0, 5 and 10 μm) with the centre on the left of the waveguide. The TE₀₀ mode is for a 1550 nm wavelength while the TE₂₀ mode is for a 775 nm wavelength.

In this figure, we can see that the energy tends to shift on a side of the waveguide due to the bending. The modes, showing two symmetry axes along the waveguide axis without bending, are then not symmetrical to the horizontal axis as soon as a bending occurs. The results found during the simulations are reported in table 4.1. The research has been performed for a TE₀₀ pump and a wavelength range for which the grating couplers designs

are already known.

Width (nm)	SH mode	Pump wavelength for $\Delta m = -2$	Conversion efficiency ($\times 10^{-18}(W^{-1})$)	Pump wavelength for $\Delta m = 2$	Conversion efficiency ($\times 10^{-18}(W^{-1})$)
500	/	/	/	/	/
600	/	/	/	/	/
700	/	/	/	/	/
800	TE ₀₁	1603.44	125.34	/	/
	TM ₃₀	1454.00	747.40	1497.78	893.40
900	TE ₃₀	1581.13	0.17	1635.11	9.20
	TM ₃₀	1570.21	690.75	1634.11	658.38
	TE ₀₁	1531.98	38.27	1594.21	170.68
1000	TE ₀₁	1507.71	1.55	1570.21	1.20
1100	TE ₀₁	1488.97	4.21	1548.81	3.97
	TE ₄₀	1470.74	0.06	1514.78	0.10
	TM ₄₀	/	/	1483.97	24.80
1200	TE ₄₀	1581.13	0.12	1638.11	0.15
	TM ₄₀	1517.78	29.19	1570.21	31.42
	TE ₀₁	1478.29	0.38	1527.98	0.24
1300	TM ₄₀	1588.21	29.94	1645.00	31.64
	TE ₀₁	1468.74	1.44	1524.98	1.49
1400	TE ₅₀	1495.28	0.03	1542.32	0.03
	TE ₀₁	1467.74	4.23	1519.38	3.86
	TM ₅₀	/	/	1478.89	24.29
1500	TE ₅₀	1581.13	0.03	1639.11	0.03
	TM ₅₀	1494.78	24.34	1545.31	27.74
	TE ₀₁	1462.31	0.05	1514.78	0.00
1600	TM ₅₀	1545.81	22.83	1603.44	26.00
	TE ₀₁	1462.31	0.70	1513.78	0.67
	TE ₆₀	/	/	1478.29	0.02
1700	TM ₅₀	/	/	1595.21	22.18
	TE ₆₀	1499.78	0.02	1553.81	0.03
	TE ₀₁	1462.31	1.75	1511.71	1.75
1800	TE ₆₀	1570.21	0.03	1634.11	0.03
	TM ₆₀	1468.74	13.16	1520.78	14.28
	TE ₀₁	1458.31	0.20	1507.71	0.28
1900	TM ₆₀	1506.71	12.42	1562.43	13.60
	TE ₀₁	1460.31	0.34	1509.71	0.36
	TE ₇₀	/	/	1487.97	0.01
2000	TM ₆₀	1542.32	10.71	1604.94	11.82
	TE ₇₀	1490.97	0.02	1548.81	0.02
	TE ₀₁	1460.81	0.72	1510.71	0.80

Table 4.1: Results of the QPM found for structures with a different width. The simulations have been performed for a wavelength between 1450 and 1650 nm to keep the results in a range that can be reached by the lasers in our laboratory.

The results, shown in table 4.1, reveal one particular mode that is more efficient than the others and is available for structures that are 800 nm or 900 nm wide. Indeed, the

TM₃₀ SH mode shows itself as the most efficient one with the restrictions that we put in place. This SHG from the TE₀₀ pump mode to the TM₃₀ SH mode has already shown some good results [30] but there are still things to learn about the generation process. For a more interesting result, a waveguide width of 850 nm has been chosen. With this, the two QPM expected wavelengths are 1505.9 and 1555.15 nm as it is shown in fig. 4.7. This makes those easier to reach with standard lasers.

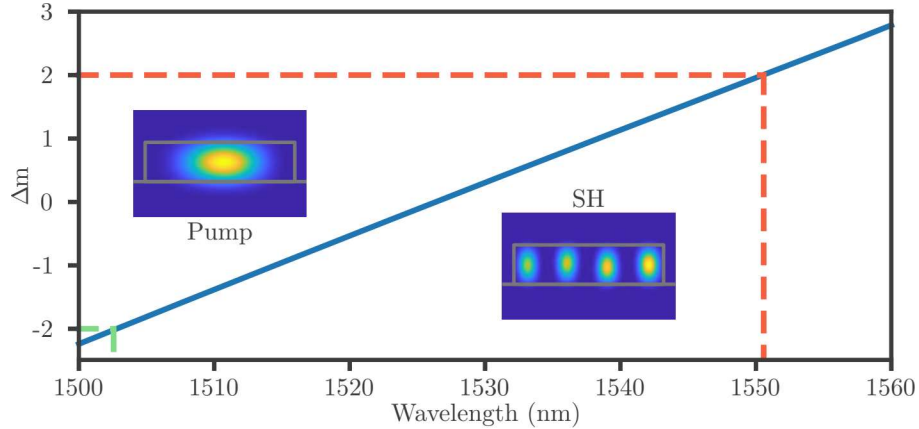


Figure 4.7: Difference of azimuthal number between the pump and the SH for an 850 nm wide and 300 nm high ring and 15 μ m radius. The azimuthal number values of -2 and 2 are highlighted there with a green and red dashed line respectively. The Poynting vector of the pump and SH modes are also shown.

Another QPM has also been found at 1566.12 nm with the TE₀₁ SH mode. Nevertheless, this last one is a third less efficient than the TM₃₀ one, but still efficient and interesting to measure.

The problem that we can expect here is that it would be difficult to have both QPM wavelengths fit with the resonances of the ring. However, increasing the ring radius reduces the FSR. We are, however, limited in the sample size (and so the FSR). The fabrication process is transfer printing for the rings, the sample size cannot exceed the stamp size (as seen in section 2.2.1.3). Here, the stamp is 1 mm long and 60 μ m wide. We thus limited ourselves to a 15 μ m ring radius. To fit a resonance of the ring with a QPM wavelength, a solution would be to change the working temperature to shift the resonances of the ring and find a suitable temperature to fit a resonance with a QPM wavelength.

Simulations have been performed here and interesting QPM have been found for reasonable structure dimensions. Experimental results will thus be presented in the following part of this chapter.

4.2.3 Experimental results

We will focus now on the experimental results obtained in the case of SHG in nanorings. At first, we are going to note the differences in structures and approach compared to the first experiments in rib waveguides.

The rings that have been used for these experiments have been fabricated thanks to the transfer printing technique (see section 2.2.1.3 for more details). This time, the injection is accomplished thanks to a grating coupler as can be seen in fig. 4.8(a). There are several advantages to this kind of device. As a first example, it acts as a polarization filter as it

can be designed to mainly let go through the waveguide a certain polarization [38]. This will help to solve the problem from an injection by the facet with a lensed fibre where the polarization state can only be known at the output. On another hand, it is also a bigger structure that makes it easier to align with a fibre compared to a direct approach of the facet with a lensed fibre. Indeed, the grating coupler can be several hundred square micrometre areas, which is much bigger than a waveguide that is usually only a few square micrometre area only. However, if it allows us to get rid of the cleave issues like the ones we had in the previous part 3.3, it is also not possible to measure the profiles of the modes with these structures as we did before. Furthermore, grating couplers are also wavelength dependent and so act as a frequency filter [38]. It has a certain bandwidth that depends on the manufacturing parameters. The centre wavelength of the transmission spectrum can nevertheless be shifted by a few nanometres according to the angle of the fibre as shown in fig 4.9.

The complete setup involved in these experiments is quite different from earlier as can be seen in fig. 4.8(b). We can see that a temperature controller system has been added to the setup in this case. It has been required here as a variation of the temperature can allow shifting the resonance of the ring as it can be seen on the fig. 4.11. This is favourable in such experiments as it can allow us to make the pump resonance fit with the QPM wavelength. This will enhance the nonlinear effects and so a higher SH conversion efficiency.

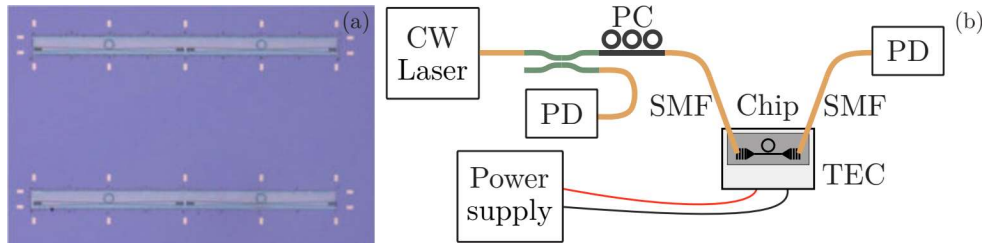


Figure 4.8: (a) Microscope picture of some GaP rings where we can see the grating couplers, the bus waveguide and the rings. (b) Experimental setup of the SHG process in nanoresonators. A continuous-wave (CW) laser goes through a 95/5 coupler before a polarization controller (PC). It is then injected into the chip thanks to a single-mode fibre (SMF) and grating couplers on the chip. The light is collected with another single-mode fibre. The power is finally measured by a dedicated photodiode (PD). The temperature of the chip is set thanks to a thermoelectric cooler (TEC) alimented with a power supply.

The setup here, as the first one, keep the possibility to control the polarization of the pump injected inside the structure. It will be tuned to maximize the transmission thanks to the photodiode at the output. With the grating couplers properties, we're almost certain that the TE_{00} mode will be the one propagating inside the structure. The amount of power sent in is checked thanks to a 95/5 coupler, placed before the polarization controller, and a photodiode connected at the 5 % output of the coupler.

The chip is placed on a thermoelectric cooler which is connected to a power supply. It is two thermoelectric coolers placed on top of each other to be allowed to reach hotter temperatures while heating the chip. We, however, need to be careful about the temperature that we set. As the sample is surrounded by air, there will be condensation on the chip if we set a temperature too low. It would lead to higher losses due to the absorption of water. Some tests have been made and we observed condensation below 13 °C so we will be careful not to set a temperature lower than this limit. We will also limit ourselves to a temperature of 60°C as it can cause some perturbations due to air convection between

the chip and the fibre for a too high temperature. This being said, we put our chip in place for the first experiments.

4.2.3.1 Impact of the chip temperature and the angle of the optical fibre for the injection

The first chip to be used in this experiment was composed of two different waveguides widths: 500 and 1000 nm. Concerning the narrower ones, no QPM was found in a suitable wavelength range as we've seen before in 4.1. For the wider one, a single SH mode that presents a QPM has been found between the TE_{00} pump mode and the TE_{01} SH mode. The values of the azimuthal number where the SHG process is expected is when it is equal to -2 or 2 as seen before. In this structure, it has been found during the simulations that the azimuthal number mismatch is equal to -2 when the wavelength is equal to 1507.71 nm and equal to 2 when the wavelength is 1570.21 nm.

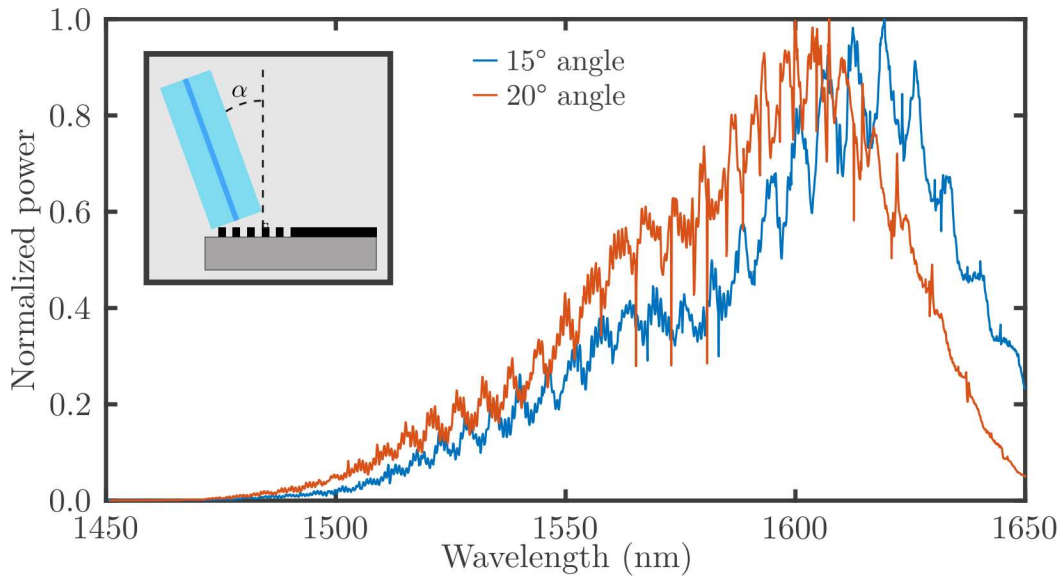


Figure 4.9: Normalized power transmitted through the structure as a function of the wavelength in the case of two different angles of the fibre used for the injection, as represented in the inset.

We first aimed for the second wavelength as a transmission scan performed with a fibre tilted at 20 ° revealed that the grating coupler let this wavelength pass while the lower wavelength wasn't as can be seen in fig 4.9. The FSR was first measured to confirm the propagation of a TE_{00} mode inside the structure. A FSR equal to 7.72 nm has been measured, as shown in fig. 4.10. From the theoretical values, we have expected a FSR of 7.69 nm. This confirms that it is indeed the TE_{00} mode that is propagating inside the ring.

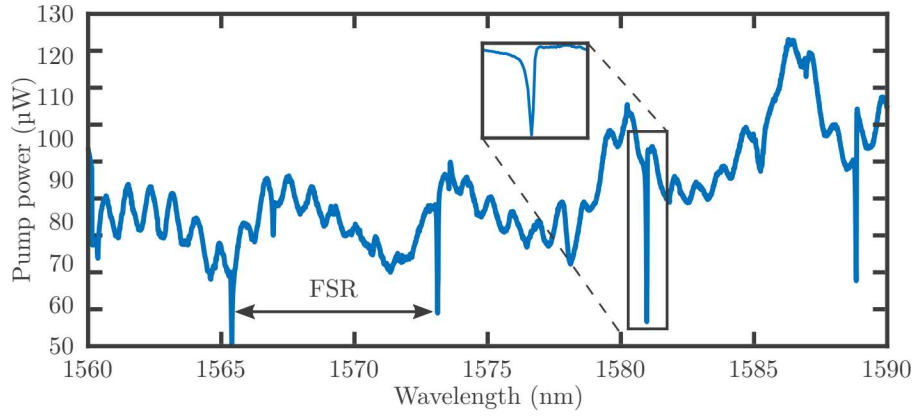


Figure 4.10: Measurement of the resonance for a 15 μm ring radius with a 1000 nm wide and 300 high waveguide profile.

We can also remark some fast oscillation with a FSR of 820 pm. This is actually due to a Fabry-Perot effect of the waveguide. Indeed, the group index of the mode is 3.38 according to the simulations. This lead to a calculated length of 442 μm which is close to the 460 μm long theoretical length of the waveguide. From a camera sensitive to the visible light that is used for the alignment, the SH was observed for a pump wavelength at 1573.49 nm. Although the grating coupler at the output is not designed to collect the SH, we still gave it a try. Fortunately, we were able to collect some SH power from the grating. To improve the SH power, we thus settled the temperature thanks to the thermoelectric cooler to shift the resonance at the same wavelength as the SHG occurs as seen in fig. 4.11(a) and (b).

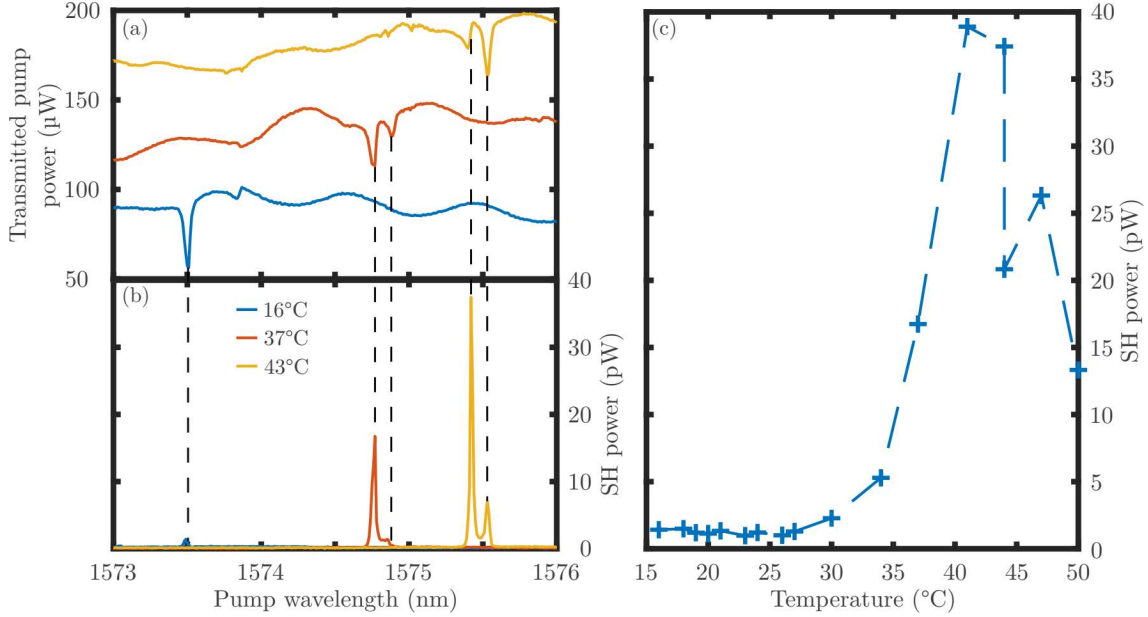


Figure 4.11: Measurement of the resonance in the ring for different temperatures (a) compared with the SH power measured for the same parameters (b). We can also see the maximum SH power measured for different temperatures (c).

We can notice in fig. 4.11(b) and (c) that the SH power increases with the temperature until a certain value and then decreases. This shows that we are indeed shifting the

resonance to make it match with the QPM wavelength value, which is also drifting due to the temperature modification. It also proves that, even if the QPM wavelength shifts under the temperature modification, the resonance shift is more important than the QPM wavelength shift. It can be explained as the FSR depends on the group index while the QPM wavelength depends on the effective index. As both vary differently with the temperature, the shift in wavelength as a function of the temperature is different for each of them.

We can also notice that there is a double resonance in fig. 4.11(a) which is unexpected as it doesn't match with the FSR of the studied mode. It is a resonance of the TM_{00} mode as it can be measured from the other peaks highlighted in fig. 4.11(a). The FSR measured there is equal to 6.61 nm which is in agreement with the theoretical value of 6.84 nm calculated for this mode. The fact that the peak becomes deeper with the temperature is because there is a transfer of energy from the TE_{00} to the TM_{00} as has already been observed [39]. It happens when there is a coupling between modes as a parameter (here the group index induced by the temperature modification).

For the second part of the experiment, the second QPM point was the goal. However, this point is for a wavelength around 1507.71 nm. But, as we said, the grating couplers act like a wavelength filter. Unfortunately, we are not able to reach this wavelength in such a case as can be seen in fig. 4.9. To be able to reach this wavelength, we need to increase the angle of the fibre. As for now, we were working with a fibre at a 20° angle. We can increase this angle (so bring the fibre closer to a horizontal position as the lab floor as a reference) to reach this position. Unfortunately, even if the transmission properties of the grating was shifted around the wanted wavelength for an angle of 37° , the lower coupling in the structure and the low conversion efficiency of this modes combination didn't allow us to observe the second QPM point.

In the meantime, a second chip designed for higher conversion efficiency, as found during the simulations, has been fabricated. This chip, specifically designed for the study of SHG in nanorings was thus put in place instead of the other.

4.2.3.2 Multimodal transmission and thermal effects

On this new chip, as said in the simulation part, the waveguide is 850 nm wide and possesses a 250 nm gap between the bus waveguide and the ring (R1). We expect the conversion efficiency to be much higher in this case. For a first measurement, the fibre has been put at a 10° angle. First measurements have been performed to find the QPM point at the higher wavelength (1555.15 nm). A wavelength sweep around the expected QPM has been performed, and the transmission obtained can be seen in fig. 4.12.

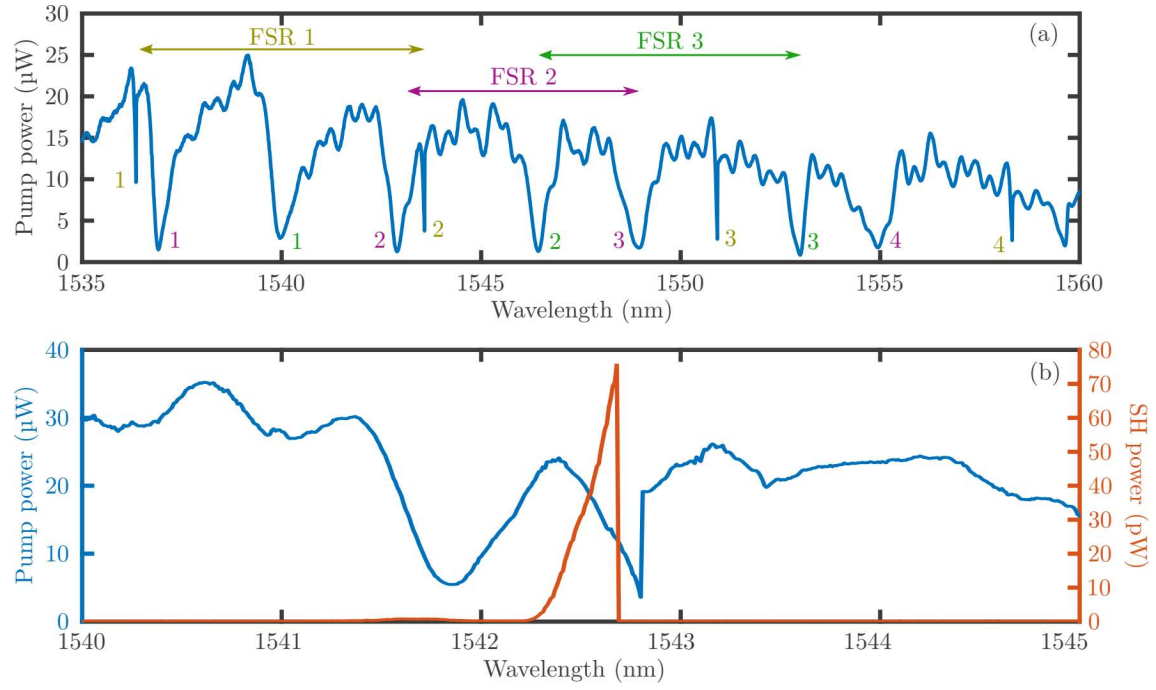


Figure 4.12: Measure of the transmission of the pump in the structure (a). Three different FSR are present here and pictures with different colours. The different peaks have been numbered according to the mode they belong to, for better visualization. A measure of the SH power, as well as the pump transmission (b) as a function of the pump wavelength, are also presented here.

We can notice in this figure that there are different resonances, and we were able to measure three different FSR. Indeed, the first FSR has been measured to be 7.23 nm which corresponds to the TE_{00} fundamental mode. The theoretical FSR of this mode is 7.46 nm from the finite difference eigenmode (FDE) solver employed. The second one corresponds to the TE_{10} as the FSR has been measured to be 5.98 nm and the last one measured has a FSR of 6.48 nm which correspond to the TM_{00} (FSR 3). It is possible to confirm their nature as it fits with the theoretical FSR extracted from our solver. Indeed, for these two other modes, the FSR are 6.03 nm for the TE_{10} and 6.39 nm for the TM_{00} . We can see that the TE_{00} resonances can be recognized from their particular sharpness compared to the others. As we have seen before, this means that the finesse is higher for this mode and so this mode stay longer in the cavity than the two others.

On another hand, a measurement of the SH has been performed as a function of the pump wavelength. The SH has been observed at a TE_{00} resonance. The thing to notice here is the particular shape of the SH power. It is a ramp shape that has already been observed in the case of microcavities [40]. It seems to be a thermal drift of the resonance. And one way to be sure of it is to perform the wavelength sweep in the other direction. As it was performed from the shorter to the higher wavelength in this measure (forward direction), the idea has been to perform the same measurement in the backward direction. The result can be seen in fig 4.13.

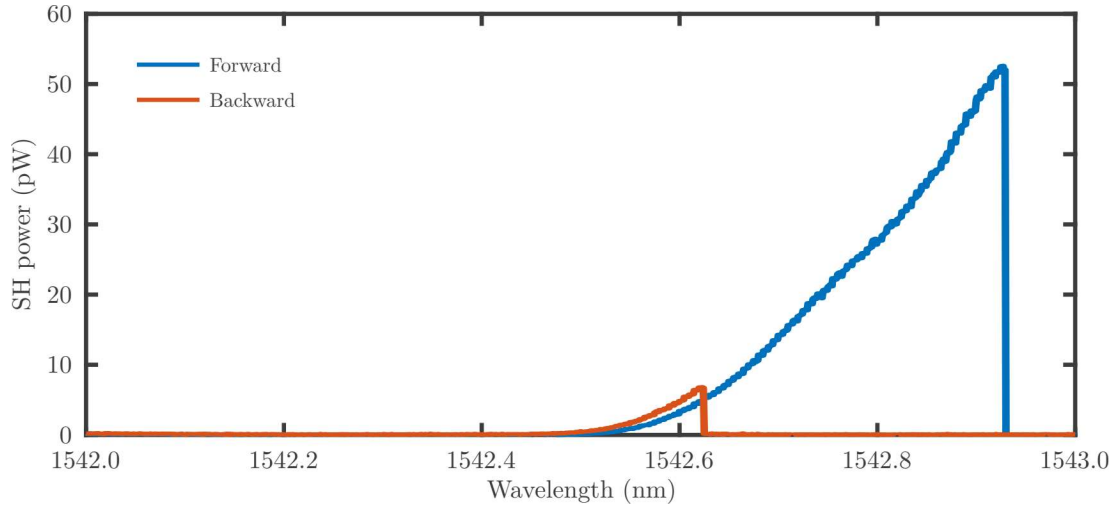


Figure 4.13: Measures of the SH power in the forward and backward direction of the wavelength sweep

We can find here the same results as reported in this paper [41]. Except for an overshoot during the backward sweep that hasn't been observed, the result fits well with the theoretical predictions and other experimental references [40, 42]. We can explain the fact that we don't observe the overshoot by a too low resolution.

4.2.3.3 Research of the two quasi-phase matching points

It is of interest to be able to also measure the other QPM point from this ring. This would show that the results from the simulations are correct, and it's also something that has never been measured to the best of my knowledge. A wavelength sweep on a larger scale has thus been performed in this waveguide as it is shown in fig. 4.14.

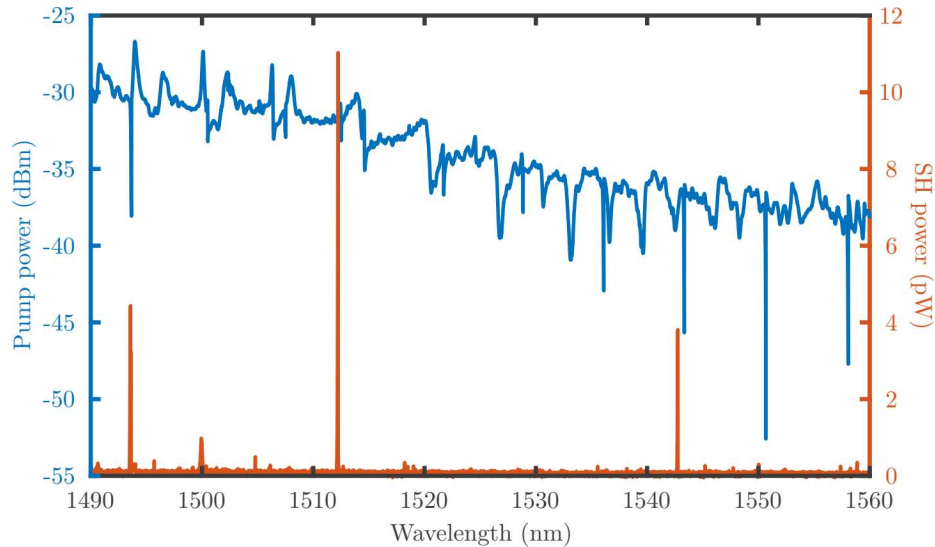


Figure 4.14: Large measure of the pump transmission and the SH power in the ring.

As we already saw in fig. 4.12, the ring measured is quite multimodal. This last measurement confirms and reveals that it is not possible to find this other QPM. Indeed, due to the unclear transmission measured, we cannot be certain of the mode that generates the

SH that we are looking for. This is a motivation to look for another ring (R2) that should be more suitable. This previous ring (R1) was the first one to be focused on as it was measured before to be the one with the best quality factor from the run. By fitting the resonance with a Lorentzian function as shown in fig. 4.15(a), we found a quality factor of 28200 for this ring.

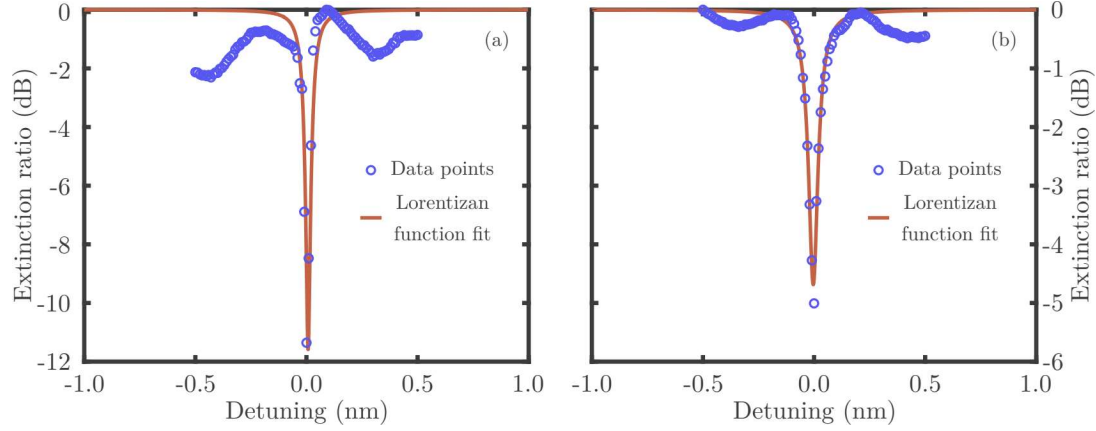


Figure 4.15: Fit of the data points measured of the resonance study for the SHG of the first ring (R1) used by a Lorentzian function (a) and for the second ring (R2) used (b).

It was also possible to extract the linear loss of the ring as explained in 4.1.1. In this ring, linear loss around 8 dB/cm has been extracted from the fit. A coupling coefficient $k^2 = 2.8 \%$ was also extracted from this fit, and so we also have $r^2 = 97.2 \%$.

We change to another ring (R2), which possess the same dimensions as the first one to find one with a better transmission spectrum but the same parameters for the SHG. The only difference is that the gap between the bus waveguide and the ring is smaller with this new one as it goes from 250 nm on the previous one to 200 nm with this one. For this one, a quality factor extracted from the fit shown in fig. 4.15(b) of 18000 was extracted while the linear loss is also measured to be around 8 dB/cm. The coupling coefficient was measured to be $k^2 = 5 \%$ and so the transmission is $r^2 = 95 \%$. This means that more light is coupled from the bus to the ring, but this also holds the other way around. So the light doesn't stay in this ring as long as in the other one.

A large wavelength sweep range measurement was performed on this ring and is displayed in fig. 4.16.

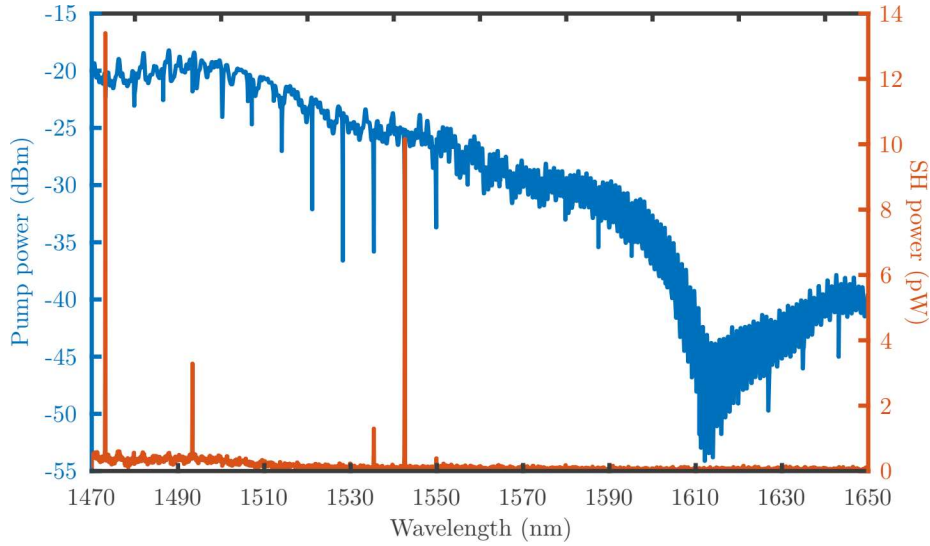


Figure 4.16: Measure of the pump transmission and the SH power in the second ring studied.

We can see in this figure that the resonances obtained are cleaner for the whole range of measurement, which should make the results more certain than before.

Another sweep is thus performed to measure the SH as it was done before. The result of the measurement can be seen in fig. 4.16. We can here see four different peaks appearing here at different wavelengths: 1473 nm, 1493 nm, 1535 nm and 1543 nm.

The FSR is easier to measure and has been measured to be equal to 7.14 nm, which corresponds to the expected FSR for the fundamental TE mode. The SH peaks thus seem to correspond to QPM for the pump mode considered. The simulation results have shown that we expect a QPM between the TE₀₀ pump mode and the TM₃₀ SH mode at 1505.9 nm and 1555.1 nm. A result that we don't find here. However, if we consider an imperfect ring dimension, especially if we consider that the width and the height are not the ones expected, we can get closer to the measurements.

Width (nm)	Height (nm)	TE ₃₀ QPM wavelength for		TM ₃₀ QPM wavelength for	
		$\Delta m = -2$	$\Delta m = +2$	$\Delta m = 2$	$\Delta m = +2$
840	290	1504.92	1548.40	1493.22	1539.09
	300	1491.21	1534.99	1496.13	1543.21
	310	1479.79	1522.82	1494.19	1542.18
850	290	1519.81	1565.23	1500.02	1546.40
	300	1505.95	1551.09	1503.10	1550.08
	310	1494.19	1539.09	1503.94	1553.62
860	290	1534.99	1581.34	1503.94	1555.72
	300	1520.81	1567.35	1513.82	1563.10
	310	1508.86	1554.67	1513.82	1563.10

Table 4.2: Results of the QPM found for structures with different widths and heights around the values of the theoretical dimensions. The simulations have been performed for the two SH modes that presented a QPM with a TE₀₀ pump.

From the simulations in table 4.2, we can see that, for a waveguide dimension of 840 nm wide and 310 nm high, simulations results get close to the results obtained in fig. 4.16. The efficiency for both QPM, as we have seen in table 4.1, is however quite different. The

numerical efficiency for the QPM with the TM_{30} SH mode is at least 10 times higher than for the TE_{30} mode. The resulting measurement in fig. 4.16 doesn't show this at all, but more the opposite.

The extraction of the conversion efficiency is quite difficult here. The grating couplers have been fabricated for a fundamental TE mode around 1550 nm, it is tough to evaluate the coupling from a higher-order mode at the SH wavelength in the output fibre. Furthermore, the coupling for one higher-order mode to another in the tapered part of the waveguide can be quite different, and it could explain the inconsistency of results measured so far. For a convincing measurement of the conversion efficiency, a way to do this is to cleave one of the grating couplers. This way, the SH will be collected from a facet and the power could be evaluated more accurately as the coupling will be the same for both SH modes.

In this chapter, we have shown how it is possible to describe the SHG process in nanorings to obtain the most efficient process possible. Simulations have been performed around it and experimental results have been presented. There is still work to be done on this last point to fully connect it to the theoretical models and simulations, but the first results obtained are promising about the nature of the process.

Bibliography

1. Kneubühl, F. K. & Sigrist, M. W. *Laser* de. ISBN: 978-3-8351-0032-9. <http://link.springer.com/10.1007/978-3-322-99688-6> (2021) (Vieweg+Teubner Verlag, Wiesbaden, 2005).
2. Kogelnik, H. & Li, T. *Laser Beams and Resonators*. en, 18.
3. Leindecker, N., Marandi, A., Byer, R. L. & Vodopyanov, K. L. Broadband degenerate OPO for mid-infrared frequency comb generation. en. *Optics Express* **19**, 6296. ISSN: 1094-4087. <https://www.osapublishing.org/oe/abstract.cfm?uri=oe-19-7-6296> (2020) (Mar. 2011).
4. Stern, B., Ji, X., Dutt, A. & Lipson, M. Compact narrow-linewidth integrated laser based on a low-loss silicon nitride ring resonator. en. *Optics Letters* **42**, 4541. ISSN: 0146-9592, 1539-4794. <https://www.osapublishing.org/abstract.cfm?URI=ol-42-21-4541> (2021) (Nov. 2017).
5. Hryniewicz, J., Absil, P., Little, B., Wilson, R. & Ho, P.-T. Higher order filter response in coupled microring resonators. en. *IEEE Photonics Technology Letters* **12**, 320–322. ISSN: 1041-1135, 1941-0174. <http://ieeexplore.ieee.org/document/826927/> (2021) (Mar. 2000).
6. Little, B., Chu, S., Haus, H., Foresi, J. & Laine, J.-P. Microring resonator channel dropping filters. en. *Journal of Lightwave Technology* **15**, 998–1005. ISSN: 0733-8724. <http://ieeexplore.ieee.org/document/588673/> (2021) (June 1997).
7. Little, B., Chu, S., Pan, W. & Kokubun, Y. Microring resonator arrays for VLSI photonics. en. *IEEE Photonics Technology Letters* **12**, 323–325. ISSN: 1041-1135, 1941-0174. <http://ieeexplore.ieee.org/document/826928/> (2021) (Mar. 2000).
8. Rabiei, P., Steier, W., Cheng Zhang & Dalton, L. Polymer micro-ring filters and modulators. en. *Journal of Lightwave Technology* **20**, 1968–1975. ISSN: 0733-8724. <http://ieeexplore.ieee.org/document/1161608/> (2021) (Nov. 2002).
9. Lin, S. *et al.* Vertical-coupled high-efficiency tunable III-V- CMOS SOI hybrid external-cavity laser. en. *Optics Express* **21**, 32425. ISSN: 1094-4087. <https://www.osapublishing.org/oe/abstract.cfm?uri=oe-21-26-32425> (2021) (Dec. 2013).
10. Sun, Y. & Fan, X. Optical ring resonators for biochemical and chemical sensing. en. *Analytical and Bioanalytical Chemistry* **399**, 205–211. ISSN: 1618-2642, 1618-2650. <http://link.springer.com/10.1007/s00216-010-4237-z> (2021) (Jan. 2011).
11. Heebner, J., Grover, R. & Ibrahim, T. *Optical Microresonators: Theory, Fabrication, and Applications* English. OCLC: 1112516122. ISBN: 978-0-387-73068-4. <https://doi.org/10.1007/978-0-387-73068-4> (2021) (2008).

12. Bogaerts, W. *et al.* Silicon microring resonators. en. *Laser & Photonics Reviews* **6**, 47–73. ISSN: 18638880. <http://doi.wiley.com/10.1002/lpor.201100017> (2021) (Jan. 2012).
13. Melloni, A., Costa, R., Monguzzi, P. & Martinelli, M. Ring-resonator filters in silicon oxynitride technology for dense wavelength-division multiplexing systems. en. *Optics Letters* **28**, 1567. ISSN: 0146-9592, 1539-4794. <https://www.osapublishing.org/abstract.cfm?URI=ol-28-17-1567> (2021) (Sept. 2003).
14. Pelc, J. S. *et al.* Picosecond all-optical switching in hydrogenated amorphous silicon microring resonators. en. *Optics Express* **22**, 3797. ISSN: 1094-4087. <https://www.osapublishing.org/oe/abstract.cfm?uri=oe-22-4-3797> (2021) (Feb. 2014).
15. Xue, X. *et al.* Programmable Single-Bandpass Photonic RF Filter Based on Kerr Comb from a Microring. en. *Journal of Lightwave Technology* **32**, 3557–3565. ISSN: 0733-8724, 1558-2213. <https://ieeexplore.ieee.org/document/6774856/> (2021) (Oct. 2014).
16. Tang, Y., Gong, Z., Liu, X. & Tang, H. X. Widely separated optical Kerr parametric oscillation in AlN microrings. en. *Optics Letters* **45**, 1124. ISSN: 0146-9592, 1539-4794. <https://www.osapublishing.org/abstract.cfm?URI=ol-45-5-1124> (2021) (Mar. 2020).
17. Jung, H., Stoll, R., Guo, X., Fischer, D. & Tang, H. X. Green, red, and IR frequency comb line generation from single IR pump in AlN microring resonator. en. *Optica* **1**, 396. ISSN: 2334-2536. <https://www.osapublishing.org/optica/abstract.cfm?uri=optica-1-6-396> (2021) (Dec. 2014).
18. Kuyken, B., Billet, M., Leo, F., Yvind, K. & Pu, M. Octave-spanning coherent supercontinuum generation in an AlGaAs-on-insulator waveguide. en. *Optics Letters* **45**, 603. ISSN: 0146-9592, 1539-4794. <https://www.osapublishing.org/abstract.cfm?URI=ol-45-3-603> (2020) (Feb. 2020).
19. Weng, H. *et al.* Near octave-spanning perfect soliton crystals in AlN microresonators. en, 6.
20. Stern, B., Ji, X., Okawachi, Y., Gaeta, A. L. & Lipson, M. Battery-operated integrated frequency comb generator. en. *Nature* **562**, 401–405. ISSN: 0028-0836, 1476-4687. <http://www.nature.com/articles/s41586-018-0598-9> (2020) (Oct. 2018).
21. Chang, L. *et al.* Ultra-efficient frequency comb generation in AlGaAs-on-insulator microresonators. en. *Nature Communications* **11**, 1331. ISSN: 2041-1723. <http://www.nature.com/articles/s41467-020-15005-5> (2020) (Dec. 2020).
22. Kippenberg, T. J., Holzwarth, R. & Diddams, S. A. Microresonator-Based Optical Frequency Combs. en. *Science* **332**. Number: 6029 Reporter: Science, 555–559. ISSN: 0036-8075, 1095-9203. <http://www.sciencemag.org/cgi/doi/10.1126/science.1193968> (2019) (Apr. 2011).
23. Diddams, S. A. The evolving optical frequency comb [Invited]. en. *Journal of the Optical Society of America B* **27**. Number: 11 Reporter: Journal of the Optical Society of America B, B51. ISSN: 0740-3224, 1520-8540. <https://www.osapublishing.org/abstract.cfm?URI=josab-27-11-B51> (2019) (Nov. 2010).
24. Haus, H. A. *Waves and fields in optoelectronics* eng. OCLC: 9465383. ISBN: 978-0-13-946053-1 (Prentice-Hall, Englewood Cliffs, NJ, 1984).

25. Rodriguez, A., Soljacic, M., Joannopoulos, J. D. & Johnson, S. G. $\chi(2)$ and $\chi(3)$ harmonic generation at a. en, 16 (2007).
26. Bi, Z.-F. *et al.* High-efficiency second-harmonic generation in doubly-resonant $\chi^{(2)}$ microring resonators. en. *Optics Express* **20**, 7526. ISSN: 1094-4087. <https://www.osapublishing.org/oe/abstract.cfm?uri=oe-20-7-7526> (2020) (Mar. 2012).
27. Dumeige, Y. & Féron, P. Whispering-gallery-mode analysis of phase-matched doubly resonant second-harmonic generation. en. *Physical Review A* **74**, 063804. ISSN: 1050-2947, 1094-1622. <https://link.aps.org/doi/10.1103/PhysRevA.74.063804> (2020) (Dec. 2006).
28. Lu, J., Li, M., Zou, C.-L., Al Sayem, A. & Tang, H. X. Toward 1% single-photon anharmonicity with periodically poled lithium niobate microring resonators. en. *Optica* **7**, 1654. ISSN: 2334-2536. <https://www.osapublishing.org/abstract.cfm?URI=optica-7-12-1654> (2021) (Dec. 2020).
29. Chen, J.-Y. *et al.* Efficient Frequency Doubling with Active Stabilization on Chip. en. *arXiv:2103.00309 [physics, physics:quant-ph]*. arXiv: 2103.00309. <http://arxiv.org/abs/2103.00309> (2021) (Feb. 2021).
30. Logan, A. D. *et al.* 400%/W second harmonic conversion efficiency in 14 μ m-diameter gallium phosphide-on-oxide resonators. en. *Optics Express* **26**, 33687. ISSN: 1094-4087. <https://www.osapublishing.org/abstract.cfm?URI=oe-26-26-33687> (2020) (Dec. 2018).
31. Schneider, K. *et al.* Gallium Phosphide-on-Silicon Dioxide Photonic Devices. en. *Journal of Lightwave Technology* **36**, 2994–3002. ISSN: 0733-8724, 1558-2213. <https://ieeexplore.ieee.org/document/8344796/> (2020) (July 2018).
32. Martin, A. *et al.* Nonlinear gallium phosphide nanoscale photonics [Invited]. en. *Photonics Research* **6**, B43. ISSN: 2327-9125. <https://www.osapublishing.org/abstract.cfm?URI=prj-6-5-B43> (2021) (May 2018).
33. Tilmann, B. *et al.* Nanostructured amorphous gallium phosphide on silica for nonlinear and ultrafast nanophotonics. en. *Nanoscale Horizons* **5**, 1500–1508. ISSN: 2055-6756, 2055-6764. <http://xlink.rsc.org/?DOI=DONH00461H> (2021) (2020).
34. Lake, D. P. *et al.* Efficient telecom to visible wavelength conversion in doubly resonant gallium phosphide microdisks. en. *Applied Physics Letters* **108**, 031109. ISSN: 0003-6951, 1077-3118. <http://aip.scitation.org/doi/10.1063/1.4940242> (2021) (Jan. 2016).
35. Haynes, W. M. *CRC handbook of chemistry and physics: a ready-reference book of chemical and physical data*. English. OCLC: 1082343666. ISBN: 978-1-4987-5428-6 (2017).
36. Shoji, I., Kondo, T., Kitamoto, A., Shirane, M. & Ito, R. Absolute scale of second-order nonlinear-optical coefficients. en. *Journal of the Optical Society of America B* **14**, 2268. ISSN: 0740-3224, 1520-8540. <https://www.osapublishing.org/abstract.cfm?URI=josab-14-9-2268> (2021) (Sept. 1997).
37. Anthur, A. P. *et al.* Second harmonic generation in gallium phosphide nano-waveguides. en. *Optics Express* **29**, 10307. ISSN: 1094-4087. <https://www.osapublishing.org/abstract.cfm?URI=oe-29-7-10307> (2021) (Mar. 2021).
38. Taillaert, D. *et al.* Grating Couplers for Coupling between Optical Fibers and Nanophotonic Waveguides. en. *Japanese Journal of Applied Physics* **45**, 6071–6077. ISSN: 0021-4922, 1347-4065. <https://iopscience.iop.org/article/10.1143/JJAP.45.6071> (2021) (Aug. 2006).

39. Stern, I., Carosi, G., Sullivan, N. & Tanner, D. Avoided Mode Crossings in Cylindrical Microwave Cavities. en. *Physical Review Applied* **12**, 044016. ISSN: 2331-7019. <https://link.aps.org/doi/10.1103/PhysRevApplied.12.044016> (2021) (Oct. 2019).
40. Kuo, P. S., Bravo-Abad, J. & Solomon, G. S. Second-harmonic generation using -quasi-phasematching in a GaAs whispering-gallery-mode microcavity. en. *Nature Communications* **5**, 3109. ISSN: 2041-1723. <http://www.nature.com/articles/ncomms4109> (2020) (May 2014).
41. Carmon, T., Yang, L. & Vahala, K. J. Dynamical thermal behavior and thermal selfstability of microcavities. en, 9 (2004).
42. Shankar, R., Bulu, I., Leijssen, R. & Lončar, M. Study of thermally-induced optical bistability and the role of surface treatments in Si-based mid-infrared photonic crystal cavities. en. *Optics Express* **19**, 24828. ISSN: 1094-4087. <https://www.osapublishing.org/oe/abstract.cfm?uri=oe-19-24-24828> (2021) (Nov. 2011).

Chapter 5

Conclusion and perspectives

In this thesis, we have studied the second-order nonlinear properties of two III-V materials: InGaP and GaP. The two belong to the same crystallographic structure (zinc-blende) and has high second-order nonlinear susceptibility. On top of that, they exhibit a high refractive index, comparable to the one of Si. This last point induces good confinement of the light in the structure and thus stronger nonlinear effects. Being really promising materials for second-order nonlinear effects, the thesis focused on them.

The first one, InGaP, has been used for the production of nanowires. In these structures, we have studied the type I and the type II phase-matching cases. A model has been developed for the type I case [1, 2] and has been adapted for the type II case [3]. The models take care of the longitudinal component of the electric fields of the pump and the SH, a crucial element in such tightly confined structures. Thanks to this, we were able to find pump wavelengths for which a PM occurs. Without paying attention to the longitudinal component, these PM would have stayed out of the study as resulting in a null overlap integral of the two modes. Two different fabrications processes have been used for the production of those structures. The final structures fabricated have been placed on an experimental setup. While exhibits high linear loss at 1550 nm (12 and 22 dB/cm for two different structures), they also reveal interesting results. The SH power as a function of the wavelength and as a function of the pump power was a good indicator of the nature of the process. Furthermore, a measurement of the profiles of the modes confirmed the expected couple of pump and SH modes involved in the interaction. The conversion efficiency was however lower than the expectations from the simulations. The high linear losses at the pump and the SH wavelength (64 dB/cm for a structure and 90 dB/cm for the other) are really limiting the possibilities here.

The other material studied, GaP, has been used in the case of nanorings. The fabrication process for these rings was different as transfer printing was used here instead of the bonding technique. A model has been applied to calculate the efficiency in nanorings made of GaP material [4, 5]. Let's remind that, in this case, there is two QPM for the same couple of modes instead of one in nanowires. The first result tends to show the validity of the model as two QPM have been found and could fit with the theory. The efficiency is nevertheless not possible to calculate in the current state. The SH power has been measured at the output of a grating coupler designed for a 1550 nm fundamental TE mode. The output coupling for a SH higher-order mode is impossible to evaluate currently. Linear loss as high as 8 dB/cm has been extracted from a fit of the resonances at the pump wavelength. This is still a high linear loss compared to the losses below 1 dB/cm that can be found in Si [6].

Linear losses are limiting parameters in these experiments. Being able to put in place

a reliable process that will drop the linear loss below 2 dB/cm will be much enjoyable. The high linear losses in these materials are a reason of other solutions. For instance, propagation can be in another low-loss medium (like Si or SiN) at first and then coupled into the III-V [7, 8]. Concerning a short-range objective, removing one of the grating couplers from the ring structure could allow measuring the efficiency of the SHG process in the ring. Also, efficient PM in nanowire have been found and not measured yet due to the small thickness required. Experiments to measure a few of them would be of interest to confirm once more the models deployed for III-V nanowires.

With further studies and fabrication development, super-efficient SHG on-chip could be expected. This will be useful for a lot of applications such as quantum circuits [9] and frequency combs stabilization [10, 11]. We could even go further in the frequency comb generation and aim for a second-order nonlinear frequency comb as predicted [12]. This could generate broadband frequency combs compared to the third-order nonlinear case. And it could also be a standalone device capable to stabilize the comb by itself.

To conclude, we provided here a way to estimate SHG in integrated structures and confirmed the models by experiments. III-V materials present interesting properties for nonlinear photonics application but still present too high linear loss. Studies to reduce this loss are required to transform III-V materials into a nonlinear photonics champion.

Bibliography

1. Poulvellarie, N. *et al.* Second-harmonic generation enabled by longitudinal electric-field components in photonic wire waveguides. en. *Physical Review A* **102**, 023521. ISSN: 2469-9926, 2469-9934. <https://link.aps.org/doi/10.1103/PhysRevA.102.023521> (2020) (Aug. 2020).
2. Ciret, C. *et al.* Influence of longitudinal mode components on second harmonic generation in III-V-on-insulator nanowires. en. *Optics Express* **28**, 31584. ISSN: 1094-4087. <https://www.osapublishing.org/abstract.cfm?URI=oe-28-21-31584> (2020) (Oct. 2020).
3. Poulvellarie, N. *et al.* Efficient type II second harmonic generation in an indium gallium phosphide on insulator wire waveguide aligned with a crystallographic axis. en. *Optics Letters* **46**, 1490. ISSN: 0146-9592, 1539-4794. <https://www.osapublishing.org/abstract.cfm?URI=ol-46-6-1490> (2021) (Mar. 2021).
4. Bi, Z.-F. *et al.* High-efficiency second-harmonic generation in doubly-resonant $\chi^{(2)}$ microring resonators. en. *Optics Express* **20**, 7526. ISSN: 1094-4087. <https://www.osapublishing.org/oe/abstract.cfm?uri=oe-20-7-7526> (2020) (Mar. 2012).
5. Rodriguez, A., Soljacic, M., Joannopoulos, J. D. & Johnson, S. G. $\chi^{(2)}$ and $\chi^{(3)}$ harmonic generation at a. en, 16 (2007).
6. Li, G. *et al.* Ultralow-loss, high-density SOI optical waveguide routing for macrochip interconnects. en. *Opt. Express* **20**, 12035. ISSN: 1094-4087. <https://www.osapublishing.org/oe/abstract.cfm?uri=oe-20-11-12035> (2021) (May 2012).
7. Tran, M. *et al.* Ultra-Low-Loss Silicon Waveguides for Heterogeneously Integrated Silicon/III-V Photonics. en. *Applied Sciences* **8**, 1139. ISSN: 2076-3417. <http://www.mdpi.com/2076-3417/8/7/1139> (2021) (July 2018).
8. Pu, M., Liu, L., Ou, H., Yvind, K. & Hvam, J. M. Ultra-low-loss inverted taper coupler for silicon-on-insulator ridge waveguide. en. *Optics Communications* **283**, 3678–3682. ISSN: 00304018. <https://linkinghub.elsevier.com/retrieve/pii/S0030401810005018> (2021) (Oct. 2010).
9. Zaske, S. *et al.* Visible-to-Telecom Quantum Frequency Conversion of Light from a Single Quantum Emitter. en. *Phys. Rev. Lett.* **109**, 147404. ISSN: 0031-9007, 1079-7114. <https://link.aps.org/doi/10.1103/PhysRevLett.109.147404> (2020) (Oct. 2012).
10. Diddams, S. A. *et al.* Direct Link between Microwave and Optical Frequencies with a 300 THz Femtosecond Laser Comb. en. *Phys. Rev. Lett.* **84**, 5102–5105. ISSN: 0031-9007, 1079-7114. <https://link.aps.org/doi/10.1103/PhysRevLett.84.5102> (2020) (May 2000).
11. Okawachi, Y. *et al.* Octave-spanning frequency comb generation in a silicon nitride chip. en. *Optics Letters* **36**, 3398. ISSN: 0146-9592, 1539-4794. <https://www.osapublishing.org/abstract.cfm?URI=ol-36-17-3398> (2021) (Sept. 2011).

12. Leo, F. *et al.* Frequency-comb formation in doubly resonant second-harmonic generation. en. *Physical Review A* **93**, 043831. issn: 2469-9926, 2469-9934. <https://link.aps.org/doi/10.1103/PhysRevA.93.043831> (2020) (Apr. 2016).